UNRAVELING THE RHEOLOGY-PRINTABILITY RELATIONSHIP OF 3D PRINTABLE BIOMATERIALS FOR FOOD APPLICATION

BY

THÉO CLAUDE ROLAND OUTREQUIN

A DISSERTATION SUBMITTED IN PARTIAL FULFILLMENT OF THE REQUIREMENTS FOR THE DEGREE OF DOCTOR OF PHILOSOPHY (ENGINEERING AND TECHNOLOGY)
SIRINDHORN INTERNATIONAL INSTITUTE OF TECHNOLOGY
THAMMASAT UNIVERSITY
ACADEMIC YEAR 2024

THAMMASAT UNIVERSITY

SIRINDHORN INTERNATIONAL INSTITUTE OF TECHNOLOGY

DISSERTATION

BY

THÉO CLAUDE ROLAND OUTREQUIN

ENTITLED

UNRAVELING THE RHEOLOGY-PRINTABILITY RELATIONSHIP
OF 3D PRINTABLE BIOMATERIALS FOR FOOD APPLICATION

was approved as partial fulfillment of the requirements for
the degree of Doctor of Philosophy (Engineering and Technology)

on October 22, 2024

Chairperson	(Assistant Professor Wanwipa Siriwatwechakul, Ph.D.)
Member and Advisor	(Associate Professor Paiboon Sreearunothai, Ph.D.)
Member and Co-advisor	(Chaiwut Gamonpilas, Ph.D.)
Member	(Associate Professor Pakorn Opaprakasit, Ph.D.)
Member	(Professor Cattaleeya Pattamaprom, Ph.D.)
Director	(Professor Pruettha Nanakorn, D.Eng.)

Dissertation Title	UNRAVELING THE RHEOLOGY-PRINTABILITY RELATIONSHIP OF 3D PRINTABLE BIOMATERIALS FOR FOOD APPLICATION
Author	Théo Claude Roland Outrequin
Degree	Doctor of Philosophy (Engineering and Technology)
Faculty/University	Sirindhorn International Institute of Technology/ Thammasat University
Dissertation Advisor	Associate Professor Paiboon Sreearunothai, Ph.D.
Dissertation Co-Advisor	Chaiwut Gamonpilas, Ph.D.
Academic Years	2024

ABSTRACT

The attraction toward 3D food printing is growing significantly since the development of extrusion-based 3D printing technology. Biopolymers are frequently incorporated into the food ink formulation to modify the rheological properties and make the formulation processable, significantly impacting the ability of food products to be printed. The 3D food printing process comprises four stages: (a) the ink preparation, (b) the ink extrusion, (c) the ink deposition, and finally (d) the formation of the 3D structure.

From a recent literature review, it has been demonstrated that the extrudability of an ink is controlled by its yield stress and rheological flow parameters, which may be obtained from the Power Law or the Herschel-Bulkley model. These parameters directly influence the minimal applied pressure required to initiate the ink's flow. Moreover, an acceptable range of viscoelastic properties resulting in stable 3D printed structure formation has been drawn. The combination of these rheological parameters

within the biopolymers-based ink formulation remains an important challenge. Printing and rheological parameters possess a strong influence on the printed object. The control over the ink deposition step is also important to obtain printed objects with dimensions closely aligned to the intended dimensions.

The first part of this study aims to understand the impact of the rheological properties on the fidelity of the printed object presented by the printed line width. Having a printed line width close to the one prepared in the model is essential to obtain a correct shape fidelity as the extrusion-based 3D printing technology corresponds to the deposition of material layer by layer. In this work, the factors affecting material spreading in 3D printing, focusing on pectin inks, are investigated. These factors include rheological properties, such as flow properties and complex modulus, which significantly influence the spreading ratio, with higher concentrations reducing spreading but complicating extrusion. The impact of printing parameters, such as nozzle diameter, pressure, and speed, on the spreading ratio were also analyzed. Balancing these factors is crucial for achieving target dimensions, considering the trade-off between reduced spreading and potential extrusion challenges. Machine learning regressions are applied to establish a robust framework comprising all the previous parameters for precise ink deposition control, advancing biomaterial 3D printing, and fostering innovation in fabricating functional, dimensionally accurate objects. The Extra Tree regression model with four features (pressure, speed, G_0^*, and n) demonstrated that the rheological properties accounted for 92% of the weight in the spreading variation, whereas the printing parameters contributed to 8%.

After studying the dimensional changes in 2D lines, a deeper focus on the parameters yielding a correct formation of a 3D structure is made. Mung bean protein isolate was added to the pectin solution to form an ink formulation with enhanced rheological properties. Moreover, the addition of protein powder promoted the development of ink with improved nutritional benefits to fabricate high-protein 3D-printed snacks. The dimensional accuracy of the printed shape is improved with the increasing protein content, as it yields stronger viscoelastic properties. Machine learning classification was utilized as a quality control tool to assess the printability of a formulation. This approach classified print samples as either 'within range' or 'out of range' based on their features and deviations, with an acceptable error range set at 10%

deviation from the target height. Additionally, the impact of baking on the shape of the printed object was examined, revealing that formulations with higher biopolymer content were more effective at preserving the shape of the 3D-printed baked snack.

Lastly, the combination of 3D food printing and Artificial Intelligence (AI) is discussed as food additive manufacturing technology has advanced rapidly to help promote the creation of diverse and customized food products. However, scaling up this process remains challenging, thus limiting its use in the food industry. Integrating AI technology into the printing process presents transformative opportunities for the food industry, especially by enhancing personalized nutrition and production efficiency. AI-driven food ink development can enable the precise formulation of inks tailored to specific dietary needs, improving both nutritional value and user satisfaction while optimizing functional properties for efficient processability. AI-driven selection of printing parameters based on the knowledge of food ink rheological properties could accelerate research and development, thus fostering innovation. Additionally, real-time monitoring and automated adjustments during printing can enhance process efficiency and ease the final quality control. Overall, the adoption of AI combined with automation in 3D food printing is foreseen to revolutionize the food industry, offering scalability to the printing process to better accommodate evolving consumer demands.

Keywords: 3D food printing, Rheology, Biopolymers, Additive manufacturing, Food proteins, Artificial intelligence, Machine learning, Smart processing

ACKNOWLEDGEMENTS

I would like to start by expressing my gratitude to my advisors, Dr. Chaiwut Gamonpilas, Asst. Prof. Dr. Wanwipa Siriwatwechakul, and Assoc. Prof. Dr. Paiboon Sreearunothai, for their support, invaluable guidance, and encouragement throughout the course of my research. Their expertise across various fields and patience have been instrumental in completing this thesis and in all the learning opportunities provided. Then, I would like to acknowledge Sirindhorn International Institute of Technology (SIIT), Thammasat University (TU), and the National Science and Technology Development Agency (NSTDA) for offering financial support through the Excellent Foreign Student (EFS) and the TU-NSTDA Excellent Research Graduate Scholarship. I appreciate the assistance offered by the National Metals and Materials Technology Center (MTEC) and, more precisely, by the Food Materials Research Team (FOMT) for providing the resources and facilities necessary for this research. I thank all my colleagues at MTEC, especially Akapong Kongjaroen, for providing insights on rheometry and food biopolymers. I also thank Asst. Prof. Dr. Somrudee Deepaisarn for introducing me to the exciting field of machine learning and AI. I express my gratitude to all SIIT professors and staff who, in one way or another, contributed to the success of this thesis.

I would also like to thank my friends Thilina Rajeendre Katugampalage and Dr. Preeti Waribam for the academic conversations we shared, but mostly for the daily conversations, beers, food, and trips we shared.

This journey would not have been possible without my family's support, encouragement, and understanding. Being a first-generation doctoral graduate was a challenging but rewarding experience. Butsaya, your encouragement and trust in me provided the strength I needed to persevere and having you by my side was invaluable.

"It's the job that's never started as takes longest to finish" – J.R.R. Tolkien.

Théo Claude Roland Outrequin

TABLE OF CONTENTS

	Page
ABSTRACT	(1)
ACKNOWLEDGEMENTS	(4)
LIST OF TABLES	(10)
LIST OF FIGURES	(12)
LIST OF SYMBOLS/ABBREVIATIONS	(18)
CHAPTER 1 INTRODUCTION	1
1.1 The rise of 3D food printing	1
1.2 The current technological landscape in 3D food printing	2
1.3 Motivation and goal of the thesis	4
1.4 Research objectives and scope	5
1.5 Thesis organization	6
CHAPTER 2 REVIEW OF LITERATURE	8
2.1 Extrusion-based 3D printing of food biopolymers: A highlight on the important rheological parameters to reach printability	8
2.1.1 Extrusion of food inks	11
2.1.1.1 Yield stress	11
2.1.1.2 Flow properties	17
2.1.2 Forming a stable 3D food structure	21
2.1.3 Importance of the ink's thermal behavior on the printing process	28
2.1.4 Other important rheological phenomena	31
2.1.4.1 Die swell	31
2.1.4.2 Extensional flow/viscosity	36
2.1.5 Conclusion and outlook	38

2.2 Parameters impacting the shape stability of printed objects 38
2.2.1 Parameters relevant to the printability of filament 39
2.2.2 Parameters relevant to the formation of the 3D structure 40
2.2.2.1 Dimensional accuracy 40
2.2.2.2 Stability of the printed object 42
2.2.3 Effect of the post-processing on the shape of the printed object 43
2.2.4 Summary and perspectives 45

CHAPTER 3 MACHINE LEARNING ASSISTED EVALUATION OF THE FILAMENT SPREADING DURING EXTRUSION-BASED 3D FOOD PRINTING: IMPACT OF THE RHEOLOGICAL AND PRINTING PARAMETERS 46
3.1 Introduction 46
3.2 Materials and methods 49
3.2.1 Materials and ink preparation 49
3.2.2 Rheological experiments 49
3.2.3 Line printing and spreading determination 50
3.2.4 Machine learning 52
3.3 Results and discussion 53
3.3.1 Rheological analysis of the pectin-based inks 53
3.3.2 Effect of the rheological properties on the spreading ratio 57
3.3.3 Effect of the printing parameters on the spreading ratio 60
3.3.4 Machine learning assessment of the filament spreading 63
3.4 Conclusion 69

CHAPTER 4 3D PRINTING OF PROTEIN-RICH PLANT-BASED SNACKS: VISCOELASTICITY AND NON-LINEAR RHEOLOGY MACHINE LEARNING BASED QUALITY CONTROL AND POST-PROCESSING 71
4.1 Introduction 71
4.2 Materials and methods 73
4.2.1 Materials 73
4.2.2 Ink preparation 73
4.2.3 Rheological analysis 73

4.2.3.1 Small Amplitude Oscillatory Shear (SAOS) 74
4.2.3.2 Large Amplitude Oscillatory Shear (LAOS) 74
4.2.4 3D food printing experiments 76
4.2.5 Printed objects analysis 77
4.2.6 Machine learning classification 78
4.2.7 Baking of 3D printed food samples 79
4.3 Results and discussion 80
4.3.1 SAOS rheological analysis 80
4.3.2 LAOS rheological analysis 83
4.3.3 Effect of the rheological properties on the shape fidelity and stability over time 92
4.3.4 Machine learning-based quality control 94
4.3.5 Formation of high protein snack: effect of baking on the fidelity of the printed objects 98
4.4 Conclusion 100

CHAPTER 5 ARTIFICIAL INTELLIGENCE ASSISTED 3D FOOD PRINTING 102
5.1 Introduction 102
5.2 AI subcategories overview 104
5.2.1 Computer Vision (CV) 104
5.2.2 Machine Learning (ML) 105
5.2.2.1 Linear Regression 106
5.2.2.2 Ridge and Lasso Regressions 106
5.2.2.3 Support Vector Machines (SVM) 106
5.2.2.4 k-Nearest Neighbors (k-NN) 106
5.2.2.5 Decision Tree (DT) 107
5.2.2.6 Random Forest (RF) 107
5.2.2.7 Other tree Models (ET, GBM, XGBoost) 107
5.2.3 Deep Learning (DL) 107
5.2.3.1 Recurrent Neural Network (RNN) 107
5.2.3.2 Convolutional Neural Network (CNN) 108
5.2.3.3 Graph Convolutional Neural Network (GNN) 108

5.2.3.4 Inverse Neural Network (INN) 108
5.3 Optimization of the food formulation using artificial intelligence tools 108
5.3.1 Improvement of the food's flavor and nutritional properties through artificial intelligence applications 109
5.3.2 Improvement of the formulation functional properties through artificial intelligence applications 112
5.4 3D food printing process monitoring and improvements using AI 113
5.4.1 AI-enhanced 3D printers and software for process monitoring 113
5.4.2 Recent developments in the field of additive manufacturing 114
5.4.3 Application to 3D food printing and future requirements 116
5.5 AI-guided post-processing and quality control of 3D printed food 121
5.5.1 Post-processing 121
5.5.2 Enhanced quality control using AI 122
5.6 Conclusion and outlook 123

CHAPTER 6 CONCLUSION 127
6.1 Summary of findings 127
6.1.1 Machine learning assisted evaluation of the filament spreading during extrusion-based 3D food printing: impact of the rheological and printing parameters 127
6.1.2 3D printing of protein-rich plant-based snacks: viscoelasticity and non-linear rheology machine learning based quality control and post-processing 128
6.1.3 Artificial intelligence assisted 3D food printing 129
6.2 Recommendation for future studies 129

REFERENCES 131

APPENDICES 155
APPENDIX A 156
APPENDIX B 157
APPENDIX C 160
APPENDIX D 163

APPENDIX E 166
APPENDIX F 169
APPENDIX G 173
APPENDIX H 177
APPENDIX I 184
APPENDIX J 186
APPENDIX K 194
APPENDIX L 195
APPENDIX M 199

BIOGRAPHY 203

LIST OF TABLES

Tables		Page
2.1	Power Law parameters determined using Phuhongsung et al. (2020) data shown in Figure 2.5.	18
2.2	Rheological values obtained from the literature for various food inks. The * indicates that the value was digitized or calculated from the authors' results.	26
2.3	Dimensional stability classification proposed by Kim et al. (2017)	43
3.1	Printing parameters used in the Chapter 3.	52
3.2	Summary of the rheological analysis of 23PT. The viscosity values are given at a shear rate of $\dot{\gamma} = 1\ s^{-1}$, and the oscillatory values are obtained from fitting with the power law model, i.e., : $G^* = G_0^* \omega^n$.	57
3.3	Regression model evaluation results. The number of features is reduced by eliminating the feature with less importance for the best model. For each number of features, the model that yields the highest prediction performance is underlined. Feature: 5 = P, V, D_0, G_0^*, and n; 4 = P, V, G_0^*, and n; 3 = V, G_0^*, and n.	65
3.4	Calculation of the relative feature importance based on the Extra Trees Regressor with 4 features	67
3.5	Testing results based on the ET model with 4 features on unseen data using an ink composed of 12 wt% pectin and 2 wt% gelatin.	68
4.1	Printing parameters used in the Chapter 4.	77
4.2	Rheological parameters extracted from the linear viscoelasticity testing. Note that G_0^* and n are determined from power law fitting on the averaged results.	83
4.3	Evolution of the dimensional stability over time.	94
4.4	Feature importance.	95
4.5	Classification model results. The number of features is reduced by recursive feature engineering. For each number of features, the model yielding the highest performance is underlined. Number of features: 4 = layer, tanδ , G_0^*, and T. 3 = layer, G_0^*, and T. 2 = G_0^*, and T.	95

4.6 Theoretical protein content in the 3D printed snacks after baking at different temperatures. 100

5.1 Summary of AI-based 3D food printing process monitoring and improvements examples from the literature. 119

F.1 Training results based on the ET model with 4 features (best model). 169

G.1 Testing results based on the ET model with 4 features (best model). 173

LIST OF FIGURES

Figures		Page
1.1	The four types of 3D food printers (Le-Bail et al., 2020).	3
2.1	Representation of the extrusion-based 3D printing process.	10
2.2	Determination of the yield stress using (a) a rotational flow sweep or (b) an oscillation amplitude sweep measurement.	12
2.3	Extrudability determined as a function of the yield stress for various food ink found in the literature. The green area represents the suitable yield stress range determined by Liu, Y. et al. (2019). Green markers mean that the inks were extrudable. Red markers mean that the inks were not extrudable. Triangle markers signify that the yield stress was determined by the viscosity drop. Circular markers signify that the yield stress was determined at the crossover of G' and G''. Data presented are obtained from Liu, Y. et al. (2019) for the orange area, Gholamipour-Shirazi et al. (2019) for the light blue area, Riantiningtyas et al. (2021) for the purple area, Liu et al. (2021) for the yellow area, Lille et al. (2018) for the grey area and Liu, Z. et al. (2019) for the dark blue area. SC stands for Sodium Caseinate, MPC for Milk Protein Concentrate, Car for Carrageenan, i-Car for iota- Carrageenan, GG for Guar Gum, LBG for Locust Bean Gum, MC for Methylcellulose, SA for Sodium Alginate, XG for Xanthan Gum, Gel for Gelatin, WPI for Whey Protein Isolate, k-Car for kappa- Carrageenan, SSMP for Semi-Skimmed Milk Powder, OPC for Plant Protein Concentrate, S for Starch and SMP for Skimmed Milk Powder.	14
2.4	Printability (= extrudability + shape holding) determined as a function of the yield stress for various food ink found in the literature. The green area represents the suitable yield stress range determined by Liu, Y. et al. (2019). Green markers mean that the inks were printable. Red markers mean that the inks were not printable. Triangle markers signify that the yield stress was determined by the viscosity drop. Circular markers signify that the yield stress was determined at the crossover of G' and G''. Data presented are	16

obtained from Liu, Y. et al. (2019) for the orange area, Gholamipour-Shirazi et al. (2019) for the light blue area, Riantiningtyas et al. (2021) for the purple area, Liu et al. (2021) for the yellow area, Lille et al. (2018) for the grey area and Liu, Z. et al. (2019) for the dark blue area. SC stands for Sodium Caseinate, MPC for Milk Protein Concentrate, Car for Carrageenan, i-Car for iota- Carrageenan, GG for Guar Gum, LBG for Locust Bean Gum, MC for Methylcellulose, SA for Sodium Alginate, XG for Xanthan Gum, Gel for Gelatin, WPI for Whey Protein Isolate, k-Car for kappa- Carrageenan, SSMP for Semi-Skimmed Milk Powder, OPC for Plant Protein Concentrate, S for Starch and SMP for Skimmed Milk Powder.

2.5 Shear viscosity as a function of shear rates for various food inks demonstrating a shear thinning behavior. Source: Data reproduced from Phuhongsung et al. (2020). 19

2.6 Evolution of the stress at collapsing as a function of the storage modulus according to the nozzle diameter. Source: Reproduced from Zhu et al. (2019). 22

2.7 Storage modulus as a function of the loss tangent obtained from the literature. The green dots represent stable three-dimensional structures, and the red dots represent non-stable three-dimensional structures. The information on the composition and reference for each point can be found in Table 2.2. Data points were obtained from Azam et al. (2018); Gholamipour-Shirazi et al. (2019); Lille et al. (2018); Liu, Z. et al. (2019) and Vancauwenberghe et al. (2017). 25

2.8 A schematic representation of the die swell in 3D printing. 32

2.9 The different printing characteristics obtained during the 3D printing of viscoelastic ink. The ink is made of a mixture of silicon elastomers. Source: Reproduced from Yuk and Zhao (2018). 35

2.10 Evolution of the maximum filament extension with increasing molecular weight of PEO. Source: Reproduced from Rauzan et al. (2018). 37

2.11 Effect of filament anomalies on the 3D printed object. Source: Reproduced from Fu et al. (2021). 39

2.12 Evolution of printed object after drying at 25 °C Source: Reproduced from Klar et al. (2019). 44

3.1 (a) 3D printing set-up.(b) Filament spreading analysis procedure. Continuous filament (large spreading) printed with 23PT7.5. (d) Continuous filament (slight spreading) printed with 23PT15. (e) Discontinuous filament printed with 23PT15. 51

3.2 Evolution of the shear viscosity as a function of the shear rate at 25 °C for (a) 23 PT at various concentrations. (b) 22PT at various concentrations. 54

3.3 Frequency sweep results. (a) Evolution of G' and G" as a function of angular frequency at 10 °C. Filled symbols represent G', and unfilled symbols represent G". (b) Evolution of G^* as a function of the angular frequency at 10 °C. (c) Evolution of G' and G" at 10 °C. Filled symbols represent G', and unfilled symbols represent G". (d) Evolution of G^* as a function of the angular frequency at 10 °C. The Power Law fitting is represented by the solid lines. 55

3.4 Evolution of the spreading ratio as a function of the rheological parameters of different pectin inks (a) shear viscosity at $\dot{\gamma} = 1\ s^{-1}$ and 10 °C, and (b) complex modulus at $\omega = 1\ rad.s^{-1}$. 59

3.5 The spreading ratio as a function of (a) the extrusion pressure between 0.5-1.5 bar at constant nozzle speed of $V = 10\ mm.s^{-1}$. (b) The printing speed is between 10-40 $mm.s^{-1}$ at a constant P of 0.5 bar. 61

3.6 Prediction error for extra trees models, with 4 features. 67

3.7 Prediction error for extra trees models, with 4 features using unseen data (23PT12G2). 68

4.1 Amplitude strain sweep results of the various MBPT ink formulations. Filled symbols represent G', and unfilled symbols represent G". 81

4.2 Frequency sweep results. (a) Evolution of G' and G" as a function of the angular frequency at 25 °C. Filled symbols represent G', and unfilled symbols represent G". (b) Evolution of G^* as a function of the angular frequency at 25 °C. The Power Law fitting is represented by the solid lines and the parameters given in Table 4.1. 82

4.3 Harmonics heat map analysis (a) for MB15PT2 at 1 rad.s^{-1}. (b) for MB22.5PT4 at 1 rad.s^{-1}. 85

4.4 Elastic Pipkin diagram (a) at 1 rad.s^{-1}. (b) at 10 rad.s^{-1}. 87

4.5 Evolution of the large-strain and minimum-strain moduli as a function of the strain at (a) 1 rad.s^{-1}. (b) 10 rad.s^{-1}. Filled symbols represent $G'_{L,}$ and unfilled symbols represent G'_{M}. Evolution of the instantaneous viscosity at the largest and lowest shear rate as a function of the strain at (c) 1 rad.s^{-1}. (d) 10 rad.s^{-1}. Filled symbols represent $\eta'_{L,}$ and unfilled symbols represent $\eta'_{M.}$ 89

4.6 Evolution of the strain-stiffening as a function of the strain at (a) 1 rad.s^{-1}. (b) 10 rad.s^{-1}. Evolution of the shear-thickening as a function of the strain at (c) 1 rad.s^{-1}. (d) 10 rad.s^{-1}. 90

4.7 Formation of the MB20PT4 printed cube (a) side view. (b) top view. 92

4.8 Evolution of the height accuracy according to the number of layers as a function of the complex modulus at 1 rad.s^{-1} determined with the power law fitting. 93

4.9 Baked prints at (a) – (g) baking temperature of 150 °C. (h) – (n) baking temperature of 180 °C. 98

5.1 The artificial intelligence (AI) framework. 103

5.2 Relationship between Food Big Data and AI. Source: Reproduced from Tseng et al. (2023). 109

5.3 The evolution of food flavor analysis. Source: Reproduced from Zeng et al. (2023). 111

5.4 Machine vision pipeline used to analyze real-time images of the extrusion process and to correct printing parameters. Source: Reproduced from Brion & Pattinson (2022). 115

5.5 CV-INN DIW optimization process. Source: reproduced from Roach et al. (2023). 116

5.6 Top view of five layers stacking ability of (a) starch-egg white protein blend with 70 g/100 g water addition. (b) starch-egg white protein blends with 50 g/100 g water addition. Source: Reproduced from Fahmy et al. (2020). 117

5.7	3D printed food image evaluation pipeline. This process is based on human and computer evaluation. Source: Reproduced from (Ma, Potappel, Schutyser, et al., 2023).	117
5.8	Flowchart of the future AI-3D food printing process.	125
A.1	G-code used in the chapter 3. Each g-code is set at a different printing speed. (a) 10 $mm.s^{-1}$, (b) 20 $mm.s^{-1}$, (c) 25 $mm.s^{-1}$, (d) 30 $mm.s^{-1}$, (e) 40 $mm.s^{-1}$.	156
C.1	Prediction error for decision trees model, with 5 features.	160
C.2	Prediction error for random forest model, with 5 features.	161
C.3	Prediction error for extra trees model, with 5 features.	161
C.4	Prediction error for gradient boosting model, with 5 features.	162
C.5	Prediction error for extreme gradient boosting model, with 5 features.	162
D.1	Prediction error for decision trees model, with 4 features.	163
D.2	Prediction error for random forest model, with 4 features.	163
D.3	Prediction error for extra trees model, with 4 features.	164
D.4	Prediction error for gradient boosting model, with 4 features.	164
D.5	Prediction error for extreme gradient boosting model, with 4 features.	165
E.1	Prediction error for decision trees model, with 3 features.	166
E.2	Prediction error for random forest model, with 3 features.	166
E.3	Prediction error for extra trees model, with 3 features.	167
E.4	Prediction error for gradient boosting model, with 3 features.	167
E.5	Prediction error for extreme gradient boosting model, with 3 features.	168
J.1	Harmonics heat map analysis for MB15PT2 at 1 $rad.s^{-1}$.	186
J.2	Harmonics heat map analysis for MB15PT4 at 1 $rad.s^{-1}$.	186
J.3	Harmonics heat map analysis for MB17.5PT2 at 1 $rad.s^{-1}$.	187
J.4	Harmonics heat map analysis for MB17.5PT4 at 1 $rad.s^{-1}$.	187
J.5	Harmonics heat map analysis for MB20PT2 at 1 $rad.s^{-1}$.	188
J.6	Harmonics heat map analysis for MB20PT4 at 1 $rad.s^{-1}$.	188
J.7	Harmonics heat map analysis for MB22.5PT2 at 1 $rad.s^{-1}$.	189
J.8	Harmonics heat map analysis for MB22.5PT4 at 1 $rad.s^{-1}$.	189
J.9	Harmonics heat map analysis for MB15PT2 at 10 $rad.s^{-1}$.	190
J.10	Harmonics heat map analysis for MB15PT4 at 10 $rad.s^{-1}$.	190

J.11 Harmonics heat map analysis for MB17.5PT2 at 10 rad.s^{-1}. 191
J.12 Harmonics heat map analysis for MB17.5PT at 10 rad.s^{-1}. 191
J.13 Harmonics heat map analysis for MB20PT2 at 10 rad.s^{-1}. 192
J.14 Harmonics heat map analysis for MB20PT4 at 10 rad.s^{-1}. 192
J.15 Harmonics heat map analysis for MB22.5PT2 at 10 rad.s^{-1}. 193
J.16 Harmonics heat map analysis for MB22.5PT4 at 10 rad.s^{-1}. 193
K.1 Viscous Pipkin diagram at (a) 1 rad.s^{-1}. (b) 10 rad.s^{-1}. 194
L.1 MB15PT2 Elastic Pipkin diagram at varied frequencies. 195
L.2 MB15PT4 Elastic Pipkin diagram at varied frequencies. 195
L.3 MB17.5PT2 Elastic Pipkin diagram at varied frequencies. 196
L.4 MB17.5PT4 Elastic Pipkin diagram at varied frequencies. 196
L.5 MB20PT2 Elastic Pipkin diagram at varied frequencies. 197
L.6 MB20PT4 Elastic Pipkin diagram at varied frequencies. 197
L.7 MB22.5PT2 Elastic Pipkin diagram at varied frequencies. 198
L.8 MB22.5PT4 Elastic Pipkin diagram at varied frequencies. 198
M.1 MB15PT2 Viscous Pipkin diagram at varied frequencies. 199
M.2 MB15PT4 Viscous Pipkin diagram at varied frequencies. 199
M.3 MB17.5PT2 Viscous Pipkin diagram at varied frequencies. 200
M.4 MB17.5PT4 Viscous Pipkin diagram at varied frequencies. 200
M.5 MB20PT2 Viscous Pipkin diagram at varied frequencies. 201
M.6 MB20PT4 Viscous Pipkin diagram at varied frequencies. 201
M.7 MB22.5PT2 Viscous Pipkin diagram at varied frequencies. 202
M.8 MB22.5PT4 Viscous Pipkin diagram at varied frequencies. 202

LIST OF SYMBOLS/ABBREVIATIONS

Symbols/Abbreviations	Terms
3D printing	Three-dimensional printing
IDDSI	International Dysphagia Diet Standardization Initiative
SLA	Stereolithography
DLP	Digital Light Processing
AI	Artificial Intelligence
τ_{yield} or σ_0	Yield stress
n	Consistency index, power law exponent
K	Flow behavior index
λ	Relaxation time
V	Nozzle movement speed
P	Extrusion pressure
C	Extrusion speed
T	Ink reservoir temperature
T_1	Printing nozzle temperature
T_2	Printing bed temperature
D_0	Nozzle diameter
	Distance nozzle - printing bed
P_{min}	Minimum pressure to initiate flow
L_N	Nozzle length
G'	Storage modulus
G"	Loss modulus
SC	Sodium Caseinate
MPC	Milk Protein Concentrate
Car	Carrageenan
i-Car	iota-carrageenan
GG	Guar gum

LBG	Locust bean gum
MC	Methylcellulose
SA	Sodium alginate
XG	Xanthan Gum
Gel	Gelatin
WPI	Whey protein isolate
k-Car	kappa-Carrageenan
SSMP	Semi-skimmed milk powder
SMP	Skimmed milk powder
σ	Shear stress
η	Viscosity
$\dot{\gamma}$	Shear rate
η_0	Zero-shear viscosity
η_∞	Viscosity at infinity shear rate
$\dot{\gamma}_c$	Cross time constant
m	Cross exponent
tanδ	Loss tangent
T_{melt}	Melting temperature
T_{gel}	Gelling temperature
B	Swell ratio
De	Deborah number
$t_{process}$	Time of observation
N_1	Shear normal difference
V^*	Non-dimensional nozzle speed
C^*	Non-dimensional nozzle tip height
α	Die swell ratio
CFD	Computational Fluid Dynamics
PEO	Poly(ethylene oxide)
H_F	Printability
h	Height of the printed object
h_0	Targeted height – model height
D_d	Diameter deviation

H_d	Height deviation
P_P	Printing precision
D_L	Diameter of printed layer
H_L	Height of the printed layer
D_L’	Diameter of model layer
H_L’	Height of the model layer
D_D	Dimensional deviation
d	Diameter of printed object
d’	Diameter of model object
P_F	Printing fidelity
A	Printed area
A’	Model area
H_0	Height of printed object
G	Shear modulus
$S_{collapsing}$	Stress at collapsing
g	Gravitational acceleration
S	Spreading ratio
W	Printed line width
PT	Pectin
DI water	Deionized water
wt%	Weight percentage
G^*	Complex modulus
G_0^*	complex shear modulus at angular frequency of 1 $rad.s^{-1}$
ω	Angular frequency
G-code	Geometric code
DIW	Direct ink writing
DT	Decision Tree
RF	Random Forest
ET	Extra Tree
GB	Gradient Boosting
XGB	Extreme Gradient Boosting

LOOCV	Leave-one-out cross-validation
RMSE	Root mean squared error
Err. %	Averaged squared relative error
R^2	Coefficient of determination
r	Coefficient of correlation
MB	Mung bean
LVER	Linear viscoelastic region
SAOS	Small amplitude oscillatory shear
LAOS	Large amplitude oscillatory shear
G_L'	Large-strain modulus
G_M'	Minimum-strain modulus
η_L'	Instantaneous viscosity at the largest shear rate
η_M'	Instantaneous viscosity at the lowest shear rate
S	Strain-stiffening ratio
T	Shear-thickening ratio
A_H	Height accuracy
LR	Linear Regression
SVM	Support Vector Machine
k-NN	k-Nearest Neighbors
TP	True positive
TN	True negative
P_{th}	Theoretical protein content
m_{print}	Object's mass before baking
C_{MB}	Mung bean protein isolate content
TPC	Total protein content
m_{baked}	Object's mass after baking
ML	Machine learning
DL	Deep learning
CV	Computer vision
NLP	Natural language processing

HOG	Histogram of Oriented Gradients algorithms
CNN	Convolutional Neural Networks
ANN	Artificial neural network
RNN	Recurrent neural network
GNN	Graph convolutional neural network
INN	Inverse neural network
CAD	Computer-aided design
FDM	Fused deposition modeling

CHAPTER 1
INTRODUCTION

Since its development in the 1990s, 3D printing technology has pursued advancements to revolutionize the industry. This innovative technology does not only apply to fabricating customized objects at home, but it unlocks a myriad of applications across diverse fields such as automotive (Wang et al., 2021), aerospace (Ghidini et al., 2015), construction (Buswell et al., 2018) or even tissue engineering (Sharifi et al., 2021). This versatility arises from its ability to produce intricate objects with remarkable reproducibility, minimal material cost, and reduced waste. From the 3D printing of large structures such as houses or bridges (Furet et al., 2019) to the precise 3D printing of small-scale devices with high fidelity using a wide range of materials, this technology is already known to revolutionize industries (Berman, 2012). It unlatches opportunities in the global food manufacturing systems to face food-related issues (Tian et al., 2016)

1.1 The rise of 3D food printing

The initial development of the 3D food printing technology started in 2006 with the development of the Fab@Home project and the three-dimensional deposition of chocolate (Malone & Lipson, 2007). The interest in 3D food printing gradually rose over the years and is booming, as demonstrated by (Derossi et al., 2021). Indeed, in 2008, less than ten documents were published in this field, whereas in 2020, more than 170 documents were published. In the literature, many foods have been shown to be printable, for example, cheese (Le Tohic et al., 2018), chocolate (Lanaro et al., 2019), yogurt (Riantiningtyas et al., 2021), surimi (Wang et al., 2018), baking dough (Fan Yang et al., 2019) or even liquid drawing in a beverage (Inoue et al., 2023). In addition, 2023 marked a significant milestone in the field of food innovation with the debut of the first commercially available 3D printed food: ‘The Filet’. This product, developed from plant-based ingredients, replicates salmon filet. As reviewed thoroughly by (Escalante-Aburto et al., 2021), 3D food printing can be used in favor of the development of personalized nutrition and in favor of health-orientated food

applications with, for example, the development of 3D printed food loaded with drugs. In space, the main food available corresponds mainly to rehydratable food. However, some studies are currently being made to use 3D printed food in space. Indeed, the ability to tune the nutritional value of printed food can help astronauts provide sufficient nutrients for long missions such as the human exploration of Mars. Thus, the non-availability of food delivery during long missions, the recent advances in growing crops in space, and the daily need for astronauts' nutrients can stand up for the 3D food printing technology in space (Enfield et al., 2022; Kim & Rhee, 2020; Obrist et al., 2019). Moreover, this technology is also considered an innovative way to transform food waste into novel food (Jagadiswaran et al., 2021; Ramachandraiah, 2021). The development of personalized nutrition can also be of high interest to people with specific diet requirements, such as athletes, pregnant women, or even dysphagic persons (Severini & Derossi, 2016). The current dysphagia food may not appear appealing, and the diet does not present a wide selection of meals. Therefore, the development of 3D printed meals meeting the International Dysphagia Diet Standardization Initiative (IDDSI) requirements can promote enhanced accessibility of nutritionally rich and visually appealing meals for individuals with swallowing difficulties (Ahlinder et al., 2023; Lee et al., 2021; Liu et al., 2021; Lorenz et al., 2022; Pant et al., 2021).

1.2 The current technological landscape in 3D food printing

Currently, four types of 3D printers are used for food applications: selective sintering printing, inkjet printing, binder jetting, and extrusion-based printing (Jiang et al., 2021; Le-Bail et al., 2020). Each method operates uniquely and requires edible materials with varying properties, Figure 1.1.

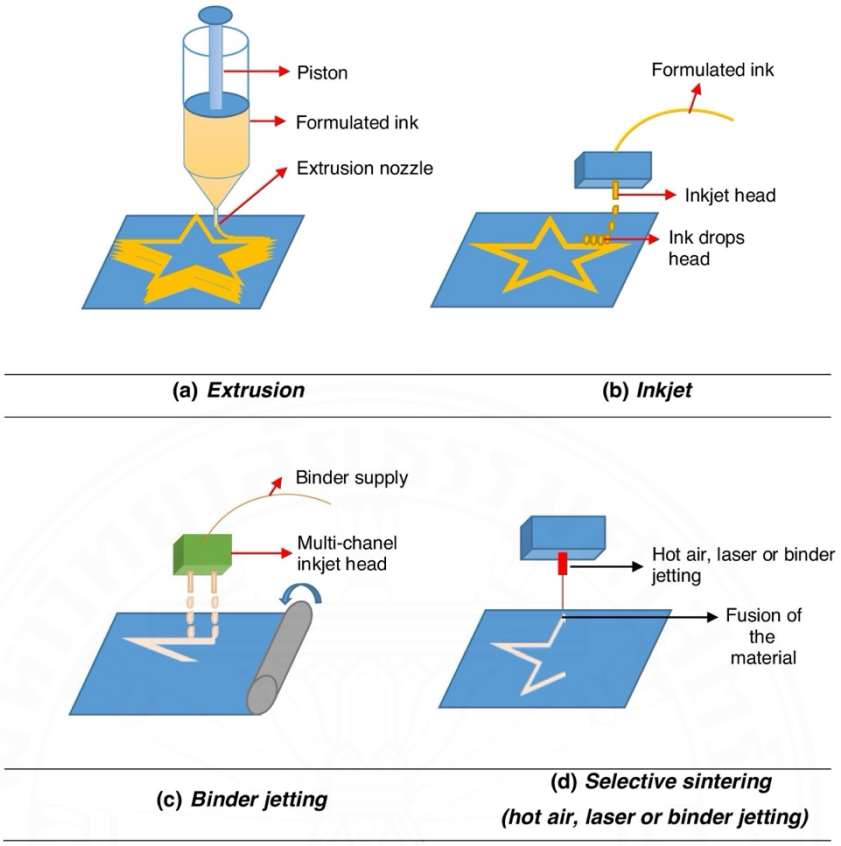

Figure 1.1 The four types of 3D food printers (Le-Bail et al., 2020).

Selective sintering printing constructs a three-dimensional structure by binding food powder using a heat source. The powder is deposited on a printing bed, and a heat source, usually a laser or hot air, melts it along a specific path. After cooling, a solid layer forms, and the process is repeated layer by layer until the desired structure is attained. In the food industry, this method finds application in materials such as sugar crystals, wheat starch, confectionery products, and pharmaceutical products like oral drugs and pellets (Awad et al., 2019; Jonkers et al., 2022; Kulinowski et al., 2021).

Inkjet printing involves the deposition of a viscous liquid in a designated location. The viscosity of printing food inks can vary greatly, from a low viscosity material, such as chocolate melt, to a high viscosity material, such as marmalade or thick tomato sauce. This technique finds valuable application in the bakery industry for decorating, coating surfaces, or filling pastries with precision (FoodJet, 2022).

Binder jetting food involves ink-jetting a binder along a precise path on a powder layer, forming a solid layer. The process is repeated layer by layer until the

desired three-dimensional structure is formed. So far, this process has not been explored in food applications, but promising studies have been developed for protein-rich food (Holland et al., 2018; Zhu et al., 2022).

Extrusion-based 3D food printing is currently the prevailing method in the food industry, involving the precise extrusion and deposition of food inks through a nozzle, repeated layer-by-layer to form a three-dimensional object. The required force to extrude the material is typically generated by a screw, a piston, or a pneumatic system (compressed air). This versatile printing method operates with a diverse selection of materials, including chocolate (Mantihal et al., 2019), food emulsions such as chocolate ganache (Kim, Woo, et al., 2022) or custard cream (Cai et al., 2022), food paste (Zhu et al., 2019), sugar candy (Kim et al., 2021) and hydrocolloids-based food inks (Gholamipour-Shirazi et al., 2019).

Among the variety of 3D food printers, extrusion-based printers are the most widely utilized, and often in combination with biopolymers, which are added into the food ink formulation to ensure a printable consistency (Derossi et al., 2021; Shahbazi & Jager, 2021). Biopolymers are polymeric materials that are of significant interest to the field owing to their renewable, sustainable, biodegradable, and biocompatible nature. The rising field of biopolymer-based 3D printing finds applications not only in food technology application where it is used to develop innovative food, but also in the biomedical domains where bioprinting aims to fabricate functional living tissues or organs to advance regenerative medicine, drug discovery, and tissue engineering (Chen et al., 2023; Szűcs et al., 2023; Z. Wang et al., 2023).

1.3 Motivation and goal of the thesis

The motivation behind this thesis arose from the burgeoning field of extrusion-based 3D food printing and its potential to revolutionize the food industry. As highlighted earlier, this technology offers a novel approach to creating food products, allowing for intricate designs and personalized nutrition. However, a critical factor in the success of 3D food printing lies in understanding the rheological behavior of the food ink used in the printing process.

Rheology, the study of the flow and deformation of materials, is crucial for determining food inks' printability and shape stability. Different rheological properties,

such as viscosity, elasticity, and yield stress, influence how well an ink can be extruded, deposited, and retain its shape during printing and subsequent handling.

This thesis aims to investigate the relationship between rheological properties and the printability and shape stability of food inks. This work seeks to uncover insights that can optimize ink formulations for enhanced performance and product quality by systematically analyzing various rheological parameters, their effects on the printing process, and the quality of the final printed object. Moreover, machine learning techniques are used to link the various parameters to the dimensional parameter of interest. This research does not only contribute to advancing the understanding of 3D food printing technology but also paves the way for the development of tailored food products with improved structural integrity and sensory attributes.

1.4 Research objectives and scope

The proposed study aims to give a deep outlook on the relationship between rheological properties and printability, primarily by analyzing how the rheological properties can enable the preparation of faithful construct from the computed model. The research objectives are detailed below:

(1) To elucidate the effect of the printing parameters and rheological properties on the spreading ratio of printed filaments.

(2) To investigate the effect of printing and rheological parameters altogether on the spreading ratio of printed filaments using a multiparametric machine-learning-based model.

(3) To study the effect of non-linear viscoelastic behavior on the accuracy of 3D printed shapes.

(4) To apply a multiparametric machine-learning classification model as a quality control tool for assessing the printability of formulations based on their rheology.

(5) To provide a critical discussion on the future of 3D food printing and how AI can benefit the process.

1.5 Thesis organization

This dissertation is structured into six chapters. Some chapter reprises published work. The thesis's organization is outlined below:

Chapter 1 presents the introduction and interests in 3D food printing, the different printing modalities currently available, the motivation and goals of the thesis, the research objectives and scope, and, lastly, the overall organization of the work.

Chapter 2 reviews relevant literature about 3D food printing. This review mainly highlights the critical rheological properties necessary to reach suitable printability. The impact of the rheological properties on the 3D printing process is first reviewed. Then, a focus on the effect of the rheological properties on the dimensions of the printed object is made. In addition, an introduction to the relevant literature on machine learning is presented. This section aims to present the models used in this thesis and review their use in 3D printing and food science. The content of this chapter has been published in the Journal of Food Engineering under the title ‘Extrusion-based 3D printing of food biopolymers: A highlight on the important rheological parameters to reach printability’.

Chapter 3 discusses the impact of printing parameters and rheological properties on the evolution of printed filaments' dimensions (width). Controlling the filament is primordial to ensure accurate object formation. Thus, the effect of rheological properties and printing parameters on the filament spreading is evaluated. Furthermore, machine learning regression techniques are applied to carry out a multi-parametric analysis of the spreading ratio. The content of this chapter has been published in the Journal of Food Engineering under the title ‘Machine learning assisted evaluation of the filament spreading during extrusion-based 3D food printing: Impact of the rheological and printing parameters’.

Chapter 4 investigates the effect of the food ink’s rheological properties on the dimensional properties of the printed objects. To enhance the printability of the pectin ink further and provide some nutritional benefits, mung bean protein isolate is added to the ink, producing protein-rich 3D printed snacks. Large amplitude oscillatory shear experiments are performed to assess the impact of the non-linear rheological behavior with the 3D printing process. Machine learning classification techniques are applied here as a quality control tool to evaluate the printability of the printed objects based on

their dimensions and rheological parameters. The effect of baking on the shape of the snack is also assessed.

Chapter 5 discusses the current use of artificial intelligence in 3D food printing and how it can improve the overall process.

Chapter 6 presents the conclusion drawn from the overall thesis. Moreover, this chapter is open to discussing the future of 3D food printing technology for food applications.

CHAPTER 2
REVIEW OF LITERATURE

2.1 Extrusion-based 3D printing of food biopolymers: A highlight on the important rheological parameters to reach printability

The recent development of 3D food printing technology opens the door to various improvements in global food manufacturing systems to address future food-related issues (Tian et al., 2016). In addition to enabling the production of visually attractive food products, this technology can lead to the feasible development of personalised foods with enhanced and customizable nutritive values (Severini and Derossi, 2016). For example, it can help people suffering from dysphagia (Lee et al., 2021; Lorenz et al., 2022) or even children with limited access to vitamins and nutrients (Derossi et al., 2018). Moreover, several studies have been carried out to develop and promote the access of this technology for future long-duration space missions, where astronauts have access to limited food resources (Enfield et al., 2022; Kim and Rhee, 2020; Obrist et al., 2019).

There are currently four types of 3D food printing technologies: extrusion-based printing, selective sintering printing, inkjet printing, and binder jetting (Jiang et al., 2021; Le-Bail et al., 2020). Each of them operates differently and requires edible materials with a range of different properties. Among these technologies, the extrusion-based printing is currently the most popularly used process in food industry. It involves the extrusion of food inks through a nozzle, followed by the layer-by-layer deposition to form a three-dimensional object. The force required to extrude the material is either generated by a screw, a piston, or a pneumatic system (compressed air). A wide range of materials have been shown to be printable using this type of printer, for example, chocolate (Mantihal et al., 2019), food emulsions such as chocolate ganache (Kim et al., 2022) or custard cream (Cai et al., 2022), paste (Zhu et al., 2019), sugar candy (Kim et al., 2021) and hydrocolloid-based food inks (Gholamipour-Shirazi et al., 2019).

As extrusion-based printers are the most commercially available and used in the food industry, this review paper will focus primarily on this type of food printing. In general, biopolymers are often added into the formulation of food inks in order to

achieve a printable consistency (Derossi et al., 2021; Shahbazi and Jager, 2021). The process of extrusion-based 3D food printing can be divided into four distinct stages, as shown in Fig. 2.1. These four stages correspond to the a) ink preparation, b) ink extrusion, c) ink deposition, and d) formation of the 3D structure. The correct setting of the printer parameters and the knowledge of the ink rheological properties at each stage of printing are essential to ensure an ideal printability with excellent reproducibility (Shahbazi and Jager, 2021).

Generally speaking, a material is considered printable when the following conditions are fulfilled: the material must be extrudable, and after the extrusion, it must be able to maintain the desired shape. In addition, the extrudate filament must be extruded continuously, and the final structure must be stable (Duty et al., 2018). Previously, the term "printability" has been defined as the ratio between the height of the printed object and the targeted height (In et al., 2021). However, this definition does not consider the ink's extrudability and shape holding properties. Hence, it is essential to keep in mind that the fidelity of the printed object to the model is also important for successful 3D printing.

The most critical step to obtaining acceptable printability is the selection of food materials with suitable rheological properties. Indeed, the ability of the ink to flow through the printer is related to its rheological parameters, such as yield stress (τ_{yield}), consistency (n), and flow behavior (K) indices. These parameters can directly impact the required pressure suitable for successful extrudability and the subsequent printing. Alongside this, correct formation and stability of the 3D structure are also required to build the self-supported 3D object. The knowledge of the viscoelastic moduli, the relaxation time (λ), and the extensional properties of the biopolymer-based food inks are thus relevant to form the 3D-dimensional food object. The importance of all these rheological parameters on successful 3D food printing has still been limitedly discussed in the literature and hence will be described in this section in more detail. Printing materials considered for this study include food mixtures whose rheological properties may be enhanced by the addition of biopolymers to achieve printable consistency, or individual food biopolymers prepared specifically as food inks. It is worth pointing out that, in food processing, temperature can be used to control how the food structure is formed and shaped, for example, using thermosensitive food biopolymers whose

properties can change from viscous liquid to gel or vice versa as a function of the temperature. Consequently, the thermal sensitivity of these biopolymers adds more complexity to the system as their rheological properties can be significantly impacted by the change in temperature.

It has been pointed out that the knowledge of ideal printing material properties alone is insufficient to achieve printability, and it must be combined with the correct adjustment of the printer settings (Yuk & Zhao, 2018). These operating parameters include the nozzle speed (V), the extrusion pressure (P), the extrusion speed (C), the temperature of the ink in the reservoir (T), the temperature of the printing nozzle (T_1), the temperature of the printing bed (T_2), the nozzle diameter (D_0) and the distance between the nozzle and the printing bed (H), as shown in Figure 2.1. The nozzle speed (V) corresponds to the travel speed of the nozzle, which can impact the filament deposition. Filament break-up can occur when V is excessively high and is also affected by the distance between the nozzle and the printed bed (H). Furthermore, the nozzle diameter (D_0) is also directly related to the required extrusion pressure (P). Therefore, an appropriate selection of these operating parameters is also pertinent to achieve a successful printing process.

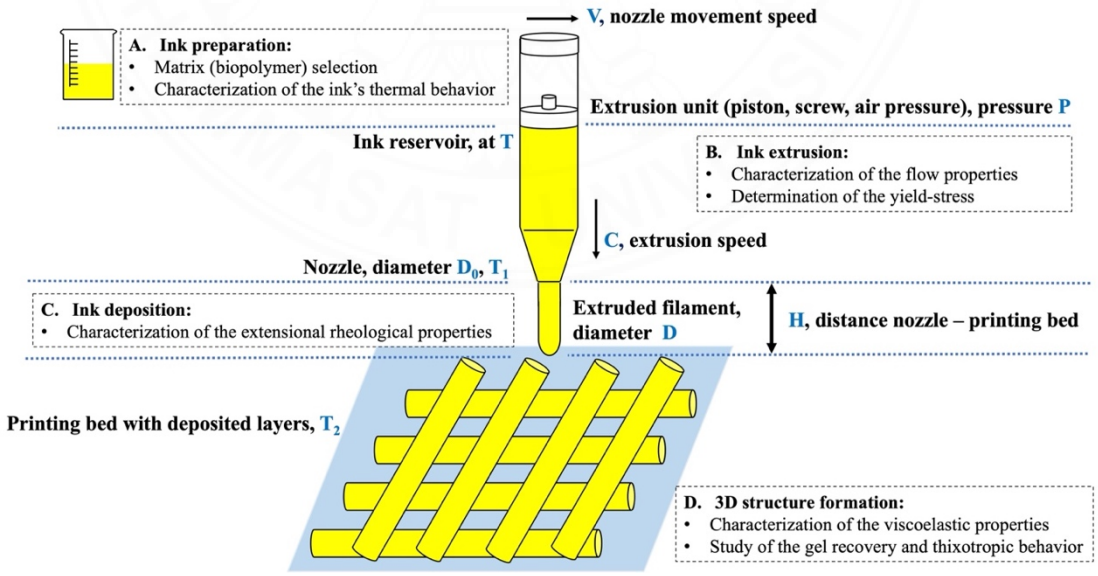

Figure 2.1 Representation of the extrusion-based 3D printing process.

As described above, the extrusion-based 3D food printing process is built upon many parameters strongly affected by the rheological properties of the ink. Therefore, in this section, we examine how the material properties can impact the shape of the printed object. Specifically, we will go into further detail and point out the importance of the knowledge of the yield stress, viscoelastic and flow properties of food inks that can be used to assess the extrudability with the correct printer parameters setting. As the temperature can directly affect the rheological behavior of many biopolymers food inks, the temperature-dependent rheological properties of food inks are also discussed, and other rheological phenomena such as the die swell and the extensional flow, which can impact the printability and shape fidelity of printed objects are also reviewed.

2.1.1 Extrusion of food inks

The extrusion is a critical step of the 3D food printing process in which the food ink is transitioned from the syringe to the printing nozzle and subsequently deposited on the printing bed (see Figure 2.1). Rheological properties of the ink strongly influence the outcome of this step. This section presents the impact of two rheological parameters: the yield stress and the flow properties of the ink, on the ease of extrusion.

2.1.1.1 Yield Stress

Yield stress (τ_{yield}), or the minimum stress required to initiate the material flow, is rheologically relevant to the 3D printing process. In practice, two different measurements can be performed to determine this parameter. The first method evaluates τ_{yield} by using the flow measurement. A varying shear rate is applied to the materials of interest at a fixed temperature. Usually, the evolution of the shear stress is collected as a function of the shear rate and τ_{yield} is determined as the value of the shear stress at shear rate approaching zero, (see Figure 2.2(a)) (Steffe, 1996). The alternative method involves carrying out an oscillation amplitude sweep in which the sample is subjected to increasing shear stress or strain at a fixed frequency and fixed temperature. The yield stress can be determined from the stress value at the crossover point when the storage modulus equals the loss modulus, as illustrated in Figure 2.2(b). As different values can be obtained, it is important for researchers to specify the method used to determine the yield stress.

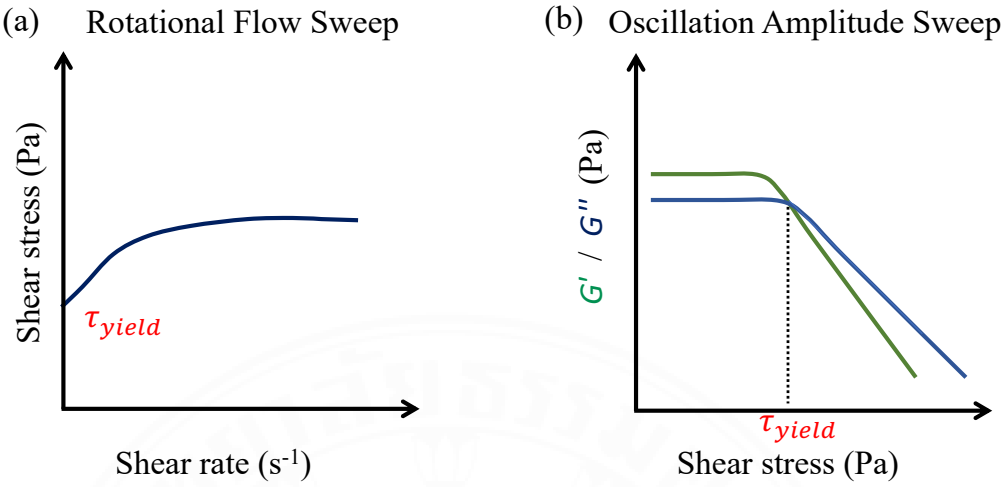

Figure 2.2 Determination of the yield stress using (a) a rotational flow sweep or (b) an oscillation amplitude sweep measurement.

Generally, the value of the yield stress of food ink depends on many factors, such as the temperature, biopolymer types, concentration, or other ingredients incorporated into the ink. The total protein content has been shown to increase the value of the τ_{yield} for inks made of a composite flour of refined flour and pea protein isolate, butter, and water (Hussain, Arora, et al., 2021). Similar observations were made when the pregelatinized starch content was increased (Maldonado-Rosas et al., 2022). Based on their experimental results, Liu and co-workers stated that the yield stress of a food ink should be between 500 to 1500 Pa to achieve suitable printability (Y. Liu et al., 2019). By defining printability as a combination of extrudability of the ink and shape holding capacity of the printed structure, it can be interesting to determine whether this proposed range of yield stress is widely applicable. Data available from literatures was collected and evaluated as shown in Figure 2.3. It is evident that some inks with lower τ_{yield} values than the proposed range could still be extruded, while some having τ_{yield} within the range were not extrudable. It is the case, for example, of an ink composed of 1% w/w *k*-carrageenan, 0.5% w/w xanthan gum, and 2% w/w starch at 35 °C with a yield stress of 551 Pa or an ink composed of 12.5% gelatin with a yield stress of 1430 Pa (Z. Liu et al., 2019; Riantiningtyas et al., 2021). These results can probably relate to the minimum

pressure that can be provided by the printer. In principle, the relationship between the yield stress and the minimum pressure (P_{min}) required to make a considered ink flow through a nozzle of specified length and diameter, can be defined as in Equation (2.1) (Pospischil et al., 2014).

$$P_{min} = \frac{4L_N}{D_0}\tau_{yield} \tag{2.1}$$

where L_N is the nozzle length, D_0 is the nozzle diameter, and τ_{yield} is the yield stress. Accordingly, the 3D printer must be able to deliver this minimum pressure for the ink extrusion to succeed. Indeed, if this pressure is not reached due to a high value of yield stress, non-extruded or broken filament can be obtained, thus leading to unsuccessful printing (Liu et al., 2021). Overall, the operative yield stress range of food inks can have a significant implication on the printer specifications or setup such that the printer must accommodate this minimum pressure value for the ink to be extruded through the nozzle. Therefore, the knowledge on the range of yield stress of food inks can be beneficial for appropriate selection and effective design of the printer to achieve successful extrusion process.

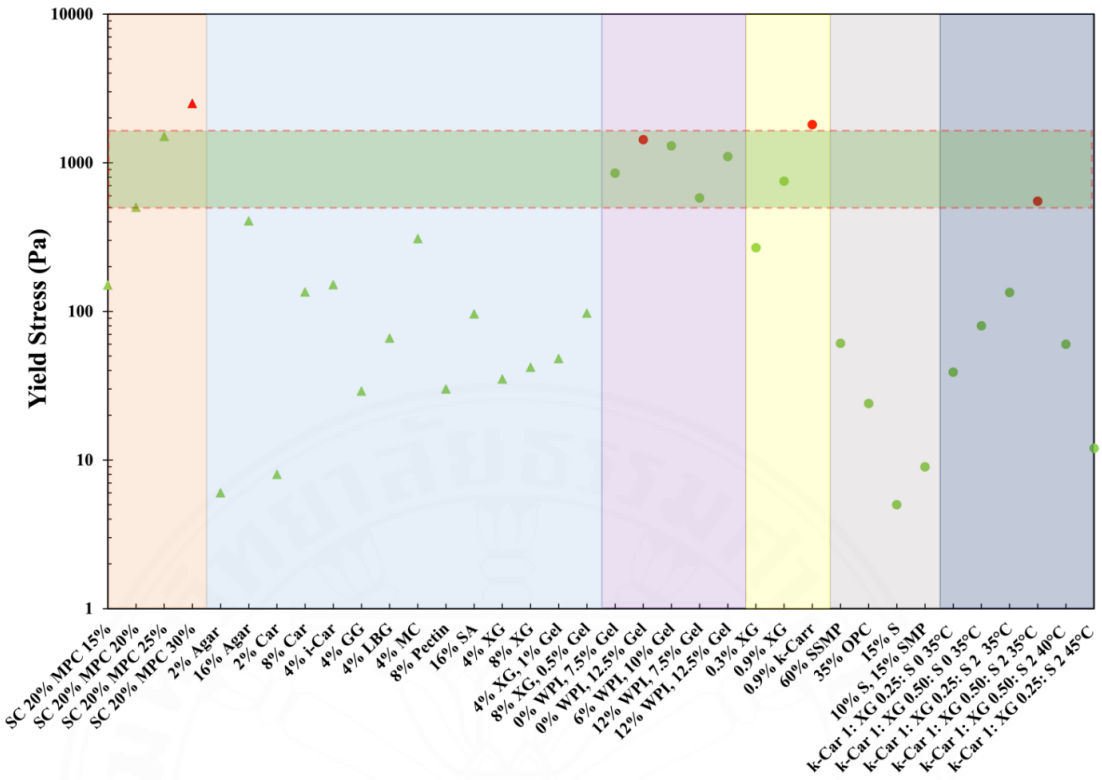

Figure 2.3 Extrudability determined as a function of the yield stress for various food ink found in the literature. The green area represents the suitable yield stress range determined by Liu, Y. et al. (2019). Green markers mean that the inks were extrudable. Red markers mean that the inks were not extrudable. Triangle markers signify that the yield stress was determined by the viscosity drop. Circular markers signify that the yield stress was determined at the crossover of G' and G''. Data presented are obtained from Liu, Y. et al. (2019) for the orange area, Gholamipour-Shirazi et al. (2019) for the light blue area, Riantiningtyas et al. (2021) for the purple area, Liu et al. (2021) for the yellow area, Lille et al. (2018) for the grey area and Liu, Z. et al. (2019) for the dark blue area. SC stands for Sodium Caseinate, MPC for Milk Protein Concentrate, Car for Carrageenan, i-Car for iota- Carrageenan, GG for Guar Gum, LBG for Locust Bean Gum, MC for Methylcellulose, SA for Sodium Alginate, XG for Xanthan Gum, Gel for Gelatin, WPI for Whey Protein Isolate, k-Car for kappa- Carrageenan, SSMP for Semi-Skimmed Milk Powder, OPC for Plant Protein Concentrate, S for Starch and SMP for Skimmed Milk Powder.

In addition, the printability, which can be defined as the ability to extrude the ink, and the ability of the extrudate to form a stable three-dimensional structure, i.e., shape holding, can be evaluated using the same results from the literature as shown in Figure 2.4. Evidently, by combining both criteria, i.e., the extrudability and the shape holding, a small number of food inks remain printable, and fewer of these inks are in the suggested ideal yield stress range to obtain a correct printability, as proposed by Liu, Y. et al. (2019). The results in this section confirm that the yield stress alone is probably not sufficient to define a correct printability, but other parameters, perhaps the viscoelastic properties mentioned, are also essential to consider. Nonetheless, the yield stress can be used as a key parameter to assess the extrudability of an ink for a given printer as it is related to the minimum pressure to initiate the flow of the ink.

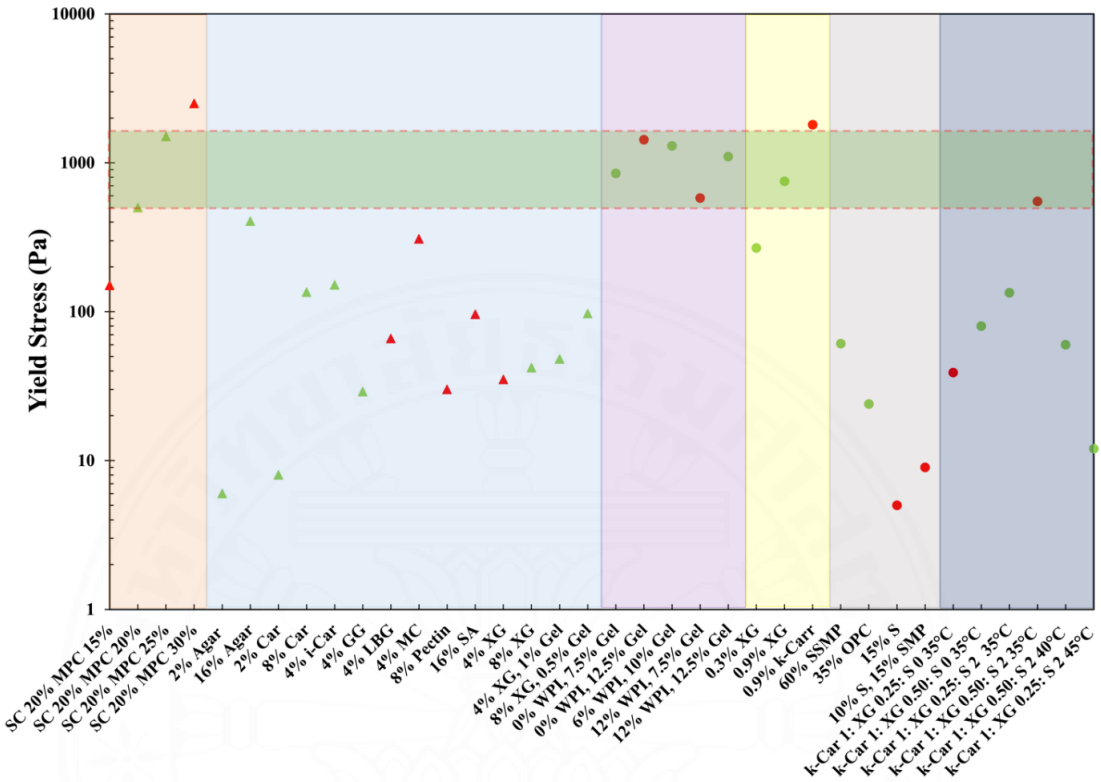

Figure 2.4 Printability (= extrudability + shape holding) determined as a function of the yield stress for various food ink found in the literature. The green area represents the suitable yield stress range determined by Liu, Y. et al. (2019). Green markers mean that the inks were printable. Red markers mean that the inks were not printable. Triangle markers signify that the yield stress was determined by the viscosity drop. Circular markers signify that the yield stress was determined at the crossover of G' and G". Data presented are obtained from Liu, Y. et al. (2019) for the orange area, Gholamipour-Shirazi et al. (2019) for the light blue area, Riantiningtyas et al. (2021) for the purple area, Liu et al. (2021) for the yellow area, Lille et al. (2018) for the grey area and Liu, Z. et al. (2019) for the dark blue area. SC stands for Sodium Caseinate, MPC for Milk Protein Concentrate, Car for Carrageenan, i-Car for iota- Carrageenan, GG for Guar Gum, LBG for Locust Bean Gum, MC for Methylcellulose, SA for Sodium Alginate, XG for Xanthan Gum, Gel for Gelatin, WPI for Whey Protein Isolate, k-Car for kappa- Carrageenan, SSMP for Semi-Skimmed Milk Powder, OPC for Plant Protein Concentrate, S for Starch and SMP for Skimmed Milk Powder.

2.1.1.2 Flow properties

It is well recognized that the composition of food inks plays a key role in affecting their viscosity and the corresponding flow behavior. For extrusion-based printing, non-Newtonian behaviors such as the shear thickening characteristic should be avoided as the increase in the viscosity with increasing shear rate may harden the extrusion process, a property generally not preferred for 3D printing (Wei et al., 2022). In general, the flow properties of food inks should be determined prior to the printing process in order to ensure effective printing. A shear rate sweep at a given temperature can be carried out to assess the flow behavior. A shear rate range of 1 to 1000 s^{-1} should be used to cover the operating shear rate range for the extrusion process.

To ease the 3D printing process, the ink should exhibit a shear-thinning behavior. In fact, this behavior has been depicted in many food inks reported in literatures (Álvarez-Castillo et al., 2021; Yang et al., 2021; Zheng et al., 2021). Many studies also used rheological models to fit the results obtained from flow measurements, so the comparison of the results can be easily made among various formulated food inks. Various flow models, describing shear stress (σ) or viscosity (η) as a function of shear rate ($\dot{\gamma}$), have been referred to, including Power Law, Herschel-Bulkley, and Cross models, as shown in Equations (2.2)-(2.4), respectively (Barnes, 2000).

$$\sigma = K\dot{\gamma}^n \tag{2.2}$$

$$\sigma = \sigma_0 + K\dot{\gamma}^n \tag{2.3}$$

$$\frac{\eta - \eta_\infty}{\eta_0 - \eta_\infty} = \frac{1}{1 + (\dot{\gamma}/\dot{\gamma}_c)^m} \tag{2.4}$$

where K is the flow consistency index, n is the flow behavior index, η_0 is the zero-shear viscosity, η_∞ is the viscosity limit at infinity shear rate, $\dot{\gamma}_c$ is the characteristic (Cross) time constant, m is the Cross exponent, σ_0 is the required shear stress to make the solution flow or can be regarded as yield stress. $n = 1$ for a Newtonian fluid and $n < 1$ signifies a shear-thinning behavior.

It has been shown that the value of n decreased with the total biopolymer addition for inks prepared using gellan gum gel incorporated with whey protein isolate beads or fiber (Oliveira et al., 2020). A stronger shear-thinning behavior was obtained with a lower n value, thus easing the extrusion process. Liu and co-workers developed 3D printed foods containing shiitake powder in a range of biopolymer matrix, e.g., gum arabic, xanthan gum, or *k*-carrageenan, for people suffering from dysphagia (Liu et al., 2021). By fitting their flow measurement results with the Power Law model, they found that the value of K increased with the addition of biopolymer. The value of K was found to be 671 $Pa.s^n$ for the ink made of shiitake powder with 0.3% k-carrageenan and 2242 $Pa.s^n$ for the ink made of shiitake powder with 0.9% k-carrageenan. The ink was thus harder to extrude at higher k-carrageenan concentration. In another work, Phuhongsung and co-workers assessed the impact of the addition of NaCl on the rheological properties of the ink made of soybean protein isolate and xanthan gum and their printability (Phuhongsung et al., 2020). All their food inks presented a shear-thinning behavior as shown in Figure 2.5. They showed that this viscosity decrease was beneficial for the 3D printing process as it was easier for the inks to flow through the nozzle. The following power law parameters highlighting a viscosity decrease were calculated from their results (see Table 2.1 and fitting in Figure 2.5).

Table 2.1 Power Law parameters determined using Phuhongsung et al. (2020) data shown in Figure 2.5.

Ink composition	**n**	**K ($Pa.s^n$)**
Soybean Protein Isolate (SPI)	0.144	117.70
SPI + xanthan gum	0.040	119.95
SPI + xanthan gum + NaCl 1g/100mL	0.103	81.15
SPI + xanthan gum + NaCl 2g/100mL	0.265	76.99
SPI + xanthan gum + NaCl 3g/100mL	0.133	40.39

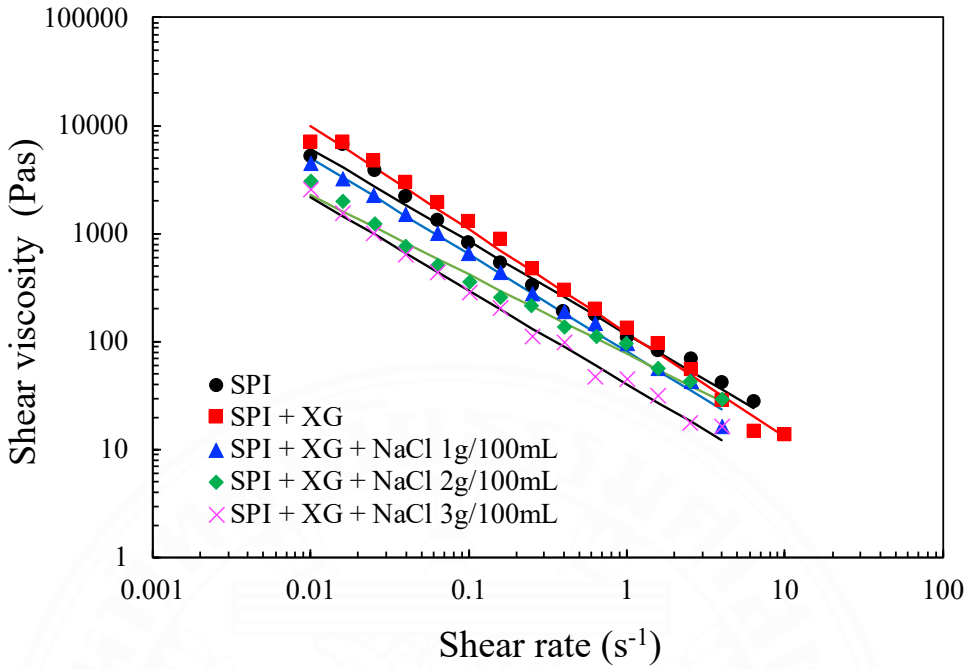

Figure 2.5 Shear viscosity as a function of shear rates for various food inks demonstrating a shear thinning behavior. Source: Data reproduced from Phuhongsung et al. (2020).

As expected, the value n decreased, and K increased with the addition of polymer. When the salt was added to the system at 1 g/100 mL, the value of K dropped approximately 1.5 times from 120 to 81 Pa.s^n, thus explaining the ease of the printing process. Some methods to counterbalance the increase of K while keeping a lower value of n can also be found in the literature. It was demonstrated that increasing the ink's temperature decreased the value of K while keeping the value of n almost constant for inks composed of carrageenan, xanthan gum, and starch (Z. Liu et al., 2019). Besides, replacing a fraction of the biopolymer content with a non-polymeric material, for example, mango puree, could also decrease the values of both rheological coefficients (Montoya et al., 2021). The addition of salt could also have a similar effect depending on the biopolymers used.

It is worth pointing out that examples of food inks discussed so far do not include added particles or suspended solids. In many cases, food ingredients that come in the form of solid particles or powders may be used to increase the nutritional properties or the hedonic aspects of the 3D printed structure. As a result, some

formulated food inks may be in the form of dense particle suspensions, such as demonstrated in the recent work by Feng et al., who carried out the 3D printing of alginate loaded with edible rose petals to produce a new type of snack food (Feng, Zhang, Bhandari, et al., 2020). In that case, the food ink's rheological behavior and printability can also be impacted by the presence of these solid particles.

In addition, it is essential to note that some food materials can exhibit a time-dependent rather than shear rate dependent viscosity characteristic. This is typically known as thixotropic behavior, in which the viscosity decreases with a constant shear rate and returns to its initial value after a period of rest. Such time-dependent behavior can present the 3D printing process with a more complex situation to properly control the flow of material out of the nozzle to allow time for the material to rebuild its structure on the printing base (Schwab et al., 2020; Shahbazi et al., 2021). This aspect is still overlooked, and further work to relate the relationship between thixotropic property and printing condition is required to improve our knowledge of how such behavior impacts the printability and shape fidelity of the printed object.

Through this section, we explain how the extrusion stage of the 3D printing process is impacted by the rheological properties of the ink. The extrudability of the ink is strongly influenced by its rheological parameters, such as the yield stress, the flow consistency, and flow behavior indices. However, it is noticeable that no universal values have been defined regardless of the type of materials used to yield an ink with good printability. All these parameters also impact the required extrusion conditions, such as pressure and flow rate. The printer must have the capacity to generate sufficient pressure to overcome the yield stress, thereby initiating the ink flow. The required pressure is also impacted by the nozzle size. Generally, a higher pressure is required to flow an ink through a smaller nozzle diameter. Additionally, the importance of the Power Law parameters n and K on the extrusion speed of various gels has already been demonstrated (Paxton et al., 2017). It can be interesting to develop a model further that assesses the extrudability of a given ink according to these parameters. Even though the process may be complicated due to the non-Newtonian behavior of the ink, it can find a strong interest in the field of 3D food printing to widen the use of this technology.

2.1.2 Forming a stable 3D food structure

Another critical step of the 3D printing process, alongside the ability to extrude the ink out of the nozzle, is the ability to yield a stable 3D structure and achieve a high shape fidelity, thus giving the printed object its attractiveness and desired properties (Pant et al., 2021). This section discusses the importance of viscoelastic properties, which can influence the ability of food ink to form a stable finished product.

Through rheological examination, it is possible to determine whether a sample behaves like a liquid, a solid, or a combination of both behaviors, commonly known as viscoelastic materials. The value of storage modulus, G', describing the solid-like behavior, and the loss modulus, G", designating the liquid-like behavior, are important for 3D printing applications. When the storage modulus is higher than the loss modulus, the material exhibits a solid-like behavior, and when the storage modulus is lower than the loss modulus, the material presents a liquid-like behavior. Additionally, the viscoelasticity can be analyzed by the loss tangent, tanδ, defined as in Equation (2.5). This dimensionless value can be used conveniently to assess the viscoelastic behavior of a given sample. That said, when the value is higher than one, the sample behaves like a liquid, and the sample behaves like a solid if the value is below one.

$$tan\delta = \frac{G"}{G'} \tag{2.5}$$

From the rheological point of view, these parameters can be determined by an oscillation frequency sweep experiment. In such measurement, the sample is submitted to a constant strain (within the linear viscoelastic region) at a varying frequency. Both G' and G" are recorded as a function of frequency. In a recent study by Zhu and co-workers, G' has been used to assess the stability of the three-dimensional printed structure. It was shown that the stress at collapse, which was related to the structure dimensions and weight, was linearly dependent on G' for a given nozzle size, as shown in Figure 2.6 (Zhu et al., 2019). In other words, a 3D structure presenting a higher storage modulus is capable of withstanding higher stress before collapsing than a structure with a lower storage modulus value at a fixed nozzle diameter. Hence, it is possible to stack more layers before the structure breakdown with a higher value of G'.

Similar observations were made by Feng et al. (2020), whose work showed that among their samples containing sodium alginate and rose petal, the ones presenting poor shape stability had a lower G', e.g., 100 and 500 Pa for inks containing 4% and 6% sodium alginate, respectively. Samples with a higher sodium alginate content and a higher storage modulus presented improved shape stability. However, the ones with too high storage modulus presented a rough surface due to the difficulty of extruding the ink, i.e., 10% sodium alginate ink with G' = 2500 Pa.

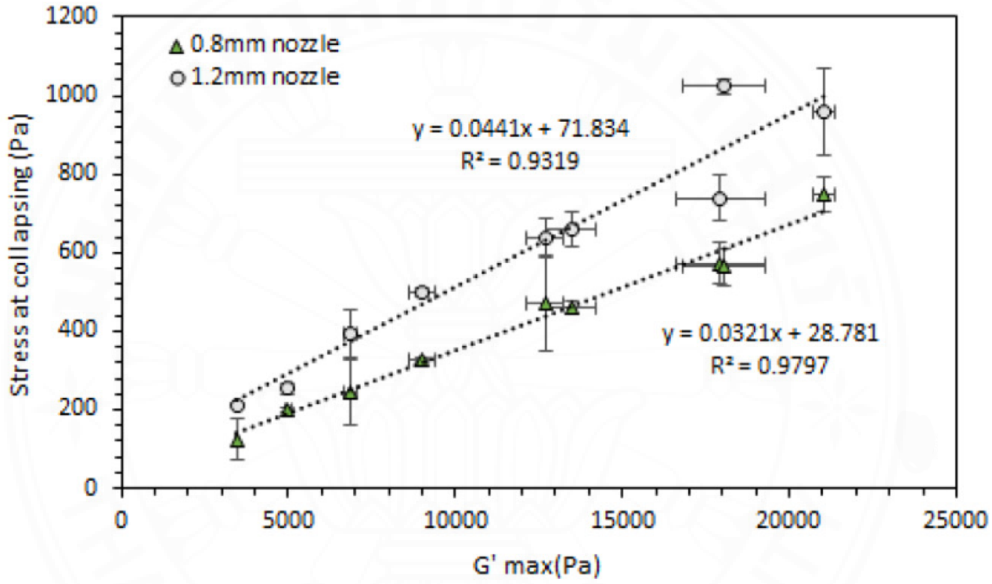

Figure 2.6 Evolution of the stress at collapsing as a function of the storage modulus according to the nozzle diameter. Source: Reproduced from Zhu et al. (2019).

As anticipated, the value of G' usually increases with increasing total biopolymer content. Nonetheless, it can be worth, especially for food applications, to keep the total biopolymer content low and add some food ingredients to obtain higher storage modulus values. It was illustrated by Kim and co-workers, who prepared a variety of food inks composed of a range of hydrocolloids, e.g., hydroxypropyl methylcellulose, locust bean gum, xanthan gum and guar gum, and vegetable powders such as broccoli, carrot, and spinach (Kim et al., 2018). In particular, they showed that adding vegetable powder to these hydrocolloid solutions increased G' values simply through concentration/solid content effect. This study thus highlighted the possibility

of tuning the rheological properties and nutrition to promote shape stability while keeping a total biopolymer content constant.

Based on the above examples, it can be said that the storage modulus is an essential parameter in assessing the shape stability of the 3D printed structure. However, no specific G' values are given in the literature to obtain a certain shape holding characteristics, and the range of G' values appears to spread more than two orders of magnitude. It was generally demonstrated that a higher value might yield improved shape stability. However, too high G', as a result of increasing concentration of biopolymer or solid content, can negatively impact the ink extrusion as the yield stress could also be increased, thus, making it more challenging to be extruded out of the nozzle.

Instead of using G' to define the stability of printed objects, some authors have suggested using the loss tangent or tanδ as a valuable parameter to describe the shape stability. Azam and co-workers carried out the 3D printing of vitamin-D enriched wheat starch food made of hydrocolloids such as xanthan gum, guar gum, k-carrageenan, or gum Arabic. They demonstrated that samples with a higher tanδ were non self-supporting, thus resulting in poor shape stability. Their results indicated that the suitable values of tanδ were ranged between 0.238-0.290. Below this range, the sample still presented correct shape stability, as shown by their samples made of kappa-carrageenan, guar gum, and xanthan gum. However, some of them were hard to extrude through the nozzle, leading to a rough surface as a result of increased elasticity. In contrast, the samples appeared to have incorrect shape holding for tanδ beyond this range (Azam et al., 2018). In another work, Gholamipour-Shirazi et al. (2019) stated that the range of tanδ could be broader and should be between $0.052 \leq \tan\delta \leq 0.268$ (Gholamipour-Shirazi et al., 2019). Similar range of tanδ values were also found in the literature for 3D printing of food inks containing sodium alginate, soy protein isolate, gelatin at various concentrations (H. Chen et al., 2019), and inks composed of potato starch, skimmed milk, icing sugar, and cream (Yang et al., 2021).

In addition, some researchers showed that the shape stability could be better defined by combining storage modulus and phase angle of printed food inks. Nijdam and co-workers prepared a three-dimensional molded structure to investigate the

parameters affecting three-dimensional objects' structural stability. Their three-dimensional objects were made of wheat starch, gelatin, and hydroxypropyl methylcellulose at different concentrations. They concluded that a high G' alone would not yield a stable 3D structure if the value of the tanδ was too high. Similarly, this is also applicable to the ink with a low value of tanδ and G' (Nijdam et al., 2021). From these findings, it can be interesting to determine more precisely a suitable range of storage modulus and loss tangent to reach the correct shape stability of the 3D printed structure. Accordingly, the values of G' and tanδ of various food inks reported in the literature were collected, and their ability to yield a stable three-dimensional structure was analyzed, as detailed in Table 2.2. In addition, the values of G' of each ink were plotted as a function of tanδ, and color was designated whether the printed shape held correctly, without any collapse or significant deformation (green), or whether the shape did not hold well (red), as shown in Figure 2.7. Interestingly, this figure can be divided into three distinct zones. The first region corresponds to tanδ >1, meaning the ink behaves as liquid-like material. Consequently, it does not yield a self-supporting structure, i.e., the printability is not achieved. Below the value of tanδ =1 is presented the materials having a solid-like behavior. Within this zone, two types of ink characteristics are shown. These characteristics are delimited by the upper tanδ value defined previously by Gholamipour-Shirazi and co-workers, with tanδ = 0.268 (Gholamipour-Shirazi et al., 2019) and a minimum storage modulus value of approximately 300 Pa to further divide the region into self-supporting and not self-supporting inks (see Figure 2.7).

The data shown in Figure 2.7 gives an approximate range of G' and tanδ of food inks that may likely lead to a stable three-dimensional structure. Thus, the rheological analysis of the ink can be conveniently carried out as a tool to determine whether the ink would have suitable rheological properties for acceptable printability. However, some limitations remain as the proposed printable zone did not have the upper G' value limit. Some authors showed that inks with too high storage modulus value may be problematic for extrusion, thus making them not printable (Z. Liu et al., 2018). Such characteristics can also be linked to high biopolymer concentration that can directly promote the yield stress, as presented in the previous section. It is worth pointing out

that this upper limit of storage modulus may not be defined explicitly as it depends directly on the printer capacity and its setup. A review of these aspects for available commercial printers and customized ones can be found in the recent work of Tan and co-authors and Derossi and co-authors (Derossi et al., 2019; Tan et al., 2018).

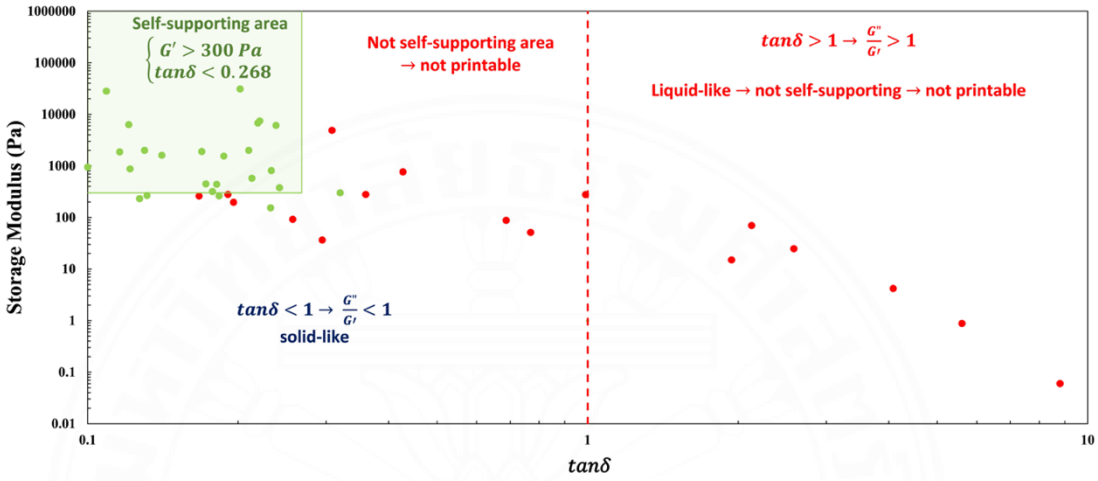

Figure 2.7 Storage modulus as a function of the loss tangent obtained from the literature. The green dots represent stable three-dimensional structures, and the red dots represent non-stable three-dimensional structures. The information on the composition and reference for each point can be found in Table 2.2. Data points were obtained from Azam et al. (2018); Gholamipour-Shirazi et al. (2019); Lille et al. (2018); Liu, Z. et al. (2019) and Vancauwenberghe et al. (2017).

Table 2.2 Rheological values obtained from the literature for various food inks. The * indicates that the value was digitized or calculated from the authors' results.

Ink composition	Storage Modulus (Pa)	tanδ	Shape holding ability	Reference
60% Semi Skimmed Milk Powder	1550	0.187	Yes	(Lille et al., 2018)
35% OPC	1900	0.169	Yes	
15% Starch	261	0.167	No	
10% Starch, 15% Skimmed Milk Powder	280	0.191	No	
4% Agar	232	0.127	Yes	Gholamipour-Shirazi et al. (2019)
8% Agar	1611	0.141	Yes	
16% Agar	31100	0.202	Yes	
2% Carrageenan	266	0.131	Yes	
4% Carrageenan	1874	0.116	Yes	
8% Carrageenan	28213	0.109	Yes	
2% Gellan Gum	877	0.122	Yes	
4% Gellan Gum	6310	0.121	Yes	
2% Guar Gum	88	0.687	No	
4% Guar Gum	767	0.427	No	
2% Locust Bean Gum	15	1.940	No	
4% Locust Bean Gum	278	0.990	No	
4% Methylcellulose	4.2	3.084	No	
2% Pectin	0.06	8.804	No	
4% Pectin	0.88	5.603	No	
8% Pectin	25	2.585	No	

16% Sodium Alginate	70	2.128	No	
4% Xanthan Gum	36	0.295	No	
8% Xanthan Gum	196	0.196	No	
4% Xanthan Gum, 0.5% Gelatin	92	0.257	No	
4% Xanthan Gum, 1% Gelatin	154	0.232	Yes	
4% Xanthan Gum, 2% Gelatin	440	0.181	Yes	
8% Xanthan Gum, 0.5% Gelatin	262	0.183	Yes	
8% Xanthan Gum, 1% Gelatin	319	0.178	Yes	
8% Xanthan Gum, 2% Gelatin	448	0.172	Yes	
15% Wheat Starch, 1% Xanthan Gum, Orange Concentrate	6870*	0.219	Yes	Azam et al. (2018)
15% Wheat Starch, 1% Guar Gum, Orange Concentrate	7400*	0.221	Yes	
15% Wheat Starch, 1% kappa-Carrageenan, Orange Concentrate	6170*	0.238	Yes	
15% Wheat Starch, 1% Arabic Gum, Orange Concentrate	4900*	0.308	No	

Kappa-Carrageenan 1: Xanthan Gum 0.25: Starch 0	51	0.769*	No	Liu, Z. et al. (2019)
Kappa-Carrageenan 1: Xanthan Gum 0.50: Starch 0	377	0.242*	Yes	
Kappa-Carrageenan 1: Xanthan Gum 0.25: Starch 2	577	0.214*	Yes	
Kappa-Carrageenan 1: Xanthan Gum 0.50: Starch 2	815	0.233*	Yes	
12.5 g/L Pectin, 12.5 mM $CaCl_2$	920*	0.100	Yes	(Vancauwenberghe et al., 2017)
35 g/L Pectin, 12.5 mM $CaCl_2$	300*	0.320	Yes	
55 g/L Pectin, 12.5 mM $CaCl_2$	280*	0.360	No	
35 g/L Pectin, 17.5 mM $CaCl_2$	2050*	0.130	Yes	
55 g/L Pectin, 17.5 mM $CaCl_2$	2180*	0.210	Yes	

2.1.3 Importance of the ink's thermal behavior on the printing process

As mentioned briefly in the introduction, temperature can have significant effect on the rheological properties of food inks, including yield stress, flow behavior and viscoelastic properties, as in the aforementioned sections. The knowledge of the melting temperature, T_{melt}, and the gelling temperature, T_{gel}, (or the temperatures at which the ink softens or hardens) can also be helpful to promote the correct setting of the printing temperature, T_1, and the printing bed temperature, T_2, respectively (see Figure 2.1). Consequently, the printing process may be eased and the layer stacking enhanced due to the proper manipulation of ink state at different stages of the printing process. The

ink preparation is considered a crucial step for successful printing. In particular, the selected ingredients for formulating food inks can directly affect the printability and its ability to form a stable three-dimensional product. The ingredient's thermal behavior makes characteristics such as viscosity and viscoelastic properties vary with the elevated temperature. Hence, the thermal dependence of the rheological behavior of food inks should be characterized prior to printing process to adjust the process temperatures ideally and thereby avoid wasting printing materials with unsuccessful trials. In this part, we highlight the importance of the thermal dependence of the rheological properties of the biopolymer-based food ink for 3D printing process.

Temperature is an important parameter influencing the rheological behavior of a sample. A higher temperature generally tends to reduce the viscosity of a material and vice versa. Two different temperatures, including gelling and melting temperature, can be used to characterize the viscoelastic properties of thermosensitive biopolymers. Below the gelling temperature $T_{gel,}$ these materials exhibit a gel-like behavior. On the contrary, above the melting temperature $T_{melt,}$ they behave like a viscous liquid. The crossover of storage (G') and loss (G'') moduli in a temperature sweep can be used to indicate a change in the material state, and these temperatures can be obtained depending on the thermal ramp, i.e., T_{gel} for a cooling ramp and T_{melt} for a heating ramp.

Many researchers showed that setting a printing temperature higher than T_{gel} yielded an ink with lower viscosity and a liquid-like behavior, which may facilitate the extrusion process. For example, a mixture of 20% w/v soy protein isolate and 0.5% w/v sodium alginate was shown to have thermosensitive behavior with the addition of gelatin at a concentration up to 10% w/v (J. Chen et al., 2019; Chen et al., 2022). The studies also demonstrated that the inks with gelatin showed a viscosity drop when the temperature increased above 20 °C, thus easing the extrusion process when printing was performed at temperature higher than this value. In addition, the inks containing a higher concentration of gelatin showed an increased viscosity and enhanced mechanical strength at a temperature lower than T_{gel}. In other words, the addition of gelatin yielded more stable printed structures while keeping a facile extrusion at the printing temperature of 35 °C (above T_{gel}) due to a reduced viscosity

Moreover, the gelling temperature of food inks can be manipulated by selecting appropriate thermosensitive biopolymers. Liu et al. studied the printability of a range

of food inks containing k-carrageenan, xanthan gum, and potato starch and showed that gelling temperatures were changed by less than 1 °C when increasing xanthan gum content from 0.25 to 0.5% w/w and by about 2 °C when changing the potato starch content from 0 to 2% w/w. In contrast, the k-carrageenan was predominantly responsible for the thermal properties of the ink, as increasing its concentration from 1% to 2% w/w increased the gelation temperature by 9 °C. Thus, they produced inks with gelling temperatures ranging from 35.4 to 47.5 °C, and they used this information to control the printing temperature accordingly (Z. Liu et al., 2019).

At this point, the works presented here only focused on the gelling temperature obtained from a rheological thermal analysis with a cooling mode. This result depicts gel's formation temperature, thus suggesting the temperature below which the printing bed temperature should be set for the ink to transition from a viscous liquid-like state to a solid-like one. Generally, the melting temperature may not be equal to the gelling temperature. Therefore, it is also of high interest to study the melting temperature in order to know the temperature at which the ink will form a viscous liquid or present a reduced viscosity, which beneficially facilitate the extrusion process. García-Segovia and co-workers carried out the 3D printing of ink composed of sugar syrup, water, xanthan gum, and konjac gum at different temperatures. They showed that the ink behaved like a solid gel at 25 °C, whereas it behaved like a viscous liquid at 50 °C, which corresponded well to its melting temperature (García-Segovia et al., 2020). Thus, printing at a higher temperature could ease the process due to the liquid-like behavior of the ink facilitating the extrusion.

The addition of other food ingredients, such as nutrients and surfactants can modify the gelling and melting temperature of its mixture. Kamlow et al. showed that adding vitamin B (thiamine) at 0 – 5% w/v did not impact the gelling temperature of 2% w/v agar ink, which remained close to 38 °C (Kamlow et al., 2021). However, they demonstrated that the gelling temperature of the k-carrageenan system was increased markedly from 42 to 60 °C when 5% w/v thiamine was added. The increase in temperature was due to the complexation of the k-carrageenan by the cationic thiamine molecule, resulting in a more robust gel network. The authors showed an increase in the storage modulus value with the addition of thiamine until the ink reached the saturation point, at a concentration higher than 2% w/v. Furthermore, the addition of

small surfactant molecules has also been demonstrated to impact the gelling temperature and rheological properties of a food ink. For example, 1% w/w Tween20 increased the gelling temperature and storage modulus of the ink composing of low acyl gellan gum and tamarind seed xyloglucan, thus making the ink more feasibly printable (Fenton et al., 2021).

Overall, the printing (nozzle) temperature T_1 should be above the melting temperature of the ink to facilitate the flow and extrudability and the printing bed temperature T_2 is below the gelling temperature so that the shape holding properties can be enhanced.

2.1.4 Other important rheological phenomena

Other rheological phenomena, such as die swell, and extensional flow/viscosity, are also important to the printability and shape fidelity of food inks (Corker et al., 2019; Ewoldt & Saengow, 2022; Shadvar et al., 2019). However, information based on these phenomena, which is especially related to 3D food printing, is still lacking. Here, these phenomena are discussed as a precaution for the design and formulation of food inks as well as setting up printing conditions to reach more effective 3D food printing.

2.1.4.1 Die Swell

The extrudate swell, i.e., die swell or Barus effect, phenomenon is a common challenge in material extrusion processing. It is principally due to the recoverable elastic deformation, resulting in the rearrangement of molecules as the material exits an extrusion die or printer nozzle. This phenomenon occurs mainly during the stand-off region when the extrudate comes out of the nozzle and during the formation of the 3D structure, thus impacting the printability and shape fidelity of the printed object. In order to assess this phenomenon, the swell ratio and the Deborah number (De) can be used. The swell ratio (B) can be defined as in Equation (2.6). It is used to indicate the extent of swelling of the polymer material after being extruded.

$$B = \frac{D}{D_0} \tag{2.6}$$

where D is the diameter of the extrudate filament, and D_0 is the diameter of the nozzle, as shown in Figure 2.8. In addition, the Deborah number can be determined as follows, Equation (2.7).

$$De = \frac{\lambda}{t_{process}} \tag{2.7}$$

where λ is the relaxation time, and $t_{process}$ is the time of observation.

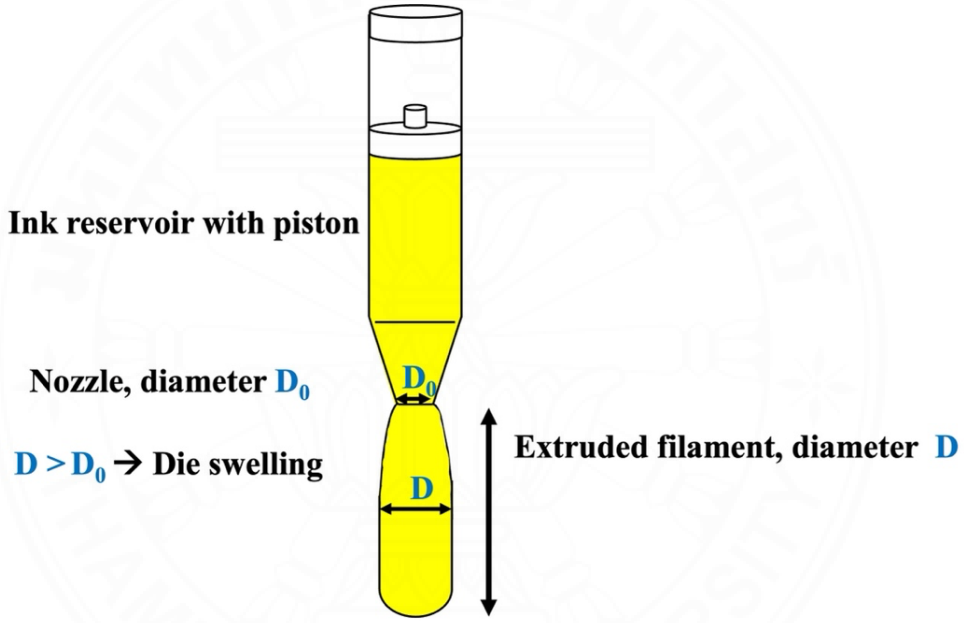

Figure 2.8 A schematic representation of the die swell in 3D printing.

The time of observation is usually the time the process takes to operate. A De = 0 signifies that the sample behaves as a viscous material, whereas a De = ∞ means that the sample is an elastic solid. A value of De > 1 implies that the relaxation time is too long compared to the time of the process, meaning that the molecules do not possess sufficient time to relax during the process, so the Barus Effect or die swell can occur. Indeed, materials or food inks that possess a longer relaxation time can exhibit a higher extent of die swell which may not be desirable in 3D food printing. In general, the relaxation time also increases with an increase in the molecular weight and degree of branching (Aho et al., 2015). Indeed, higher molecular weight, and an increase in

concentration can result in a more pronounced chain entanglement which in turn can lead to a greater die swell. Therefore, precautions should be taken in selecting food biopolymers to prepare food ink formulations. Controlling the length of the die can also be useful for this type of process as a longer die may allow sufficient time for the polymer chains to adapt to their new orientation and thus resulting in a lesser extent of die swell.

From the rheological perspective, various methods can be used to determine the relaxation time (λ). It can be determined by frequency sweep or by stress relaxation measurement. For the determination with frequency experiment, the relaxation time corresponds to the inverse of the frequency at the crossover point, when G' equals G". Moreover, λ can be determined by fitting flow data, i.e., viscosity as a function of the shear rate, with rheological flow models, for example, the Carreau–Yasuda model, Equation (2.8) (Morrison, 2001).

$$\eta = \eta_\infty + (\eta_0 - \eta_\infty)[1 + (\lambda\dot{\gamma})^a]^{\frac{n-1}{a}} \quad (2.8)$$

where η corresponds to the viscosity, η_∞ and η_0 are the infinite and zero shear viscosity, respectively, λ is the relaxation time, a is a dimensionless parameter, $\dot{\gamma}$ is the shear rate, and n is the rheological index. In addition, the shear normal difference N_1 can also be used to predict the die swell phenomenon (Baird & Collias, 2014; Ewoldt & Saengow, 2022). A positive N_1 is indicative that die swell may likely occur and reformulation of food inks or proper controlling of printing condition, i.e., decreasing ink flow rate, may be required to suppress this phenomenon.

Although examples of die swell in 3D food printing are limited, the problem has been shown to impact the 3D printing process of molten polymer filament. A review work by Mackay (2018), considering the rheological behavior affecting the extrusion 3D printing of molten polymer filament, explained that the die swell could be impacted by parameters such as the Reynolds number, the first normal stress difference, and the shear rate (Mackay, 2018). However, many questions remained unanswered, especially on how the die swell can be limited by the material's rheology or considered by the printer algorithm. Das and co-workers also decrypted some important parameters

impacting this behavior. They explained that printing parameters such as the printing speed, the temperature, or even the extrusion speed significantly affect the die swell, thus negatively impacting the overall quality of the printed object. They showed that a high flow rate, related to the extrusion speed, can generate oscillations in the diameter of the extruded filament. In addition, an increase in the temperature of the ink can be beneficial in limiting this phenomenon. Indeed, as the temperature increased, the die swell was reduced because the polymer chains presented higher molecular mobility, so the stress relaxation time was significantly reduced (Das et al., 2021). In addition, Yuk and Zhao (2018) demonstrated that various aspects of the extruded filament could be obtained by applying control over various printer parameters (Yuk & Zhao, 2018). Using these parameters, they defined two non-dimensional printing parameters related to nozzle speeds and the tip height from printing bed, as given in Equations (2.9) and Equation (2.10), respectively.

$$V^* \equiv \frac{V}{C} \tag{2.9}$$

$$C^* \equiv \frac{H}{\alpha D} \tag{2.10}$$

where V^* is the non-dimensional nozzle speed, C^* the non-dimensional nozzle tip height, V the nozzle movement speed, C the extrusion speed, H distance between the printing bed and the printing head, D the nozzle diameter, and α the die swelling ratio.

By varying these two dimensionless parameters, the extruded filament displayed a range of different characteristics such as accumulation, coiling, die swell, equidimensional, thinning, or discontinuous aspect, as shown in Figure 2.9. There is a certainly strong dependence of the extruded results on the properties of the materials. Indeed, the parameter α, defined as the die swelling ratio, depends on the material used. Moreover, the extrusion speed C, depends on the ink rheological properties and the applied pressure. So, it is essential to know the rheological properties to determine the extrusion speed to print in a targeted mode. Interestingly, the authors also showed that a resolution finer than the nozzle diameter (thinning) could be attained by stretching the

extruded ink. This stretching property also points to the importance of the extensional rheological properties of the ink, which will be discussed in the next section. Such a kind of study using food inks is still missing but is encouraged so that better understanding on the rheological property-3D printing process relationship can be established, thus, accelerating the application of 3D printing in food industry in the near future.

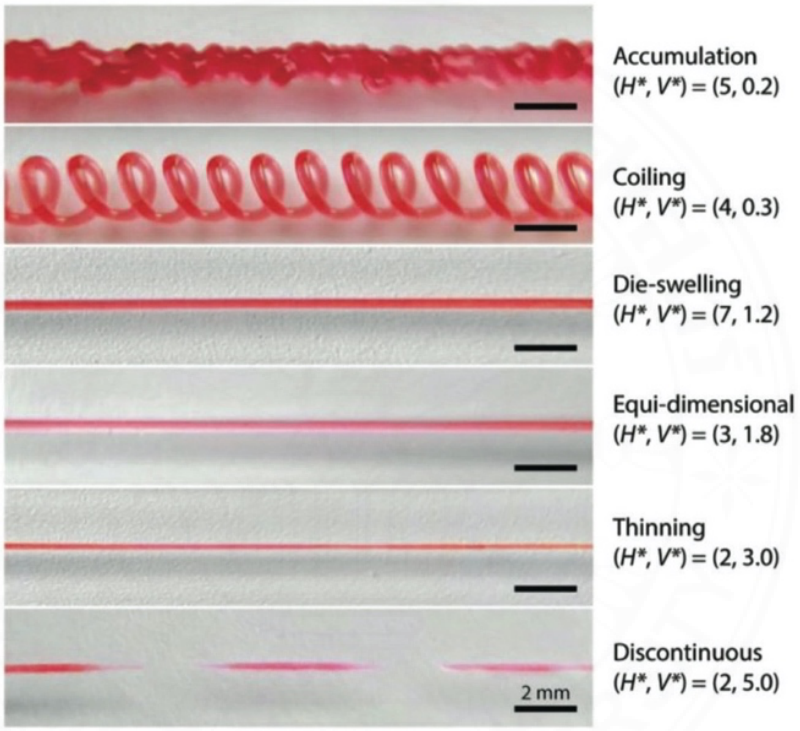

Figure 2.9 The different printing characteristics obtained during the 3D printing of a viscoelastic ink. The ink is made of a mixture of silicon elastomers. Source: Reproduced from Yuk and Zhao (2018).

To reduce experimental trials, Computational Fluid Dynamics (CFD) can be beneficially used as a tool to assess the printing parameters impacting the die swell in 3D food printing. Parameters such as the flow rate, the shear rate, the pressure, the length of the ink reservoir, the nozzle diameter, and the temperature were found to play a role in the die swell (Oyinloye & Yoon, 2022). CFD studies also concluded that the die swell resulted in unequal repartition of the tensile stress within the printed object yielding deformation in the printed object (Oyinloye & Yoon, 2021). Yang et al. (2019)

used CFD to simulate the 3D printing process of gels made of lemon juice and starch (Fanli Yang et al., 2019). They showed that the flow parameters, which were stable in the barrel section and not in the nozzle section, were impacted by the viscosity and the relaxation time of the ink. Subsequently, die swell was observed after extruding the food ink, but they also suggested that limiting the filling rate to 90% could diminish the swelling phenomenon.

2.1.4.2 Extensional flow/viscosity

During the 3D printing process, and more precisely, when the extracted filament comes out of the nozzle, the ink is subjected to an extensional/elongation flow before reaching the printing bed. This phenomenon can strongly impact the process as it can cause filament thinning, necking, or even rupture. As a consequence, the printed object does not display continuous printed lines, thus resulting in weakening the final structure or unsuccessful printing.

From a rheological point of view, various types of extensional flow measurements can be performed to assess the extensional properties of printing materials. These include uniaxial extension, capillary breakup, biaxial extension, and planar extension. The uniaxial extension is the type of extensional flow found in the 3D printing process. In that case, a constant volume of material is stretched along one dimension, and shrinking the other two dimensions (Steffe, 1996). Numerous parameters are known to affect the extensional properties of materials. The molecular weight, the molecular weight distribution, the degree of branching as well as interaction among different constituents within the formulated food inks are among the most important parameters (Barnes, 2000). Similar to shear rheology, an extensional viscosity can be defined as a function of the strain. This type of experiment gives helpful information regarding the extensional behavior of stretched material. For example, behavior such as strain softening, or strain hardening can be determined. However, this measurement presents some drawbacks as it is hard to ideally create a well-controlled purely extensional flow due to the presence of shear flows at the boundaries, gravitational effects, and surface tensions. As a result, this method is less used than shear rheology, especially to study 3D printing applications.

As shown in Figure 2.9, various aspects of the printed filament can be obtained after the extrusion. This rupture of the extruded filament is not desired as it can impact the printed shape by yielding an incomplete printing. It has been shown that an increase in extensibility properties of an emulsion by increasing the molecular weight of poly(ethylene oxide) (PEO) enabled to print an ink at a higher distance between the nozzle and the surface, shown in Figure 2.10 (Rauzan et al., 2018). Thus, it can affect the setting of the parameters C^* and V^* as defined by Yuk and Zhao (2018).

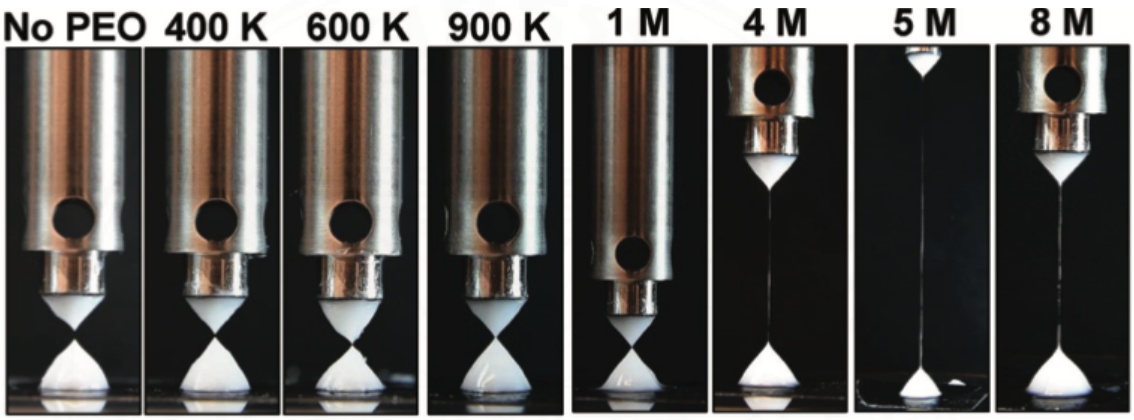

Figure 2.10 Evolution of the maximum filament extension with increasing molecular weight of PEO. Source: Reproduced from Rauzan et al. (2018).

These findings highlight the importance of the extensional rheological properties of the ink for the 3D printing process during the stand-off region. As we described in this section, fewer works focusing on this particular aspect of the 3D printing process are available, and to the best of our knowledge, no work dealing with the impact of the extensional properties on 3D food printing is yet available. This lack of study can be linked to the difficulties of carrying out extensional rheological experiments. Nevertheless, it can be interesting to pursue the study in this area to limit the negative impacts of the extensional flow on the relaxation behavior of the ink. Moreover, perfectly controlling the thinning properties of the extruded filament may permit the printing process with larger nozzle diameters. Thus, it may ease the printing process by requiring a reduced extrusion pressure to achieve higher printing resolution.

2.1.5 Conclusion and outlook

This review assesses the importance of various rheological parameters on the extrusion-based 3D printing of biopolymer-based foods. It is strongly believed that this knowledge applies to a greater extent to food inks. From the analysis of the results obtained in the literature, a suitable range for the viscoelastic properties, given in terms of tanδ and G', has been suggested to yield a stable 3D printed food structure. This range corresponds to tanδ ≤ 0.268 and G' ≥ 300 Pa. The extrudability of a food ink is also governed by its yield stress and rheological flow parameters K and n, that may be obtained from the Power Law model. These three factors have been shown to impact the minimum pressure required to initiate the ink flow during the process. This pressure should be lower than the maximum pressure provided by the printer. Furthermore, the thermal properties of biopolymer-based food inks also play an essential role in controlling successful printing, and this knowledge is required to set the 3D food printing process temperatures correctly. Other rheological phenomena, including die swell and extensional flow, are also important in 3D food printing, but limited studies exist. Combining all these rheological aspects together is still challenging and limited information is available for 3D food printing at present. As a result, there is still a need to deepen and extend the knowledge in this field, especially regarding the relationship between the rheological properties of food inks and the printing conditions for effective printability of food structure. Further research is also needed to assess the overall impact of the extensional rheological properties of food inks in the printing process and to develop better control of the swelling of the extrudate to achieve high printing accuracy. By filling these gaps, it is anticipated that more food materials can be printed, and successful printed structures can be obtained, presenting enhanced fidelity and a better reproducibility to widen the use of this technology to prepare tailored 3D printed foods for personalized nutrition in the near future.

2.2 Parameters impacting the shape stability of printed objects

In addition to the importance of the rheological properties reviewed previously, it is also of high interest to review the parameters defining the formation of the printed shape and its stability. More precisely, this section will review studies highlighting the important criteria for shape fidelity and shape stability for 2D and 3D printing.

2.2.1 Parameters relevant to the printability of filament

The 3D printing process corresponds to the layer-by-layer deposition of material to form a three-dimensional object. Before focusing on the formation of the complete object, it is relevant to pinpoint the properties impacting the printability of a single filament. Indeed, controlling the printed filament is essential because defaults can significantly impact the formation of the complete 3D object, as demonstrated by Fu et al. (2021), Figure 2.11 (Fu et al., 2021).

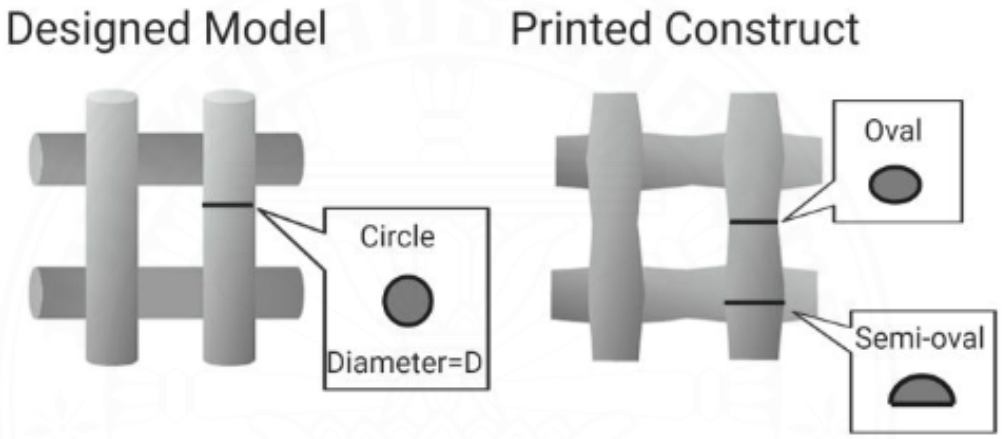

Figure 2.11 Effect of filament anomalies on the 3D printed object. Source: Reproduced from Fu et al. (2021).

Several authors have studied the effect of the printing parameters on the printed line width. He et al. (2016) studied the parameters affecting the printability of hydrogels. They raised specific attention to the accuracy of printing, and their results displayed the impact of various printing parameters, such as the nozzle movement speed and the distance between the nozzle and the printing bed on the line width. They demonstrated that an increase in nozzle movement speed decreased the width of the printed line. Increasing the distance displayed an increase in the printed line width. However, the printed line obtained was larger than the nozzle diameter. Increasing the distance also affected the printing pattern as sharp corners became curved. Moreover, the authors highlighted the negative effect of overlapping during sharp-angle printing and suggested reducing the extrusion rate to avoid material accumulation (He et al., 2016). Similar observations were observed regarding the effect of the nozzle movement speed

and the flow rate, which can be linked to the applied pressure (Roehm & Madihally, 2017). Maldona-Rosas et al. (2022) observed that increasing the biopolymer concentration yielded 2D structures with a better shape fidelity, but no linkage with the rheological properties was proposed (Maldonado-Rosas et al., 2022). These studies reveal the printing parameters' importance on the filament's width; however, no effect of the rheological properties is presented.

2.2.2 Parameters relevant to the formation of the 3D structure

Throughout the literature, printing quality has been characterized by various parameters, many associated with dimensional accuracy or the general stability of the printed objects. This section will present some methods used to assess these parameters.

2.2.2.1 Dimensional accuracy

The dimensional accuracy refers to the degree to which the dimensions of the printed food match the dimensions of the model. Several parameters have been presented and will introduced here.

The first parameter introduced in the literature is the printability (%), Equation (2.11) (Azam et al., 2018). Note that the term printability is presented here as defined by the authors; it differs from the definition of printability presented previously. It could be relevant to refer to it as height fidelity (H_F). In this equation, h is the height achieved by the printed object, and h_0 is the targeted height.

$$H_F \text{ or } printability\ (\%) = \frac{h}{h_0} \times 100 \tag{2.11}$$

Some authors also choose to determine the dimensional accuracy by focusing on the width and height of the layer in the 3D printed objects, Equations (2.12) – (2.14) (Bareen et al., 2021; Huang et al., 2020). These terms are the diameter deviation D_d, the height deviation H_d, and the printing precision P_p. In these equations, D_L is the diameter of the printed layer, H_L is the height of the printed layer, D_L' is the diameter of the layer in the model and, H_L' is the height of the layer in the model.

$$D_d = \frac{D_L - D_{L'}}{D_{L'}} \times 100 \quad (2.12)$$

$$H_d = \frac{H_L - H_{L'}}{H_{L'}} \times 100 \quad (2.13)$$

$$P_p = \frac{D_L}{D_{L'}} \times 100 \quad (2.14)$$

A more complete presentation of the dimensional accuracy, including several dimensional parameters, can be found in the literature. Dick et al. (2021) used the dimensional deviation (D_D) as an indicator of the dimensional accuracy of their printed objects, Equation (2.15) (Dick et al., 2021). In this equation, d is the diameter of the printed object, h is the height of the printed object, d' is the object's diameter in the model and h' is the object's height in the model.

$$D_D = \frac{(d - d') + (h - h')}{(d' + h')} \times 100 \quad (2.15)$$

This section outlines various methods for assessing the dimensional accuracy of 3D printed food items. It is worth emphasizing that the authors chose the equations provided selectively based on their specific requirements. Guo et al. (2021) studied the printing fidelity of objects with hollow sections (Guo et al., 2021). They defined their parameter for dimensional accuracy as presented in Equation (2.16). In this equation, A designs the printed area, and A' the designed area (model).

$$P_F = \left(1 - \frac{|A - A'|}{A'}\right) \times 100 \quad (2.16)$$

Moreover, it is crucial to note that different shapes of printed objects may necessitate distinct formulas for accurate evaluation. The ink rheological properties have been shown to strongly affect the printing accuracy (Kadival et al., 2022). Viscoelastic properties or yield stress correlate with better shape fidelity (In et al., 2021; Zhenbin Liu et al., 2018).

2.2.2.2 Stability of the printed object

The stability has been demonstrated to be fair when tanδ ≤ 0.268 and G' ≥ 300 Pa. However, what parameters can be used to define the stability of the printed object? This section will introduce several parameters defining the stability of the printed objects as presented in the literature.

The formation of the 3D shape is crucial in the 3D printing process, and several parameters have been defined to assess the stability of the printed object. Several authors have evaluated the shape stability over time (Azam et al., 2018; In et al., 2021; Riantiningtyas et al., 2021). To do so, the evolution of the dimensions (usually the height) is compared after printing and after a fixed resting time (varying from 0.5 to 24 hours) and referred to as stability, Equation (2.17). In this equation, H_0 is the height of the printed objects immediately after printing and H_t is the height measured after a fixed time.

$$Stability\ (\%) = \frac{H_t}{H_0} \times 100 \tag{2.17}$$

The rheological properties have been presented as an important parameter affecting the stability. In et al. (2021), Chen et al. (2019) showed that having higher storage modulus and yield stress values yielded structures with improved stability and printability (H. Chen et al., 2019; In et al., 2021). Heckl et al. (2023) also evaluated the parameters promoting a correct shape fidelity for hydrocolloids-starch based inks. Their study displayed the importance of the storage modulus and the yield stress to obtain a correct shape stability. Kim et al. (2017) studied the dimensional stability of various 3D-printed foods compared to a model material (methylcellulose at 5 – 14%) using the shear modulus (G). A classification system was developed based on their results, Table 2.3 (Kim et al., 2017).

Table 2.3 Dimensional stability classification proposed by Kim et al. (2017).

Classification	Shear modulus	Printable range
A	> 5000	80 mm cylinder
B	2000 - 5000	40 mm cylinder
C	500 - 2000	20 mm cylinder
D	< 500	No 3D structure

Maldona-Rosas et al. (2022) determined the stress at collapsing ($S_{collapsing}$) from several 3D printed objects, Equation (2.18). In this equation, m is the mass of the printed structure in kg, g is the gravitational acceleration in $m.s^{-2}$ and A is the surface area in m^2.

$$S_{collapsing} = \frac{m \times g}{A} \quad (2.18)$$

The authors pinpointed that a structure with a higher storage modulus can withstand higher stress at collapsing. In addition, Zhu et al. (2019) demonstrated the significance of the yield stress on the ability of a structure to withstand higher stress at collapsing (Zhu et al., 2019). Oyinloye & Yoon (2022) also used the finite element method to evaluate the total deformation of a printed construct. It was concluded that the deformation was linked to the nozzle diameter. For their ink composed of surimi paste, printing with a nozzle diameter of 1.0 mm yielded a more accurate object as simulated (Oyinloye & Yoon, 2022).

2.2.3 Effect of the post-processing on the shape of the printed object

Most 3D printed foods are not directly edible and require additional post-processing steps. Various post-processing methods are available and depend on the targeted application and needs. These methods include microwaving, baking, frying, drying, air frying, steaming, or even freeze-drying (Wen et al., 2024). However, this necessary step impacts the dimensional properties of the printed objects due to the reduction of moisture content in most cases (Hussain, Malakar et al., 2021).

Microwave and baking have been demonstrated to impact the dimensional properties of the printed food negatively (Keerthana et al., 2020; Pulatsu et al., 2022). Exercising controlled baking by fixing the baking time and temperature has been shown to limit the dimensional changes and to maintain a correct shape fidelity (Guénard-Lampron et al., 2021; Zhang et al., 2018). The baking process has been shown to be more suitable than microwaves as the printed object's surface was more pleasant (Yin et al., 2024). In addition, baking enables the browning of the printed food, promoting its desirability (Kewuyemi et al., 2022). In contrast, baking at low temperatures or drying the 3D printed food objects may not be suitable for obtaining a high shape fidelity. Indeed, as shown by Klar et al. (2019), drying 3D printed samples at low temperatures (25 °C) greatly reduces the dimensions of the printed object, Figure 2.12 (Klar et al., 2019). In that contest, the water slowly evaporates through the objects, while during baking, at high temperatures, the water remains trapped inside the object due to the formation of a crust.

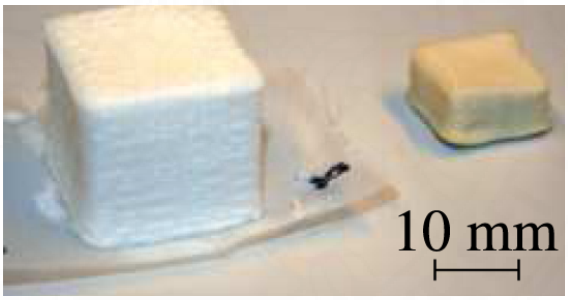

Figure 2.12 Evolution of printed object after drying at 25 °C Source: Reproduced from Klar et al. (2019).

Using steaming, Liu et al. (2020) processed their 3D printed food object. Their results present a correct shape stability of the food sample as reduced variations in the dimensions were noticed (Y. Liu et al., 2020). Air frying is also a method that enables the correct fidelity of shape. Liu et al. (2020) used this method to develop 3D printed potato snack with a reduced oil content (Z. Liu et al., 2020). Freeze-drying presses correct shape stability, as Feng et al. (2020) demonstrated. However, this method remains costly and time-consuming (Feng, Zhang, Liu, et al., 2020).

2.2.4 Summary and perspectives

This chapter highlights the critical role of rheological parameters in extrusion-based 3D printing of biopolymer-based food inks. Key factors influencing the printability and stability include viscoelastic properties ($\tan\delta \leq 0.268$ and $G' \geq 300$ Pa), yield stress, and rheological flow parameters. Moreover, the dimensional accuracy assessed through several metrics is crucial for evaluating the printed food's feasibility and quality. Post-processing methods like baking, microwaving, or freeze-drying further impact the printed food shape; challenges persist in understanding the rheological properties' full impact, and further research is necessary to enhance print accuracy and stability across various formulations to promote further 3D food printing as a novel food production process.

As 3D food printing is an additive processing method, this research first aims to understand the impact of rheological properties and printing parameters on the deposited filament dimensions, specifically the spreading ratio. Controlling filament spreading is essential for the accurate formation of each layer. A machine learning approach is introduced to optimize the filament spreading, thus improving the accuracy of the printed objects. Moreover, this work extends further to improving the 3D printability of food inks by adding mung bean protein isolate to pectin-based inks enabling the formation of protein-rich 3D printed snacks. Machine learning classification techniques are applied as quality control tools based on dimensions and rheological properties. Additionally, the influence of post-processing, particularly baking, on the shape of the printed snacks is examined. These studies aim to refine the printing process and expand the potential for creating customized, nutritionally enhanced 3D printed foods.

CHAPTER 3
MACHINE LEARNING ASSISTED EVALUATION OF THE FILAMENT SPREADING DURING EXTRUSION-BASED 3D FOOD PRINTING: IMPACT OF THE RHEOLOGICAL AND PRINTING PARAMETERS

3.1 Introduction

The recent surge of 3D printing technology has revolutionized various industries (Berman, 2012), enabling the fabrication of objects from large-scale engineering structures (Furet et al., 2019) to intricate, small-scale devices. In some of these applications, biopolymers are added to manipulate the rheology of printing inks, thereby facilitating the 3D printing process. These polymers are widely used in fields such as biomedical or food, for their intrinsic properties, including thickening, gelling, or film-forming properties (Ozilgen & Bucak, 2018). In addition, they are renewable, sustainable, and biodegradable and possess the added benefits of being edible and biocompatible. 3D food printing holds immense potential to transform how we produce and consume food. The surge of this technology in the food industry is driven by its potential in many aspects, for instance, to create appealing meals for individuals suffering from dysphagia (Ahlinder et al., 2023; Zhenbin Liu et al., 2023; Pant et al., 2021), or to target specifically nutritional properties for personalized nutrition (Chow et al., 2021; Derossi et al., 2018), or to produce meat and fish substitute (Chen et al., 2021; Kim, Wen, et al., 2022; H. Shi et al., 2023), and to contribute to the reduction in food waste (Muthurajan et al., 2021; Pant et al., 2022).

A fundamental challenge in 3D food printing lies in achieving precise dimensional accuracy and shape fidelity. To create foods with the desired form and function, controlling the behavior of materials during and after the printing process is essential. The rheological properties of biopolymer-based inks play a dominant role in determining their printability. These properties, including viscosity, complex modulus, and yield stress, influence the ink's ability to flow through the nozzle, maintain its shape post-extrusion, and ultimately build stable 3D structures (Cheng et al., 2022; Outrequin et al., 2023; Uribe-Alvarez et al., 2023; Zhu et al., 2023).

Several factors controlling the printed dimensions have been previously highlighted. For instance, In and co-authors (2021) demonstrated that a higher storage modulus correlates with better shape fidelity (In et al., 2021). Controlling process parameters is crucial for avoiding ink overlap and decreasing the fidelity while printing sharp corners (He et al., 2016). Heckl and co-authors also correlated the rheological properties with the printing accuracy (Heckl et al., 2023). Kadival et al. (2022) emphasized the importance of numerous parameters such as shear thinning behavior and elastic dominant nature on the formation of 3D printed food. Post-printing treatments have also been shown to impact the shape of the printed food (Klar et al., 2019). A key metric for assessing dimensional accuracy in extrusion-based 3D printing is the spreading ratio as defined in Equation (3.1). This ratio (S) compares the width of the printed line (W) to the nozzle diameter (D_0), with a value closer to unity indicating greater fidelity to the intended dimensions. While studies have explored the effects of individual factors like rheological properties or process parameters on print fidelity, a comprehensive understanding of their combined influence on the spreading ratio remains elusive. This knowledge gap hinders our ability to achieve precise control in 3D food printing.

$$S = \frac{W}{D_0} \tag{3.1}$$

This study addresses this challenge by systematically investigating the complex interplay between ink rheology and printing parameters in determining the spreading ratio. Importantly, we introduce the novel application of machine learning to analyze this relationship. Machine learning will not only quantify the relative importance of each factor but also enable the development of predictive models. Such models will offer a powerful tool to optimize 3D food printing processes, ultimately leading to enhanced dimensional control and greater precision in food fabrication. The integration of deep learning and machine learning in the field of food science has proven innovative for analyzing extensive datasets across various applications such as food classification (Fröhlich-Wyder et al., 2023; Jeong et al., 2021), oral processing (Oppen et al., 2023)

or prebiotic development (Lam et al., 2020). Applications such as computer vision (Ma, Potappel, Schutyser, et al., 2023) and machine learning classification (Lu et al., 2023) have also been used for food printing.

The integration of machine learning into 3D food printing can offer a novel approach for understanding the complex interplay between ink properties and printing parameters. Machine learning models can discern complex patterns within the experimental data, revealing the relative importance of different rheological properties and process parameters in predicting the spreading ratio. Furthermore, the predictive models developed using machine learning will enable us to tailor ink formulations and printing parameters to achieve specific spreading ratios, and ultimately, fabricate 3D printed foods with the desired dimensions and properties. This ability is crucial for advancing 3D food printing as a viable manufacturing technique for customized and functional food products.

Pectin, a biopolymer frequently used in the food industry and tissue engineering, is an ideal ink model for this investigation due to its tunable rheological properties (Agarwal et al., 2021; Chan et al., 2017; Vancauwenberghe et al., 2017). By varying pectin concentration, we can explore the impact of viscosity, complex modulus, and other rheological parameters on the spreading behavior of printed filaments. Alongside ink rheology, process parameters such as nozzle diameter, extrusion pressure, and printing speed also influence the spreading ratio. By carefully controlling and varying these parameters, we can gain a comprehensive understanding of how they interact with ink properties to determine the final dimensions of printed food structures.

In this study, we formulated pectin inks with varying concentrations, characterized their rheological properties, and systematically explored the impact of process parameters on filament spreading during printing. Machine learning regression models were then trained to quantify the relative importance of each factor and predict the spreading ratio. Our findings are expected to enhance process control and design flexibility in 3D food printing, contributing to the development of customized food products with greater precision.

3.2 Materials and methods

3.2.1 Materials and ink preparation

Two batches of low methoxyl pectin (LM 104 AS-BG) were provided by Winner Group Enterprise PLC (Thailand). These two batches are named 22PT and 23PT, representing different viscosity ranges. Gelatin from porcine skin (gel strength 300, type A) was supplied by A.C.S. Xenon Limited Partnership (Thailand). Deionized (DI) water was used for all the experiments.

Pectin-based printing inks were formulated by dissolving pectin in DI water in a water bath at 60°C for one hour. Pectin concentrations ranging between 5-15 wt% were used in this study. Additionally, a mixture of pectin (12 wt%) and gelatin (2 wt%) ink was prepared by dissolving both biopolymers in DI water at 60°C for an hour. This ink was formulated for the specific purpose of validating the machine learning model employed in this study. Ink formulations were designated with the nomenclature XPTY, where X represents the batch number and Y indicates the concentration in wt%. After preparation, inks were transferred to syringes and allowed to rest overnight at room temperature until further analyses.

3.2.2 Rheological experiments

Rheological experiments were performed using a stress-controlled rheometer (Kinexus ultra plus, Malvern Instrument, UK) equipped with a 40 mm diameter parallel plate geometry and a gap size of 1 mm. After loading, samples were pre-sheared at a constant shear rate of 0.1 s^{-1} for 60 s and allowed to rest for 120 s to reach thermal equilibrium. Three replicates were performed for each experiment, and the average results are presented along with their standard deviation.

(1) Flow Sweep: A flow sweep was performed by varying the shear rate from 0.01 to 100 s^{-1} at a temperature of 25 °C, representing the extrusion temperature. The evolution of the viscosity as a function of the shear stress was obtained from these measurements.

(2) Stress Sweep: A stress sweep was conducted from 0.01 to 100 Pa at 10 °C, corresponding to the printing bed temperature. The linear viscoelastic region (LVR) was determined and used for further rheological analysis.

(3) Frequency Sweep: A frequency sweep from angular frequency (ω) of 0.0628 to 628 rad.s^{-1} was carried out at a constant stress within the LVR and at 10 °C. The evolution of the viscoelastic parameters, i.e., storage modulus (G'), loss modulus (G''), and complex modulus (G*) as a function of the frequency was evaluated. Furthermore, a power law model was employed to describe the relationship between the complex modulus and the angular frequency: $G^* = G_0^* \omega^n$, where G_0^* is the complex shear modulus at angular frequency of 1 rad.s^{-1}, and n is the power-law exponent, determining the frequency dependence of the complex modulus.

3.2.3 Line printing and spreading ratio determination

A modified BIQU®B1 (BigTreeTech, Shenzhen, China) extrusion-based 3D printer was used for printing experiments. The printing head was modified to accommodate luer-lock syringes, enabling the pneumatic dispensing of viscoelastic materials. The 3D printer was also paired with a Peltier cooling plate fixed on the printing bed to reduce the temperature of the extruded ink to 10 °C upon deposition (see Figure 3.1(a)). Printing experiments were carried out according to the parameters given in Table 3.1. Geometric codes, commonly referred to as G-code in additive manufacturing, are programming languages used to operate computer-controlled machines. These codes were prepared using Ultimaker Cura software and manually modified according to the needs. The complete g-code for this study and its visualization are presented in Appendix A.

The printed line length was fixed at 70 mm for each experiment. Printed lines were photographed immediately after printing using an iPhone 13 Pro (12 MP) Ultra Wide Camera. Three replicates were carried out for each ink formulation, and the line width analyses were performed using ImageJ software (Schneider et al., 2012). Five measurements were taken for each printing trial at a defined location along the printed line (see Figure 3.1(b)). The average spreading ratio, as defined in Equation (3.1), was then calculated and compared among different ink formulations. Two printing patterns

depending on the ink concentration and printing parameters were observed in this study, including continuous (either with large spreading or reduced spreading) and discontinuous filament as shown in Figure 3.1(c) to (e). These characteristics of printing behavior were also observed in conventional direct ink writing (DIW), as demonstrated in the previous work of Yuk and Zhao (2018).

(a)

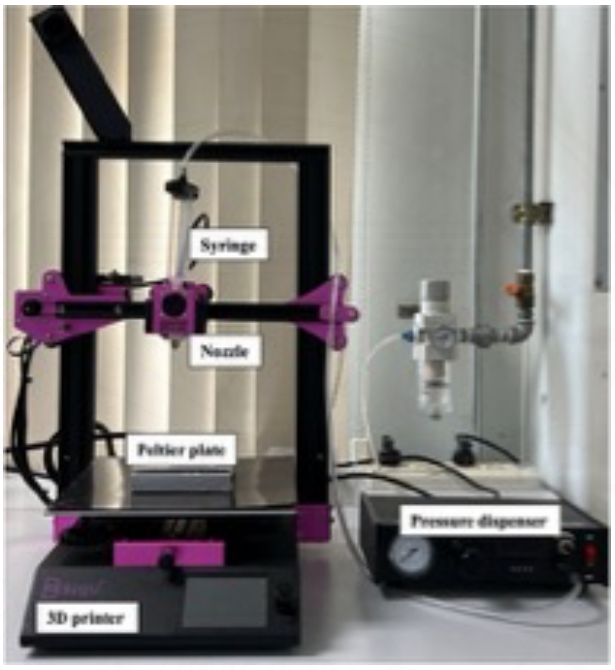

(b)

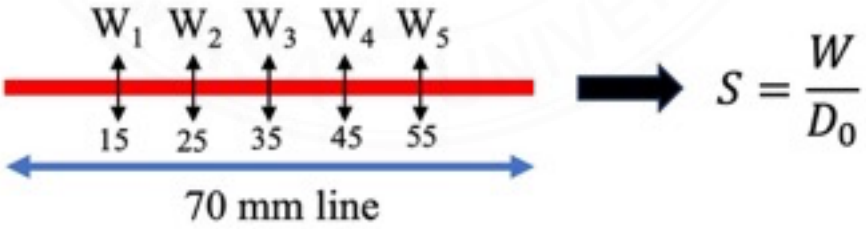

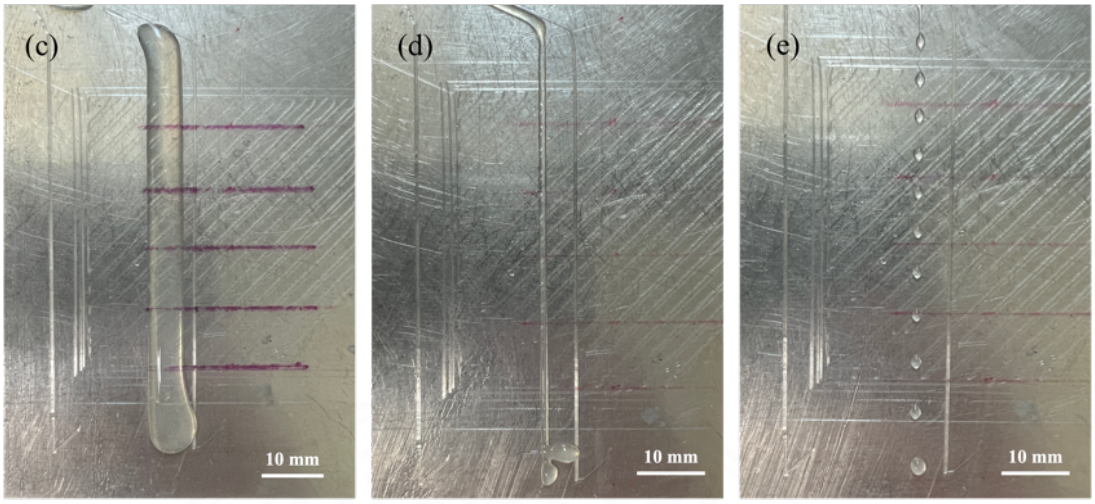

Figure 3.1 (a) 3D printing set-up. (b) Filament spreading analysis procedure. (c) Continuous filament (large spreading) printed with 23PT7.5. (d) Continuous filament (slight spreading) printed with 23PT15. (e) Discontinuous filament printed with 23PT15.

Table 3.1 Printing parameters used in the Chapter 3.

Parameter	Symbol	Value
Nozzle diameter	D_0	0.4 – 0.8 mm
Extrusion pressure	P	0.5 – 1.5 bar
Ink reservoir temperature	T	25 °C
Nozzle temperature	T_1	25 °C
Printing bed temperature	T_2	10 °C
Nozzle movement speed	V	10 – 40 $mm.s^{-1}$
Distance nozzle – printing bed	H	0.8 mm

3.2.4 Machine Learning

The machine learning analysis was performed using Python with the machine learning libraries scikit-learn and Xgboost (Chen & Guestrin, 2016; Pedregosa et al., 2011). Supervised learning techniques were used to model regressions where the spreading ratio was the target variable. Input features included the process parameters, P, V, and D_0, and the viscoelastic rheological parameters, G_0^* and n. The averaged

spreading ratio served as the ground truth values for model evaluation. Five decision tree models were examined, e.g., one single tree model and four ensemble tree models. These models include Decision Tree Regressor (DT), Random Forest Regressor (RF), Extra Trees Regressor (ET), Gradient Boosting Regressor (GB), and Extreme Gradient Boosting Regressor (XGB). The dataset consists of a total of 133 measurements with varied parameters, as described in Table 3.1. The regression models were trained using leave-one-out cross-validation (LOOCV) to ensure a robust evaluation of the dataset. In LOOCV, a unique data point is excluded from the training phase at a time to acquire a test set. This technique is normally performed for small datasets because it maximizes the amount of data available for training during each iteration (Martinez & Martinez, 2015). The average models' performance on training and testing datasets was evaluated based on their root mean squared error (RMSE), the averaged squared relative error (Err. %), and the coefficient of determination (R^2) calculated based on predicted and ground truth values. Feature importance analysis was performed to identify the key features for optimized model training. The developed code is given in Appendix B.

3.3 Results and discussion

3.3.1 Rheological analysis of the pectin-based inks

Shear rheological results are presented in Figure 3.2. The analysis was conducted at 25 °C, representing the temperature at which the ink undergoes extrusion. As anticipated, the viscosity of the ink increased with increasing concentration of pectin. At a shear rate of $\dot{\gamma} = 1\ s^{-1}$, the viscosity increased from 0.39 Pa.s for 23PT5 to 44.65 Pa.s for 23PT15. At this temperature, the results show that inks at concentrations lower than 7.5 wt% generally exhibited a Newtonian behavior, whereas the higher concentration inks demonstrated a non-Newtonian behavior with shear thinning characteristics. Chan and co-workers reported that the critical concentration value of pectin required to obtain the transition from Newtonian to non-Newtonian depends on the pectin molecular weight (Chan et al., 2017). The shear thinning behavior arises from the breakdown of the entangled structural network, leading to an alignment of the polymer chains with the shear flow. This behavior is crucial for facilitating smooth extrusion (Armstrong et al., 2022; Shahbazi & Jager, 2021; Wu et al., 2014).

(a)

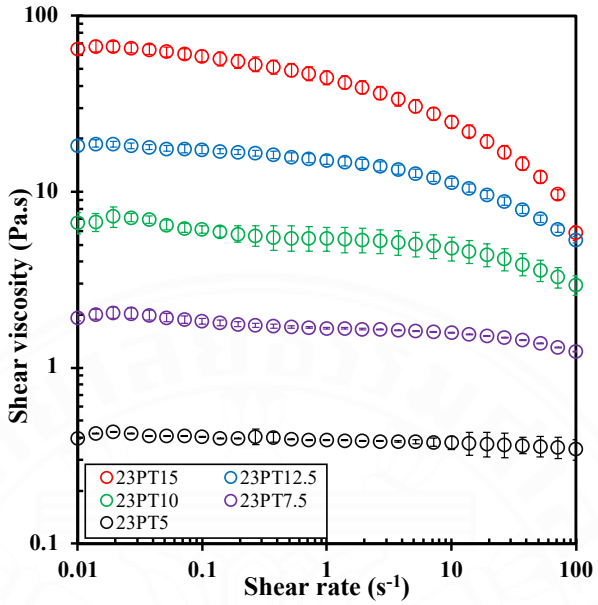

(b)

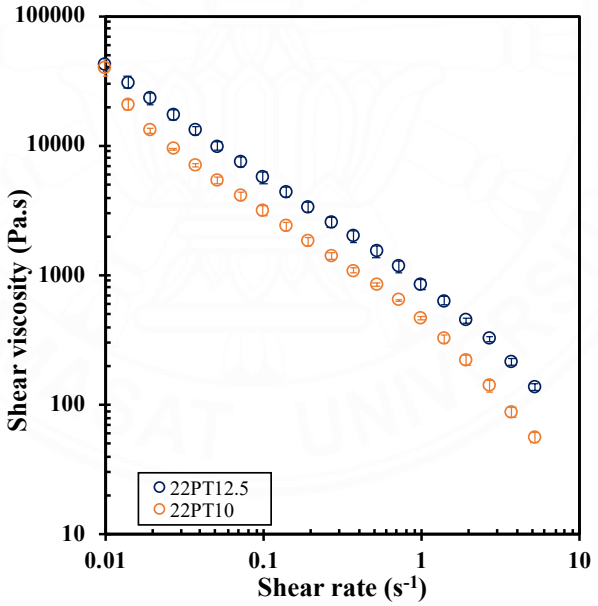

Figure 3.2 Evolution of the shear viscosity as a function of the shear rate at 25 °C for (a) 23PT at various concentrations. (b) 22PT at various concentrations.

Frequency sweep results are presented in the Figure 3.3. At 10 °C, pectin inks from batch 23, with a concentration ranging between 5 - 10 wt% display a liquid-like behavior as the value of G" is higher than that of G', as shown in Figure 3.3(a). This

liquid-like behavior is unsuitable for extrusion-based 3D printing applications due to the lack of shape-holding properties (Outrequin et al., 2023). At 12.5 wt%, pectin ink displays a noticeable viscoelastic behavior as there is a crossover between G" and G' as the frequency increases. Above this concentration, the ink exhibits a solid-like behavior with a weak gel characteristic, as G' is higher than G" across the studied frequency range and both moduli are frequency dependent A similar observation is made for the pectin inks from batch 22 (Figure 3.3 (c) and (d)).

(a)

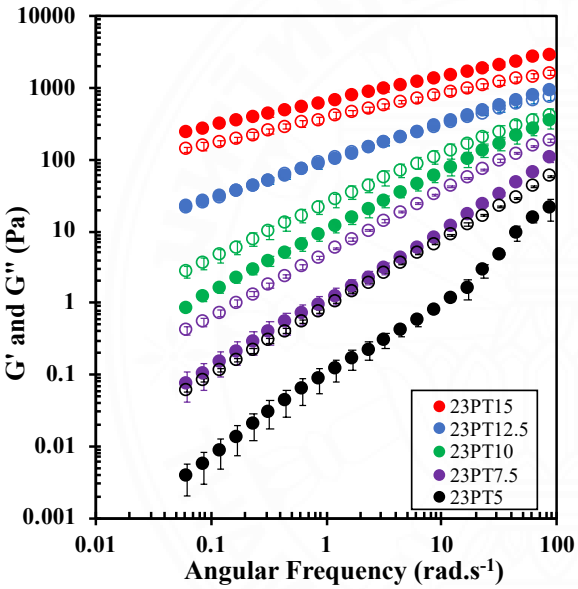

(b)

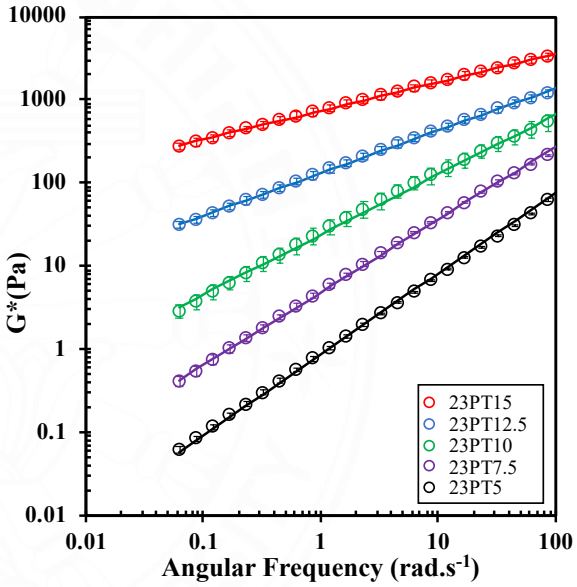

(c) (d)

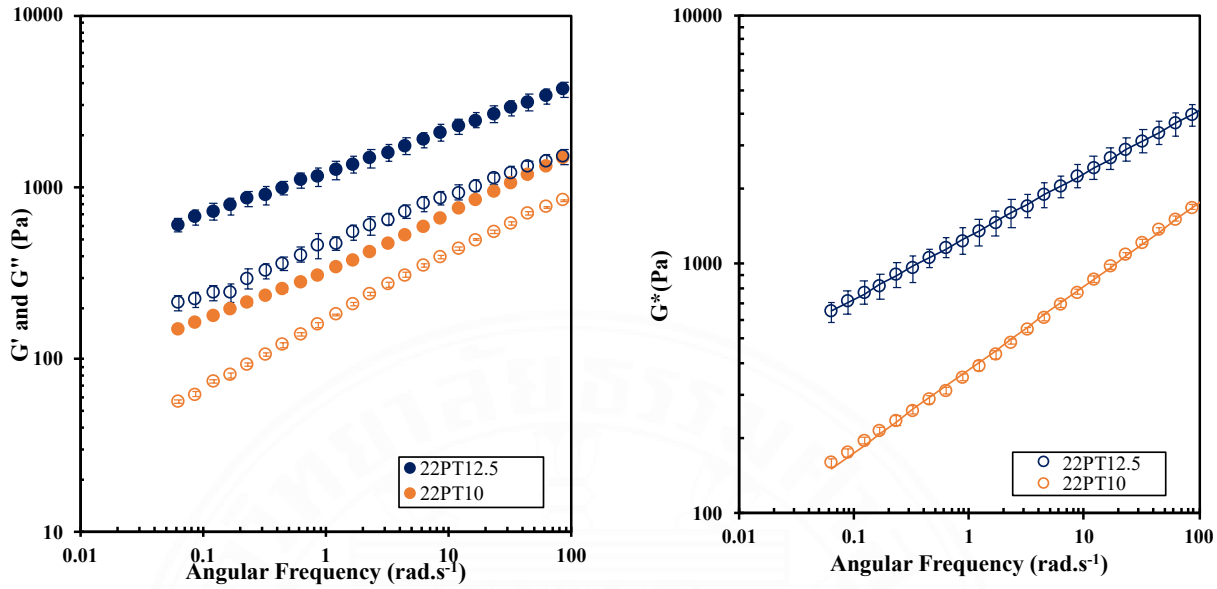

Figure 3.3 Frequency sweep results. (a) Evolution of G' and G'' as a function of angular frequency at 10 °C. Filled symbols represent G', and unfilled symbols represent G''. (b) Evolution of G^* as a function of the angular frequency at 10 °C. (c) Evolution of G' and G'' at 10 °C. Filled symbols represent G', and unfilled symbols represent G''. (d) Evolution of G^* as a function of the angular frequency at 10 °C. The Power Law fitting is represented by the solid lines.

Additionally, the magnitude of G^*, the complex modulus, is plotted as a function of the angular frequency Figure 3.3(b). This rheological parameter can be used to evaluate the material's resistance to deformation. As anticipated, the value of G^* rises correlatively with the evolution of the concentration, indicating a stronger elastic response due to an enhanced polymer chain entanglement. The complex modulus was then fitted with a power law model. The results are reported in Table 3.2. The value of G_0^* evolves from 0.86 Pa for 23PT5 to 737.91 for 23PT15 and the value of n decreases from 0.97 for 23PT5 to 0.34 for 23PT15, indicating a reduced frequency dependency with increasing pectin concentration.

This section details the rheological analysis of the inks based on 23PT and 22PT. In the context of this study, a diverse selection of pectin inks was deliberately chosen to evaluate the impact of the rheological properties on the spreading of the

printed filament. The selected inks span from low viscosity materials to higher viscosity materials exhibiting a solid-like behavior.

Table 3.2 Summary of the rheological analysis of 23PT. The viscosity values are given at a shear rate of $\dot{\gamma} = 1\ s^{-1}$, and the oscillatory values are obtained from fitting with the power law model, i.e., : $G^* = G_0^* \omega^n$.

	23PT5	**23PT7.5**	**23PT10**	**23PT12.5**	**23PT15**
η (Pa.s)	0.39	1.68	5.44	15.17	44.65
G_0^*(Pa)	0.86	4.83	23.89	130.77	737.91
n	0.97	0.88	0.72	0.51	0.34

3.3.2 Effect of the rheological properties on the spreading ratio

The evolution of the spreading ratio was investigated as a function of various rheological parameters, i.e., viscosity (η) at $\dot{\gamma} = 1\ s^{-1}$, and complex modulus (G_0^*) derived from the different formulations. The selection of these rheological parameters was deliberate, as the viscosity reflects the flow resistance of a material, while G_0^* serves as an indicator of the entire viscoelastic behavior at a fixed frequency of 1 $rad.s^{-1}$. Pectin inks, representing a diverse range of rheological properties achieved by incrementally increasing the total pectin content, were extruded under controlled conditions. An applied pressure of 0.5 bar, a printing temperature maintained at 25 °C to align to the room environment's temperature, a bed temperature fixed at 10 °C using the Peltier cooling plate, a nozzle movement speed set at 10 $mm.s^{-1}$, a nozzle to printing bed distance fixed at 0.8 mm, and various nozzle diameters ranging from 0.4 to 0.8 mm were employed. The results are presented in Figure 3.4.

The results depict a strong influence of the rheological properties on the spreading ratio. The graphs exhibit a notably similar trend (r = 0.988), indicating a strong, positive correlation between viscosity and complex modulus. At low viscosity values or low complex modulus values, the extruded ink presents a large filament spreading ratio (surpassing 60). This is undesirable for 3D printing applications as it leads to printed line widths significantly larger than the aimed dimensions (usually equal to the diameter of the nozzle).

As the viscosity increases above 10 Pa.s, or the complex modulus reaches values beyond 100 Pa, the spreading ratio decreases noticeably for all nozzle diameters. This behavior continues at higher viscosity and complex modulus value, with the spreading ratio approaching towards the ideal value of one but without reaching it.

Using inks with increasing pectin content enhances the rheological properties, transforming the ink from a liquid-like system into a more viscous state with improved solid-like behavior. It positively shifted the spreading ratio toward lower values, improving the fidelity of printed lines toward their intended dimensions. However, high-concentration inks require higher extrusion pressures due to their increased yield stress, which can challenge the printing process (Ainis et al., 2023; Outrequin et al., 2023).This study showed that using low viscosity ink, with a viscosity lower than 10 Pa.s, was unsuitable for extrusion-based 3D printing, as it led to an excessive spreading of the printed filaments. Nonetheless, such inks may find applicability in extrusion-based embedded 3D printing, where a support bath possessing suitable rheological properties aids in shaping the structure before further processing, resulting in the solidification of the object (Friedrich & Begley, 2020). In this context, the printed material undergoes a crucial solidification phase through subsequent post-processing steps, such as cross-linking or thermal variation, to yield the final 3D structure.

(a)

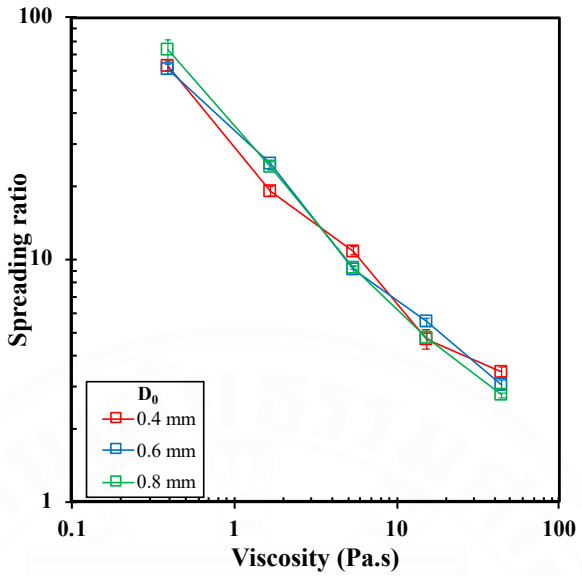

(b)

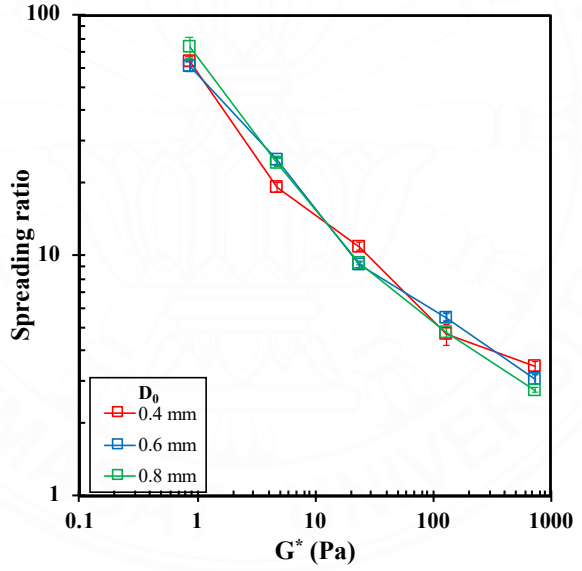

Figure 3.4 Evolution of the spreading ratio as a function of the rheological parameters of different pectin inks (a) shear viscosity at $\dot{\gamma} = 1\ s^{-1}$ and 10 °C, and (b) complex modulus at $\omega = 1\ rad.s^{-1}$.

Effective control over the filament spreading during the material deposition is crucial for achieving accurate dimensions before post-processing and ensuring the production of a high-fidelity printed structure afterward. Increasing biopolymer concentration significantly improves resistance to deformation by enhancing viscosity

and complex modulus. That, in turn, fosters a more robust solid-like behavior due to increasing numbers of chain entanglement. Balancing the attainment of the desired dimensions while maintaining a reasonable biopolymer concentration adds an extra layer of complexity to the exploration of optimal printing conditions. Understanding this balance can provide valuable insights for precise 3D printing while maintaining practical biopolymer concentration.

3.3.3 Effect of the printing parameters on the spreading ratio

As discussed in the previous section, obtaining the desired dimensions presents challenges and requires careful ink formulation. However, increasing the biopolymer concentration is not always suitable since it can harden the overall process by yielding non-extrudable inks or not unsuitable for food applications due to high polymer content. Therefore, this section evaluates how printing parameters affect the spreading of printed filaments. The evolution of the spreading ratio for 12.5 and 15 wt% pectin inks was studied by varying the process parameters, i.e., the applied pressure P, the nozzle movement speed V, and the nozzle diameter D_0. The results are displayed in Figure 3.5. Unless otherwise specified, the printing parameters were as follows: P = 0.5 bar, V = 10 $mm.s^{-1}$, T_2 = 10 °C, and H = 0.8 mm. Each ink was printed using different nozzle diameters (0.4, 0.6, and 0.8 mm).

(a)

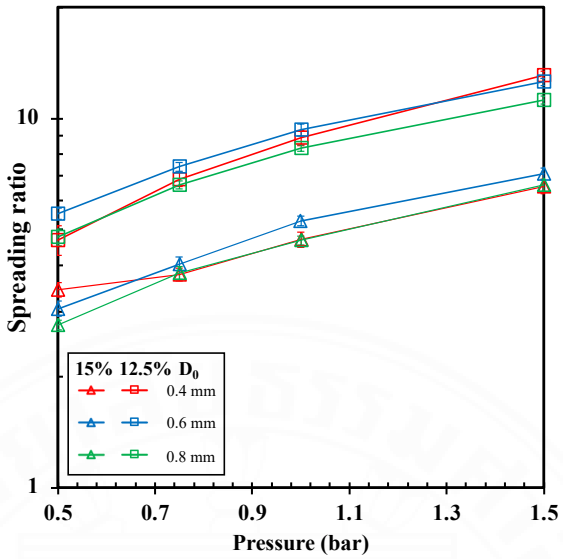

(b)

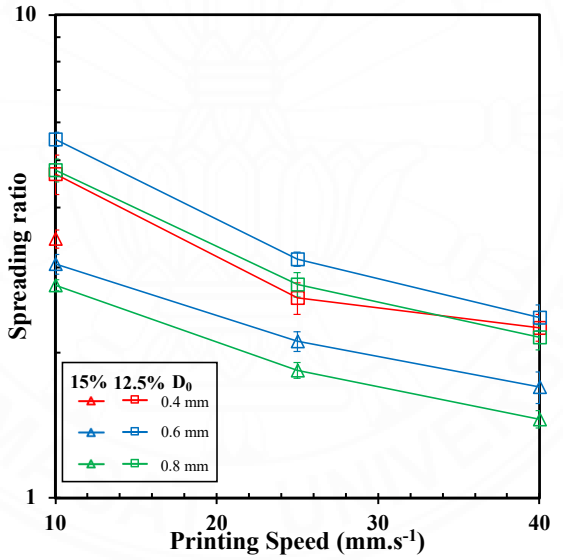

Figure 3.5 The spreading ratio as a function of (a) the extrusion pressure between 0.5-1.5 bar at constant nozzle speed of V = 10 $mm.s^{-1}$. (b) The printing speed is between 10-40 $mm.s^{-1}$ at a constant P of 0.5 bar.

Figure 3.5(a) displays the effect of an increase in the applied extrusion pressure, leading to a more extensive spreading ratio. Specifically, for the 12.5 wt% pectin ink, the spreading ratio exhibited a significant evolution, from a value of 4.69 at 0.5 bar to 10.59 at 1.5 bar when employing a 0.4 mm nozzle diameter. This trend was consistent across all nozzle diameters. In contrast, the ink composed of 15 wt% pectin exhibited a

less pronounced response to increased extrusion pressure. Indeed, its spreading ratio increased from 3.44 to 6.44 with a 0.4 mm diameter and a pressure of 0.5 bar. Similar behavior was observed for larger nozzle diameters. The effect of printing speed is illustrated in Figure 3.5(b), showing that an increase in printing speed correlates with a decrease in the spreading of the printed filament. For example, with the 12.5 wt% ink, increasing the printing speed from 10 to 40 $mm.s^{-1}$ reduced the spreading ratio by half across all the nozzle diameters. As the ink concentration increased to 15 wt% pectin, the decrease in the spreading ratio was less pronounced but remained significant. It is evident that a higher printing speed consistently leads to a reduction in the spreading ratio for all ink concentrations and nozzle diameters studied. Moreover, the printability of this ink was discontinuous when the printing speed increased above 10 $mm.s^{-1}$ as illustrated in Figure 3.1(e). The results obtained are consistent with previous literatures (He et al., 2016; Ma et al., 2021; Roehm & Madihally, 2017).

These results highlight the influence of the process parameters on the spreading of the filament dynamics. By increasing the applied pressure, higher shear rates are generated. This, in turn, causes the ink viscosity to reduce as a result of its shear-thinning properties, thus leading to a higher spreading ratio. On the other hand, the extrusion process with a higher nozzle movement speed deposits less material, resulting in narrower printed lines. The material's thinning properties are possibly responsible for the filament spreading reduction when the printing speed increases. It has been shown that carefully calibrating the printing speed is vital to limit the thinning of the extruded filament and to refrain the material from fracturing as the deposition occurs (Li et al., 2023; Yuk & Zhao, 2018). The findings also shed light on the influence of nozzle diameter on the spreading ratio, revealing a subtle effect when compared to other printing parameters. Nonetheless, the nozzle diameter remains important to consider, as detailed by Oyinloye and Yoon (2022); increasing the nozzle diameter decreases the shear rate locally at the nozzle exit (Oyinloye & Yoon, 2022). These phenomena emphasize the importance of precise control over extrusion parameters to achieve the desired printed dimensions.

Overall, the ink concentration emerges as a critical factor in shaping the resulting printed lines. As observed, the ink formulation containing 12.5 wt% pectin appeared more responsive to increased pressure than the one at 15 wt%. As the concentration

increased, there was a noticeable reduction in the spreading ratio at a fixed nozzle diameter and under the same applied pressure. This correlation relates to the impact of the rheological properties of the ink, with higher concentrations contributing to enhanced elastic behavior, thereby limiting the spreading of the filament during the extrusion process. In opposition, there is a less pronounced reduction in the spreading ratio for increased printing speed when the elasticity is higher. In that case, a stronger elastic behavior acts as a limiting factor, affecting the response to changes in printing speed. The interaction between extrusion pressure, nozzle movement speed, and ink concentration emphasizes the intricate relationship between process parameters and rheological properties in governing the dimensions of the 3D printed line.

This section demonstrates the pivotal role of the printing conditions on the behavior of the filament during the material deposition. Effective control over the applied pressure, the nozzle movement speed, and the nozzle diameter are essential for obtaining the desired dimensions. Further methods can be employed to determine the contributing weight of each process and rheological parameters on the spreading ratio. In the following section, a machine learning approach is proposed to establish a relationship between all these parameters and the spreading ratio.

3.3.4 Machine Learning assessment of the filament spreading

Machine learning regression was used to analyze the correlation between filament spreading of pectin inks (batches 22PT and 23PT) and various printing and rheological parameters. The studied parameters, which are also known as features in the machine learning implementation, consisted of P, V, D_0, G_0^*, and n. It is worth pointing out that an initial study was carried out incorporating the flow properties, such as the viscosity and flow behavior index. These terms were correlated with the oscillatory rheological parameters and thus removed to ensure that unique feature characteristics were taken into the models. Five tree-based regression models with increased complexity were employed: Decision Tree Regressor (DT), Random Forest Regressor (RF), Extra Trees Regressor (ET), Gradient Boosting Regressor (GB), and Extreme Gradient Boosting Regressor (XGB). These models were selected due to their popularity in machine learning applications due to their versatility and performance. The main differences among them lie in their ensemble strategies, randomness in

feature selection, and optimization techniques. Table 3.3 summarizes the different model performances using the root mean squared error (RMSE), the averaged squared relative error (Err. %), and the coefficient of determination (R^2). These metrics were calculated based on predicted versus ground truth values for all leave-one-out training and testing results, respectively. The number of features incorporated in model training is reduced one by one by removing the feature presenting the lowest importance. It is performed to make the model simpler and to improve the model's performance by reducing overfitting.

Table 3.3 Regression model evaluation results. The number of features is reduced by eliminating the feature with less importance for the best model. For each number of features, the model that yields the highest prediction performance is underlined. Feature: 5 = P, V, D_0, G_0^*, and n; 4 = P, V, G_0^*, and n; 3 = V, G_0^*, and n.

	Training			**Testing**		
	RMSE	**R^2**	**Err. (%)**	**RMSE**	**R^2**	**Err. (%)**
Gradient Boosting Regressor (GB)						
5 features	<u>0.7181</u>	<u>0.9949</u>	<u>1.13</u>	<u>1.8895</u>	<u>0.9664</u>	<u>2.67</u>
4 features	1.5343	0.9765	1.98	2.4186	0.9417	3.62
3 features	<u>2.4008</u>	<u>0.9425</u>	<u>15.09</u>	<u>3.0638</u>	<u>0.9068</u>	<u>19.30</u>
Extra Trees Regressor (ET)						
5 features	0.3358	0.9989	0.15	2.3530	0.9475	2.48
4 features	<u>1.5012</u>	<u>0.9775</u>	<u>1.54</u>	<u>2.3747</u>	<u>0.9441</u>	<u>3.58</u>
3 features	2.4013	0.9425	15.06	3.0717	0.9063	19.57
Extreme Gradient Boosting Regressor (XGB)						
5 features	0.3359	0.9989	0.15	2.2775	0.9566	2.21
4 features	1.5012	0.9775	1.54	2.4059	0.9426	3.71
3 features	2.4001	0.9425	15.06	3.0716	0.9063	19.57
Decision Tree Regressor (DT)						
5 features	0.3358	0.9989	0.15	2.6756	0.9377	4.57
4 features	1.5012	0.9775	1.54	2.5672	0.9349	4.36
3 features	2.4001	0.9425	15.06	3.0717	0.9063	19.57
Random Forest Regressor (RF)						
5 features	0.8869	0.9930	0.46	2.3047	0.9495	2.67
4 features	1.5738	0.9761	1.64	2.4991	0.9412	3.54
3 features	2.4191	0.9423	15.10	3.0646	0.9078	19.79

The findings indicate that all the tree models perform well across the different number of features studied. In all models, the performance slightly drops when applied to the test data compared to the training performance, hence showing light overfitting

behavior. This is a common occurrence in small datasets (Ying, 2019). It can also be observed that the models comprising 5 features present the lowest RMSE and the highest R^2, close to one. By looking closely, this model comprises the nozzle diameter $D_{0,}$ which is included in the calculation of the spreading ratio, explaining the high performance of all the models. Removing this parameter reduces R^2 while maintaining a satisfactory performance with 94% of the variability of the spreading ratio explained. The models based only on three features present the lowest performance, explaining 91% of the variability of the spreading ratio.

Overall, these results show that the ensemble methods, which are based on several trees, outperform the single tree method but present more complexity in the interpretation. All models also present an accepted level of generalization performance on unseen (test) data, as revealed by the low RMSE, low Err. %, and high R^2 obtained for all the regression models.

The model presenting the best overall performance is the Extra Trees Regressor with four features (P, V, G_0^*, and n). The prediction error plot for this model is presented in Figure 3.6. All the prediction error results developed through this study are presented in Appendices C-E. The comparison of the results between the experimental and predicted values, based on the training and testing sets shows the high performance of the model fit (with high R^2 value). The feature importance is also highlighted in Table 3.4. These results reveal that n is the most important feature in this model, followed by G_0^*, V and P. In this model, the rheological parameters govern over 92% of the filament spreading prediction, confirming the critical effect of these properties to control the spreading of the printed filament detailed in a previous section. In addition, the averaged squared relative error over the complete dataset is 1.54% for the training and 3.58% for the testing, demonstrating its accuracy. A closer inspection of the results, detailed in Appendices F and G, reveals that the largest errors occur when the ink exhibits the largest G_0^* and the lowest n.

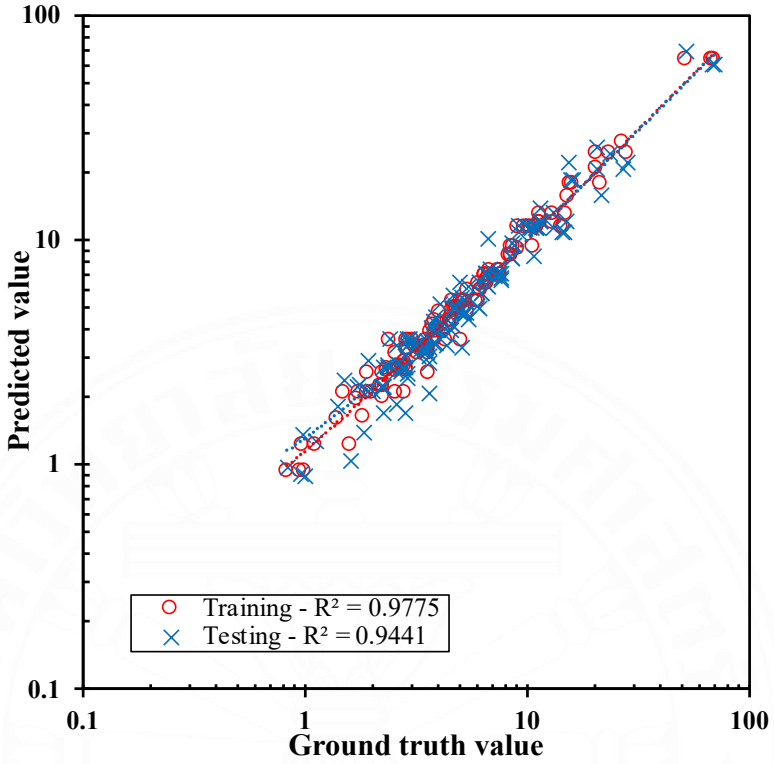

Figure 3.6 Prediction error for extra trees models, with 4 features.

Table 3.4 Calculation of the relative feature importance based on the Extra Trees Regressor with 4 features.

Printing parameters		**Rheological parameters**	
P	**V**	**n**	$\mathbf{G_0^*}$
0.036	0.039	0.217	0.708

An additional unseen batch of ink was formulated to ensure the validity of the Extra Trees Regressor with four features. This ink, 23PT12G2, was composed of 12 wt% pectin and 2 wt% gelatin. The prediction error plot is reported in Figure 3.7, and the results are presented in Table 3.4. The model maintained excellent performance, with a high R^2 (0.9771), and a low RMSE of 0.76. This indicates the model's ability to accurately capture the relationships within the data and highlights the capacity of the

model to perform well within its parametric window. These findings validate and confirm the effectiveness of the model.

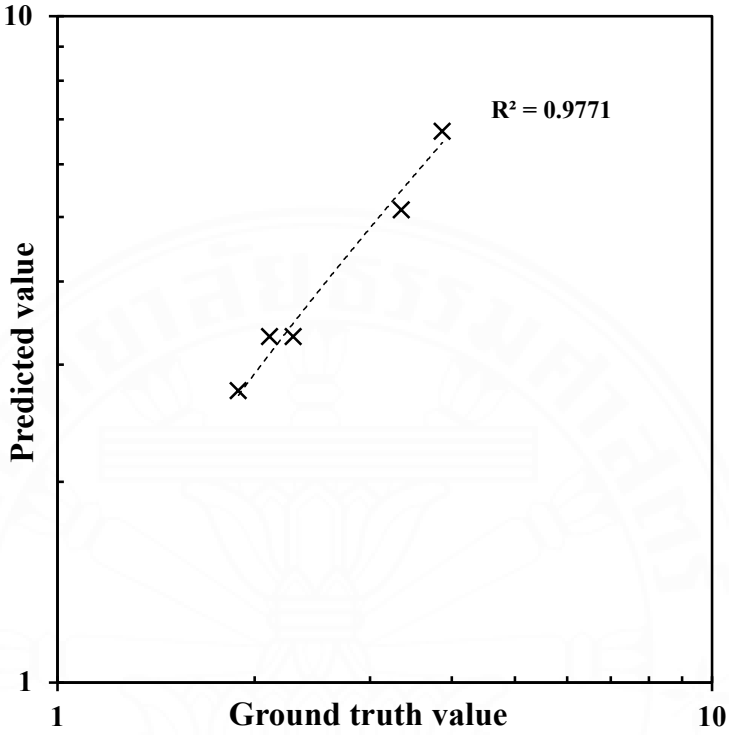

Figure 3.7 Prediction error for extra trees models, with 4 features using unseen data (23PT12G2).

Table 3.5 Testing results based on the ET model with 4 features on unseen data using an ink composed of 12 wt% pectin and 2 wt% gelatin.

Pressure (Pa)	Speed ($mm.s^{-1}$)	G_0^*	n	S exp	S testing
0.5	20	381.36	0.43	2.11	3.30
0.5	20	381.36	0.43	2.29	3.30
0.5	30	381.36	0.43	1.89	2.74
1	20	381.36	0.43	3.87	6.72
1	30	381.36	0.43	3.35	5.13

This section demonstrates the power of machine learning, specifically tree-based models, to predict the complex outcome of filament spreading with 94% accuracy. This study aligns with a recent work where machine learning algorithms have been used to assess dimensional parameters in the field of 3D printing of soft materials (X. Shi et al., 2023). However, we provide a more comprehensive approach by incorporating both ink's rheological properties and printing parameters for greater predictive power.

Based on the results shown in this study, it can be stated that the printing parameters, especially the printing speed, are important in evaluating the spreading of the printed filament, but the rheological properties of the ink wield a greater influence on the precision of the dimension of printed filament. Among the five regression models tested, the best model for the prediction of filament spreading ratio is based on the Extra Trees Regressor developed with four features. This model explains 96% of the spreading ratio's variability and shows excellent predictability performance on unknown data. Specifically, it is important to point out that the rheological parameters alone account for over 92% of the spreading ratio prediction, highlighting their dominant influence compared to other printing parameters.

3.4 Conclusion

This study elucidates the complex interplay of factors influencing material spreading in extrusion-based 3D printing, using pectin as a biopolymer model ink. Machine learning techniques were crucial in providing valuable insights and predictive capabilities. The sole examination of rheological parameters, such as viscosity and complex modulus, revealed a noticeable effect on the spreading ratio. Higher rheological values, while yielding printed lines with desirable reduced spreading, present challenges during the printing process. Their increased viscoelastic properties can hinder extrudability, necessitating precise pressure calibration to ensure smooth material flow. Furthermore, the study revealed that increasing the applied pressure causes an increase in flow rate, leading to a greater spreading ratio. The higher printing speed reduces the spreading ratio due to the thinning of the extruded filament. However, it is crucial to note that excessively high printing speeds generate risks of filament instability, potentially causing breakage and compromising the continuity of printed

lines. These findings emphasize the importance of balancing process parameters and ink properties to achieve precise dimensional control through the modulation of the spreading ratio. Extending beyond traditional approaches, the integration of machine learning techniques enriches our understanding and improves the predictive capabilities in 3D food printing. The results obtained from a variety of tree-based models unequivocally confirm the dominant influence of rheological properties on the spreading behavior of printed filaments. The best model, based on the Extra Trees Regressor with four features, attributed 92% of the importance to these properties, whereas the printing parameters accounted for the remaining 8%. The synergy between experimental insights and predictive modeling establishes a robust framework for achieving precise control over ink deposition, ensuring the desired dimensions and properties in the final printed products. This multidimensional perspective contributes to the advancement of 3D food printing processes and paves the way for further exploration and innovation in the fabrication of future food products.

The inks studied in this section were revealed to be unsuitable to form 3D printed shapes due to their poor viscoelastic properties yielding to no shape holding properties (Outrequin et al., 2023). Furthermore, the inks formulated as presented in this section do not present nutritional benefits. Thus, in the following chapter, mung bean protein isolates were added to the pectin matrix to form food inks with enhanced rheological properties and upgraded nutritional profiles.

CHAPTER 4
3D PRINTING OF PROTEIN-RICH PLANT-BASED SNACKS: VISCOELASTICITY AND NON-LINEAR RHEOLOGY MACHINE LEARNING BASED QUALITY CONTROL AND POST-PROCESSING

4.1 Introduction

The recent progress in 3D food printing technology enables the development of novel foods and diets. This technology presents a solid potential to advance personalized nutrition, sustainability, and innovative food design. Examples of printed food, including vegetable snacks (Ahmadzadeh et al., 2024), fish analogs (H. Shi et al., 2023), beef products (Dick et al., 2021), and soft cheese (Bareen et al., 2021), are commonly reported. This technology facilitates the development of foods enriched with active compounds and vitamins tailored to meet the specific nutritional needs of different groups of consumers, such as dysphagic patients or elderly (Zhenbin Liu et al., 2023; Qiu et al., 2024). The interest in plant-based nutrition and alternative proteins has accelerated in recent years, motivated by consumer demand for sustainable, health-conscious, and ethically sourced foods. 3D food printing meets this demand by enabling the creation of novel formulations that incorporate plant-based proteins, providing customized solutions to these modern dietary needs (Chen et al., 2021; Hu et al., 2023).

As detailed in the previous chapter, pectin, a biopolymer commonly used in the food industry, plays a vital role in modifying the rheological properties of food formulation (Agarwal et al., 2021; Chan et al., 2017). It has been shown that pectin alone was not printable due to weak viscoelastic properties. Additional ingredients such as protein can be added to the formulation to improve the rheological and nutritional properties. Mung bean protein is a plant-based protein extracted from mung beans (*Vigna radiata* L.), a leguminous plant commonly cultivated in Asia. Mung bean protein is gaining popularity in the food industry due to its functional properties, such as solubility, water-holding capacity, gelling, foaming, and emulsification (Du et al., 2018; Huang et al., 2024). These properties make it an excellent ingredient in various food applications, including plant-based meat alternatives, protein-rich snacks, and

dairy substitutes (Ashraf et al., 2024; Seetapan et al., 2023). Its rising use in food applications aligns with the growing demand for sustainable, plant-based proteins.

The success of the 3D food printing process mainly depends on the rheological properties of the food ink. Indeed, it governs how the material flows and layers during the printing process. Fundamental properties include parameters such as the ink's viscosity, viscoelasticity, and yield stress, which all govern printability (Outrequin et al., 2023). Optimizing these parameters is essential to achieving high printability and maintaining the object's structural integrity over time. Thus, we can explore their combined effect on the printed objects' dimensional properties by varying pectin and mung bean concentrations. Several parameters are defined in the literature to evaluate the dimensional properties of printed food ink formulation, such as the accuracy (Cheng et al., 2024) and structural stability over time (In et al., 2021; Riantiningtyas et al., 2021).

In the previous chapter, we analyzed the effect of printing and rheological parameters on the dimensions of the deposited filament. A machine learning model was developed, and the impact of the viscoelasticity was shown to be of the utmost importance. In this chapter, we focus on the formation of the 3D object. Similarly, we aim to develop a machine-learning model as a quality control tool to highlight the suitable printed pectin–mung bean protein isolate formulations based on their rheological properties and the number of layers. Quality control in food processing is essential for ensuring the safety and quality of the products provided to consumers. Image analysis and computer vision are often used to analyze the quality of the food product. Ma et al. demonstrated the use of computer vision to assess the fibrousness of meat analog. There are strong correlations between automated results and trained sensory panels (Ma, Schlangen, et al., 2023). This underlines AI tools' effectiveness and potential in food manufacturing, especially in areas like 3D food printing and the development of innovative plant-based products.

This study investigates how rheological properties influence the accuracy and long-term shape stability of protein-rich 3D printed snacks. The rheological properties include the frequently studied viscoelasticity and the non-linear behavior. Indeed, as the 3D food printing process involves rapid and significant deformation, a focus on large amplitude oscillatory shear is made to reveal the important non-linear behavior

affecting the 3D food printing process, and the thickening ratio is added into the model to represent this sudden large deformation. Machine learning classification models are employed as a quality control tool to assess printability, utilizing these rheological parameters and the total number of printed layers. Additionally, we examine the impact of baking on the visual characteristics of the printed food items, providing insights into the post-processing requirements for protein-rich 3D printed snacks. Our findings aim to support the development of dimensionally stable, high-protein 3D printed food products.

4.2 Materials and methods

4.2.1 Materials

Low methoxyl pectin (LM 104 AS-BG), batch 23PT, was provided by Winner Group Enterprise PLC (Thailand). Mung bean protein isolate (total protein content = 77.08%) was supplied by ET CHEM (China). Deionized water was used for all the experiments.

4.2.2 Ink preparation

The food printing inks were formulated by dissolving pectin in DI water in a water bath at 60°C for one hour and left overnight at room temperature. The total pectin concentrations ranged between 2-4 wt%. Mung bean protein isolate, at a concentration ranging from 15 to 22.5 wt%, was dispersed into the pectin solution using a Philips ProMix for 60 seconds to form the food inks. Ink formulations were designated with the nomenclature MBXPTY, where X represents the mung bean protein concentration in wt%, and Y indicates the pectin concentration in wt%. After preparation, inks were directly used for rheological analysis and transferred to syringes for 3D printing experiments.

4.2.3 Rheological analysis

Rheological experiments were performed using a strain-controlled rheometer (ARES G2, TA Instruments) equipped with a 25 mm diameter cross-hatched parallel plate geometry and a gap size of 1 mm. The environmental temperature was fixed at 25 °C, and a thin layer of silicon oil was applied to avoid sample drying during the analysis.

After loading, samples were pre-sheared at a constant shear rate of 0.1 s^{-1} for 60 s and allowed to rest for 120 s to reach thermal equilibrium. Three replicates were performed for each experiment, and the average results are presented along with their standard deviation.

4.2.3.1 Small Amplitude Oscillatory Shear (SAOS)

An amplitude strain sweep was conducted from 0.01 to 100 % at 25 °C. The yield point was determined by this test. The linear viscoelastic region (LVER) was obtained at the strain where the storage modulus (G') deviated from its plateau value by 5%. The yield point and the strain within the LVER are used for further rheological analysis.

A frequency sweep from angular frequency (ω) of 0.0628 to 628 rad.s^{-1} was carried out at constant strain within the LVER and at 25 °C. The evolution of the viscoelastic parameters, i.e., storage modulus (G'), loss modulus (G''), loss tangent (tanδ) and complex modulus (G^*) as a function of the frequency were evaluated. Furthermore, a power law model was employed to describe the relationship between the complex modulus and the angular frequency: $G^* = G_0^* \omega^n$, where G_0^* is the complex shear modulus at an angular frequency of 1 rad.s^{-1}, and n is the power-law exponent, determining the frequency dependence of the complex modulus.

4.2.3.2 Large Amplitude Oscillatory Shear (LAOS)

Large amplitude oscillatory shear (LAOS) experiments were performed to analyze the mechanical properties of the various printing inks upon a large range of applied strain. This approach aimed to capture both the linear viscoelastic behavior and the pronounced non-linear responses of the inks. The LAOS analysis employed a strain amplitude sweep test. A strain, $\gamma(t) = \gamma_0 \sin \omega t$, ranging from 0.1% to 100%, was applied to the samples at a constant frequency of 1 rad.s^{-1} or 10 rad.s^{-1} and a temperature of 25 °C. Data at 1, 10, 50, and 100% strain were extracted and analyzed using the VAOS software (Madsen et al., 2022). The stress (σ)-strain data was converted using Fourier transformation, and the highest significant harmonic was selected for further analysis. The resulting data was presented in a Pipkin diagram to compare the different formulations quickly. In addition, the evolution of G_L' the large-strain modulus, G_M' the

minimum-strain modulus, η_L' the instantaneous viscosity at the largest shear rate, and η_M' the instantaneous viscosity as the lowest shear rate, defined in Equations (4.1) – (4.4), were analyzed as a function of the applied strain. Non-linear rheological behaviors are observed when the values of G'_L and G'_M or η'_L and η'_M begin to diverge.

$$G'_L = \left.\frac{\sigma}{\gamma}\right|_{\gamma=\gamma_0} \tag{4.1}$$

$$G'_M = \left.\frac{d\sigma}{d\gamma}\right|_{\gamma=0} \tag{4.2}$$

$$\eta'_L = \left.\frac{\sigma}{\dot{\gamma}}\right|_{\dot{\gamma}=\dot{\gamma}_0} \tag{4.3}$$

$$\eta'_M = \left.\frac{d\sigma}{d\dot{\gamma}}\right|_{\dot{\gamma}=0} \tag{4.4}$$

Lastly, the non-linear behavior was further analyzed and quantified using the strain-stiffening (S) and the shear-thickening (T) ratios calculated by Equation (4.5) and Equation (4.6), as defined by Ewoldt et al. (2008) (Ewoldt et al., 2008). The analysis of these parameters reveals the intra-cycle elastic and viscous non-linearities. Determining the S and T ratios provides quantitative insights into the intra-cycle strain and shear thickening/thinning behavior at the different stages of the food printing process. Indeed, values different from zero represent non-linear viscoelastic behavior. A strain-stiffening behavior is obtained when $S > 0$, while a strain-softening behavior is obtained when $S < 0$. Similarly, $T > 0$ indicates a shear-thickening behavior, and $T < 0$ is a shear-thinning behavior. Since the traditional flow shear-thinning information could not be obtained from flow analysis due to the ink's solid-like behavior, the parameter T was

utilized for further analysis to indicate the ink's thinning behavior during the printing process.

$$S \equiv \frac{G'_L - G'_M}{G'_L} \tag{4.5}$$

$$T \equiv \frac{\eta'_L - \eta'_M}{\eta'_L} \tag{4.6}$$

4.2.4 3D food printing experiments

As presented in the previous chapter, 3D printing experiments were performed using a modified BIQU®B1 (BigTreeTech, Shenzhen, China) extrusion-based 3D printer. Printing experiments were carried out according to the parameters given in Table 4.1. G-codes were prepared using the software Ultimaker Cura and manually modified according to the needs. The complete g-code for this study is presented in Appendix H. This code yields the formation of a 20 mm cube with 25 layers, with a fixed distance of 2.5 mm between each line in the pattern. In addition, the first and the last layers were filled with material. The g-code was edited to generate continuous nozzle movements and to avoid movement overlaps. This g-code was also modified such that the printing process is paused temporarily at layers 5,10,15, 20, and 25 to enable image capture.

Table 4.1 Printing parameters used in the Chapter 4.

Parameter	Symbol	Value
Nozzle diameter	D_0	1 mm
Extrusion pressure	P	0.5 – 4.0 bar
Ink reservoir temperature	T	25 °C
Nozzle temperature	T_1	25 °C
Printing bed temperature	T_2	25 °C
Nozzle movement speed	V	25 $mm.s^{-1}$
Distance nozzle – printing bed	H	0.8 mm

4.2.5 Printed objects analysis

With the 3D printing experiments completed, the next critical step was to analyze the printed objects to assess their dimensional accuracy and stability over time. This analysis is essential for understanding how well the printed structures retain their intended shape and size. To do so, the image analysis was performed using a custom-made image capture setup. This setup comprised two Raspberry Camera module 3 (12 MP) connected to a Raspberry Pi 5. This setup captured the printed objects' top and side views. A Python code was developed to control the cameras and simultaneously capture images from both cameras, Appendix I. Images were captured after printing 5, 10, 15, 20, and 25 layers. Nine replicates were carried out for each ink formulation, and the dimensions were measured using ImageJ software (Schneider et al., 2012). Among these nine printed objects, three were used for analyzing the evolution of the printed dimensions over time, and the other six were further post-processed using baking method.

The dimensions of the printed cubes were fixed at 20 mm for each experiment. Three measurements were taken for each printing trial at each edge and in the middle of the cube. The parameters studied were the height accuracy A_H defined in Equation (4.7) (Cheng et al., 2024). Larger A_H values imply a more significant difference between the printed and model dimensions.

$$A_H = \frac{H - H'}{H'} \tag{4.7}$$

In this equation, H is the height (mm) the printed object achieves, and H' is the targeted height (mm).

Furthermore, the stability of the printed object over time was studied by evaluating and recording the dimension changes of the printed objects at different times: immediately after printing (t_0), after four hours (t_4), and after one day (t_{24}). The printed objects' dimensional stability (%) was calculated in detail in a previous chapter, Equation (4.8). In this equation, H_0 is the height (mm) of the printed objects immediately after printing, and H_t is the height (mm) measured after a fixed time.

$$Stability = \frac{H_t}{H_0} \times 100 \tag{4.8}$$

4.2.6 Machine learning classification

As in the previous chapter, the machine learning analysis was conducted using Python, combined with the scikit-learn and XGBoost libraries (Chen & Guestrin, 2016; Pedregosa et al., 2011). Here, the objective of the analysis was to classify the inks' printability by measuring their dimensional deviation from the model, defined as the ratio of the printed height to the model's height. A class was then attributed to each printed result, 0 for inks 'out of range' and 1 for inks 'within range'. The threshold value was fixed at a 10% deviation. The studied features comprised the number of layers and rheological parameters, i.e., tanδ, G_0^*, and T. A standardization step was added to the algorithm to ensure correct feature scaling for optimal performance. This step included centering each feature by subtracting its mean and then scaling it by the standard deviation. It resulted in a dataset where each feature has a mean of zero and a standard deviation of one. Eight machine learning models were selected for the analysis. The models studied are Logistic Regression (LR), Support Vector Machine (SVM), K-Nearest Neighbors (kNN), Decision Tree (DT), Extra Tree (ET), Random Forest (RF), Gradient Boosting (GB), and Extreme Gradient Boosting (XGB). The performance of each model was evaluated across different numbers of features through

recursive feature elimination. Stratified k-fold cross-validation was applied to split the dataset into ten equal parts and to ensure that each fold present the same proportion of each class (Santos et al., 2018). Lastly, the model's performance was evaluated using four key metrics used in machine learning classification problems: accuracy, precision, recall, and F1 score, as defined in Equations (4.9) – (4.12). Accuracy represents the ratio of correctly predicted classes to the total number of classes. It provides an overall measure of model correctness. Precision reflects the proportion of correctly predicted positive classes out of all predicted positives. It indicates how many of the predicted positive classes are actually positive. Recall, or sensitivity, measures the proportion of actual positives correctly identified by the model. Finally, the F1 score performs as the mean of precision and recall. This metric is beneficial in balancing the two last metrics, especially in imbalanced datasets, where it provides a more complete measure of the model's effectiveness.

$$Accuracy = \frac{TP + TN}{TP + FP + TN + FN} \tag{4.9}$$

$$Precision = \frac{TP}{TP + FP} \tag{4.10}$$

$$Recall = \frac{TP}{TP + FN} \tag{4.11}$$

$$F1\ score = 2 \times \frac{Precision\ \times Recall}{Precision + Recall} \tag{4.12}$$

In these equations, TP represents true positive, TN true negative, FP false positive, and FN false negative predicted classes.

4.2.7 Baking of 3D printed food samples

The printed objects were post-processed using different baking temperatures. Baking was used to turn the printed objects into edible 3D printed protein-rich snacks. The effect of the baking temperature on the evolution of the shape and weight of the

printed objects was investigated. The baking was performed using a convection oven at 150 or 180 °C for 20 minutes. Baked printed cubes were allowed to cool to room temperature before being photographed using the previous dual camera system. The weight was recorded before and after baking to determine the water loss. Moreover, the theoretical protein content of the protein snack was determined on baked samples based on Equation (4.13).

$$P_{th} = \frac{(m_{print} \times C_{MB}) \times TPC}{m_{baked}} \quad (4.13)$$

In this equation, P_{th} is the percentage of protein in the final printed object after baking (%), m_{print} is the mass of the object before baking (g), C_{MB} is the mung bean protein isolate content (from 15 to 22.5 wt%), TPC = 77.07% is the total protein content in the mung bean protein isolate and m_{baked} is the mass of the object after baking (g).

4.3 Results and discussion

4.3.1 SAOS Rheological analysis

Amplitude strain sweep results are displayed in Figure 4.1. This analysis was performed to the limit of the viscoelastic region (LVER) for further analysis. The results show that the printing inks present a solid-like behavior over all the strain ranges studied. Moreover, the magnitude of this behavior increases with the total biopolymer content as the value of G' and G" gradually rose from 1400 and 380 Pa for MB15PT2, the ink having the lowest biopolymer content, to more than 20000 and 5000 Pa for MB22.5PT4. This increasing solid-like behavior pinpoints the need to use higher extrusion pressure as the biopolymer content increases.

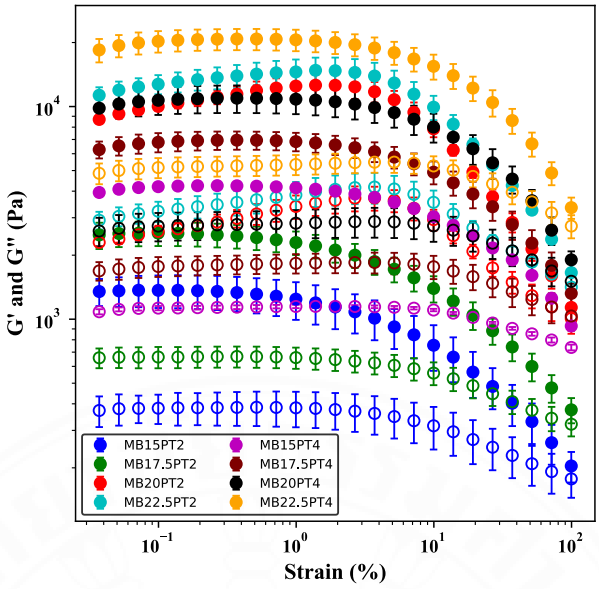

Figure 4.1 Amplitude strain sweep results of the various MBPT ink formulations. Filled symbols represent G', and unfilled symbols represent G".

The results of the frequency sweep are presented in Figure 4.2. All the inks studied presented a solid-like behavior, demonstrated by G' being higher than G" across all the frequency ranges, as depicted in Figure 4.2(a). These inks also exhibit a frequency-dependent behavior, with both modulus values progressively increasing in response to variations in the testing frequency. Analyzing the values of tanδ and G', extracted at 1 rad.s^{-1}, Table 4.1, it can be believed that all these ink formulations are self-supporting. Indeed, the values are comprised within the range demonstrated in a previous chapter, i.e., G' > 300 Pa and tanδ < 0.268. Figure 4.2(b) illustrates the variation of G*, the complex modulus, with the angular frequency. This rheological parameter is used to evaluate the material's resistance to deformation. As expected, G* gradually increased with the concentration of mung bean protein and pectin, suggesting a stronger elastic response due to stronger entanglement of the polymeric network. A power law model was applied to fit this rheological parameter, with results summarized in Table 4.2. The value of G_0^* transitioned from 1250 to 8630 Pa when the mung bean protein concentration rose from 15 to 22.5 wt%, at 2 wt% pectin, while this value evolved from 3946 to 22463 Pa for the same concentrations with 4 wt% pectin. As explained previously, all inks are frequency dependent. Nevertheless, these findings

indicate consistent frequency-dependent behavior across all ink formulations, as the exponent n obtained from the fitting remained constant.

(a)

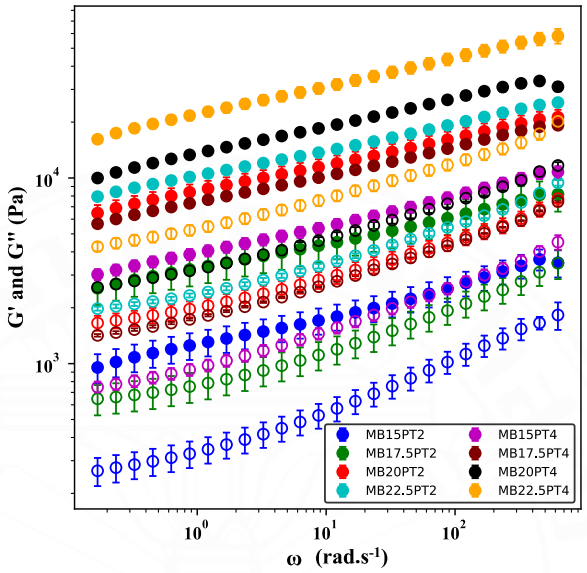

(b)

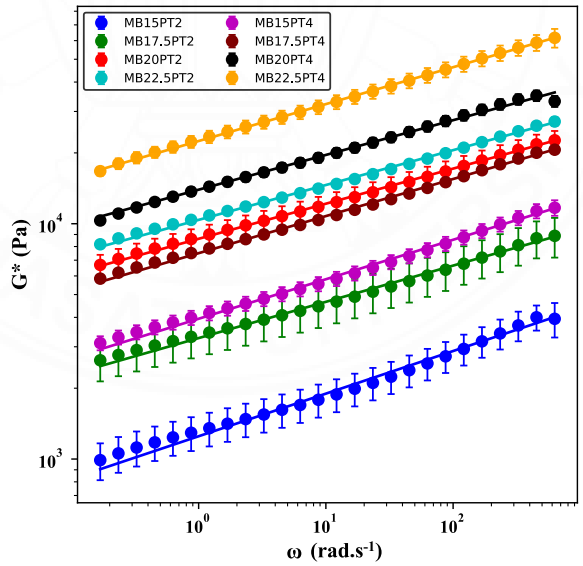

Figure 4.2 Frequency sweep results. (a) Evolution of G' and G" as a function of the angular frequency at 25 °C. Filled symbols represent G', and unfilled symbols represent G". (b) Evolution of G^* as a function of the angular frequency at 25 °C. The power law fitting is represented by the solid lines and the parameters given in Table 4.1.

Table 4.2 Rheological parameters extracted from the linear viscoelasticity testing. Note that G_0^* and n are determined from power law fitting on the averaged results.

Formulation	G_0^* (Pa)	n	tanδ (1 rad.s^{-1})
MB15PT2	1250	0.18	0.263 ± 0.003
MB17.5PT2	3266	0.15	0.234 ± 0.002
MB20PT2	8630	0.15	0.235 ± 0.001
MB22.5PT2	10385	0.15	0.230 ± 0.001
MB15PT4	3946	0.17	0.240 ± 0.001
MB17.5PT4	7496	0.16	0.238 ± 0.001
MB20PT4	13954	0.15	0.237 ± 0.001
MB22.5PT4	22463	0.16	0.241± 0.002

This section presents the general rheological analysis of the food inks studied. The mung bean protein and pectin content impact the rheological properties, with higher concentrations of biopolymers leading to stronger solid-like behavior. All the inks presented here are suitable for 3D food printing applications. This analysis remains general in 3D food printing and only focuses on linear behavior. Additional tests, such as flow sweep or thixotropic analysis, could have been performed but were not included in this study. In the next section, we propose to study large amplitude oscillatory strain, focusing on non-linear behavior, which is common for food applications but still infrequently used in 3D food printing. This behavior is crucial for 3D food printing as it reveals how ink responds to large and sudden deformation, which can affect its printability.

4.3.2 LAOS rheological analysis

During the 3D printing process, the ink is subjected to rapid and significant deformation. Thus, linear behavior does not apply. Large amplitude oscillatory shear analyses were performed to gain insights into the non-linear behavior of the food inks at large deformation. Moreover, LAOS testing allows for studying a broad spectrum of conditions as both strain amplitude and frequency can be varied (Hyun et al., 2011). This technique is getting increasing interest in the field of food science (Dahl et al., 2024; Wang & Selomulya, 2022) and 3D food printing applications (Cheng et al., 2024;

Zipeng Liu et al., 2023). In these experiments, the strain-stress relationship follows a non-linear stress waveform that the Fourier series, Equation 4.14, can represent. The stress response corresponds to an infinite sum of sine and cosine functions with increasing harmonics. The material response to strain depends only on the first harmonics up to the limit of the linear viscoelastic region (LVER). After the LVER, the stress signal becomes distorted; therefore, higher harmonics appear significant. It is paramount to select the highest number of significant harmonics to gather maximal information. Moreover, the literature has shown that only odd harmonics are significant in representing the fluid's rheological response with respect to the shear strain directionality (Ewoldt et al., 2008; Kamkar et al., 2022). Even harmonics might be obtained from effects such as fluid inertia, wall slip, and secondary flow but are considered less pertinent (Yazar et al., 2019).

$$\sigma = \gamma_0 \sum_{n=1,\ odd}^{N} [G'_n(\omega, \gamma_0) \sin n\omega t + G''_n(\omega, \gamma_0) \cos n\omega t \,] \tag{4.14}$$

In this equation, σ is the shear stress, γ_0 is the amplitude of the deformation, i.e., the strain, n is the number of harmonics, ω is the angular frequency, t is the time, G'_n and G''_n are the loss and storage Fourier moduli at the nth harmonic.

Using the VAOS software, harmonics are studied, and heat maps are produced. Two heat maps are presented in Figure 4.3 for two inks, MB15PT2 and MB22.5PT4, at a frequency of 1 rad.s^{-1}. All the heat maps for each ink formulation and frequency are presented in Appendix J. Here, we retain only the positive normalized harmonics. From these results, it can be observed that a larger number of harmonics is significant for ink with the lowest biopolymer content. Thus, five harmonics were selected for this study to perform the Fourier transformation.

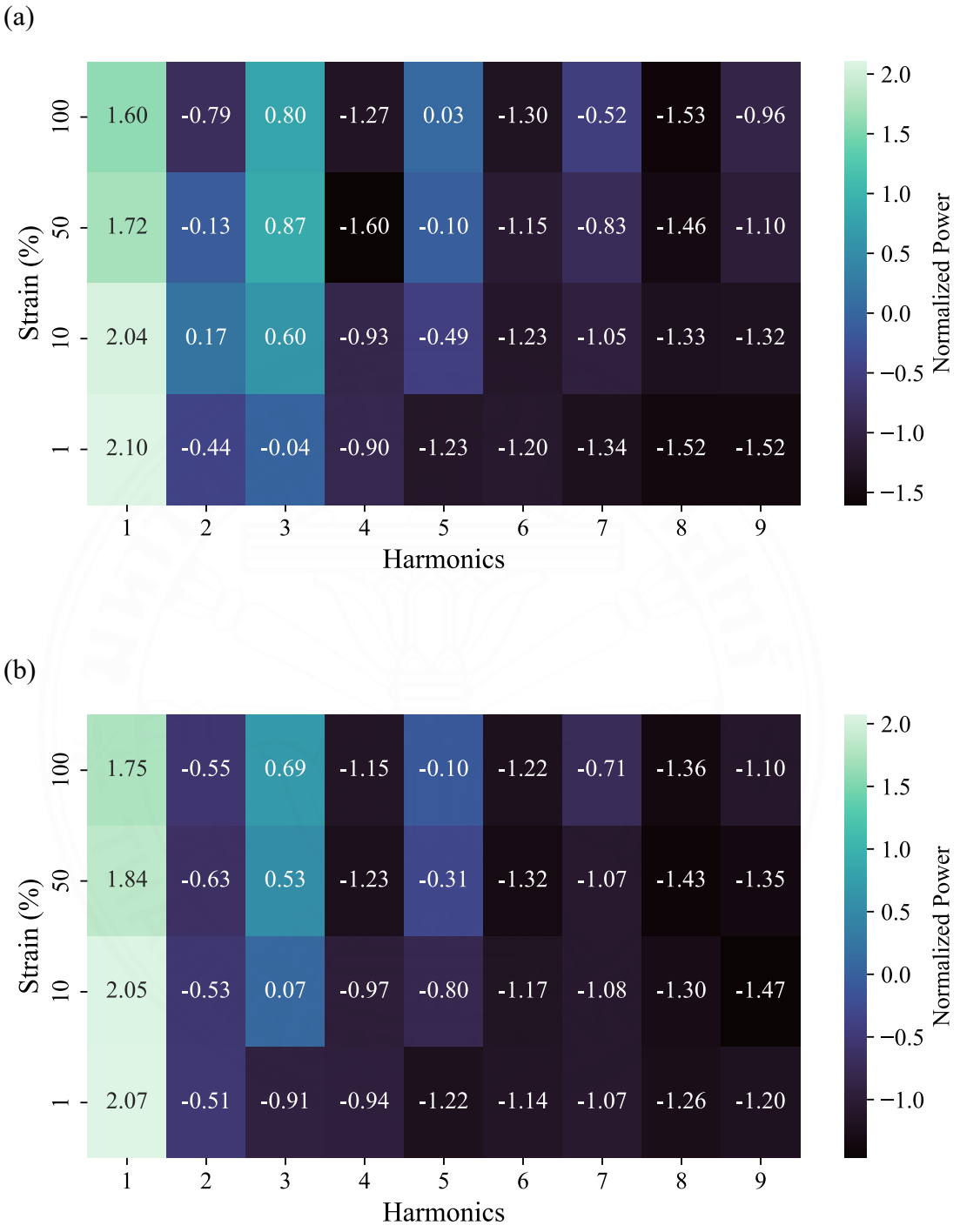

Figure 4.3 Harmonics heat map analysis (a) for MB15PT2 at 1 rad.s^{-1}. (b) for MB22.5PT4 at 1 rad.s^{-1}.

In LAOS rheology, Lissajous diagrams represent the relationship between the shear stress σ and the strain during an oscillatory shear test. The specific shape of the obtained curve reveals the balance between viscous and elastic behavior. An elliptical

look reveals a dominant elastic response, while a more open and distorted loop signifies a more viscous material (Ewoldt et al., 2010). Pipkin diagrams, built upon a collection of Lissajous curves plotted at various frequencies, strains, or concentrations, form a fingerprint of a material viscoelastic response (Ewoldt et al., 2008). Elastic Pipkin diagrams were plotted at different frequencies according to the strain amplitude and food ink formulation, Figure 4.4.

At 1 rad.s^{-1}, the Elastic Lissajous plots present an elliptical aspect for linear response, Figure 4.4(a). As the shear strain amplitude increases above 10% for a given formulation, the plots start to deform and become non-elliptical, thus pinpointing the non-linear response at higher strain. The area under the curve also becomes larger, indicating highly deformable materials and reduced elastic behavior, especially for MB15PT2, which presents the strongest strain sensitivity due to the lower biopolymer content. The area's evolution implies that viscous forces increase in the non-linear regime, strengthening the fluid-like properties of the formulation. The effect of pectin and mung bean concentration on the LAOS behavior is also investigated. As demonstrated with these results, for a fixed concentration of pectin, the loops present reduced area when the mung bean content increased. The loop area decreased when the pectin concentration increased at fixed mung bean protein isolate content. Similar observations can be made at 10 rad.s^{-1}, Figure 4.4(b). Moreover, comparing both frequencies shows that the areas at 10 rad.s^{-1} are larger than at 1 rad.s^{-1} validating the frequency dependence of the viscoelastic discussed previously. As demonstrated by these results, the formulation biopolymer content impacts the linearity, and a lower biopolymer content affects the LAOS behavior of the ink, the viscoelastic behavior, and the strain-sensitivity due to reduced entanglement.

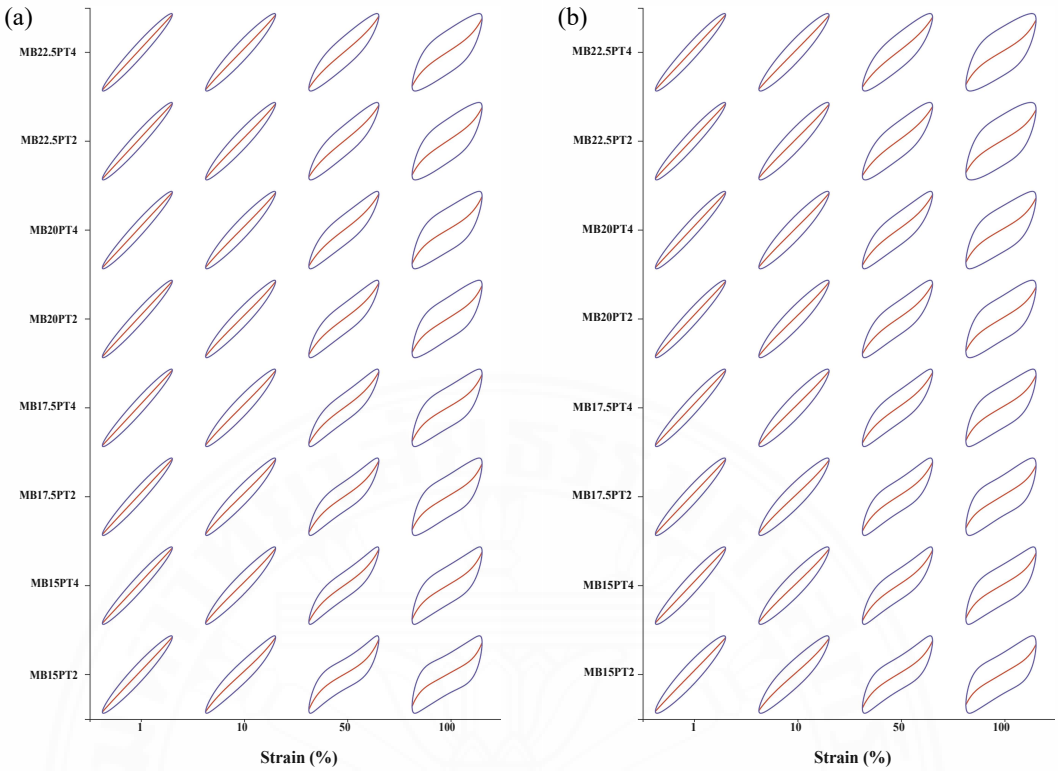

Figure 4.4 Elastic Pipkin diagram (a) at 1 rad.s^{-1}. (b) at 10 rad.s^{-1}.

Appendix K presents the viscous Pipkin diagram. As the strain increases, the area of the ellipse becomes narrower, indicating a more liquid-like behavior. Due to the lower biopolymer content, this behavior is stronger for the ink containing 15 wt% mung bean protein isolate and 2 wt% pectin. The effect of the frequency is further presented in Appendices L and M, where Pipkin diagrams (elastic and viscous) across formulations are plotted for varying frequencies. Overall, at an increased frequency, the loops are larger for elastic projection and narrower for viscous projection. This confirms the effect of increasing frequency, rendering the ink less elastic.

Additional parameters are extracted from the Fourier transformation and are defined to capture the nonlinear viscoelastic behavior of materials under large deformations. These parameters are the large-strain modulus, the minimum-strain modulus, and the instantaneous viscosities, as described previously in Equations (4.1) – (4.4). The large-strain modulus reflects the material's stiffness at the largest applied strain, while the minimum-strain modulus indicates the material's stiffness in the linear viscoelastic regime. The instantaneous viscosity at the largest shear rate represents the

material's flow resistance at the highest deformation rates, and the instantaneous viscosity at the lowest shear rate reflects the material's viscosity under minimal deformation conditions. These parameters, analyzed as functions of the applied strain, provide a comprehensive understanding of the material's viscoelastic properties across different deformation regimes. Within the LVER, $G'_L = G'_M$, and $\eta'_L = \eta'_M$; therefore, any deviations reveal non-linear behavior (Ewoldt et al., 2008).

The evolution of the large strain modulus, minimum strain modulus, and instantaneous viscosity at the largest and lowest shear rate are presented for various frequencies in Figure 4.5. At 1 rad.s^{-1}, Figure 4.5(a), an increase in pectin or mung bean protein content increases the overall magnitude of both moduli. These results also show that increasing the pectin content at a fixed mung bean protein isolate content increases the strain limitation between the linear and non-linear regions. For all concentrations in the non-linear region, $G'_L > G'_M$ describes an intra-cycle strain stiffening, and the reduction of G'_M as the strain amplitude is varied highlights inter-cycle softening (Ewoldt et al., 2008). Similar observations can be made at 10 rad.s^{-1}, Figure 4.5(b), with a reduced magnitude for both moduli. Moreover, the transition between linear and non-linear behavior occurs at higher frequencies at reduced strain amplitude. For example, for MB15PT2, the transition occurs at 3.7% at 1 rad.s^{-1} and 7.2 % at 10 rad.s^{-1}.

Similarly, Figure 4.5(c) shows that the concentration impacts the magnitude of instantaneous viscosity. Higher biopolymer content yields higher values of instantaneous viscosity, indicating higher viscous and/or solid-like behavior. For all formulations, a shear-thinning behavior is observed when $\eta'_M > \eta'_L$ as the strain increases. This shear-thinning behavior is shown to occur at larger strains as total biopolymer content increases. Increasing the frequency, as demonstrated in Figure 4.5(d), decreases the instantaneous viscosity values for all the food ink and highlights a reduced solid-like behavior. Moreover, the shear-thinning appears to occur at reduced strain amplitudes. As the frequency increases, the inks become more strain-sensitive and present reduced solid-like behavior, which can be suitable for 3D food printing applications as the ink flow is eased.

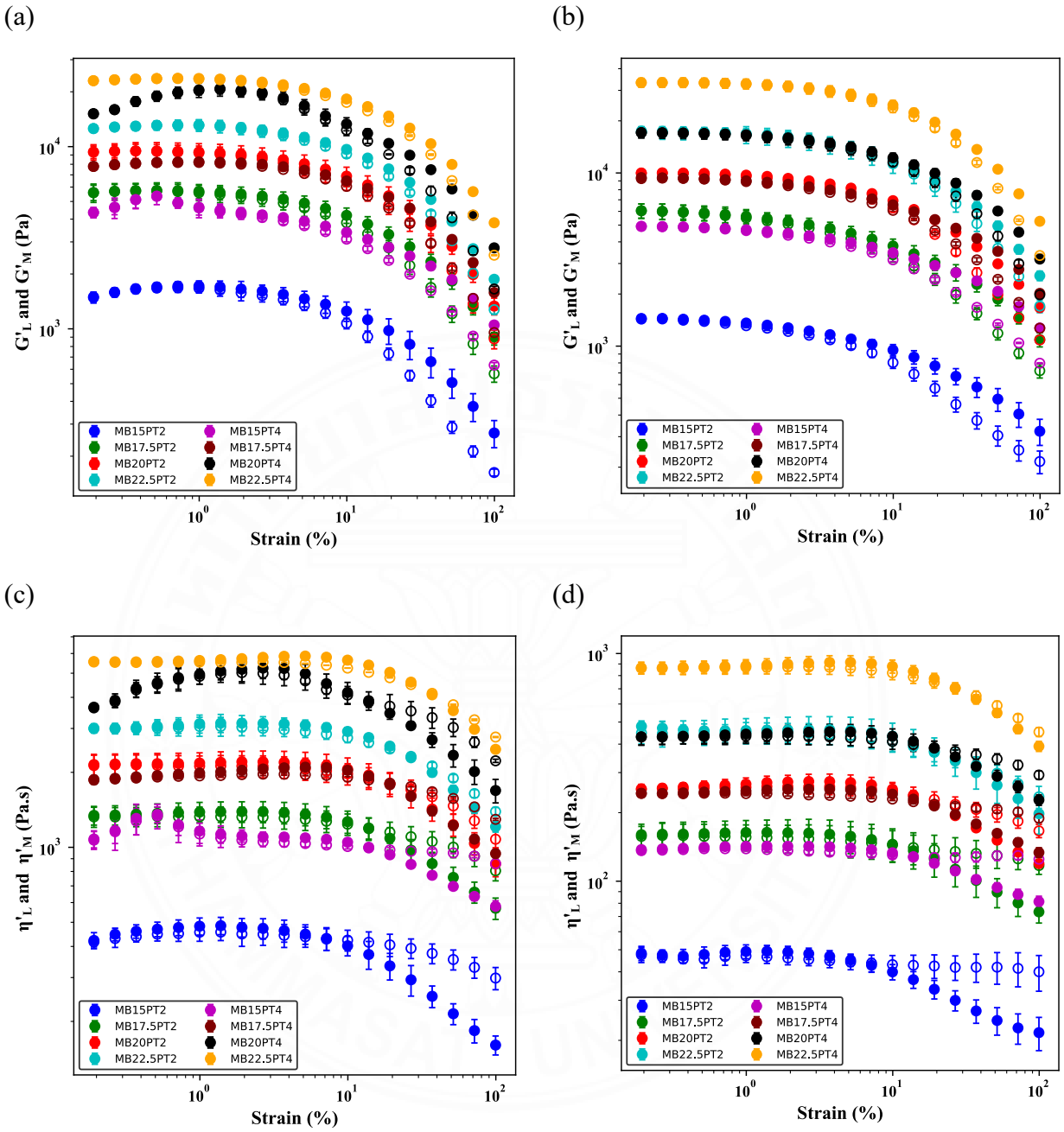

Figure 4.5 Evolution of the large-strain and minimum-strain moduli as a function of the strain at (a) 1 rad.s^{-1}. (b) 10 rad.s^{-1}. Filled symbols represent G'$_L$, and unfilled symbols represent G'$_M$. Evolution of the instantaneous viscosity at the largest and lowest shear rate as a function of the strain at (c) 1 rad.s^{-1}. (d) 10 rad.s^{-1}. Filled symbols represent η'$_L$, and unfilled symbols represent η'$_M$.

The strain-stiffening properties are further analyzed in Figure 4.6 (a)-(d). As the strain increases, Figure 4.6(a) and (b) show that all the formulations display an intra-

cycle strain-stiffening as S > 0. The magnitude of this behavior is found to be stronger at low biopolymer content and increased test frequency. This suggests that reducing the biopolymer concentration enhances the material's tendency to stiffen under strain, possibly due to a more fluid-like matrix that allows for greater polymeric chain alignment.

Shear-thinning behavior is presented for all the formulations as the value of T becomes negative with increasing strain, Figure 4.6(c) and (d). It is interesting to note that the shear-thinning is stronger at lower biopolymer content. Ink at lower biopolymer content will flow easily and require lower extrusion pressure. These results also demonstrate that the testing frequency also impacts T. Overall, higher frequencies promote stronger shear-thinning. In the literature, similar behavior, i.e., strain stiffening combined with shear thinning, has been observed by Yazar et al. (2016) on hard wheat flour dough (Yazar et al., 2016).

(a)

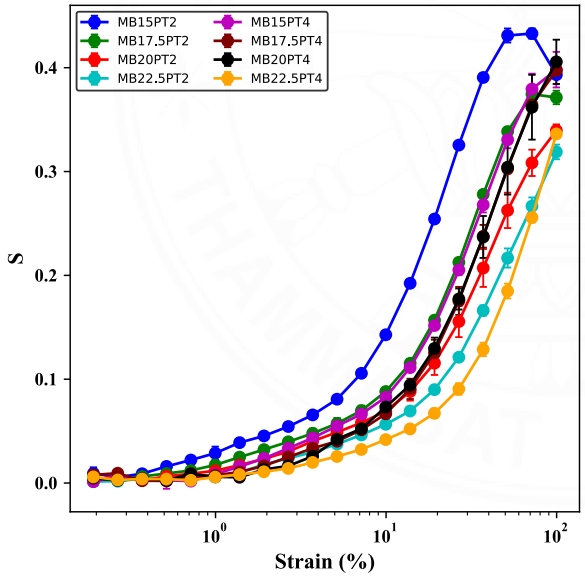

(b)

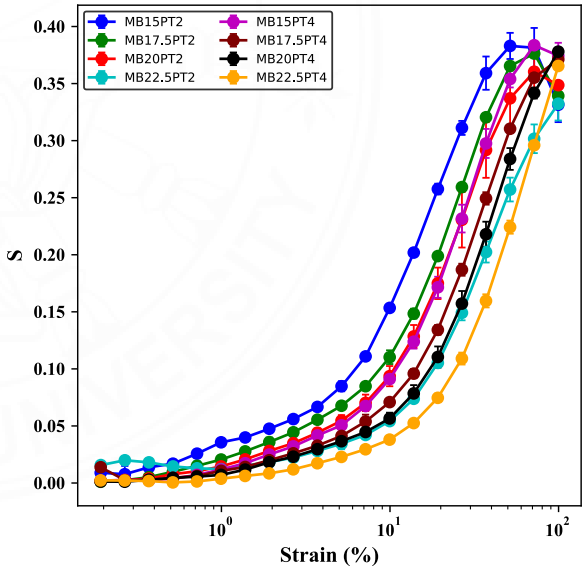

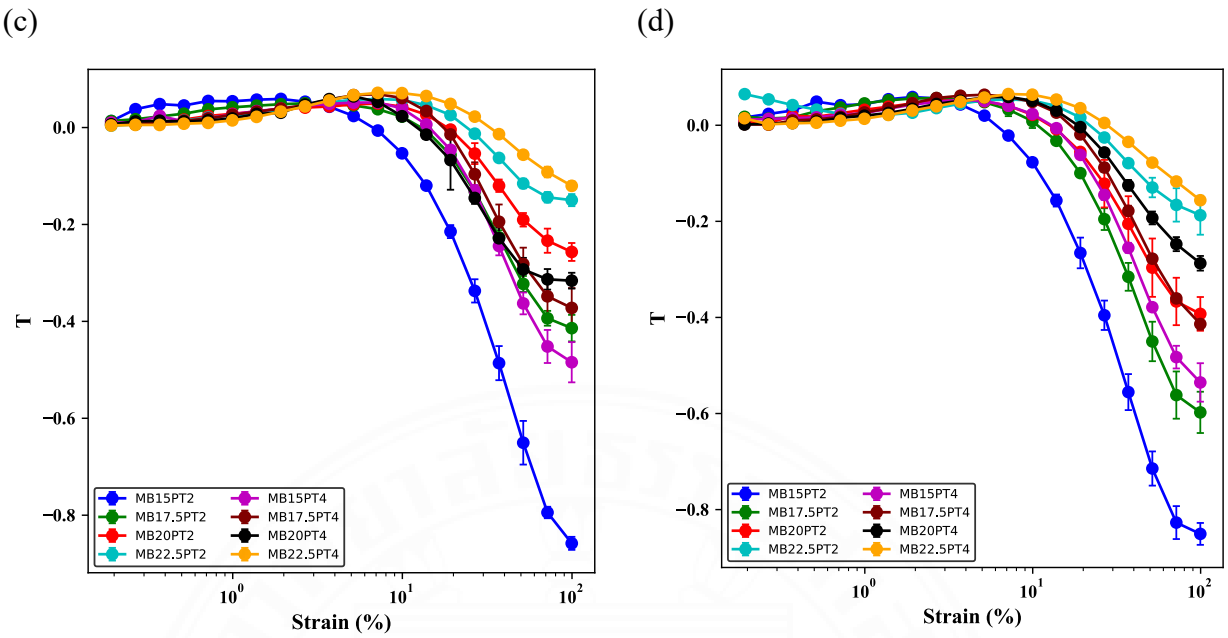

Figure 4.6 Evolution of the strain-stiffening as a function of the strain at (a) 1 rad.s^{-1}. (b) 10 rad.s^{-1}. Evolution of the shear-thickening as a function of the strain at (c) 1 rad.s^{-1}. (d) 10 rad.s^{-1}.

The LAOS analysis displayed the formulation and strain's impact on the food ink's viscoelastic behavior. Overall, increasing the biopolymer content yields inks with a larger linear region and stronger viscoelastic properties. Furthermore, increasing the frequency accelerates the transition from linear to non-linear behavior and the overall viscoelastic properties, as higher frequency results in more rapid deformation and reduced recovery time. As the deformation increases, all formulations exhibit non-linear behavior, such as intra-cycle strain stiffening and shear-thinning, which are crucial for maintaining shape fidelity and enabling efficient material deposition. The value of T at a higher frequency and large strain of 100% was selected to evaluate the shear thinning resented by the ink during the extrusion step (rapid and high deformation) and used for the machine learning model development presented in a following section.

4.3.3 Effect of the rheological properties on the shape fidelity and stability over time

The various mung bean protein isolate–pectin ink formulations were printed as a cube shape to form bite-size 3D printed food. During the printing process, the extrusion of the ink was stopped at different layer levels, and images were captured to observe the formation of the object as presented for MB20PT4, Figure 4.7.

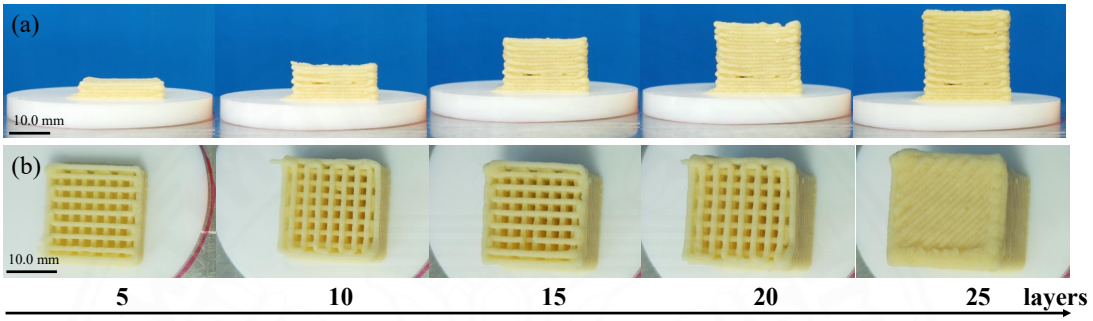

Figure 4.7 Formation of the MB20PT4 printed cube (a) side view. (b) top view.

Eight measurements were performed on each printed formulation to calculate the height accuracy according to Equation (4.7). The evolution of the accuracy is then plotted for each number of layers against the complex modulus at 1 rad.s^{-1} determined with the power law fitting, Figure 4.8. The results show that increasing the G_0^* presents a positive effect on accuracy. Indeed, as observed in this figure, the value of A_H decreases with increasing G_0^*, meaning that the printed dimensions are closer to the model's dimensions. Below the threshold of G_0^* = 8000 Pa, A_H drops strongly when the number of layers is above ten, highlighting structural bending and sagging when adding additional layers. The object above this number of layers is not capable of supporting its own weight without deformation. Above 8000 Pa, the evolution of the accuracy reaches a plateau, meaning that no deformation occurred. Moreover, the results show that the number of layers also affects the accuracy. A larger number of layers results in a higher height accuracy, meaning a stronger deviation from the targeted dimensions. This effect may be linked to filament swelling after extrusion due to the relaxation of the polymeric chains.

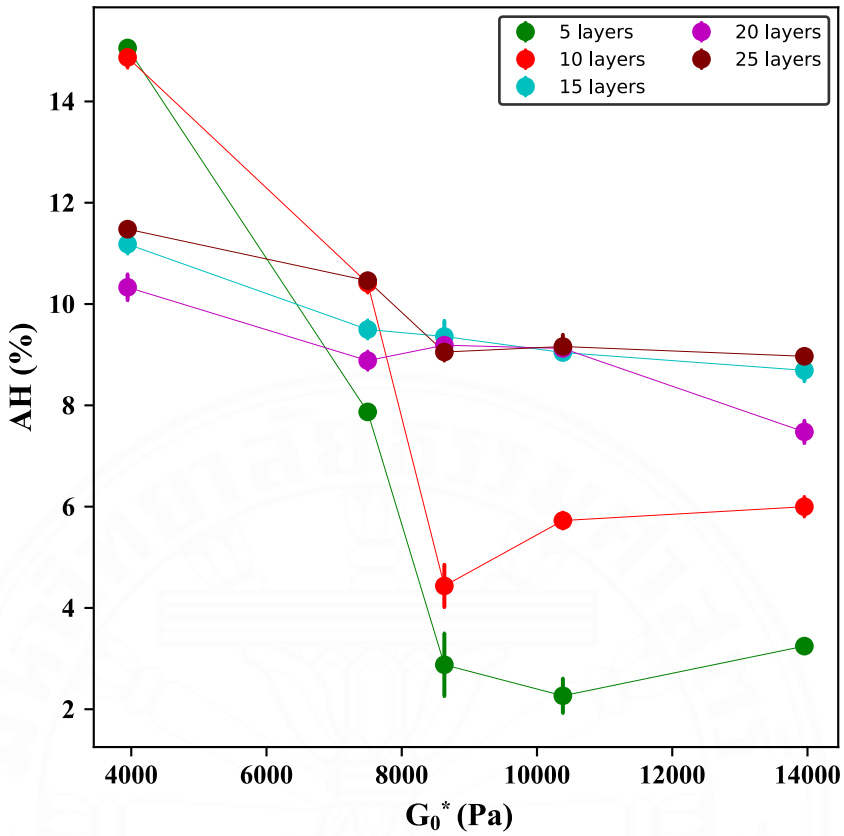

Figure 4.8 Evolution of the height accuracy according to the number of layers as a function of the complex modulus at 1 rad.s^{-1} determined with the power law fitting.

The results presented here confirm the conclusion from the previous chapter 3. Printing ink with increased viscoelastic properties improves their overall printability. However, the ink formulation remains to be controlled as higher viscoelasticity often strongly correlates with higher yield stress, which can be unsuitable according to the 3D printing system used. This is the case for the ink composed of 22.5 wt% mung bean and 4 wt% pectin. This ink was not extrudable at high pressure (P > 5 bar), within the printer's limit, due to high viscoelastic behavior.

Table 4.3 presents the evolution of shape stability, Equation (4.8), as a function of time. MB15PT2 displays poor stability due to the collapse of the object occurring during the printing process. This ink possesses the lowest solid-like behavior, i.e., G_0^* = 1250 Pa, explaining its weak ability to maintain its shape over time. After four hours, all the other concentrations present a dimensional stability quite acceptable, i.e., above

95%. However, the stability drops after 24 hours for all these inks. MB20PT4 presents the best stability over time, due to stronger solid-like behavior with G_0^* = 13954 Pa.

Table 4.3 Evolution of the dimensional stability over time.

Formulation	Stability (%) – t_4	Stability (%) – t_{24}
MB15PT2	84.00 ± 3.65	84.44 ± 3.08
MB17.5PT2	95.49 ± 2.78	82.57 ± 1.87
MB20PT2	96.92 ± 2.67	85.04 ± 4.25
MB22.5PT2	95.95 ± 2.93	85.32 ± 0.97
MB15PT4	96.88 ± 1.56	85.60 ± 1.97
MB17.5PT4	95.24 ± 3.81	86.43 ± 2.13
MB20PT4	96.47 ± 3.61	89.87 ± 2.92

4.3.4 Machine learning-based quality control

Quality control is an essential step in food processing to ensure the quality and consistency of food products. In this section, machine learning classification was applied as a quality control tool. The objective was to evaluate the applicability of various models in classifying the printability of different formulations and to further predict the class for an ink according to its rheological parameters and the number of printed layers. The error between the printed cube and its models was calculated and used to classify ink printability as either 'within range' (1) or 'out of range' (0), based on a threshold value of 10%. The studied features comprised the number of layers, tanδ, G_0^*, and T. The study initially comprised additional features, such as S which was removed due to a strong correlation with G_0^*. Eight models were examined, including Logistic Regression (LR), Support Vector Machine (SVM), k-Nearest Neighbors (kNN), Decision Tree (DT), Extra Tree (ET), Random Forest (RF), Gradient Boosting (GB), and XGBoost (XGB). Recursive feature engineering was applied to gradually eliminate the feature that presented lower importance based on the results from the RF model. The results of the importance of the feature are presented in Table 4.4.

Table 4.4 Feature importance.

Features	number of layers	tanδ	G_0^*	T
4	0.278	0.093	0.310	0.319
3	0.243	-	0.399	0.358
2	-	-	0.495	0.505

From these results, the least important feature in the model is tanδ. The other rheological parameters, G_0^* and T, are the two most important features affecting the class given to the printed object. The classification performance was evaluated across each set of features (4, 3, and 2) and is presented in Table 4.5. The objective was to determine the optimal combination of features and models that would provide the highest accuracy, precision, recall, and F1 score, particularly on the testing data, which is crucial for generalization to new, unseen data. However, as the classes were slightly imbalanced, the F1 score was selected to compare the models' performance across training and testing sets.

Table 4.5 Classification model results. The number of features is reduced by recursive feature engineering. For each number of features, the model yielding the highest performance is underlined. Number of features: 4 = layer, tanδ , G_0^*, and T. 3 = layer, G_0^*, and T. 2 = G_0^*, and T.

	Training				Testing			
Features	Accuracy	Precision	Recall	F1 score	Accuracy	Precision	Recall	F1 score
Linear Regression (LR)								
4	0.7704	0.7875	0.8523	0.8185	0.7593	0.7886	0.8349	0.8086
3	0.7704	0.7834	0.8597	0.8198	0.7704	0.7902	0.8592	0.8209
2	0.7704	0.7834	0.8597	0.8198	0.7704	0.7902	0.8592	0.8209
Support Vector Machine (SVM)								
4	0.7704	0.7834	0.8597	0.8198	0.7704	0.7902	0.8592	0.8209
3	0.7704	0.7834	0.8597	0.8198	0.7704	0.7902	0.8592	0.8209
2	0.7704	0.7834	0.8597	0.8198	0.7704	0.7902	0.8592	0.8209

k-Nearest Neighbors (kNN)								
4	0.7745	0.7773	0.8814	0.8260	0.7333	0.7627	0.8298	0.7914
3	0.7691	0.7787	0.8679	0.8201	0.7333	0.7622	0.8290	0.7918
2	0.7132	0.6976	0.9370	0.7989	0.7185	0.7086	0.9327	0.8025
Decision Tree (DT)								
4	0.7786	0.7966	0.8537	0.8240	0.7444	0.7805	0.8169	0.7961
3	0.7786	0.7966	0.8537	0.8240	0.7444	0.7805	0.8169	0.7961
2	0.7704	0.7834	0.8597	0.8198	0.7704	0.7902	0.8592	0.8209
Extra Tree (ET)								
4	0.7786	0.7966	0.8537	0.8240	0.7444	0.7805	0.8169	0.7961
3	0.7786	0.7966	0.8537	0.8240	0.7444	0.7805	0.8169	0.7961
2	0.7704	0.7834	0.8597	0.8198	0.7704	0.7902	0.8592	0.8209
Random Forest (RF)								
4	0.7728	0.7799	0.8726	0.8235	0.7630	0.7777	0.8654	0.8172
3	0.7712	0.7826	0.8632	0.8209	0.7667	0.7866	0.8592	0.8187
2	0.7704	0.7834	0.8597	0.8198	0.7704	0.7902	0.8592	0.8209
Gradient Boosting (GB)								
4	0.7630	0.7504	0.9160	0.8245	0.7259	0.7394	0.8654	0.7944
3	0.7630	0.7504	0.9160	0.8245	0.7259	0.7394	0.8654	0.7944
2	0.7704	0.7834	0.8597	0.8198	0.7704	0.7902	0.8592	0.8209
Extreme Gradient Boosting (XGB)								
4	0.7691	0.7663	0.8936	0.8246	0.7556	0.7568	0.8897	0.8162
3	0.7704	0.7834	0.8597	0.8198	0.7704	0.7902	0.8592	0.8209
2	0.7704	0.7834	0.8597	0.8198	0.7704	0.7902	0.8592	0.8209

When all features were included in the model, the Random Forest (RF) model appeared to perform best. It achieved a balanced performance across training and testing sets, with a training F1 score of 0.8235 and a testing F1 score of 0.8172. It suggests that the RF model efficiently captured the relationships between the rheological properties and the number of layers, resulting in accurate predictions of the printability class for the different ink formulations. The slight difference between the

training and testing F1 scores indicates a correct model generalization to unseen data while avoiding significant overfitting.

After removing the feature with the lowest importance, i.e., tanδ, the RF model continued to yield the best performance with a testing accuracy of 0.7667 and an F1 score of 0.8187. This showed that the model could generalize well even with a reduced number of features. The results suggest that the removal of tanδ did not significantly impact the model's performance, pinpointing the importance of G_0^* and T in determining the class of the printed objects.

Finally, when only two features were included in the model, almost all the models achieved similar and high performance on training and testing results. These models include LR, SVM, DT, ET, RF, GB, and XGB. In that case, LR is considered a more viable option when a more straightforward and interpretable model is preferred.

In conclusion, the RF model with all four features provided the best overall performance, capturing the complex interactions between the number of layers, G_0^*, T, and tanδ predicted the ink's printability class. However, the RF model with three features or the LR model with two features presents strong alternatives when simplicity is preferred. The findings underscore the importance of G_0^*, and T as the most critical factors in predicting the printability class. It highlights their direct influence on the ink's structural integrity and behavior under stress during the printing process. This study strengthens the importance of the rheological properties demonstrated in the previous chapters on the overall printability of food inks. Moreover, using machine learning for quality control in 3D printing reflects its potential to significantly improve ink formulations' classification based on a defined error range, ensuring higher quality and consistency in printed structures to enhance reproducibility and improve the overall 3D food printing process. Further development could also be investigated, such as using computer vision automated image analysis to automatically determine the dimensions of the printed objects and then run the machine learning algorithm to determine if the print is 'within range' or not. Several computer vision algorithms have been applied to food printing and plant-based meat analogs to enhance printability or food analysis (Fahmy et al., 2020; Ma, Schlangen, et al., 2023).

4.3.5 Formation of high protein snack: effect of baking on the fidelity of the printed objects

The shape retainment after baking was analyzed. To do so, 3D-printed objects were baked at two different temperatures, 150 and 180 °C. The dimensional variations were analyzed, and the aspect of the baked foods was visually evaluated. Figure 4.9. This figure shows the evolution of the visual aspect after baking across different samples and temperatures. It can be observed that the samples containing the lowest biopolymer content, i.e., MB15PT2, present strong deformation and burst aspects. This is mainly due to the highest water content. As the temperature increases during the baking, the water starts to boil and finally bursts out of the printed object, impacting its shape after baking. Here, we can observe that the formulation impacts the final desired object, with a reduced biopolymer content being undesirable. The best formulation contains more than 20 wt% mung bean protein from these observations. The effect of temperature did not strongly affect the baked 3D printed objects. Only a stronger browning and enhanced dry aspect due to reduced water content are observed at higher baking temperatures.

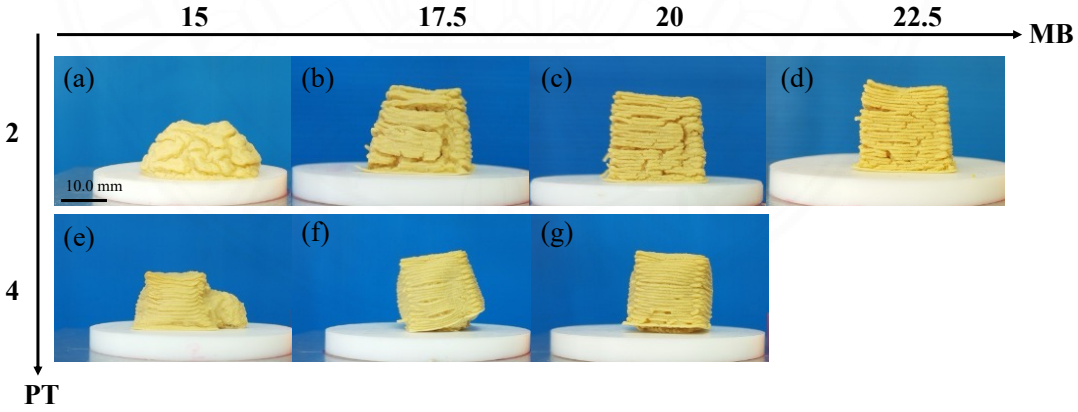

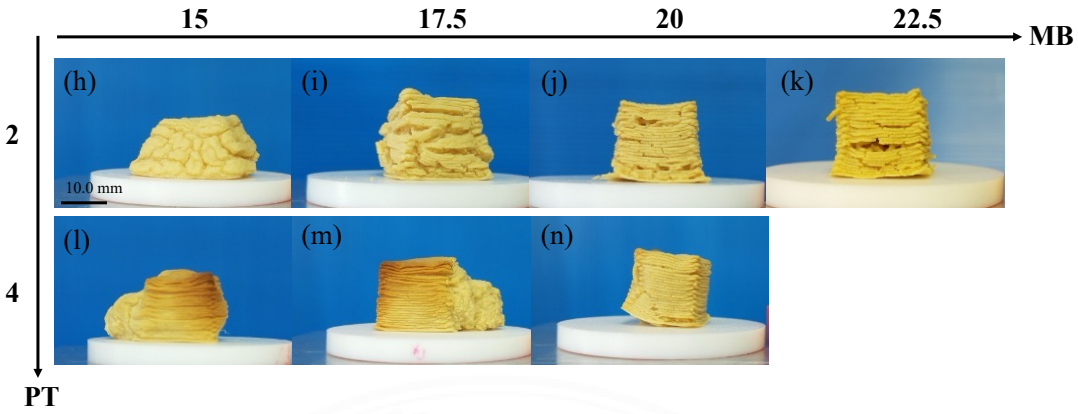

Figure 4.9 Baked prints at (a) – (g) baking temperature of 150 °C. (h) – (n) baking temperature of 180 °C.

Furthermore, the total protein content in the theoretical final printed object was evaluated using Equation (4.13). The results show that the formulation presenting the highest theoretical protein content after baking is MB22.5PT2, Table 4.6. In this study, we produced bite-sized 3D printed snacks with a weight ranging from 2 to 4 g, containing 20 to 33 wt% of protein. Further analysis will be required to determine the actual protein content after baking and human evaluation through panel testing to quantify the hedonic properties of the developed snacks. However, these results remain promising for developing protein-rich 3D printed snacks.

Table 4.6 Theoretical protein content in the 3D printed snacks after baking at different temperatures.

Formulation	P_{th} (150 °C) (%)	P_{th} (180 °C) (%)
MB15PT2	18.96 ± 0.51	21.38 ± 0.76
MB17.5PT2	23.05 ± 0.50	27.47 ± 1.35
MB20PT2	26.29 ± 1.05	36.41 ± 2.15
MB22.5PT2	31.05 ± 1.65	37.85 ± 2.33
MB15PT4	19.46 ± 0.98	20.43 ± 1.02
MB17.5PT4	22.19 ± 0.79	27.10 ± 1.21
MB20PT4	25.39 ± 1.04	31.05 ± 0.66

4.4 Conclusion

This chapter presented a complete analysis of the 3D printing process for protein-rich plant-based snacks, focusing on the critical role of rheological properties and the impact of the selected post-processing method, i.e., baking. Through detailed rheological analysis, including both small and large amplitude oscillatory shear tests, we demonstrated how variations in biopolymer content influence the ink's rheological properties and printing behavior. The findings confirmed that higher concentrations of mung bean protein and pectin contribute to stronger solid-like behavior, affecting the accuracy and dimensional stability of the printed objects. The machine learning-based quality control model further highlighted the importance of rheological parameters, such as G_0^* and T, to predict ink's printability. The RF model provided the most balanced and accurate prediction, pinpointing its robustness in handling complex interactions between features. Baking has been shown to impact the final shape of the developed snack significantly. Material bursting occurred for formulations containing low biopolymer content, but this negative behavior was reduced when the total biopolymer content increased. The baking temperature did not significantly impact the shape of the final 3D printed protein-rich snack. These insights are crucial for

optimizing the ink's formulation and processing conditions to obtain the desired quality in 3D printed food.

It has been demonstrated that the joint integration of rheological analysis, quality machine learning classification-based quality control, and post-processing can improve the quality and consistency of 3D printed food products. The rheological analysis and machine learning quality control provided a complete comparison of the different ink formulations. Inks with higher concentrations of mung bean protein isolate and pectin displayed stronger solid-like behavior, which yielded better dimensional accuracy, stability, and resistance to baking after the printing process. These are considered strong candidates for further development in 3D food printed protein-rich snacks. In contrast, formulations with lower biopolymer content, such as MB15PT2, had difficulties retaining their shape during the 3D food printing process, resulting in shape infidelity. These formulations also showed reduced stability over time. Furthermore, MB15PT2 could not hold its shape after baking, with a complete burst of materials out of the structure, resulting in a distorted baked snack. This comparative analysis underscores the importance of selecting the appropriate biopolymer concentrations to achieve the desired printability and stability in 3D printed food products. The findings presented in this chapter lay a solid basis for further research and applications in 3D food printing, more precisely in developing high-protein, plant-based snacks.

CHAPTER 5
ARTIFICIAL INTELLIGENCE ASSISTED 3D FOOD PRINTING

5.1 Introduction

The advancement of 3D food printing started in 2006 with the Fab@Home project and the first 3D printed chocolate (Malone & Lipson, 2007). Since then, the technology has advanced immensely, and numerous foods have been printed. Examples of 3D printed foods comprise surimi (Wang et al., 2018), vegetable snacks (Ahmadzadeh et al., 2024), chocolate (Mantihal et al., 2019), beef paste (Dick et al., 2021), dairy products (Le Tohic et al., 2018; Riantiningtyas et al., 2021), and even moon cake (X. Wang et al., 2023). Recently, the innovation has leaped forward with the arrival of "The Filet", the first commercially available 3D printed food by Revo Foods. This plant-based product mimics a salmon filet using ingredients such as mycoproteins, algae oils, vegetable oils, and vitamins, showcasing the exciting potential of this technology (Revo Foods, 2024). In addition, 3D food printing holds immense promise for personalized nutrition and health-focused applications. It can create foods loaded with active compounds and vitamins or accommodate the specific dietary needs of various groups of consumers, such as athletes, pregnant women, or dysphagic patients (Azam et al., 2018; Escalante-Aburto et al., 2021; Zhenbin Liu et al., 2023; Lorenz et al., 2022; Severini & Derossi, 2016). Researchers have also explored its application in space, where 3D-printed food could replace rehydratable food and be customized for long-duration missions (Enfield et al., 2022). Additionally, this technology can transform food waste into entirely new and visually attractive food products, thus promoting the circular economy (Hooi Chuan Wong et al., 2022; Muthurajan et al., 2021). The current development of additive manufacturing technology has extended beyond 3D food printing to even 4D/5D/6D printing (Fahmy et al., 2023; Ghazal et al., 2023). Even though this technology is promising and attractive due to its wide range of applications and possibilities, a number of important uncertainties remain regarding the upscaling ability of this process.

Artificial intelligence (AI) gathers a broad range of technologies and methodologies designed to enable machines to perform tasks that typically require

human intelligence. AI systems can learn from data to effectively improve their performance. Among its many subfields, as represented in Figure 5.1, machine learning (ML) is a key category of AI where algorithms learn from and make predictions based on data. Deep learning (DL), which is a subset of ML, involves neural networks with many layers that can analyze vast amount of complex data, making it powerful for image and speech recognition. Furthermore, computer vision (CV) is an application where algorithms extract meaningful information from images or videos. Natural language processing (NLP) is another application focusing on the interaction between computers and humans through language. Robotics, another branch of AI, involves designing and creating robots that can perform tasks autonomously, often employing CV, ML, and DL techniques to improve their functionality over time. The development of AI technology has increased significantly in the past decade due to the reduced cost of electronic components, cameras, and microcontrollers such as Arduino boards and Raspberry Pi, making these technologies more accessible, thus easing the development of small and adaptable systems for a wide range of applications.

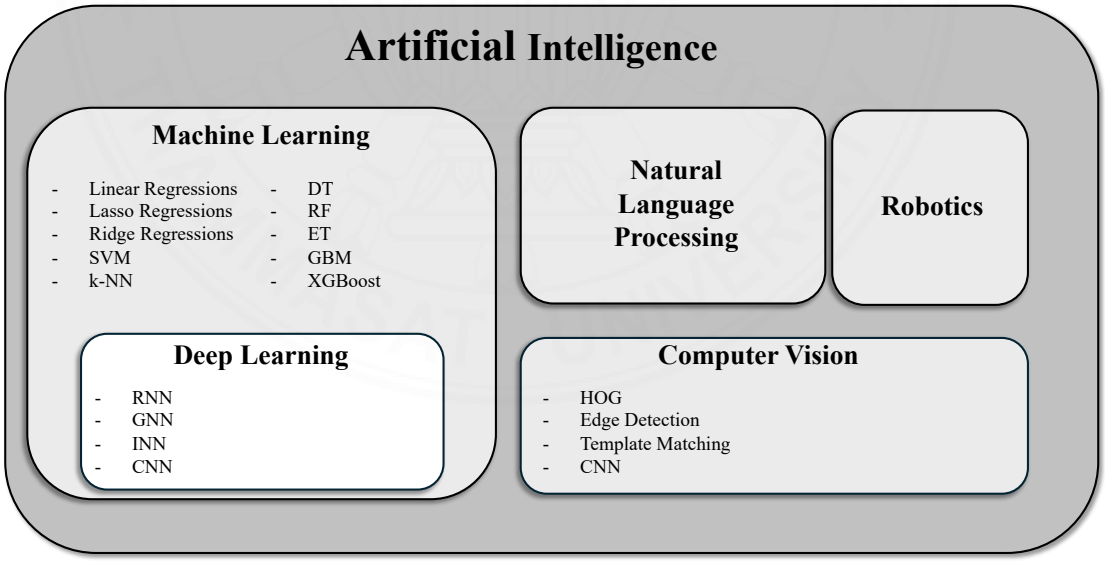

Figure 5.1 The artificial intelligence (AI) framework.

The interest in combining AI and food science has received greater attention in recent years, especially for food production. Indeed, AI is emerging as a new technological tool to improve the processing and quality of food products (Addanki et

al., 2022). It is already applied in several fields in food science, such as beverage analysis (Ordukaya & Karlik, 2016), beer brewing (Vassileva & Mileva, 2014), dairy products (Freire et al., 2024), and dough (Guha et al., 2017). Some applications are already used for 3D food printing, but the use of this technology is still limited (Lu et al., 2023; Ma, Potappel, Chauhan, et al., 2023; Outrequin et al., 2024; Yoo & Park, 2021).

This chapter aims to detail how the combination of two technological rising stars can revolutionize the food industry. The first section presents generalities about the most frequent Artificial Intelligence (AI) models encountered. The second section presents how AI and its subsets are used to optimize food ink formulation. Subsequently, AI applications in monitoring and improving traditional additive manufacturing processes are described. Moreover, how these applications could benefit 3D food printing is discussed. The fourth section highlights the current use of AI in food post-processing and quality control and how it could be beneficially applied to 3D food printing. Lastly, the concluding section summarizes the key information presented in this chapter. It also stresses forward opportunities for developing the AI-assisted 3D food printing process.

5.2 AI subcategories overview

As presented previously, Artificial Intelligence comprises several subfields with different specificities and applications. This section will briefly present the subfields commonly used in additive manufacturing, i.e., computer vision, machine learning, and deep learning, and introduce some algorithms.

5.2.1 Computer Vision (CV)

Computer Vision is a discipline that enables computers to extract meaningful information from visual data such as images and videos. In particular, machine vision is an application of computer vision, which applies visual systems to industrial or manufacturing settings to optimize efficiency, ensure quality control, and guide operations through defect detection and product inspection tasks. It combines the use of cameras, suitable lighting, and relevant software or codes to automate inspections, measurements, and process monitoring tasks. The field of computer vision is built

around several models according to the application. For example, Histogram of Oriented Gradients algorithms (HOG) can be used for object detection (Dalal & Triggs, 2005), Edge Detection algorithms can be used to detect edges in an image (Sun et al., 2022), Template Matching algorithms are used to find part of an image matching with a template (Hashemi et al., 2016), and applied Convolutional Neural Networks (CNN) algorithms are used for image classification, segmentation, and object detection (Voulodimos et al., 2018). All these algorithms are frequently used through Open CV, PyTorch, or TensorFlow Python libraries (Abadi & TensorFlow, 2016; Paszke et al., 2019; Pulli et al., 2012). Other libraries are also available for different programming languages including MATLAB or R.

5.2.2 Machine Learning (ML)

Machine Learning is a segment of Artificial Intelligence that uses different algorithms to predict a defined output from various input variables or features. These algorithms automatically detect patterns in data and use those patterns to make predictions. Four different categories of learning algorithms exist; (i) supervised, (ii) unsupervised, (iii) semi-supervised, and (iv) reinforcement learning. Supervised learning algorithm uses labeled input and output data. Through an iterative learning cycle, the algorithm learns a function capable of predicting an output when a new set of features is provided. On the contrary, unsupervised learning determines hidden patterns among unlabeled datasets. It is frequently used to detect anomalies or clustering datasets. Semi-supervised learning combines the previous two learning methods, which are mostly used when the dataset is partially labeled. Lastly, reinforced learning uses algorithms that learn through trial and error. This learning process is based on punishment and reward techniques and aims to maximize cumulative rewards over time. Reinforcement learning is mainly used for robotics or game playing (Mahesh, 2020; Qiang & Zhongli, 2011; Shinde & Shah, 2018). Numerous algorithms are available; here, we will present some of the most common ones in this chapter. Other models can be found in the literature and textbooks (Ray, 2019; Suthaharan, 2016).

5.2.2.1 Linear Regression

Linear regression is a fundamental algorithm in machine learning used to model the relationship between a dependent variable and one or more independent variables by fitting a linear equation. This algorithm is easy to implement and interpret but can present issues with non-linear relationships and outliers.

5.2.2.2 Ridge and Lasso Regressions

Ridge and Lasso regressions are extensions of linear regression that address some of its limitations, particularly overfitting. Ridge regression introduces a penalty term to the loss function to shrink coefficients, thereby improving the model's generalization. Lasso regression, on the other hand, performs feature selection by forcing some coefficients to be exactly zero. These methods are valuable for models requiring regularization to handle multicollinearity or when feature selection is essential.

5.2.2.3 Support Vector Machines (SVM)

Support Vector Machines are supervised learning algorithms used for classification and regression tasks. By mapping data into a higher-dimensional space, SVM finds a hyperplane that best separates the data into classes. SVM is robust against overfitting, especially in high-dimensional spaces, making it useful for complex classification tasks.

5.2.2.4 k-Nearest Neighbors (k-NN)

k-Nearest Neighbors is a simple, instance-based learning algorithm for classification and regression. It classifies data points based on the majority class of their nearest neighbors. While k-NN is easy to understand and implement, it can be computationally expensive for large datasets.

5.2.2.5 Decision Tree (DT)

A decision tree is a versatile machine learning algorithm used for classification and regression. It models decisions and their possible consequences, forming a tree-like structure. Decision trees are intuitive and can handle both numerical and categorical

data, making them suitable for various applications. However, decision trees are more sensitive to overfitting, especially with complex datasets.

5.2.2.6 Random Forest (RF)

Random Forest is an ensemble learning method combining multiple decision trees to improve prediction accuracy and control overfitting. By aggregating the outputs of several trees, it provides more robust and accurate predictions. Random Forest is particularly effective for high-dimensional data.

5.2.2.7 Other Tree Models (ET, GBM, XGBoost)

Ensemble methods like Extra Trees (ET), Gradient Boosting Machine (GBM), and Extreme Gradient Boosting (XGBoost) are built upon several decision trees to improve model performance. ET increases diversity among trees by selecting random splits. GBM sequentially builds trees to correct errors of previous ones, and XGBoost enhances GBM by optimizing the model using gradient descent.

It is worth pointing out that all models presented here can be easily accessed using Python libraries such as Scikit-learn, XGBoost, and Lightgbm (Chen & Guestrin, 2016; Ke et al., 2017; Pedregosa et al., 2011).

5.2.3 Deep Learning (DL)

Deep learning is a subclass of machine learning that uses complex models similar to humans' neural networks to analyze intricate data sets. These models, known as artificial neural networks (ANNs), consist of multiple processing layers that enable the extraction of complex patterns from raw input data. Deep learning has significantly advanced fields such as computer vision, natural language processing, and speech recognition, allowing machines to learn from large amounts of data (LeCun et al., 2015).

5.2.3.1 Recurrent Neural Network (RNN)

Recurrent Neural Networks are a type of ANN designed to handle temporal or sequential data. RNNs have connections that form directed cycles, allowing them to maintain a hidden state that captures information about previous inputs. This feature

makes RNNs particularly suitable for tasks such as language modeling, time series forecasting, and speech recognition, where the order of data points is crucial.

5.2.3.2 Convolutional Neural Network (CNN)

Convolutional Neural Networks are specialized ANNs for processing spatial data, such as images. CNNs use convolutional layers to automatically and adaptively learn spatial hierarchies of features from input images. This makes them highly effective for tasks like image classification, object detection, and image segmentation as applied to computer vision tasks (Dhillon & Verma, 2019).

5.2.3.3 Graph Convolutional Neural Network (GNN)

Graph Convolutional Networks are designed to work with graph-structured data, where data points are connected by edges. GNNs generalize the concept of convolutional neural networks to graphs, enabling the learning of node and edge representations that capture the graph's structure.

5.2.3.4 Inverse Neural Network (INN)

Inverse Neural Networks are a less common type of ANN that aims to invert the processes of a forward neural network. These networks can be useful for applications that require reconstructing inputs from outputs or solving inverse problems.

It is useful to point out that the implementation of these deep learning models is eased by readily available libraries such as PyTorch and TensorFlow (Abadi & TensorFlow, 2016; Paszke et al., 2019).

5.3 Optimization of the food formulation using artificial intelligence tools

The recent improvement in computational techniques, more precisely of AI combined with the creation of food databases, is expected to significantly advance the fields of food science and food chemistry by enabling more efficient and accurate data analysis and promoting innovation in food-related research and development, as presented in Figure 5.2 (Tseng et al., 2023). This section explores how artificial

intelligence can be applied in food science to optimize flavor development, enhance nutritional value, and improve functional properties.

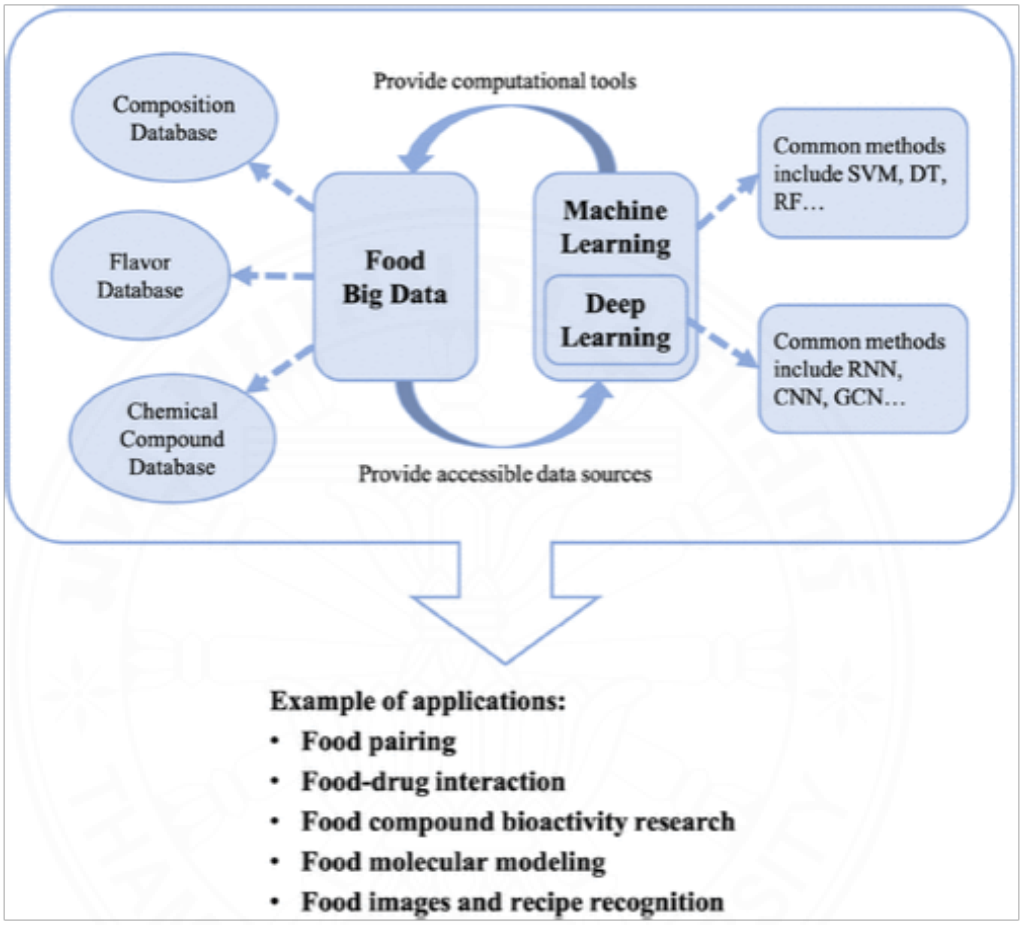

Figure 5.2 Relationship between Food Big Data and AI. Source: Reproduced from Tseng et al. (2023).

5.3.1 Improvement of the food's flavor and nutritional properties through artificial intelligence applications

3D food printing is commonly applied to render food products more visually attractive. However, the visual aspect is not consumers' only important hedonic aspect. Nutritive properties and flavor are also paramount. Fewer studies are presenting how 3D food printing can be used to tune a meal's flavor. However, Fahmy and co-authors presented an interesting use of 3D printing toward this ideal. In their work, they present a method to enhance saltiness by distributing sodium chloride inhomogeneously across

the layers while keeping a printed food product with a reduced sodium content (Fahmy et al., 2021). Achieving the ideal flavor in food products has long been an essential pursuit in food science. Traditionally, this has relied on experience, intuition, and trial-and-error experimentation. However, recent advancements in artificial intelligence offer a powerful new approach to achieve this goal more efficiently.

As presented in Figure 5.3, food flavor analysis has evolved through four stages. The first stage relied on human sensory evaluation to detect and assess food characteristics such as flavor and taste profile. This method, however, suffers from low repeatability and is largely dependent on trained experts. The introduction of instrumental analysis allows for detecting volatile and soluble components in foods and beverages, including compounds with low volatilities and olfactory limits, thus providing additional information on the flavor. Then, the combined integration of sensory and instrumental analysis connects human sensory evaluation and instrumental detection. Lastly, the integration of machine learning for automatic data analysis is applied to address limitations and enhance flavor analysis's objectivity and efficiency (Zeng et al., 2023). Several tools can be used to characterize the flavor data for machine learning, such as panel evaluation (Bahramparvar et al., 2014), infrared spectroscopy and GC-MS (Ji et al., 2023), as well as electronic nose and tongue (Men et al., 2017).

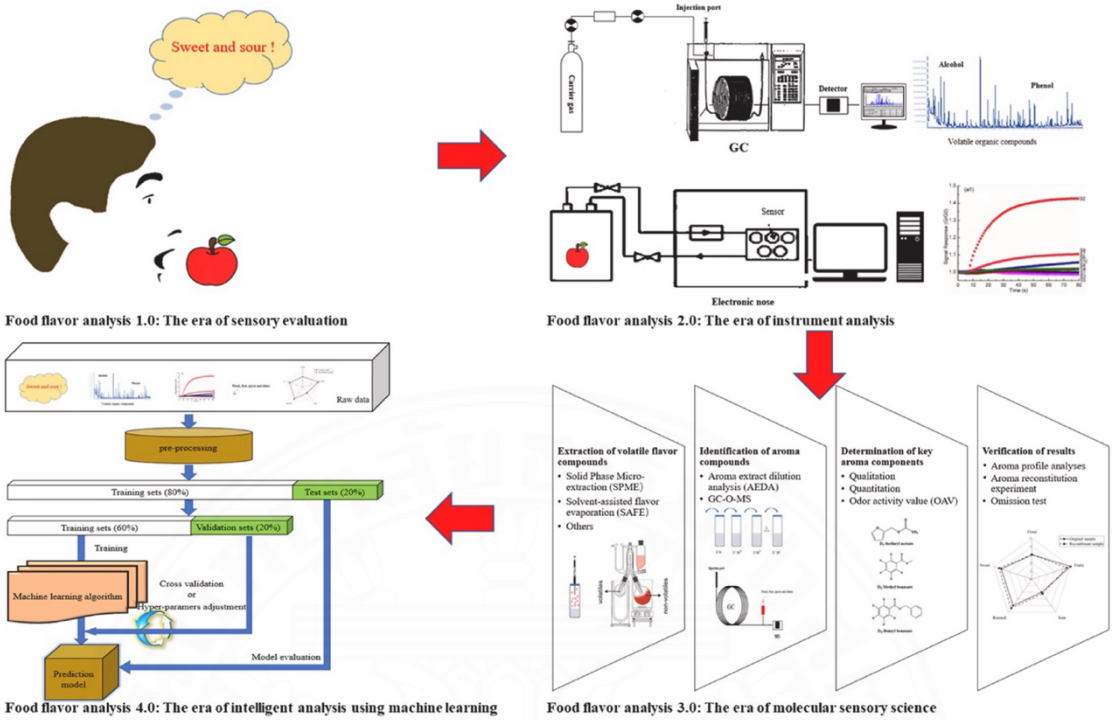

Figure 5.3 The evolution of food flavor analysis. Source: Reproduced from Zeng et al. (2023).

Examples of machine learning techniques used to predict and improve the flavor of food and beverages are wide-ranging (Bi et al., 2019; Chang et al., 2021). Schreurs and co-authors developed an extensive study on predicting and improving beer flavor using several machine learning algorithms. Their extensive analysis was based on 200 chemical and sensory properties of 250 different beers. Ten regression machine learning models were used, including linear regression, ET, RF, GB, SVM, and XGBoost, and their study shows that GB was the best-performing model (Schreurs et al., 2024). By combining flavor analysis with AI, the precise customization of flavors can be achieved, and the authors believe that it can revolutionize the field of 3D food printing and enable the creation of personalized culinary experiences.

The evolution of 3D food printing technology has further sparked interest in developing high-nutritional-value food formulations. Existing literature provides several examples of such ideas for 3D printed foods enriched with proteins (Hussain, Arora, et al., 2021; Zhu et al., 2022), vitamins (Azam et al., 2018), fibers (Ahlinder et al., 2023), and other bioactive compounds such as flavonoids, terpenoids, or carotenoids (Ahmadzadeh et al., 2023). On the contrary, less work has highlighted the

use of AI to optimize food formulation. Therefore, it can be interesting to develop models that gather the interactions between food ingredients, a person's specific diet requirements, allergies, and taste to propose optimized, tailored novel food formulations. Moreover, AI can also be applied to formulate specific food for disease management risk and provide patients with sufficient nutrients (Tapkire & Arun, 2023).

5.3.2 Improvement of the formulation functional properties through artificial intelligence applications

Rheology plays a crucial role in food printing as it directly affects the printability of the ink and the structural integrity of the final printed product. The rheological properties of the food materials, such as viscosity and viscoelasticity, determine how the material flows and sets during the printing process, ensuring precise layer deposition and maintaining correct shape fidelity (Outrequin et al., 2023). Besides, food printing enables fine-tuning textural properties by adjusting ingredient formulations and processing conditions. This customization allows for the creation of tailored textures, opening new possibilities for innovative food applications, including personalized nutrition (Escalante-Aburto et al., 2021) and enhanced food accessibility for populations with special requirements, such as the elderly or those with swallowing difficulties (Lee et al., 2021; Pant et al., 2021). This concept finds application in using 3D food printing to obtain programmable food textures through efficient CAD and food formulation tuning (Oral et al., 2021).

Deep learning techniques have been used to predict various rheological properties of several food systems. Properties such as pomegranate viscoelastic behavior, grape molasses' creep recovery properties, and honey viscosity have been modelized using neural networks (Al-Mahasneh et al., 2013; Saeidirad et al., 2013; Toker & Dogan, 2013). As suggested by Nnyigide and Hyun, applying machine learning techniques in food science could be beneficial in reducing the time and cost of developing food systems by targeting specific rheological behaviors (Nnyigide & Hyun, 2023). Furthermore, additional improvements can be made to the food system's formulation. Becker and co-authors presented the development of a fully automated closed-loop system to optimize the preparation of liquid formulations employing a milli-fluidic laboratory. Their system couples a robotic platform for dosing the

chemical, carrying the reaction, and measuring the viscosity and the turbidity with a machine learning model to optimize food production (Becker et al., 2023). Machine learning techniques are also used to predict food textural properties. Lie-Piang and co-workers explore the applications of machine learning techniques, including linear regression, polynomial regression, neural network, random forest, regularization, or spline regression, to predict the textural properties of pea protein gels. The neural network model was deemed more suitable for predicting the gel stiffness of the pea-based formulations (Lie-Piang et al., 2023).

In the context of food printing, AI could be used to optimize formulations for 3D printed foods by predicting how the different ingredients and structures will behave during and after the printing process. Moreover, AI models could also simulate the rheological properties of the food and textural properties of the final printed product, ensuring that they meet the desired properties. The integration of AI could also reduce extensive trial-and-error experimentation by determining the ideal food formulation to achieve the aimed rheological and textural properties.

5.4 3D food printing process monitoring and improvements using AI

Process optimization is currently at high stake in the field of 3D food printing. Several anomalies are known to occur during the process, such as over-extrusion of the food ink, under-extrusion of the food ink, discontinuity of the filament, coiling, collapse of the printed object, and dimensional anomalies (Fribus et al., 2024; C. Liu et al., 2019; Lv et al., 2024; Outrequin et al., 2023; Yuk & Zhao, 2018). Detecting these issues in real-time and facing them during the process will surely improve the overall 3D food printing process and ease its upscaling production.

5.4.1 AI-enhanced 3D printers and software for process monitoring

In the field of additive manufacturing, detecting print defects is of great importance. To do so, cameras are often added to the 3D printer frame with a top-down or a side view to generate a large image data set. Manually assessing image data sets is tedious; improvements have been made, and one of the main methods used is computer vision, a field of artificial intelligence. It involves the development of algorithms and models that allow machines to process and analyze images or video data automatically. Several

models have been built based on real-time image analysis to detect print defaults (Li et al., 2021; Petsiuk & Pearce, 2020; Wu et al., 2016). Commercially, AI-embedded 3D printers are starting to emerge for FDM. The Creality K1C is among the recently developed 3D printing using this advanced technology (Creality, 2024). This 3D printer is equipped with an AI camera system to monitor the printing process and inform the user when an issue is detected during the printing.

Another example is the Bambu Lab X1 Series, which is equipped with AI tools and a Lidar system enabling micrometer-level precision to inspect the first layer height and detect the formation of spaghetti during the printing process (BambuLab, 2024). So far, the number of 3D printers equipped with such systems remains limited, but the authors strongly believe that the catalog will widen in the following years. However, these systems must still be adapted for commercially available and customer-made 3D food printers. Besides, some software has been developed to provide FDM users with AI-print defect detections. These softwares, such as PrintWatch and 3DPrinterOS, observe the printing process in real time and notify the user when any anomaly issues occur. These systems rely on computer vision models and are adaptable to many 3D printers; however, they do not yet provide any controls to solve the occurring issues during the printing process (3D Control Systems, 2024; printpal.io, 2024).

5.4.2 Recent developments in the field of additive manufacturing

Some research groups have been working on detecting and correcting 3D printing errors during the printing process. Brion and co-workers have developed a machine vision framework capable of analyzing the printed layers, detecting issues, and correcting them by varying printing parameters. The authors used a fleet of height 3D printers equipped with camera systems focusing on the nozzle tip to generate the data to achieve this. The images of the extrusion process are further gathered and analyzed in a multi-head neural network model. Four features are studied in this model: the flow rate, the lateral speed, the z offset, and the hot end temperature. The machine vision control system follows the pipeline presented in Figure 5.4. Briefly, this model aims to classify each feature into categories, either as low, good, or high, using the images of the extrusion process. Then, the required adjustments are determined, and the corrected

g-code is sent to the printer. Lastly, the print is made, and the results are validated (Brion & Pattinson, 2022).

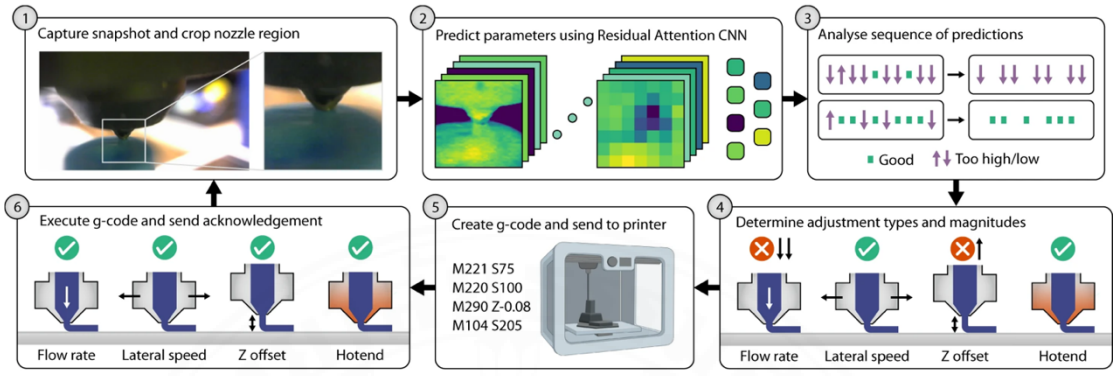

Figure 5.4 Machine vision pipeline used to analyze real-time images of the extrusion process and to correct printing parameters. Source: Reproduced from Brion & Pattinson (2022).

Recently, Roach et al. (2023) equipped their DIW printer with an automated real-time control of the extrusion. This system combines computer vision with an inverse neural network (INN) model, as depicted in Figure 5.5 (Roach et al., 2023). The process monitors the printing in real-time using a computer vision algorithm; it measures the printed line width and determines whether it matches the targeted line width; if it matches, the process continues; otherwise, it stops and determines the optimal printing parameters using the INN model. Then, the new parameters are implemented into the g-code, and the process starts again. Several other methods exist to control defects using computer vision and machine learning models during the 3D printing process (Khan et al., 2021; Nguyen et al., 2022; Paraskevoudis et al., 2020).

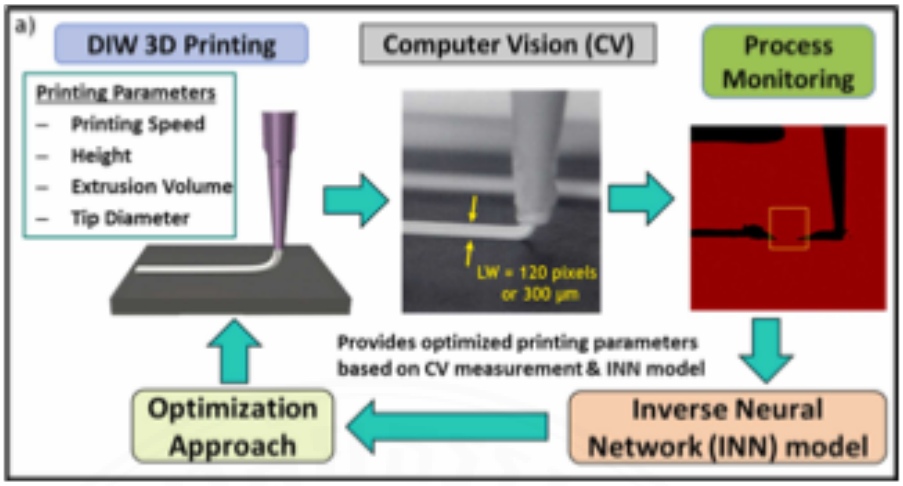

Figure 5.5 CV-INN DIW optimization process. Source: reproduced from Roach et al. (2023).

5.4.3 Application to 3D food printing and future requirements

Research is also being carried out for 3D food printing to improve the overall deposition process. Fahmy and co-authors performed a study to propose a method enabling the characterization of the morphological aspect of 3D printed cereal-based inks with varying water content (Fahmy et al., 2020). Using a dual-camera system capturing simultaneously top-down and side views, the authors developed a computer vision sequence to analyze printed lines. They pointed out the important effect of rheological properties on the printer results, especially the yield strength, which can provoke over or under-extrusion characteristics, delay in the flow initiation, or deformation of the final object. This is illustrated in Figure 5.6, in which Figure 5.6(a) displays a slumping behavior due to the high water content of the ink, whereas Figure 5.6(b) shows a coiling behavior. Ma and co-authors developed a CV-based system to measure the width of the printed filament and the instant extrusion rate to prevent under-extrusion. These methods were demonstrated to help improve the printed filament accuracy; however, improvements are still required to automate the optimization of 3D printing parameters by applying this method in the close-loop control of the printer (Ma, Potappel, Chauhan, et al., 2023).

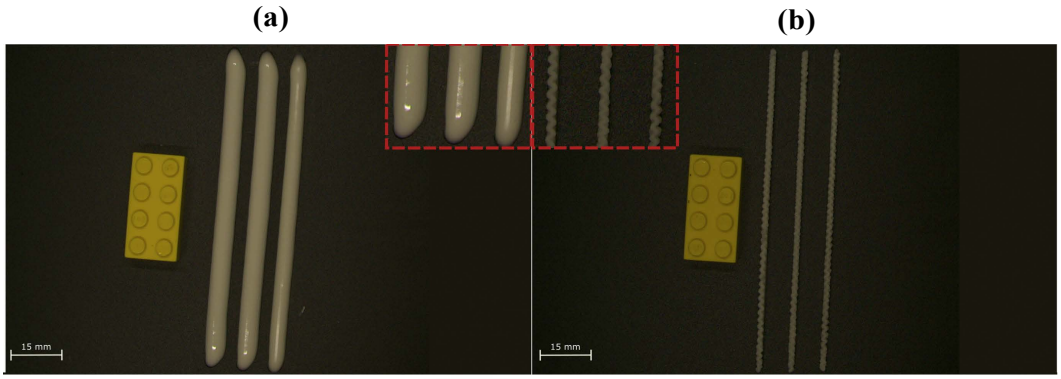

Figure 5.6 Top view of five layers stacking ability of (a) starch-egg white protein blend with 70 g/100 g water addition. (b) starch-egg white protein blends with 50 g/100 g water addition. Source: Reproduced from Fahmy et al. (2020).

Image analysis systems have also been developed to detect layer-wise printing inaccuracies such as under and over-extrusion on fresh and baked samples, as presented in Figure 5.7. This system also competed against human evaluation, demonstrating that human interpretation tends to be under-extrusion (Ma, Potappel, Schutyser, et al., 2023).

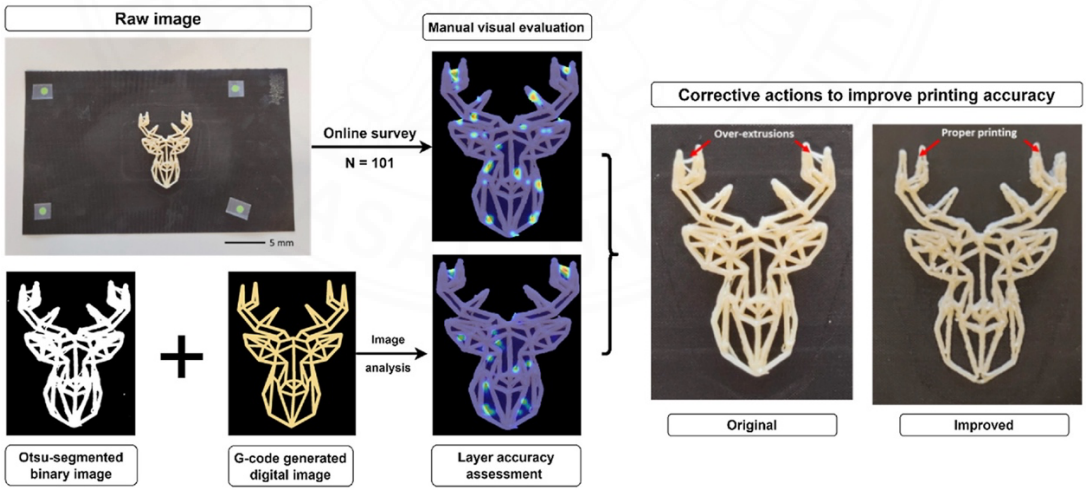

Figure 5.7 3D printed food image evaluation pipeline. This process is based on human and computer evaluation. Source: Reproduced from (Ma, Potappel, Schutyser, et al., 2023).

Machine learning techniques have also been used to evaluate and optimize the printed dimensions. For example, machine learning classification coupled with Canny edge image analysis has been used to study the effect of rheological and printing parameters on dimensional properties such as the node width, the printed height, and width consistency for several food products (Ma et al., 2021). Moreover, Outrequin and co-authors studied the influence of printing and rheological parameters inherent to the food ink formulation on the spreading of the deposited filament, defined as $S = D/D_0$, where S is the spreading ratio, D is the diameter of the printed filament, and D_0 is the printing nozzle diameter (Outrequin et al., 2024). Five tree-based regression models were used to analyze the effect of the various parameters on the filament spreading: DT, RF, ET, GBM, and XGBoost. The findings indicate that all tree models performed well across different numbers of features studied, with a slight drop in performance on test data compared to training data, suggesting light overfitting, a typical issue with small datasets (Ying, 2019). Their results displayed the strong impact of the viscoelastic properties as they accounted for over 90% of weight in the spreading determination, followed by the printing speed and extrusion pressure. The findings presented in this section are summarized in Table 5.1.

Table 5.1 Summary of AI-based 3D food printing process monitoring and improvements examples from the literature.

Ink formulation	Objectives	Methodology	Findings	References
- Hydrated flour dough - Hydrated wheat starch-egg white protein paste	- Understand the effect of viscoelasticity during 3D food printing.	- Morphological image processing, top down and side view - Greyscale conversion, image thresholding, segmentation, edge detection, boundary detection	- Higher yield strength and lower water content promote under-extrusion. - Formation of gluten network promote structural stabilization. - Effect of viscoelasticity and geometrical attributes on defects.	Fahmy et al. (2020)
- Concentrated sodium caseinate dispersion. - Processed cheese slices and cheese spread. - Chocolate spread. - Coconut butter spread.	- Develop a predictive model to assess the extrudability. - Develop a predictive model to assess the line geometry.	- Top-down view image analysis, Canny Edge detection. - Binary classification, RF model. Features = flow index, consistency coefficient, flow rate exponent, flow rate coefficient, pressure, and nozzle speed. Output = mode width, line height and width consistency.	- Modeling of printing, rheological properties and extrudability. - Strong effect of the printing parameters on the node width. - Important effect of the rheological properties on the width consistency.	Ma et al. (2021)
- Hydrogels prepared using low methoxyl pectin and cellulose nanocrystals.	- Develop a predictive classification model to assess the effect of ink formulation and rheological properties on a printability metrics.	- Binary classification of the width and roughness based on rheological and formulation parameters, RF model. Features = flow index, flow transition index, storage modulus, loss modulus, loss factor, recovery and yield stress. Output = width, roughness, and combination of both factors.	- High accuracy of the RF model in predicting the printed accuracy based on the rheological properties of the food ink.	Lu et al. (2023)

- Cookie dough (fresh and baked)	- Develop a layer-wise accuracy analysis tool.	- Consumer visual evaluation. - Digital image generated from the g-code parsed into cartesian coordinates and printing settings. Accuracy using this digital image as model versus Otsu-segmented binary image of the printed object.	- Oozing and over extrusion are detected as defaults by human panel and camera system. - Under extrusion is not detected as defect by the panel but is by the intelligent monitoring system.	Ma, Potappel, Schutyser, et al. (2023)
- White chocolate spread. - Lemon curd. - Dry cookie dough mix. - Processed cheese.	- Propose a CV-based determination of the instantaneous flow rate and filament width. - Calibration of the nozzle movement speed based on determined instantaneous flow rate and its implementation.	- Computer vision analysis of controlled extruded samples.	- Improvement of filament accuracy. - Prevention of under-extrusion.	Ma, Potappel, Chauhan, et al. (2023)
- Low methoxyl pectin ink formulation.	- Quantify of the relative importance of printing and rheological parameters on the spreading ratio. - Predict the spreading of the deposited material.	- Image analysis - Machine learning regressions, trees models: DT, RF, ET, GBM, XGBoost. Features = D_0 (nozzle diameter), P (extrusion pressure), V (printing speed), G_0^* and n (extracted from power law fitting of frequency sweep results). Output variable = S (spreading ratio).	- Overall good performance of each model. - ET is the best model with four features, P (extrusion pressure), V (printing speed), G_0^* and n (extracted from power law fitting of frequency sweep results). - Feature importance: G_0^*> n > V > P.	Outrequin et al. (2024)

Moving forward, there is a need to continue fostering the adaptation of these systems for 3D food printing applications. It would be highly beneficial to improve the overall process. Indeed, it will help promote the successful formation of 3D printed food, reducing the reliance on experimental trials to determine the correct printing parameters and ink formulation. Moreover, this approach can be further refined. For example, as the rheological properties are paramount to rendering a material printable, steps can be added into the computer vision – machine learning optimization framework to incorporate the effect of the various rheological parameters extracted from the food ink in selecting printing parameters. Furthermore, developing an algorithm that can adapt the print parameters in real-time, such as extrusion pressure, flow rate, nozzle movement speed, and temperature, based on real-time observations of the printing process, would further increase the success rate. This real-time adjustment would make the overall process easier to scale up and facilitate further research, focusing on novel food formulations with enhanced nutritive properties. However, this method can face several challenges, such as the effectiveness of the computer vision protocol. Indeed, the contour of the 3D printed objects may not be as neat and well-defined as obtained with the traditional fused deposition modeling, thus hardening the accurate detection.

5.5 AI-guided post-processing and quality control of 3D printed food

5.5.1 Post-processing

Post-processing is a critical step in food production that ensures food products' safety, quality, and sensory attributes. Effective post-processing can extend shelf life, enhance flavor, and maintain nutritional value, making it an important component in the food production chain. Post-processing measures are essential to prevent microbial contamination and spoilage, thereby protecting consumer health (Fellows, 2022). In 3D food printing, post-processing step presents even more significance. Food printing often requires additional steps to ensure the printed food is safe to consume and meets quality standards. Indeed, most 3D printed foods are not directly edible and require additional post-processing steps. Various post-processing methods are available and depend on the targeted application and needs. These methods include microwaving, baking, frying, drying, air frying, steaming, or even freeze-drying (Wen et al., 2024). Techniques such as microwaving (Keerthana et al., 2020; Pulatsu et al., 2022), baking

(Guénard-Lampron et al., 2021; Zhang et al., 2018), and drying (Klar et al., 2019) have been shown to impact the final food product. Thus, it is important to enhance the control over this step. These steps can help stabilize the structure of printed foods, making them more palatable and visually appealing by producing, for example, browning of the food (Kewuyemi et al., 2022).

Integrating artificial intelligence in the food industry has revolutionized traditional methods, particularly in post-processing stages. In baking, AI technologies, such as machine vision, enhance inspection and quality control. A computer vision system has been employed to evaluate the browning property of cheddar and mozzarella cheeses, with the browning factor serving as an index for cheese browning. This method provided non-contact, continuous measurement, overcoming limitations related to cheese's temperature, size, and shape, and was more efficient than conventional colorimeters for surfaces with uneven color distributions (Wang & Sun, 2003). In addition, Abdanan Mehdizadeh (2022) illustrated the application of a machine vision-based intelligent oven designed for the baking inspection of cupcakes. This system not only automates the inspection process but also ensures uniformity in baking, identifying defects that human inspectors might miss (Abdanan Mehdizadeh, 2022).

5.5.2 Enhanced quality control using AI

Quality control in food processing is a critical step that ensures the safety, quality, and consistency of food products presented to the customers. By implementing rigorous quality control measures, food processing facilities can detect and mitigate potential hazards, adhere to regulatory standards, and meet consumer expectations. Quality control processes include a variety of checks and balances, such as raw material inspection, in-process monitoring, and final product evaluation, all aimed at maintaining high standards of hygiene, nutrition, and taste. In this section, we will only discuss the quality control of the final food product.

Several AI tools are already used for food quality control. Tools such as computer vision and electronic noses have frequently been used to assess properties such as color or microbial contamination (Falasconi et al., 2012; Wu & Sun, 2013). Further developments have been pursued to analyze specific food-related parameters. For example, Ma and co-authors reported using computer vision techniques to evaluate

the fibrousness of meat analogs. They also point out that the results obtained from the automated analysis strongly correlate with those obtained from a trained panel, pinpointing the efficiency of their method and its interest in further application in food manufacturing (Ma, Schlangen, et al., 2023). This analysis method presents significant interest in 3D food printing, particularly in developing novel plant-based foods.

5.6 Conclusion and outlook

Integrating AI technology into the 3D food printing process offers many advantages that can revolutionize the food industry. AI-driven food ink development enables the precise targeting of specific nutritional values, facilitating personalized nutrition to meet individual dietary needs and preferences. This not only enhances the nutritional properties of food products but also supports broader health and wellness initiatives. By analyzing vast datasets related to nutrition and user preferences, AI can formulate food inks that are both nutritious and appealing, promoting better health and an enhanced eating experience. Moreover, the AI-driven ink formulation development can be applied to prepare food inks with the required rheological properties to ensure a smooth printing process.

Furthermore, with the recent advancements in natural language processing, where humans and machines directly interact through text, the G-code preparation for 3D food printing could also be simplified for the design and customization stage. Users could input simple text commands detailing the object design properties, limitations, and all their customization requirements to generate even more complex printing instructions, which would make the technology more accessible and user-friendly. During the 3D food printing process, AI can also enable real-time monitoring and enhanced control and optimize each step for quality and consistency. Future advancements suggest that 3D food printers could automatically adjust settings based on real-time computer vision monitoring and automated printed dimensions measurements. This would enhance printing precision and efficiency, thus allowing printers to adapt instantly to varying conditions and ensuring the highest quality output while minimizing waste and experimental trials.

Another promising thought development is the automatic selection of printing parameters based on the rheological properties of the food ink. AI systems could

determine optimal printing conditions by inputting data about viscosity, flow properties, and viscoelasticity of printing inks. This development would be particularly important for research and development, where precise control over the process is important for experimenting with new materials and formulations. Indeed, an automated parameter selection would enable researchers to focus on innovation rather than machine calibration, accelerating the development of new food products and improving the scalability of 3D food printing technologies.

Additionally, integrating computer vision monitoring, sensors like electronic noses, and automated analysis in the 3D printed food production chain ensures that final products meet quality control, nutritional, aesthetic, and dimensional standards. This combination is essential for achieving consumer satisfaction and complying with regulatory requirements.

Combining all the discussed aspects is viewed to be valuable in improving the 3D food printing process and its upscaling ability. Moreover, automation could also enhance the overall flow of the process. An interesting example is the work carried out by Gongora and co-authors. In their work, they developed an automated 3D printing and analysis system using a programmed robotic arm and a fleet of 3D printers (Gongora et al., 2020). Adding similar automation would greatly benefit the 3D food printing process and enhance overall production by reducing the need for human interaction. An ideal overall flowchart of the future of 3D food printing combining the ideas presented in this work is presented in Figure 5.8.

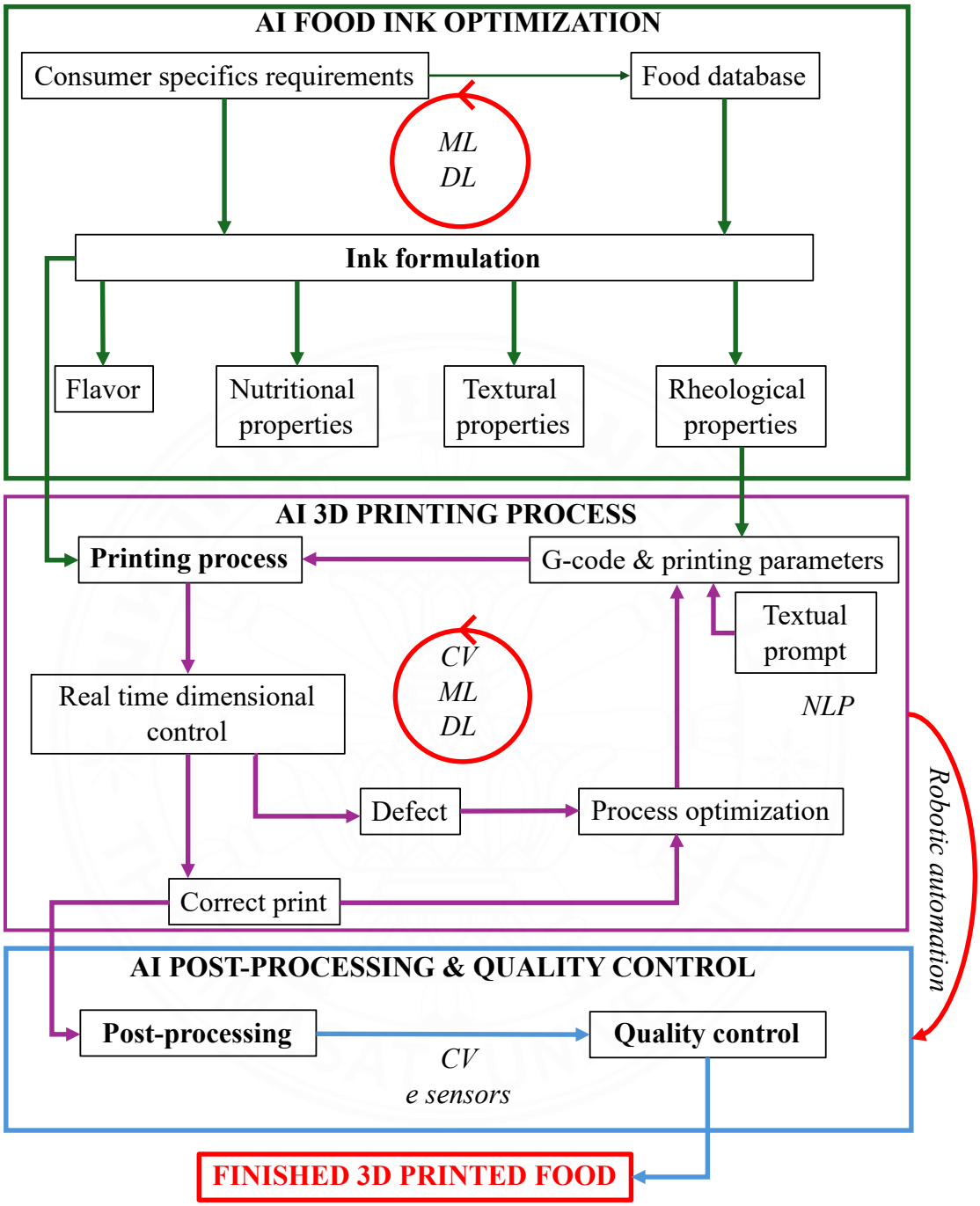

Figure 5.8 Flowchart of the future AI-3D food printing process.

Overall, the synergy between AI and 3D food printing holds transformative potential. It promises to enhance customization, efficiency, and quality in food production, paving the way for innovative culinary experiences, the use of novel food ingredients, and healthier eating options. As these technologies evolve, they likely help

to address global food security challenges, improve public health, and change consumption habits. Continuous research and development in this field will be crucial in realizing these benefits, ensuring that AI-driven 3D food printing reaches its full potential.

CHAPTER 6
CONCLUSION

6.1 Summary of findings

As detailed in the literature review, the success of the 3D food printing process is strongly correlated with the rheological properties of the food ink used. Several parameters are presented as important in determining the success of the process. Based on the detailed analysis of the existing literature, the ink must be extrudable, i.e., its yield stress should be lower than the maximal pressure applied by the printer. Moreover, the ink should exhibit shear-thinning to facilitate the extrusion. The rheological properties of the ink also impact the stability of the 3D printed object, and a specific range of viscoelastic properties, represented by $\tan\delta \leq 0.268$ and $G' \geq 300$ Pa, has been proposed. Given the effect of temperature on rheological behavior, thermal properties are also vital for optimizing process temperature settings. Additional parameters, such as the die swell and the extensional flow, are relevant, but limited research is available. This study presents a more profound outlook on the rheology-printability relationship by looking at the effect of rheology during the object's formation. Moreover, with the rise of AI technology and the challenges posed by the 3D food printing process upscaling, the applicability of AI tools is discussed to present solutions for process control and making real-time formulation adjustments, ultimately improving scalability.

6.1.1 Machine learning assisted evaluation of the filament spreading during extrusion-based 3D food printing: impact of the rheological and printing parameters

The first study developed in this thesis highlights the relationship between the food ink spreading upon deposition and process and rheological parameters. Rheological parameters, including viscosity and complex modulus, significantly impacted the spreading ratio. More robust viscoelastic behavior resulted in reduced spreading but also raised difficulties with extrudability, requiring increased extrusion pressure. The study also demonstrated that increasing pressure yielded a higher flow

rate and spreading ratio, while higher printing speeds reduced spreading due to filament thinning. Excessive speeds caused filament instability and rupture. These findings stress the intricate balance between process parameters and ink properties for accurate dimensional control. By incorporating machine learning, the study confirmed that rheological properties predominantly influence filament spreading. Using four features, the Extra Trees Regressor model attributed 92% importance to these properties. This combination of experimental and predictive analysis provided a comprehensive framework for precise ink deposition, contributing to advancements in 3D food printing and fostering innovation in future food fabrication.

6.1.2 3D printing of protein-rich plant-based snacks: viscoelasticity and non-linear rheology machine learning based quality control and post-processing

After studying the layer-wise dimensional accuracy, the second study developed in this thesis focuses on the dimensional accuracy and stability of 3D printed protein-rich plant-based snacks. It highlights the critical role of rheology and post-processing in the final food product. Through complete rheological testing, variations in biopolymer content were shown to significantly influence the ink's properties, printing, and baking behavior. Baking affected the final shape, with lower biopolymer content formulations showing material bursting, while higher content formulations displayed improved shape retention. The results confirmed that higher concentrations of mung bean protein and pectin promoted more robust solid-like behavior, improving printed structures' dimensional accuracy and stability. These formulations are considered strong candidates for further development of 3D printed snacks. A machine learning-based quality control model also presented the importance of rheological parameters such as G_0^* and T in classifying ink printability. The insights developed from this study are crucial for optimizing ink formulations and processing conditions to achieve high-quality 3D printed foods. The combination of rheological analysis, machine learning quality control, and baking provides a comprehensive approach to improving the development of printed snacks.

6.1.3 Artificial intelligence assisted 3D food printing

Lastly, the integration of AI technology in the 3D food printing process and how it could transform the food industry are discussed in this thesis. Three main aspects are presented: AI-driven food ink development, AI 3D food printing process optimization, and AI-enhanced quality control and post-processing. AI-driven food ink development allows for precise targeting of specific nutritional values. By analyzing large datasets on nutrition and consumer preferences, food inks that are nutritious and appealing could be developed, enhancing health and promoting personalized nutrition. Additionally, AI could be applied to ensure that food inks possess the required rheological properties for the printing process. During the 3D printing process, AI could enable real-time monitoring and optimize each step to yield printed objects with acceptable quality. Future-developed 3D food printers could automatically adjust their settings based on real-time process data analysis to improve efficiency. Moreover, AI could facilitate the automatic selection of printing parameters based on the food ink's rheological properties. The detailed synergy between AI and 3D food printing holds great potential for enhancing the overall 3D food printing process customization, efficiency, and scalability.

6.2 Recommendation for future studies

As outlined in this thesis, 3D food printing holds great significance in shaping the future of food production for various consumer groups and incorporating novel ingredients. The rheological properties of the food ink are the central component of the process's success. While the overall knowledge is progressing, several challenges remain. First, rheological studies need to be extended to include the effect of extensional flow or non-linear properties. Studies focusing on these parameters remain currently limited. Complex multi-component inks can be developed by deepening the knowledge of the required rheological properties at each step of the process, thereby enhancing nutritional and hedonic properties. As additionally discussed in this thesis, process conditions influence the accuracy of the 3D printed object. Future efforts should focus on hardware advancements, particularly developing a 3D food printer with extensive control of the process parameters. Further development is needed to integrate AI more effectively into the 3D food printing process, greatly enhancing its scalability.

Computer vision algorithms with cameras embedded in the 3D food printer would be beneficial to improve real-time process monitoring. Still, improvements on the detection accuracy threshold are necessary to avoid over- or underestimating the printed dimensions. Finally, future studies should also evaluate the impact of post-processing methods on 3D printed objects, as post-processing is a critical step that ensures the quality and properties of the final 3D printed food.

REFERENCES

3D Control Systems. (2024). *3D Printing Spaghetti Detector and Failure Detection*. https://www.3dprinteros.com/3d-printing-spaghetti-failure-detection

Abadi, M., Barham, P., Chen, J., Chen, Z., Davis, A., Dean, J., Devin, M., Ghemawat, S., Irving, G., Isard, M., Kudlur, M., Levenberg, J., Monga, R., Moore, S., Murray, D. G., Steiner, B., Tucker, P., Vasudevan, V., Warden, P., Wicke, M., Yu, Y., & Zheng, X. (2016). Large-scale machine learning on heterogeneous distributed systems. *Proceedings of the 12th USENIX Symposium on Operating Systems Design and Implementation (OSDI'16)*, 265-283, Savannah, GA, USA.

Abdanan Mehdizadeh, S. (2022). Machine vision based intelligent oven for baking inspection of cupcake: Design and implementation. *Mechatronics*, *82*, 102746.

Addanki, M., Patra, P., & Kandra, P. (2022). Recent advances and applications of artificial intelligence and related technologies in the food industry. *Applied Food Research*, *2*(2), 100126.

Agarwal, T., Costantini, M., & Maiti, T. K. (2021). Extrusion 3D printing with Pectin-based ink formulations: Recent trends in tissue engineering and food manufacturing. *Biomedical Engineering Advances*, *2*, 100018.

Ahlinder, A., Höglund, E., Öhgren, C., Miljkovic, A., & Stading, M. (2023). Towards attractive texture modified foods with increased fiber content for dysphagia via 3D printing and 3D scanning. *Frontiers in Food Science and Technology*, *2*, 1058641.

Ahmadzadeh, S., Clary, T., Rosales, A., & Ubeyitogullari, A. (2024). Upcycling imperfect broccoli and carrots into healthy snacks using an innovative 3D food printing approach. *Food Science & Nutrition*, *12*(1), 84-93.

Ahmadzadeh, S., Lenie, M. D. R., Mirmahdi, R. S., & Ubeyitogullari, A. (2023). Designing future foods: Harnessing 3D food printing technology to encapsulate bioactive compounds. *Critical Reviews in Food Science and Nutrition*, 1-17.

Aho, J., Boetker, J. P., Baldursdottir, S., & Rantanen, J. (2015). Rheology as a tool for evaluation of melt processability of innovative dosage forms. *International journal of pharmaceutics*, *494*(2), 623-642.

Ainis, W. N., Feng, R., van den Berg, F. W. J., & Ahrné, L. (2023). Comparing the rheological and 3D printing behavior of pea and soy protein isolate pastes. *Innovative Food Science & Emerging Technologies*, *84*, 103307.

Al-Mahasneh, M. A., Rababah, T. M., & Ma'Abreh, A. S. (2013). Evaluating the Combined Effect of Temperature, Shear Rate and Water Content on Wild-Flower Honey Viscosity Using Adaptive Neural Fuzzy Inference System and Artificial Neural Networks. *Journal of Food Process Engineering*, *36*(4), 510-520.

Álvarez-Castillo, E., Oliveira, S., Bengoechea, C., Sousa, I., Raymundo, A., & Guerrero, A. (2021). A rheological approach to 3D printing of plasma protein based doughs. *Journal of Food Engineering*, *288*, 110255.

Armstrong, C. D., Yue, L., Deng, Y., & Qi, H. J. (2022). Enabling direct ink write edible 3D printing of food purees with cellulose nanocrystals. *Journal of Food Engineering*, *330*, 111086.

Ashraf, Z. u., Gani, A., Shah, A., & Gani, A. (2024). Techno-Functional Characterization of Pulse Proteins (Broad Bean, Mung Bean, and Lentil Bean) as Sustainable Plant-Based Meat and Dairy Alternatives. *ACS Food Science & Technology*.

Awad, A., Fina, F., Trenfield, S. J., Patel, P., Goyanes, A., Gaisford, S., & Basit, A. W. (2019). 3D Printed Pellets (Miniprintlets): A Novel, Multi-Drug, Controlled Release Platform Technology. *Pharmaceutics*, *11*(4), 148.

Azam, R. S. M., Zhang, M., Bhandari, B., & Yang, C. (2018). Effect of Different Gums on Features of 3D Printed Object Based on Vitamin-D Enriched Orange Concentrate. *Food Biophysics*, *13*(3), 250-262.

Bahramparvar, M., Salehi, F., & Razavi, S. M. A. (2014). Predicting Total Acceptance of Ice Cream Using Artificial Neural Network. *Journal of Food Processing and Preservation*, *38*(3), 1080-1088.

Baird, D. G., & Collias, D. I. (2014). *Polymer processing: principles and design*. John Wiley & Sons.

BambuLab. (2024). *Bambu Lab X1 Series*. https://bambulab.com/en/x1

Bareen, M. A., Joshi, S., Sahu, J. K., Prakash, S., & Bhandari, B. (2021). Assessment of 3D printability of heat acid coagulated milk semi-solids ‘soft cheese’ by

correlating rheological, microstructural, and textural properties. *Journal of Food Engineering*, *300*, 110506.

Barnes, H. A. (2000). *A handbook of elementary rheology*. University of Wales, Institute of Non-Newtonian Fluid Mechanics.

Becker, D., Schmitt, C., Bovetto, L., Rauh, C., McHardy, C., & Hartmann, C. (2023). Optimization of complex food formulations using robotics and active learning. *Innovative Food Science & Emerging Technologies*, *83*, 103232.

Berman, B. (2012). 3-D printing: The new industrial revolution. *Business Horizons*, *55*(2), 155-162.

Bi, K., Zhang, D., Qiu, T., & Huang, Y. (2019). GC-MS Fingerprints Profiling Using Machine Learning Models for Food Flavor Prediction. *Processes*, *8*(1), 23.

Brion, D. A. J., & Pattinson, S. W. (2022). Generalisable 3D printing error detection and correction via multi-head neural networks. *Nature Communications*, *13*(1), 4654.

Buswell, R. A., Leal de Silva, W. R., Jones, S. Z., & Dirrenberger, J. (2018). 3D printing using concrete extrusion: A roadmap for research. *Cement and Concrete Research*, *112*, 37-49.

Cai, Q., Zhong, Y., Xu, M., Huang, Q., & Lu, X. (2022). 3D printed high oil custard cream: Effects of whey protein isolate, hydroxypropylated starch and carrageenan on physicochemical properties and printing performance. *Lwt*, *156*, 113039.

Chan, S. Y., Choo, W. S., Young, D. J., & Loh, X. J. (2017). Pectin as a rheology modifier: Origin, structure, commercial production and rheology. *Carbohydrate Polymers*, *161*, 118-139.

Chang, Y. T., Hsueh, M. C., Hung, S. P., Lu, J. M., Peng, J. H., & Chen, S. F. (2021). Prediction of specialty coffee flavors based on near-infrared spectra using machine- and deep-learning methods. *Journal of the Science of Food and Agriculture*, *101*(11), 4705-4714.

Chen, A., Wang, W., Mao, Z., He, Y., Chen, S., Liu, G., Su, J., Feng, P., Shi, Y., & Yan, C. (2023). Multimaterial 3D and 4D bioprinting of heterogenous constructs for tissue engineering. *Advanced Materials*, 2307686.

Chen, H., Xie, F., Chen, L., & Zheng, B. (2019). Effect of rheological properties of potato, rice and corn starches on their hot-extrusion 3D printing behaviors. *Journal of Food Engineering*, *244*, 150-158.

Chen, J., Mu, T., Goffin, D., Blecker, C., Richard, G., Richel, A., & Haubruge, E. (2019). Application of soy protein isolate and hydrocolloids based mixtures as promising food material in 3D food printing. *Journal of Food Engineering*, *261*, 76-86.

Chen, T., & Guestrin, C. (2016). Xgboost: A scalable tree boosting system. *Proceedings of the 22nd ACM SIGKDD International Conference on Knowledge Discovery and Data Mining (KDD'16)*, 785-794, New York, New York, USA.

Chen, Y., Zhang, M., & Bhandari, B. (2021). 3D Printing of Steak-like Foods Based on Textured Soybean Protein. *Foods*, *10*(9), 2011.

Chen, Y., Zhang, M., Sun, Y., & Phuhongsung, P. (2022). Improving 3D/4D printing characteristics of natural food gels by novel additives: A review. *Food Hydrocolloids*, *123*, 107160.

Cheng, Y., Fu, Y., Ma, L., Yap, P. L., Losic, D., Wang, H., & Zhang, Y. (2022). Rheology of edible food inks from 2D/3D/4D printing, and its role in future 5D/6D printing. *Food Hydrocolloids*, *132* 107855.

Cheng, Y., Wang, B., Lv, W., Zhong, Y., & Li, G. (2024). Effect of xanthan gum on physicochemical properties and 3D printability of emulsion-filled starch gels. *Food Hydrocolloids*, *149*, 109613.

Chow, C. Y., Thybo, C. D., Sager, V. F., Riantiningtyas, R. R., Bredie, W. L. P., & Ahrné, L. (2021). Printability, stability and sensory properties of protein-enriched 3D-printed lemon mousse for personalised in-between meals. *Food Hydrocolloids*, *120*, 106943.

Corker, A., Ng, H. C., Poole, R. J., & Garcia-Tunon, E. (2019). 3D printing with 2D colloids: designing rheology protocols to predict 'printability' of soft-materials. *Soft Matter*, *15*(6), 1444-1456.

Creality. (2024). *K1C*. https://www.creality.com/products/k1c-carbon-3d-printer

Dahl, J. F., Gregersen, S. B., Andersen, U., Schulz, H.-J., & Corredig, M. (2024). Small and large deformation rheology on pizza cheese as an example of application to

study anisotropic properties of food soft materials. *Food Hydrocolloids*, *148*, 109456.

Dalal, N., & Triggs, B. (2005). Histograms of oriented gradients for human detection. *2005 IEEE Computer Society Conference on Computer Vision and Pattern Recognition (CVPR'05)*, 886-893, San Diego, CA, USA.

Das, A., Gilmer, E. L., Biria, S., & Bortner, M. J. (2021). Importance of Polymer Rheology on Material Extrusion Additive Manufacturing: Correlating Process Physics to Print Properties. *ACS Applied Polymer Materials*, *3*(3), 1218-1249.

Derossi, A., Caporizzi, R., Azzollini, D., & Severini, C. (2018). Application of 3D printing for customized food. A case on the development of a fruit-based snack for children. *Journal of Food Engineering*, *220*, 65-75.

Derossi, A., Caporizzi, R., Paolillo, M., Oral, M. O., & Severini, C. (2021). Drawing the scientific landscape of 3D Food Printing. Maps and interpretation of the global information in the first 13 years of detailed experiments, from 2007 to 2020. *Innovative Food Science & Emerging Technologies*, *70*, 102689.

Derossi, A., Caporizzi, R., Ricci, I., & Severini, C. (2019). Critical variables in 3D food printing. In *Fundamentals of 3D food printing and applications* (pp. 41-91). Elsevier.

Dhillon, A., & Verma, G. K. (2019). Convolutional neural network: a review of models, methodologies and applications to object detection. *Progress in Artificial Intelligence*, *9*(2), 85-112.

Dick, A., Bhandari, B., & Prakash, S. (2021). Printability and textural assessment of modified-texture cooked beef pastes for dysphagia patients. *Future Foods*, *3*, 100006.

Du, M., Xie, J., Gong, B., Xu, X., Tang, W., Li, X., Li, C., & Xie, M. (2018). Extraction, physicochemical characteristics and functional properties of Mung bean protein. *Food Hydrocolloids*, *76*, 131-140.

Duty, C., Ajinjeru, C., Kishore, V., Compton, B., Hmeidat, N., Chen, X., Liu, P., Hassen, A. A., Lindahl, J., & Kunc, V. (2018). What makes a material printable? A viscoelastic model for extrusion-based 3D printing of polymers. *Journal of Manufacturing Processes*, *35*, 526-537.

Enfield, R. E., Pandya, J. K., Lu, J., McClements, D. J., & Kinchla, A. J. (2022). The future of 3D food printing: Opportunities for space applications. *Critical Reviews in Food Science and Nutrition*, *63*(29) 1-14.

Escalante-Aburto, A., Trujillo-de Santiago, G., Álvarez, M. M., & Chuck-Hernández, C. (2021). Advances and prospective applications of 3D food printing for health improvement and personalized nutrition. *Comprehensive Reviews in Food Science and Food Safety*, *20*(6), 5722-5741.

Ewoldt, R. H., Hosoi, A., & McKinley, G. H. (2008). New measures for characterizing nonlinear viscoelasticity in large amplitude oscillatory shear. *Journal of Rheology*, *52*(6), 1427-1458.

Ewoldt, R. H., & Saengow, C. (2022). Designing complex fluids. *Annual Review of Fluid Mechanics*, *54*(1), 413-441.

Ewoldt, R. H., Winter, P., Maxey, J., & McKinley, G. H. (2010). Large amplitude oscillatory shear of pseudoplastic and elastoviscoplastic materials. *Rheologica acta*, *49*, 191-212.

Fahmy, A. R., Amann, L. S., Dunkel, A., Frank, O., Dawid, C., Hofmann, T., Becker, T., & Jekle, M. (2021). Sensory design in food 3D printing – Structuring, texture modulation, taste localization, and thermal stabilization. *Innovative Food Science & Emerging Technologies*, *72*, 102743.

Fahmy, A. R., Becker, T., & Jekle, M. (2020). 3D printing and additive manufacturing of cereal-based materials: Quality analysis of starch-based systems using a camera-based morphological approach. *Innovative Food Science & Emerging Technologies*, *63*, 102384.

Fahmy, A. R., Derossi, A., & Jekle, M. (2023) Four-Dimensional (4D) Printing of dynamic foods - Definitions, considerations, and current scientific status. *Foods, 12*, 3410.

Falasconi, M., Concina, I., Gobbi, E., Sberveglieri, V., Pulvirenti, A., & Sberveglieri, G. (2012). Electronic Nose for Microbiological Quality Control of Food Products. *International Journal of Electrochemistry*, *2012*, 1-12.

Fellows, P. J. (2022). *Food processing technology: principles and practice*. Woodhead publishing.

Feng, C., Zhang, M., Bhandari, B., Wang, Y., & Wang, B. (2020). Improvement of 3D printing properties of rose-sodium alginate heterogeneous gel by adjusting rose material. *Journal of Food Process Engineering*, *44*(1), e13583.

Feng, C., Zhang, M., Liu, Z., Mujumdar, A., Wang, Y., & Chang, L. (2020). Effect of drying method on post-processing stability and quality of 3D printed rose-yam paste. *Drying Technology*, *39*(9), 1196-1204.

Fenton, T., Gholamipour-Shirazi, A., Daffner, K., Mills, T., & Pelan, E. (2021). Formulation and additive manufacturing of polysaccharide-surfactant hybrid gels as gelatin analogues in food applications. *Food Hydrocolloids*, *120*, 106881.

FoodJet. (2022). *Our solutions*. https://www.foodjet.com/our-solutions

Freire, P., Freire, D., & Licon, C. C. (2024). A comprehensive review of machine learning and its application to dairy products. *Critical Reviews in Food Science and Nutrition*, 1-16.

Fribus, R., Kant, J., Fahmy, A. R., & Jekle, M. (2024). Texture modulation of starch-based materials using microfoaming-assisted 3D printing. *Future Foods*, *9*, 100311.

Friedrich, L., & Begley, M. (2020). Changes in Filament Microstructures During Direct Ink Writing with a Yield Stress Fluid Support. *ACS Applied Polymer Materials*, *2*(7), 2528-2540.

Fröhlich-Wyder, M.-T., Bachmann, H.-P., & Schmidt, R. S. (2023). Classification of cheese varieties from Switzerland using machine learning methods: Free volatile carboxylic acids. *Lwt*, *184*, 115095.

Fu, Z., Naghieh, S., Xu, C., Wang, C., Sun, W., & Chen, X. (2021). Printability in extrusion bioprinting. *Biofabrication*, *13*(3), 033001.

Furet, B., Poullain, P., & Garnier, S. (2019). 3D printing for construction based on a complex wall of polymer-foam and concrete. *Additive Manufacturing*, *28*, 58-64.

García-Segovia, P., García-Alcaraz, V., Balasch-Parisi, S., & Martínez-Monzó, J. (2020). 3D printing of gels based on xanthan/konjac gums. *Innovative Food Science & Emerging Technologies*, *64*, 102343.

Ghazal, A. F., Zhang, M., Mujumdar, A. S., & Ghamry, M. (2023). Progress in 4D/5D/6D printing of foods: Applications and R&D opportunities. *Critical Reviews in Food Science and Nutrition, 63(25)*, 7399-7422.

Ghidini, T., Pambaguian, L., & Blair, S. (2015). Joining the third industrial revolution: 3D printing for space. *European Space Agency Bulletin*, *2015*(163), 24-33.

Gholamipour-Shirazi, A., Norton, I. T., & Mills, T. (2019). Designing hydrocolloid based food-ink formulations for extrusion 3D printing. *Food Hydrocolloids*, *95*, 161-167.

Gongora, A. E., Xu, B., Perry, W., Okoye, C., Riley, P., Reyes, K. G., Morgan, E. F., & Brown, K. A. (2020). A Bayesian experimental autonomous researcher for mechanical design. *Science advances*, *6*(15), eaaz1708.

Guénard-Lampron, V., Masson, M., Leichtnam, O., & Blumenthal, D. (2021). Impact of 3D printing and post-processing parameters on shape, texture and microstructure of carrot appetizer cake. *Innovative Food Science & Emerging Technologies*, *72*, 102738.

Guha, P., Bhatnagar, T., Pal, I., Kamboj, U., & Mishra, S. (2017). Prediction of properties of wheat dough using intelligent deep belief networks. *Journal of Experimental & Theoretical Artificial Intelligence*, *29*(6), 1283-1296.

Guo, C., Zhang, M., & Devahastin, S. (2021). Improvement of 3D printability of buckwheat starch-pectin system via synergistic Ca2+-microwave pretreatment. *Food Hydrocolloids*, *113*, 106483.

Hashemi, N. S., Aghdam, R. B., Ghiasi, A. S. B., & Fatemi, P. (2016). Template matching advances and applications in image analysis. *arXiv preprint arXiv:1610.07231*.

He, Y., Yang, F., Zhao, H., Gao, Q., Xia, B., & Fu, J. (2016). Research on the printability of hydrogels in 3D bioprinting. *Scientific Reports*, *6*(1), 29977.

Heckl, M. P., Korber, M., Jekle, M., & Becker, T. (2023). Relation between deformation and relaxation of hydrocolloids-starch based bio-inks and 3D printing accuracy. *Food Hydrocolloids*, *137*, 108326.

Holland, S., Foster, T., MacNaughtan, W., & Tuck, C. (2018). Design and characterisation of food grade powders and inks for microstructure control using 3D printing. *Journal of Food Engineering*, *220*, 12-19.

Hooi Chuan Wong, G., Pant, A., Zhang, Y., Kai Chua, C., Hashimoto, M., Huei Leo, C., & Tan, U. X. (2022). 3D food printing– sustainability through food waste upcycling. *Materials Today: Proceedings*, *70*, 627-630.

Hu, Y., Cheng, L., Lee, S. J., & Yang, Z. (2023). Formation and characterisation of concentrated emulsion gels stabilised by faba bean protein isolate and its applications for 3D food printing. *Colloids and Surfaces A: Physicochemical and Engineering Aspects*, *671*, 131622.

Huang, M. s., Zhang, M., & Guo, C. f. (2020). 3D printability of brown rice gel modified by some food hydrocolloids. *Journal of Food Processing and Preservation*, *44*(7), e14502.

Huang, Z., Li, Y., Fan, M., Qian, H., & Wang, L. (2024). Recent advances in mung bean protein: From structure, function to application. *International Journal of Biological Macromolecules*, *273*, 133210.

Hussain, S., Arora, V. K., & Malakar, S. (2021). Formulation of protein-enriched 3D printable food matrix and evaluation of textural, rheological characteristics, and printing stability. *Journal of Food Processing and Preservation*, *45*(2), e15182.

Hussain, S., Malakar, S., & Arora, V. K. (2021). Extrusion-Based 3D Food Printing: Technological Approaches, Material Characteristics, Printing Stability, and Post-processing. *Food Engineering Reviews*, *14*(1), 100-119.

Hyun, K., Wilhelm, M., Klein, C. O., Cho, K. S., Nam, J. G., Ahn, K. H., Lee, S. J., Ewoldt, R. H., & McKinley, G. H. (2011). A review of nonlinear oscillatory shear tests: Analysis and application of large amplitude oscillatory shear (LAOS). *Progress in Polymer Science*, *36*(12), 1697-1753.

In, J., Jeong, H., Song, S., & Min, S. C. (2021). Determination of Material Requirements for 3D Gel Food Printing Using a Fused Deposition Modeling 3D Printer. *Foods*, *10*(10), 2272.

Inoue, I., Hanasaki, I., Suetsugu, D., & Kudo, T. (2023). Drawing 3D fluid patterns in beverages using a robotic nozzle. *Journal of Food Engineering*, *357*, 111555.

Jagadiswaran, B., Alagarasan, V., Palanivelu, P., Theagarajan, R., Moses, J. A., & Anandharamakrishnan, C. (2021). Valorization of food industry waste and by-products using 3D printing: A study on the development of value-added functional cookies. *Future Foods*, *4*, 100036.

Jeong, S., Kim, H., & Lee, S. (2021). Rheology-Based Classification of Foods for the Elderly by Machine Learning Analysis. *Applied Sciences*, *11*(5), 2262.

Ji, H., Pu, D., Yan, W., Zhang, Q., Zuo, M., & Zhang, Y. (2023). Recent advances and application of machine learning in food flavor prediction and regulation. *Trends in Food Science & Technology*, *138*, 738-751.

Jiang, Q., Zhang, M., & Mujumdar, A. S. (2021). Novel evaluation technology for the demand characteristics of 3D food printing materials: a review. *Critical Reviews in Food Science and Nutrition*, *62*(17), 4669-4683.

Jonkers, N., van Dommelen, J. A. W., & Geers, M. G. D. (2022). Selective Laser Sintered food: A unit cell approach to design mechanical properties. *Journal of Food Engineering*, *335*, 111183.

Kadival, A., Kour, M., Meena, D., & Mitra, J. (2022). Extrusion-Based 3D Food Printing: Printability Assessment and Improvement Techniques. *Food and Bioprocess Technology*, *16*(5), 987-1008.

Kamkar, M., Salehiyan, R., Goudoulas, T. B., Abbasi, M., Saengow, C., Erfanian, E., Sadeghi, S., Natale, G., Rogers, S. A., Giacomin, A. J., & Sundararaj, U. (2022). Large amplitude oscillatory shear flow: Microstructural assessment of polymeric systems. *Progress in Polymer Science*, *132*, 101580.

Kamlow, M.-A., Vadodaria, S., Gholamipour-Shirazi, A., Spyropoulos, F., & Mills, T. (2021). 3D printing of edible hydrogels containing thiamine and their comparison to cast gels. *Food Hydrocolloids*, *116*, 106550.

Ke, G., Meng, Q., Finley, T., Wang, T., Chen, W., Ma, W., Ye, Q., & Liu, T.-Y. (2017). Lightgbm: A highly efficient gradient boosting decision tree. *Advances in neural information processing systems*, *30*.

Keerthana, K., Anukiruthika, T., Moses, J. A., & Anandharamakrishnan, C. (2020). Development of fiber-enriched 3D printed snacks from alternative foods: A study on button mushroom. *Journal of Food Engineering*, *287*, 110116.

Kewuyemi, Y. O., Kesa, H., Meijboom, R., Alimi, O. A., & Adebo, O. A. (2022). 3D food printing improves color profile and structural properties of the derived novel whole-grain sourdough and malt biscuits. *Scientific Reports*, *12*(1), 12347.

Khan, M. F., Alam, A., Siddiqui, M. A., Alam, M. S., Rafat, Y., Salik, N., & Al-Saidan, I. (2021). Real-time defect detection in 3D printing using machine learning. *Materials Today: Proceedings*, *42*, 521-528.

Kim, H. B., Kim, S. W., Ko, J. B., Yang, Y. J., Oh, G. Y., Kim, Y. W., & Kim, H. C. (2021). Optimization of extrusion process for 3D hard candy manufacture. *Journal of Manufacturing Processes*, *71*, 580-588.

Kim, H. W., Bae, H., & Park, H. J. (2017). Classification of the printability of selected food for 3D printing: Development of an assessment method using hydrocolloids as reference material. *Journal of Food Engineering*, *215*, 23-32.

Kim, H. W., Lee, J. H., Park, S. M., Lee, M. H., Lee, I. W., Doh, H. S., & Park, H. J. (2018). Effect of Hydrocolloids on Rheological Properties and Printability of Vegetable Inks for 3D Food Printing. *Journal of Food Science*, *83*(12), 2923-2932.

Kim, H. W., & Rhee, M. S. (2020). Space food and bacterial infections: Realities of the risk and role of science. *Trends in Food Science & Technology*, *106*, 275-287.

Kim, S. M., Wen, Y., Kim, H. W., & Park, H. J. (2022). Textural and sensory qualities of low-calorie surimi with carrageenan inserted as a protein substitute using coaxial extrusion 3D food printing. *Journal of Food Engineering*, *333*.

Kim, S. M., Woo, J. H., Kim, H. W., & Park, H. J. (2022). Formulation and evaluation of cold-extruded chocolate ganache for three-dimensional food printing. *Journal of Food Engineering*, *314*, 111141.

Klar, V., Pere, J., Turpeinen, T., Karki, P., Orelma, H., & Kuosmanen, P. (2019). Shape fidelity and structure of 3D printed high consistency nanocellulose. *Scientific Reports*, *9*(1), 3822.

Kulinowski, P., Malczewski, P., Pesta, E., Łaszcz, M., Mendyk, A., Polak, S., & Dorożyński, P. (2021). Selective laser sintering (SLS) technique for pharmaceutical applications—Development of high dose controlled release printlets. *Additive Manufacturing*, *38*, 101761.

Lam, K.-L., Cheng, W.-Y., Su, Y., Li, X., Wu, X., Wong, K.-H., Kwan, H.-S., & Cheung, P. C.-K. (2020). Use of random forest analysis to quantify the importance of the structural characteristics of beta-glucans for prebiotic development. *Food Hydrocolloids*, *108*, 106001.

Lanaro, M., Desselle, M. R., & Woodruff, M. A. (2019). Chapter 6 - 3D Printing Chocolate: Properties of Formulations for Extrusion, Sintering, Binding and Ink Jetting. In F. C. Godoi, B. R. Bhandari, S. Prakash, & M. Zhang (Eds.), *Fundamentals of 3D Food Printing and Applications* (pp. 151-173). Academic Press.

Le Tohic, C., O'Sullivan, J. J., Drapala, K. P., Chartrin, V., Chan, T., Morrison, A. P., Kerry, J. P., & Kelly, A. L. (2018). Effect of 3D printing on the structure and textural properties of processed cheese. *Journal of Food Engineering*, *220*, 56-64.

Le-Bail, A., Maniglia, B. C., & Le-Bail, P. (2020). Recent advances and future perspective in additive manufacturing of foods based on 3D printing. *Current Opinion in Food Science*, *35*, 54-64.

LeCun, Y., Bengio, Y., & Hinton, G. (2015). Deep learning. *Nature*, *521*(7553), 436-444.

Lee, A. Y., Pant, A., Pojchanun, K., Lee, C. P., An, J., Hashimoto, M., Tan, U. X., Leo, C. H., Wong, G., Chua, C. K., & Zhang, Y. (2021). Three-Dimensional Printing of Food Foams Stabilized by Hydrocolloids for Hydration in Dysphagia. *International Journal of Bioprinting*, *7*(4), 393.

Li, M., Yu, P., Guo, Z., Liu, Y., & Zhao, J. (2023). High-resolution and programmable line-morphologies of material-extrusion 3D printed self-leveling inks. *Additive Manufacturing*, *71*, 103582.

Li, R., Jin, M., & Paquit, V. C. (2021). Geometrical defect detection for additive manufacturing with machine learning models. *Materials & Design*, *206*, 109726.

Lie-Piang, A., Garre, A., Nissink, T., van Beek, N., van der Padt, A., & Boom, R. (2023). Machine learning to quantify techno-functional properties - A case study for gel stiffness with pea ingredients. *Innovative Food Science & Emerging Technologies*, *83*, 103242.

Lille, M., Nurmela, A., Nordlund, E., Metsä-Kortelainen, S., & Sozer, N. (2018). Applicability of protein and fiber-rich food materials in extrusion-based 3D printing. *Journal of Food Engineering*, *220*, 20-27.

Liu, C., Law, A. C. C., Roberson, D., & Kong, Z. (2019). Image analysis-based closed loop quality control for additive manufacturing with fused filament fabrication. *Journal of Manufacturing Systems*, *51*, 75-86.

Liu, Y., Tang, T., Duan, S., Qin, Z., Li, C., Zhang, Z., Liu, A., Wu, D., Chen, H., Han, G., Lin, B., He, J., & Wu, W. (2020). Effects of sodium alginate and rice variety on the physicochemical characteristics and 3D printing feasibility of rice paste. *Lwt*, *127*, 109360.

Liu, Y., Yu, Y., Liu, C., Regenstein, J. M., Liu, X., & Zhou, P. (2019). Rheological and mechanical behavior of milk protein composite gel for extrusion-based 3D food printing. *Lwt*, *102*, 338-346.

Liu, Z., Bhandari, B., Guo, C., Zheng, W., Cao, S., Lu, H., Mo, H., & Li, H. (2021). 3D Printing of Shiitake Mushroom Incorporated with Gums as Dysphagia Diet. *Foods*, *10*(9), 2189.

Liu, Z., Bhandari, B., Prakash, S., Mantihal, S., & Zhang, M. (2019). Linking rheology and printability of a multicomponent gel system of carrageenan-xanthan-starch in extrusion based additive manufacturing. *Food Hydrocolloids*, *87*, 413-424.

Liu, Z., Chen, L., & Zheng, B. (2023). New insights into the effects of starch-oleic acid-chlorogenic acid interactions on structural formation by hot-extrusion 3D printing: From perspective of nonlinear rheology. *Food Hydrocolloids*, *144*, 109024.

Liu, Z., Dick, A., Prakash, S., Bhandari, B., & Zhang, M. (2020). Texture Modification of 3D Printed Air-Fried Potato Snack by Varying Its Internal Structure with the Potential to Reduce Oil Content. *Food and Bioprocess Technology*, *13*(3), 564-576.

Liu, Z., Xing, X., Mo, H., Xu, D., Hu, L., Li, H., & Chitrakar, B. (2023). 3D printed dysphagia diet designed from Hypsizygus marmoreus by-products with various polysaccharides. *Journal of Food Engineering*, *343*, 111395.

Liu, Z., Zhang, M., & Bhandari, B. (2018). Effect of gums on the rheological, microstructural and extrusion printing characteristics of mashed potatoes. *International Journal of Biological Macromolecules*, *117*, 1179-1187.

Liu, Z., Zhang, M., Bhandari, B., & Yang, C. (2018). Impact of rheological properties of mashed potatoes on 3D printing. *Journal of Food Engineering*, *220*, 76-82.

Lorenz, T., Iskandar, M. M., Baeghbali, V., Ngadi, M. O., & Kubow, S. (2022). 3D Food Printing Applications Related to Dysphagia: A Narrative Review. *Foods*, *11*(12), 1789.

Lu, Y., Rai, R., & Nitin, N. (2023). Image-based assessment and machine learning-enabled prediction of printability of polysaccharides-based food ink for 3D printing. *Food Research International*, *173*, 113384.

Lv, S., Li, H., Liu, Z., Cao, S., Yao, L., Zhu, Z., Hu, L., Xu, D., & Mo, H. (2024). Preparation of Pleurotus eryngii protein baked food by 3D printing. *Journal of Food Engineering*, *365*, 111845.

Ma, Y., Potappel, J., Chauhan, A., Schutyser, M. A. I., Boom, R. M., & Zhang, L. (2023). Improving 3D food printing performance using computer vision and feedforward nozzle motion control. *Journal of Food Engineering*, *339*, 111277.

Ma, Y., Potappel, J., Schutyser, M. A. I., Boom, R. M., & Zhang, L. (2023). Quantitative analysis of 3D food printing layer extrusion accuracy: Contextualizing automated image analysis with human evaluations: Quantifying 3D food printing accuracy. *Current Research in Food Science*, *6*, 100511.

Ma, Y., Schlangen, M., Potappel, J., Zhang, L., & van der Goot, A. J. (2023). Quantitative characterizations of visual fibrousness in meat analogues using automated image analysis. *Journal of Texture Studies*, *55*(1), e12806.

Ma, Y., Schutyser, M. A. I., Boom, R. M., & Zhang, L. (2021). Predicting the extrudability of complex food materials during 3D printing based on image analysis and gray-box data-driven modelling. *Innovative Food Science & Emerging Technologies*, *73*, 102764.

Mackay, M. E. (2018). The importance of rheological behavior in the additive manufacturing technique material extrusion. *Journal of Rheology*, *62*(6), 1549-1561.

Madsen, J., Sode, L., Dahl, J. F., Corredig, M., & Schulz, H. J. (2022, October). Visual Exploration of Rheological Test Results from Soft Materials. In *2022 First International Workshop on Visualization in Testing of Hardware, Software, and Manufacturing (TestVis)* (pp. 1-7). IEEE.

Mahesh, B. (2020). Machine Learning Algorithms - A Review. *International Journal of Science and Research (IJSR)*, *9*(1), 381-386.

Maldonado-Rosas, R., Tejada-Ortigoza, V., Cuan-Urquizo, E., Mendoza-Cachú, D., Morales-de la Peña, M., Alvarado-Orozco, J. M., & Campanella, O. H. (2022). Evaluation of rheology and printability of 3D printing nutritious food with complex formulations. *Additive Manufacturing*, *58*, 103030.

Malone, E., & Lipson, H. (2007). Fab@ Home: the personal desktop fabricator kit. *Rapid Prototyping Journal*, *13*(4), 245-255.

Mantihal, S., Prakash, S., & Bhandari, B. (2019). Textural modification of 3D printed dark chocolate by varying internal infill structure. *Food Research International*, *121*, 648-657.

Martinez, W. L., & Martinez, A. R. (2015). *Computational Statistics Handbook with MATLAB*. Chapman and Hall/CRC.

Men, H., Shi, Y., Fu, S., Jiao, Y., Qiao, Y., & Liu, J. (2017). Mining Feature of Data Fusion in the Classification of Beer Flavor Information Using E-Tongue and E-Nose. *Sensors (Basel)*, *17*(7), 1656.

Montoya, J., Medina, J., Molina, A., Gutiérrez, J., Rodríguez, B., & Marín, R. (2021). Impact of viscoelastic and structural properties from starch-mango and starch-arabinoxylans hydrocolloids in 3D food printing. *Additive Manufacturing*, *39*, 101891.

Morrison, F. A. (2001). *Understanding rheology* (Vol. 1). Oxford university press New York.

Muthurajan, M., Veeramani, A., Rahul, T., Gupta, R. K., Anukiruthika, T., Moses, J. A., & Anandharamakrishnan, C. (2021). Valorization of Food Industry Waste Streams Using 3D Food Printing: A Study on Noodles Prepared from Potato Peel Waste. *Food and Bioprocess Technology*, *14*(10), 1817-1834.

Nguyen, P. D., Nguyen, T. Q., Tao, Q. B., Vogel, F., & Nguyen-Xuan, H. (2022). A data-driven machine learning approach for the 3D printing process optimisation. *Virtual and Physical Prototyping*, *17*(4), 768-786.

Nijdam, J. J., LeCorre-Bordes, D., Delvart, A., & Schon, B. S. (2021). A rheological test to assess the ability of food inks to form dimensionally stable 3D food structures. *Journal of Food Engineering*, *291*, 110235.

Nnyigide, O. S., & Hyun, K. (2023). A comprehensive review of food rheology: analysis of experimental, computational, and machine learning techniques. *Korea-Australia Rheology Journal*, *35*(4), 279-306.

Obrist, M., Tu, Y., Yao, L., & Velasco, C. (2019). Space Food Experiences: Designing passenger's eating experiences for future space travel scenarios. *Frontiers in Computer Science*, *1*, 3.

Oliveira, S. M., Fasolin, L. H., Vicente, A. A., Fuciños, P., & Pastrana, L. M. (2020). Printability, microstructure, and flow dynamics of phase-separated edible 3D inks. *Food Hydrocolloids*, *109*, 106120.

Oppen, D., Attig, T., Weiss, J., & Krupitzer, C. (2023). Anticipating food structure of meat products from mastication physics applying machine learning. *Food Research International*, *174*, 113576.

Oral, M. O., Derossi, A., Caporizzi, R., & Severini, C. (2021). Analyzing the most promising innovations in food printing. Programmable food texture and 4D foods. *Future Foods*, *4*, 100093.

Ordukaya, E., & Karlik, B. (2016). Fruit juice–alcohol mixture analysis using machine learning and electronic nose. *IEEJ Transactions on Electrical and Electronic Engineering*, *11*, S171-S176.

Outrequin, T. C. R., Gamonpilas, C., Siriwatwechakul, W., & Sreearunothai, P. (2023). Extrusion-based 3D printing of food biopolymers: A highlight on the important rheological parameters to reach printability. *Journal of Food Engineering*, *342*, 111371.

Outrequin, T. C. R., Gamonpilas, C., Sreearunothai, P., Deepaisarn, S., & Siriwatwechakul, W. (2024). Machine learning assisted evaluation of the filament spreading during extrusion-based 3D food printing: Impact of the rheological and printing parameters. *Journal of Food Engineering*, *381*, 112166.

Oyinloye, T. M., & Yoon, W. B. (2021). Application of Computational Fluid Dynamics (CFD) Simulation for the Effective Design of Food 3D Printing (A Review). *Processes*, *9*(11), 1867.

Oyinloye, T. M., & Yoon, W. B. (2022). Investigation of flow field, die swelling, and residual stress in 3D printing of surimi paste using the finite element method. *Innovative Food Science & Emerging Technologies*, *78*, 103008.

Ozilgen, S., & Bucak, S. (2018). Functional biopolymers in food manufacturing. In *Biopolymers for food design* (pp. 157-189). Elsevier.

Pant, A., Lee, A. Y., Karyappa, R., Lee, C. P., An, J., Hashimoto, M., Tan, U. X., Wong, G., Chua, C. K., & Zhang, Y. (2021). 3D food printing of fresh vegetables using food hydrocolloids for dysphagic patients. *Food Hydrocolloids*, *114*, 106546.

Pant, A., Xin Ni, P. L., Chua, C. K., & Tan, U. X. (2022). Valorisation of vegetable food waste utilising three-dimensional food printing. *Virtual and Physical Prototyping*, *18*(1), e2146593.

Paraskevoudis, K., Karayannis, P., & Koumoulos, E. P. (2020). Real-time 3D printing remote defect detection (stringing) with computer vision and artificial intelligence. *Processes*, *8*(11), 1464.

Paszke, A., Gross, S., Massa, F., Lerer, A., Bradbury, J., Chanan, G., Killeen, T., Lin, Z., Gimelshein, N., & Antiga, L. (2019). Pytorch: An imperative style, high-performance deep learning library. *Advances in neural information processing systems*, *32*.

Paxton, N., Smolan, W., Böck, T., Melchels, F., Groll, J., & Jungst, T. (2017). Proposal to assess printability of bioinks for extrusion-based bioprinting and evaluation of rheological prope rties governing bioprintability. *Biofabrication*, *9*(4), 044107.

Pedregosa, F., Varoquaux, G., Gramfort, A., Michel, V., Thirion, B., Grisel, O., Blondel, M., Prettenhofer, P., Weiss, R., & Dubourg, V. (2011). Scikit-learn: Machine learning in Python. *the Journal of machine Learning research*, *12*, 2825-2830.

Petsiuk, A. L., & Pearce, J. M. (2020). Open source computer vision-based layer-wise 3D printing analysis. *Additive Manufacturing*, *36*, 101473.

Phuhongsung, P., Zhang, M., & Devahastin, S. (2020). Investigation on 3D printing ability of soybean protein isolate gels and correlations with their rheological and textural properties via LF-NMR spectroscopic characteristics. *Lwt*, *122*, 109019.

Pospischil, M., Specht, J., Konig, M., Horteis, M., Mohr, C., Clement, F., & Biro, D. (2014). Paste Rheology Correlating With Dispensed Finger Geometry. *IEEE Journal of Photovoltaics*, *4*(1), 498-503.

printpal.io. (2024). *3D Printing, simplified.* https://printpal.io/printwatch/

Pulatsu, E., Su, J.-W., Kenderes, S. M., Lin, J., Vardhanabhuti, B., & Lin, M. (2022). Restructuring cookie dough with 3D printing: Relationships between the mechanical properties, baking conditions, and structural changes. *Journal of Food Engineering*, *319*, 110911.

Pulli, K., Baksheev, A., Kornyakov, K., & Eruhimov, V. (2012). Real-time computer vision with OpenCV. *Communications of the ACM*, *55*(6), 61-69.

Qiang, W., & Zhongli, Z. (2011). Reinforcement learning model, algorithms and its application. *2011 International Conference on Mechatronic Science, Electric Engineering and Computer (MEC)*, 1143-1146, Jilin, China.

Qiu, L., Zhang, M., Adhikari, B., Lin, J., & Luo, Z. (2024). Preparation and characterization of 3D printed texture-modified food for the elderly using mung bean protein, rose powder, and flaxseed gum. *Journal of Food Engineering*, *361*, 111750.

Ramachandraiah, K. (2021). Potential Development of Sustainable 3D-Printed Meat Analogues: A Review. *Sustainability*, *13*(2), 938.

Rauzan, B. M., Nelson, A. Z., Lehman, S. E., Ewoldt, R. H., & Nuzzo, R. G. (2018). Particle-Free Emulsions for 3D Printing Elastomers. *Advanced Functional Materials*, *28*(21), 1707032.

Ray, S. (2019). A quick review of machine learning algorithms. *2019 International Conference on Machine Learning, Big Data, Cloud and Parallel Computing (COMITCon)*, 35-39, Faridabad, India.

Revo Foods. (2024). *The Filet*. https://shop-revo-foods.com/products/the-filet

Riantiningtyas, R. R., Sager, V. F., Chow, C. Y., Thybo, C. D., Bredie, W. L. P., & Ahrne, L. (2021). 3D printing of a high protein yoghurt-based gel: Effect of protein enrichment and gelatine on physical and sensory properties. *Food Research International*, *147*, 110517.

Roach, D. J., Rohskopf, A., Leguizamon, S., Appelhans, L., & Cook, A. W. (2023). Invertible neural networks for real-time control of extrusion additive manufacturing. *Additive Manufacturing*, *74*, 103742.

Roehm, K. D., & Madihally, S. V. (2017). Bioprinted chitosan-gelatin thermosensitive hydrogels using an inexpensive 3D printer. *Biofabrication*, *10*(1), 015002.

Saeidirad, M. H., Rohani, A., & Zarifneshat, S. (2013). Predictions of viscoelastic behavior of pomegranate using artificial neural network and Maxwell model. *Computers and Electronics in Agriculture*, *98*, 1-7.

Santos, M. S., Soares, J. P., Abreu, P. H., Araujo, H., & Santos, J. (2018). Cross-validation for imbalanced datasets: avoiding overoptimistic and overfitting approaches [research frontier]. *ieee ComputatioNal iNtelligeNCe magaziNe*, *13*(4), 59-76.

Schneider, C. A., Rasband, W. S., & Eliceiri, K. W. (2012). NIH Image to ImageJ: 25 years of image analysis. *Nature Methods*, *9*(7), 671-675.

Schreurs, M., Piampongsant, S., Roncoroni, M., Cool, L., Herrera-Malaver, B., Vanderaa, C., Thesseling, F. A., Kreft, L., Botzki, A., Malcorps, P., Daenen, L., Wenseleers, T., & Verstrepen, K. J. (2024). Predicting and improving complex beer flavor through machine learning. *Nature Communications*, *15*(1), 2368.

Schwab, A., Levato, R., D'Este, M., Piluso, S., Eglin, D., & Malda, J. (2020). Printability and shape fidelity of bioinks in 3D bioprinting. *Chemical reviews*, *120*(19), 11028-11055.

Seetapan, N., Raksa, P., Limparyoon, N., Srirajan, S., Makmoon, T., Israkarn, K., Gamonpilas, C., Methacanon, P., & Fuongfuchat, A. (2023). High moisture extrusion of meat analogues using mung bean (Vigna radiata L.) protein and flour blends: investigations on morphology, texture and rheology. *International Journal of Food Science & Technology*, *58*(4), 1922-1930.

Severini, C., & Derossi, A. (2016). Could the 3D Printing Technology be a Useful Strategy to Obtain Customized Nutrition? *Journal of Clinical Gastroenterology*, *50 Supplemment 2, Proceedings from the 8th Probiotics, Prebiotics & New Foods for Microbiota and Human Health meeting held in Rome, Italy on September 13-15, 2015*, S175-S178.

Shadvar, N., Foroozmehr, E., Badrossamay, M., Amouhadi, I., & Dindarloo, A. S. (2019). Computational analysis of the extrusion process of fused deposition modeling of acrylonitrile-butadiene-styrene. *International Journal of Material Forming*, *14*(1), 121-131.

Shahbazi, M., & Jager, H. (2021). Current Status in the Utilization of Biobased Polymers for 3D Printing Process: A Systematic Review of the Materials, Processes, and Challenges. *ACS Applied Bio Materials*, *4*(1), 325-369.

Shahbazi, M., Jäger, H., Ettelaie, R., & Chen, J. (2021). Construction of 3D printed reduced-fat meat analogue by emulsion gels. Part I: Flow behavior, thixotropic feature, and network structure of soy protein-based inks. *Food Hydrocolloids*, *120*, 106967.

Sharifi, M., Bai, Q., Babadaei, M. M. N., Chowdhury, F., Hassan, M., Taghizadeh, A., Derakhshankhah, H., Khan, S., Hasan, A., & Falahati, M. (2021). 3D bioprinting of engineered breast cancer constructs for personalized and targeted cancer therapy. *Journal of Controlled Release*, *333*, 91-106.

Shi, H., Li, J., Xu, E., Yang, H., Liu, D., & Yin, J. (2023). Microscale 3D printing of fish analogues using soy protein food ink. *Journal of Food Engineering*, *347*, 111436.

Shi, X., Sun, Y., Tian, H., Abhilash, P. M., Luo, X., & Liu, H. (2023). Material Extrusion Filament Width and Height Prediction via Design of Experiment and Machine Learning. *Micromachines (Basel)*, *14*(11), 2091.

Shinde, P. P., & Shah, S. (2018). A review of machine learning and deep learning applications. *2018 Fourth International Conference on Computing Communication Control and Sutomation (ICCUBEA)*, 1-6, Pune, India.

Steffe, J. F. (1996). *Rheological methods in food process engineering*. Freeman press.

Sun, R., Lei, T., Chen, Q., Wang, Z., Du, X., Zhao, W., & Nandi, A. K. (2022). Survey of image edge detection. *Frontiers in Signal Processing*, *2*, 826967.

Suthaharan, S. (2016). Machine learning models and algorithms for big data classification. *Integrated Series in Information Systems*, *36*, 1-12.

Szűcs, D., Fekete, Z., Guba, M., Kemény, L., Jemnitz, K., Kis, E., & Veréb, Z. (2023). Toward better drug development: Three-dimensional bioprinting in toxicological research. *International Journal of Bioprinting*, *9*(2).

Tan, C., Toh, W. Y., Wong, G., & Li, L. (2018). Extrusion-based 3D food printing–Materials and machines. *International Journal of Bioprinting*, *4*(2).

Tapkire, M. D., & Arun, V. (2023). Application of artificial intelligence to corelate food formulations to disease risk prediction: a comprehensive review. *Journal of Food Science and Technology*, *60*(9), 2350-2357.

Tian, J., Bryksa, B. C., & Yada, R. Y. (2016). Feeding the world into the future – food and nutrition security: the role of food science and technology. *Frontiers in Life Science*, *9*(3), 155-166.

Toker, O. S., & Dogan, M. (2013). Effect of temperature and starch concentration on the creep/recovery behaviour of the grape molasses: modelling with ANN, ANFIS and response surface methodology. *European Food Research and Technology*, *236*(6), 1049-1061.

Tseng, Y. J., Chuang, P. J., & Appell, M. (2023). When Machine Learning and Deep Learning Come to the Big Data in Food Chemistry. *ACS Omega*, *8*(18), 15854-15864.

Uribe-Alvarez, R., Murphy, C. P., Coleman-Vaughan, C., & O'Shea, N. (2023). Evaluation of ionic calcium and protein concentration on heat- and cold-induced gelation of whey protein isolate gels as a potential food formulation for 3D food printing. *Food Hydrocolloids*, *142*, 108777.

Vancauwenberghe, V., Katalagarianakis, L., Wang, Z., Meerts, M., Hertog, M., Verboven, P., Moldenaers, P., Hendrickx, M. E., Lammertyn, J., & Nicolaï, B. (2017). Pectin based food-ink formulations for 3-D printing of customizable porous food simulants. *Innovative Food Science & Emerging Technologies*, *42*, 138-150.

Vassileva, S., & Mileva, S. (2014). Ai-Based Software Tools for Beer Brewing Monitoring and Control. *Biotechnology & Biotechnological Equipment*, *24*(3), 1936-1939.

Voulodimos, A., Doulamis, N., Doulamis, A., & Protopapadakis, E. (2018). Deep Learning for Computer Vision: A Brief Review. *Computational Intelligence and Neuroscience*, *2018*, 7068349.

Wang, H.-H., & Sun, D.-W. (2003). Assessment of cheese browning affected by baking conditions using computer vision. *Journal of Food Engineering*, *56*(4), 339-345.

Wang, L., Zhang, M., Bhandari, B., & Yang, C. (2018). Investigation on fish surimi gel as promising food material for 3D printing. *Journal of Food Engineering*, *220*, 101-108.

Wang, S., Yu, X., Shen, L., Yang, A., Chen, E., Fieldhouse, J., Barton, D., & Kosarieh, S. (2021). Noise reduction of automobile cooling fan based on bio-inspired design. *Proceedings of the Institution of Mechanical Engineers, Part D: Journal of Automobile Engineering*, *235*(2-3), 465-478.

Wang, X., Zhang, M., Mujumdar, A. S., & Li, J. (2023). Easy-to-swallow mooncake using 3D printing: Effect of oil and hydrocolloid addition. *Food Research International*, *164*, 112404.

Wang, Y., & Selomulya, C. (2022). Food rheology applications of large amplitude oscillation shear (LAOS). *Trends in Food Science & Technology*, *127*, 221-244.

Wang, Z., Liang, X., Wang, G., Wang, X., & Chen, Y. (2023). Emerging bioprinting for wound healing. *Advanced Materials*, 2304738.

Wei, M., Lin, K., & Sun, L. (2022). Shear thickening fluids and their applications. *Materials & Design*, *216*, 110570.

Wen, Y., Che, Q. T., Wang, S., Park, H. J., & Kim, H. W. (2024). Elaboration of dimensional quality in 3D-printed food: Key factors in process steps. *Comprehensive Reviews in Food Science and Food Safety*, *23*(1), e13267.

Wu, B. C., Degner, B., & McClements, D. J. (2014). Soft matter strategies for controlling food texture: formation of hydrogel particles by biopolymer complex coacervation. *Journal of Physics: Condensed Matter*, *26*(46), 464104.

Wu, D., & Sun, D.-W. (2013). Colour measurements by computer vision for food quality control – A review. *Trends in Food Science & Technology*, *29*(1), 5-20.

Wu, M., Phoha, V. V., Moon, Y. B., & Belman, A. K. (2016). Detecting Malicious Defects in 3D Printing Process Using Machine Learning and Image Classification. *Proceedings of the ASME 2016 International Mechanical Engineering Congress and Exposition. Volume 14: Emerging Technologies;*

Materials: Genetics to Structures; Safety Engineering and Risk Analysis, V014T07A004, Phoenix, Arizone, USA.

Yang, F., Cui, Y., Guo, Y., Yang, W., Liu, X., & Liu, X. (2021). Internal structure and textural properties of a milk protein composite gel construct produced by three-dimensional printing. *Journal of Food Science*, *86*(5), 1917-1927.

Yang, F., Guo, C., Zhang, M., Bhandari, B., & Liu, Y. (2019). Improving 3D printing process of lemon juice gel based on fluid flow numerical simulation. *Lwt*, *102*, 89-99.

Yang, F., Zhang, M., Fang, Z., & Liu, Y. (2019). Impact of processing parameters and post-treatment on the shape accuracy of 3D-printed baking dough. *International Journal of Food Science & Technology*, *54*(1), 68-74.

Yazar, G., Caglar Duvarci, O., Yildirim Erturk, M., & Kokini, J. L. (2019). LAOS (large amplitude oscillatory shear) applications for semisolid foods. In *Rheology of semisolid foods* (pp. 97-131). Springer International Publishing.

Yazar, G., Duvarci, O. C., Tavman, S., & Kokini, J. L. (2016). Effect of mixing on LAOS properties of hard wheat flour dough. *Journal of Food Engineering*, *190*, 195-204.

Yin, Y., Wang, Y., Fang, Q., Xiang, M., Zhao, X., Xu, X., & Li, C. (2024). Effects of pre-formulation and post-cooking method on the rheological and gelation properties of 3D printed chicken products. *Food Chemistry*, *446*, 138857.

Ying, X. (2019). An Overview of Overfitting and its Solutions. *Journal of Physics: Conference Series*, *1168*(2), 022022.

Yoo, H., & Park, D. (2021). AI-based 3D food printing using standard composite materials. *Data Science and Digital Transformation in the Fourth Industrial Revolution*, 123-135.

Yuk, H., & Zhao, X. (2018). A New 3D Printing Strategy by Harnessing Deformation, Instability, and Fracture of Viscoelastic Inks. *Advanced Materials*, *30*(6), 1704028.

Zeng, X., Cao, R., Xi, Y., Li, X., Yu, M., Zhao, J., Cheng, J., & Li, J. (2023). Food flavor analysis 4.0: A cross-domain application of machine learning. *Trends in Food Science & Technology*, *138*, 116-125.

Zhang, L., Lou, Y., & Schutyser, M. A. I. (2018). 3D printing of cereal-based food structures containing probiotics. *Food Structure*, *18*, 14-22.

Zheng, L., Liu, J., Liu, R., Xing, Y., & Jiang, H. (2021). 3D printing performance of gels from wheat starch, flour and whole meal. *Food Chem*, *356*, 129546.

Zhu, S., Stieger, M. A., van der Goot, A. J., & Schutyser, M. A. I. (2019). Extrusion-based 3D printing of food pastes: Correlating rheological properties with printing behaviour. *Innovative Food Science & Emerging Technologies*, *58*, 102214.

Zhu, S., Vazquez Ramos, P., Heckert, O. R., Stieger, M., van der Goot, A. J., & Schutyser, M. (2022). Creating protein-rich snack foods using binder jet 3D printing. *Journal of Food Engineering*, *332*, 111124.

Zhu, Y., Di, W., Song, M., Chitrakar, B., & Liu, Z. (2023). Correlating 3D printing performance with sol-gel transition based on thermo-responsive k-carrageenan affected by fructose. *Journal of Food Engineering*, *340*, 111316.

APPENDICES

APPENDIX A
G-CODE USED IN CHAPTER 3 AND VISUALIZATION

(a)

G0 F600 X110 Y150 Z0.8

G1 F600 E0G1 F600 X110 Y80 E6.59881

G1 F600 E19.39524

(b)

G0 F1200 X110 Y150 Z0.8

G1 F1200 E0

G1 F1200 X110 Y80 E6.59881

G1 F1200 E19.39524

(c)

G0 F1500 X110 Y150 Z0.8

G1 F1500 E0

G1 F1500 X110 Y80 E6.59881

G1 F1500 E19.39524

(d)

G0 F1800 X110 Y150 Z0.8

G1 F1800 E0

G1 F1800 X110 Y80 E6.59881

G1 F1800 E19.39524

(e)

G0 F2400 X110 Y150 Z0.8

G1 F2400 E0

G1 F2400 X110 Y80 E6.59881

G1 F2400 E19.39524

Figure A.1 G-code used in the chapter 3. Each g-code is set at a different printing speed. (a) 10 $mm.s^{-1}$, (b) 20 $mm.s^{-1}$, (c) 25 $mm.s^{-1}$, (d) 30 $mm.s^{-1}$, (e) 40 $mm.s^{-1}$.

APPENDIX B
MACHINE LEARNING CODE DEVELOPED FOR THE CHAPTER 3

A snippet of the Python code developed to carry out the machine learning analysis presented in Chapter 3 can be found in this section. Note that some libraries need to be installed beforehand.

```
## Initialization of the study
# Loading the dataset
data = pd.read_csv('specify file location/file name.csv')

X = data.drop(columns=['S_AVG']) #S_AVG corresponds to the spreading ratio
y = data['S_AVG']

# Models definition
models = {
   "ET": ExtraTreesRegressor(),
   "GB": GradientBoostingRegressor(),
   "RF": RandomForestRegressor(),
   "DT": DecisionTreeRegressor(),
   "XGB": XGBRegressor()
}

# Leave One Out Cross Validation (LOOCV)
n_splits = len(X)
cv = KFold(n_splits=n_splits)

for name, model in models.items():
   print("Training", name)

   fold_results_train = []
   fold_results_test = []
```

```
## Running the different models and carrying out the cross validation
    # Cross-validation
    for fold, (train_index, test_index) in enumerate(cv.split(X), 1):
        X_train_fold, X_test_fold = X.iloc[train_index], X.iloc[test_index]
        y_train_fold, y_test_fold = y.iloc[train_index], y.iloc[test_index]

        # Model training
        model.fit(X_train_fold, y_train_fold)

        # Predict on the testing fold
        y_test_pred = model.predict(X_test_fold)
        fold_results_test.append(pd.DataFrame({
            'Index': test_index,
            'Features': X_test_fold.apply(lambda x: ', '.join(map(str, x)), axis=1),
            'Experimental Result': y_test_fold.values,
            'Predicted Result': y_test_pred
        }))

    # Calculate average RMSE and R2 across folds for training
    avg_rmse_train = fold_df_train.groupby('Index')['RMSE (Training)'].mean()
    avg_r2_train = fold_df_train.groupby('Index')['R2 (Training)'].mean()

    # Store results in dictionary
    summary_data[name] = {
        'Average RMSE (Training)': avg_rmse_train.mean(),
        'Average R2 (Training)': avg_r2_train.mean()
    }

    # Display averaged training results
    print(f"Averaged Training Results for {name}:")
    print(f"Average RMSE: {avg_rmse_train.mean():.2f}")
    print(f"Average R2: {avg_r2_train.mean():.2f}")
    print()

        # Compute feature importances
        feature_importance = model.feature_importances_
        feature_importance_df = pd.DataFrame({
            'Feature': X.columns,
```

```
            f'Importance ({name})': feature_importance
        })
        feature_importance_dfs[name] = feature_importance_df

# Best model based on average R2 with training
best_model_loocv = max(summary_data, key=lambda x: summary_data[x]['Average R2 (Training)'])

print("\nBest Model (based on average R2 with LOOCV):", best_model_loocv)
print("Results of the Best Model (based on average R2 with LOOCV):")
best_model_results = summary_data[best_model_loocv]
for key, value in best_model_results.items():
    print(f" (Tian et al.): {value:.2f}")

## Model validation on an unseen set of data
```

APPENDIX C
5 FEATURES PREDICTION ERROR

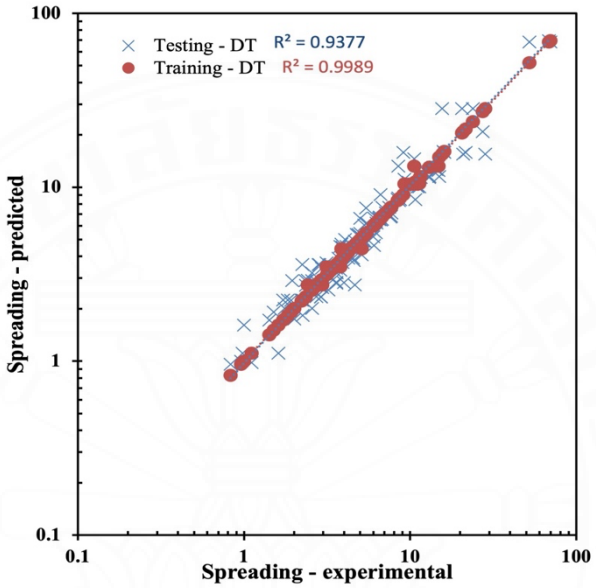

Figure C.1 Prediction error for decision trees model, with 5 features.

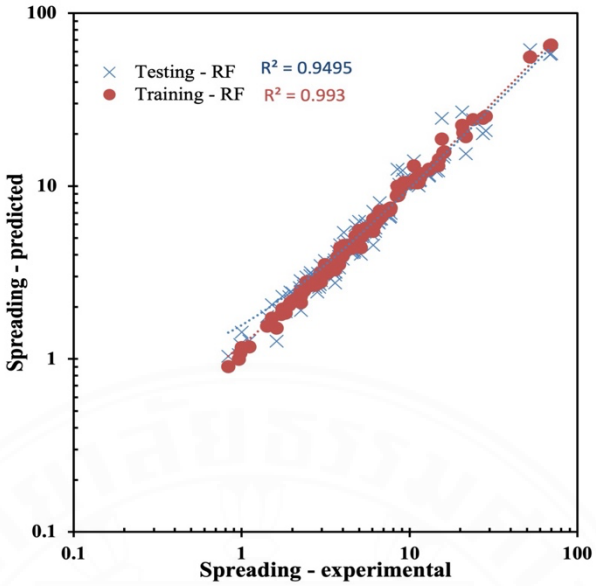

Figure C.2 Prediction error for random forest model, with 5 features.

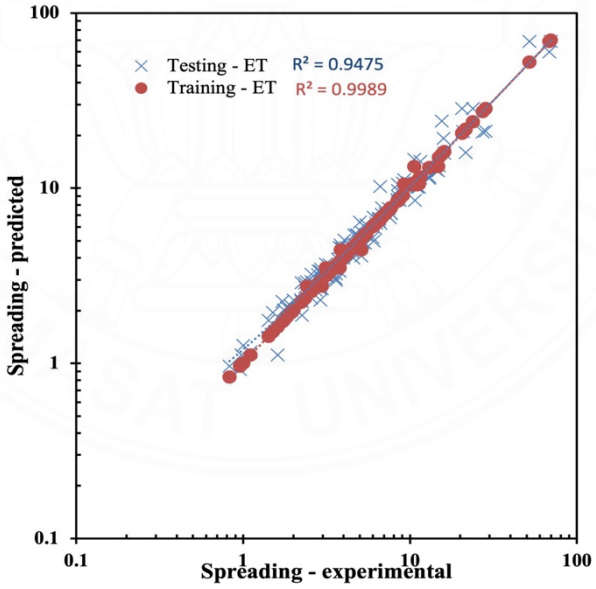

Figure C.3 Prediction error for extra trees model, with 5 features.

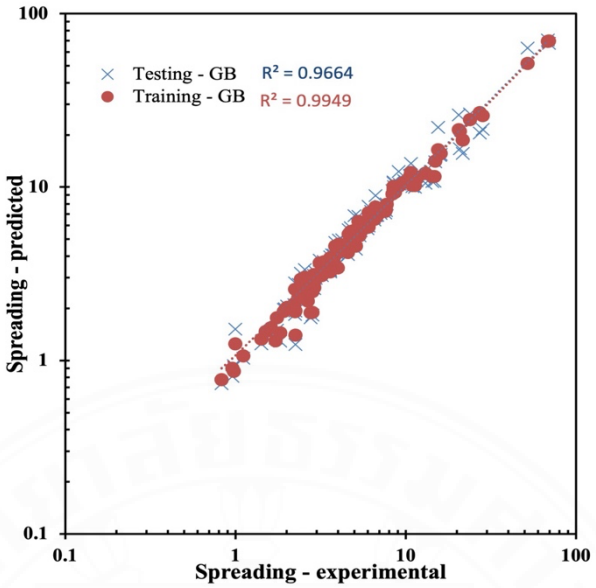

Figure C.4 Prediction error for gradient boosting model, with 5 features.

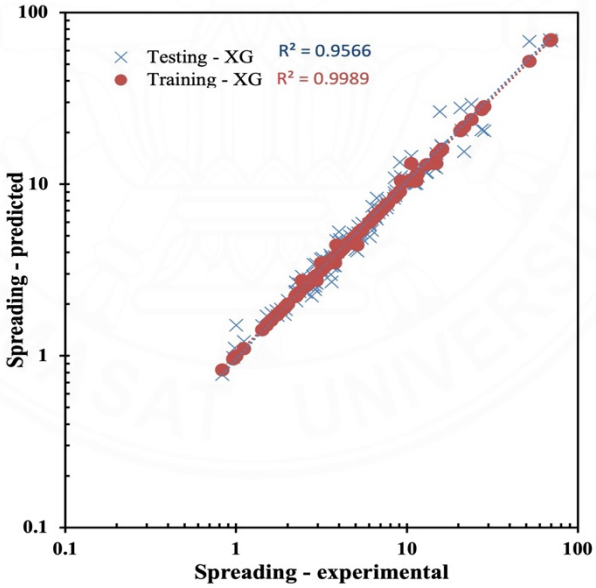

Figure C.5 Prediction error for extreme gradient boosting model, with 5 features.

APPENDIX D
4 FEATURES PREDICTION ERROR

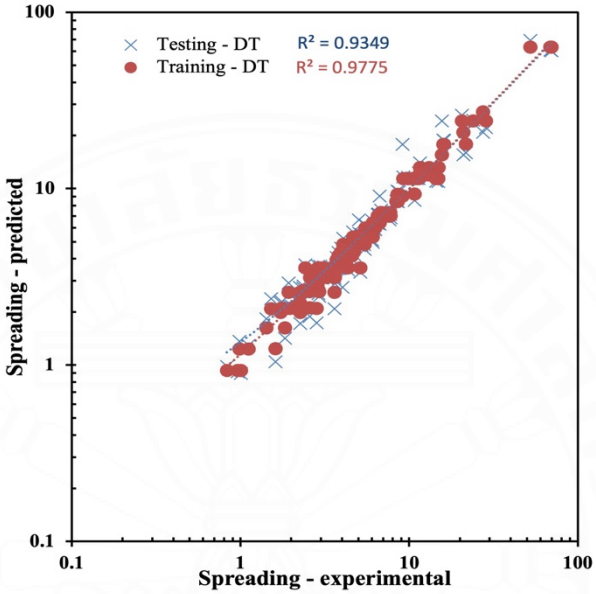

Figure D.1 Prediction error for decision trees model, with 4 features.

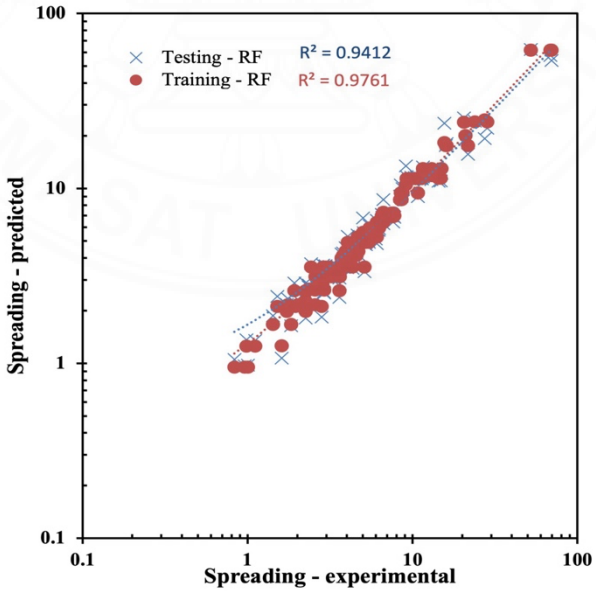

Figure D.2 Prediction error for random forest model, with 4 features.

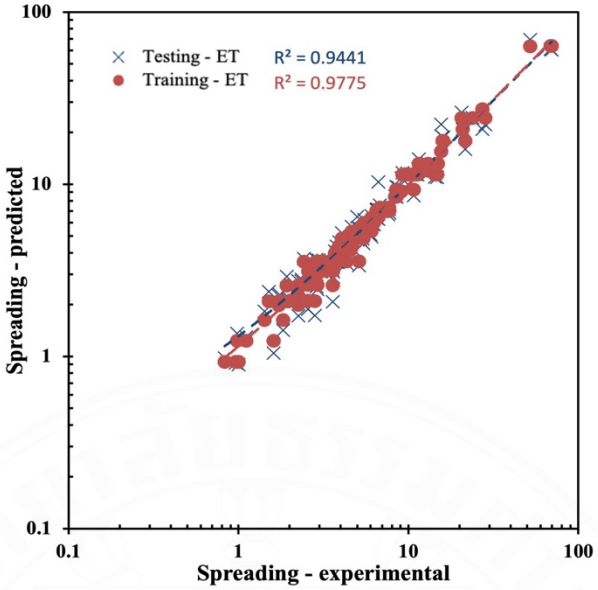

Figure D.3 Prediction error for extra trees model, with 4 features.

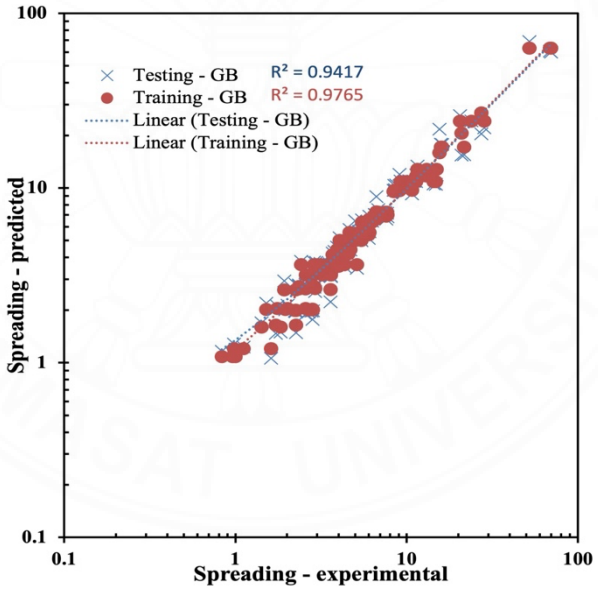

Figure D.4 Prediction error for gradient boosting model, with 4 features.

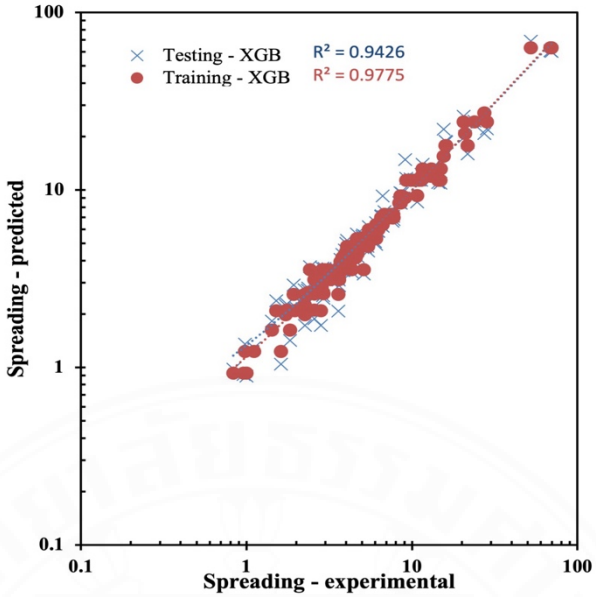

Figure D.5 Prediction error for extreme gradient boosting model, with 4 features.

APPENDIX E
3 FEATURES PREDICTION ERROR

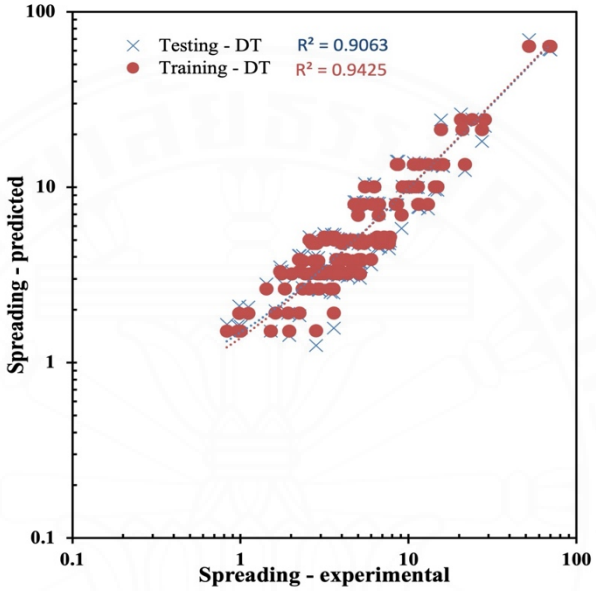

Figure E.1 Prediction error for decision trees model, with 3 features.

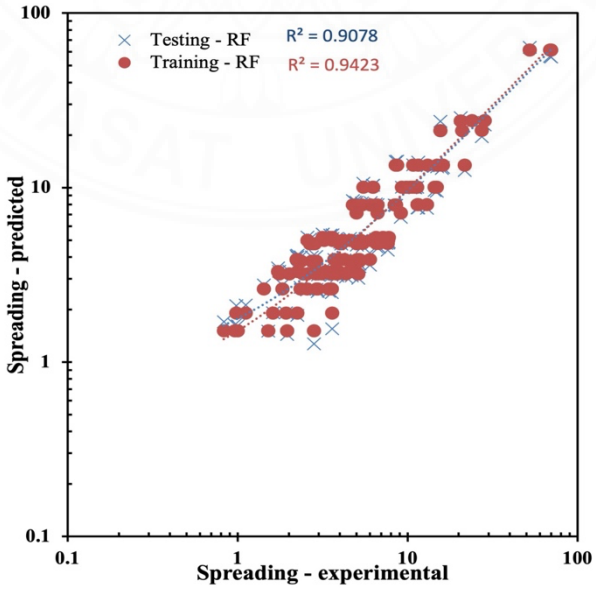

Figure E.2 Prediction error for random forest model, with 3 features.

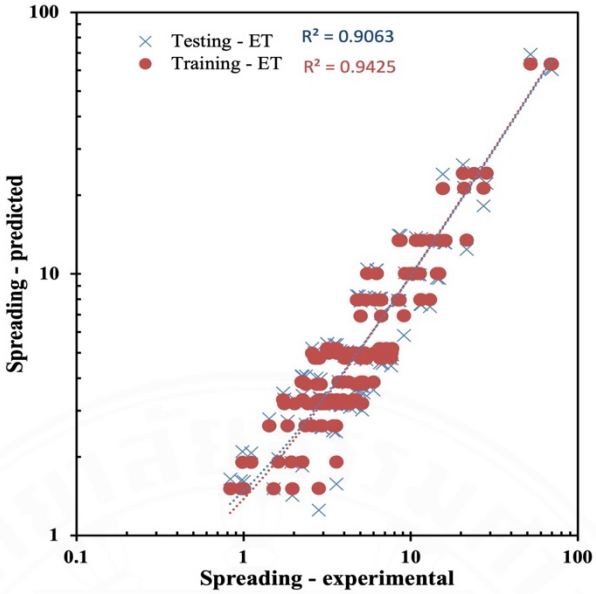

Figure E.3 Prediction error for extra trees model, with 3 features.

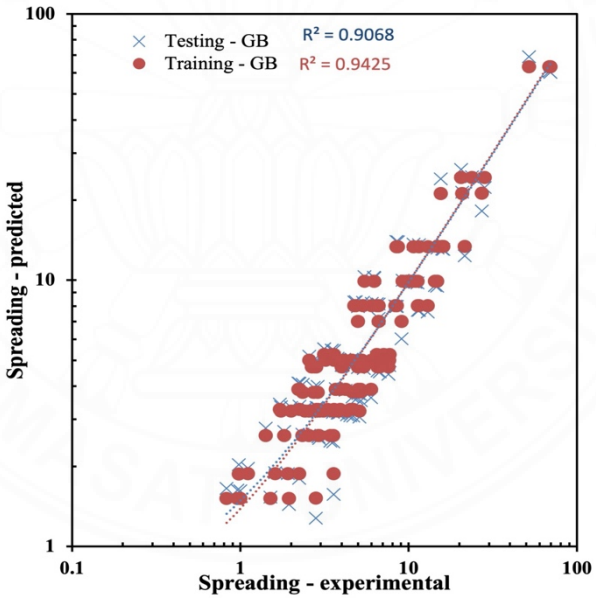

Figure E.4 Prediction error for gradient boosting model, with 3 features.

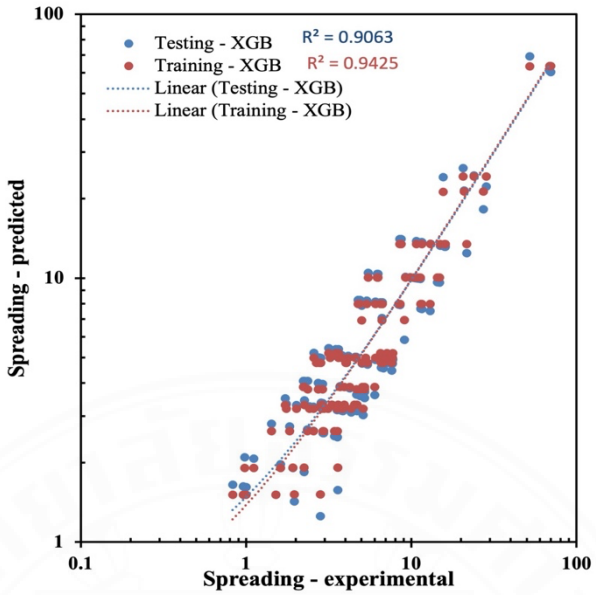

Figure E.5 Prediction error for extreme gradient boosting model, with 3 features.

APPENDIX F
TRAINING RESULTS ON EXTRA TREE REGRESSOR WITH 4 FEATURES

Table F.1 Training results based on the ET model with 4 features (best model).

Pressure (Pa)	Speed ($mm.s^{-1}$)	G_0^*	n	S exp	S testing	Err. (%)
0.5	10	737.91	0.34	3.61	3.14	1.73
0.75	10	737.91	0.34	4.14	4.17	0.00
1	10	737.91	0.34	5.28	5.32	0.01
1	25	737.91	0.34	3.3	3.27	0.01
1	40	737.91	0.34	2.56	2.60	0.03
1.5	10	737.91	0.34	7.46	7.31	0.04
1.5	25	737.91	0.34	4.69	4.38	0.44
1.5	40	737.91	0.34	3.57	3.31	0.51
0.5	10	737.91	0.34	3.22	3.13	0.07
0.5	25	737.91	0.34	2.25	1.99	1.37
0.5	40	737.91	0.34	1.83	1.63	1.24
0.75	10	737.91	0.34	4.57	4.17	0.77
0.75	25	737.91	0.34	2.84	2.84	0.00
1	10	737.91	0.34	6.06	5.33	1.47
1	25	737.91	0.34	3.6	3.27	0.85
1	40	737.91	0.34	2.91	2.60	1.10
1.5	10	737.91	0.34	7.67	7.31	0.22
1.5	25	737.91	0.34	4.52	4.38	0.10
1.5	40	737.91	0.34	3.43	3.31	0.11
0.5	10	737.91	0.34	2.57	3.13	4.77
0.5	25	737.91	0.34	1.72	1.98	2.34
0.5	40	737.91	0.34	1.42	1.62	2.05
0.75	10	737.91	0.34	3.79	4.17	0.98
1	10	737.91	0.34	4.63	5.32	2.23
1	25	737.91	0.34	2.9	3.27	1.59
1	40	737.91	0.34	2.34	2.60	1.26
1.5	10	737.91	0.34	6.8	7.31	0.56
1.5	25	737.91	0.34	3.92	4.37	1.35
1.5	40	737.91	0.34	2.94	3.31	1.60
0.5	10	130.76	0.51	4.76	5.00	0.25
0.5	25	130.76	0.51	2.66	2.75	0.12
0.5	40	130.76	0.51	2.22	2.24	0.01

0.75	10	130.76	0.51	6.05	6.40	0.33
1	10	130.76	0.51	8.48	8.46	0.00
1	25	130.76	0.51	5.43	4.83	1.21
1	40	130.76	0.51	4.24	3.95	0.45
1.5	10	130.76	0.51	12.99	11.98	0.61
1.5	25	130.76	0.51	7.6	6.97	0.68
1.5	40	130.76	0.51	5.98	5.41	0.92
0.5	10	130.76	0.51	5.37	5.00	0.47
0.5	25	130.76	0.51	2.83	2.75	0.07
0.5	40	130.76	0.51	2.25	2.24	0.00
0.75	10	130.76	0.51	6.65	6.40	0.14
0.75	25	130.76	0.51	4	4.00	0.00
1	10	130.76	0.51	8.54	8.46	0.01
1	25	130.76	0.51	5.01	4.83	0.13
1	40	130.76	0.51	3.92	3.95	0.01
1.5	10	130.76	0.51	11.39	11.97	0.26
1.5	25	130.76	0.51	6.76	6.97	0.10
1.5	40	130.76	0.51	5.19	5.40	0.17
0.5	10	130.76	0.51	4.87	5.00	0.07
0.5	25	130.76	0.51	2.77	2.75	0.00
0.5	40	130.76	0.51	2.24	2.24	0.00
0.75	10	130.76	0.51	6.49	6.40	0.02
1	10	130.76	0.51	8.37	8.46	0.01
1	25	130.76	0.51	4.05	4.83	3.68
1	40	130.76	0.51	3.7	3.95	0.47
1.5	10	130.76	0.51	11.54	11.97	0.14
1.5	25	130.76	0.51	6.55	6.97	0.41
1.5	40	130.76	0.51	5.04	5.40	0.52
0.5	10	23.89	0.72	10.73	9.30	1.78
0.75	10	23.89	0.72	14.91	13.18	1.35
1	10	23.89	0.72	21.6	17.86	3.00
0.5	10	23.89	0.72	8.48	9.29	0.91
0.5	25	23.89	0.72	5	5.00	0.00
0.75	10	23.89	0.72	11.54	13.16	1.98
0.75	25	23.89	0.72	6.64	6.64	0.00
1	10	23.89	0.72	15.87	17.84	1.54
1	25	23.89	0.72	9.08	9.08	0.00
0.5	10	23.89	0.72	8.67	9.29	0.51
0.75	10	23.89	0.72	13.06	13.17	0.01
1	10	23.89	0.72	16.07	17.84	1.21
0.5	10	4.83	0.88	20.5	24.21	3.27

0.5	10	4.83	0.88	28.33	24.24	2.09
0.5	25	4.83	0.88	15.54	15.54	0.00
0.75	25	4.83	0.88	20.84	20.84	0.00
1	25	4.83	0.88	27.29	27.29	0.00
0.5	10	4.83	0.88	23.84	24.22	0.03
0.5	10	0.86	0.97	52.08	63.37	4.70
0.5	10	0.86	0.97	68.56	63.44	0.56
0.5	10	0.86	0.97	69.61	63.44	0.79
0.5	10	377.96	0.33	6.26	5.99	0.19
1	10	377.96	0.33	10.59	11.37	0.55
1	20	377.96	0.33	7.72	7.00	0.88
1	40	377.96	0.33	5.2	4.92	0.29
1	10	377.96	0.33	14.78	11.38	5.30
1	10	377.96	0.33	14.34	11.38	4.27
0.5	10	377.96	0.33	6.22	5.99	0.14
1	10	377.96	0.33	9.81	11.37	2.54
1	20	377.96	0.33	7.13	7.00	0.04
1	40	377.96	0.33	4.9	4.92	0.00
1	10	377.96	0.33	11.06	11.38	0.08
1	10	377.96	0.33	10.34	11.37	1.00
0.5	10	377.96	0.33	5.48	5.98	0.85
1	10	377.96	0.33	9.21	11.37	5.52
1	20	377.96	0.33	6.5	7.00	0.58
1	40	377.96	0.33	4.65	4.92	0.33
1	10	377.96	0.33	11.32	11.38	0.00
1	10	377.96	0.33	10.93	11.38	0.17
0.5	20	377.96	0.33	3.61	3.38	0.40
0.5	20	377.96	0.33	3.5	3.38	0.11
0.5	20	377.96	0.33	3.15	3.38	0.54
0.5	40	377.96	0.33	2.89	2.66	0.65
0.5	40	377.96	0.33	2.73	2.66	0.07
0.5	40	377.96	0.33	2.35	2.66	1.69
0.5	10	1296.63	0.25	2.56	2.11	3.11
1	10	1296.63	0.25	3.85	3.56	0.58
1	20	1296.63	0.25	3.59	2.59	7.80
1	40	1296.63	0.25	2.81	2.09	6.52
1	10	1296.63	0.25	5.11	3.56	9.24
1	10	1296.63	0.25	4.32	3.56	3.13
0.5	10	1296.63	0.25	2.01	2.11	0.23
1	10	1296.63	0.25	3.13	3.56	1.85
1	20	1296.63	0.25	2.24	2.58	2.33

1	40	1296.63	0.25	1.95	2.09	0.51
1	10	1296.63	0.25	3.79	3.56	0.38
1	10	1296.63	0.25	3.55	3.56	0.00
0.5	10	1296.63	0.25	1.75	2.11	4.12
1	10	1296.63	0.25	2.42	3.55	21.98
1	20	1296.63	0.25	1.92	2.58	11.85
1	40	1296.63	0.25	1.51	2.09	14.64
1	10	1296.63	0.25	2.87	3.55	5.70
1	10	1296.63	0.25	2.96	3.55	4.04
0.5	20	1296.63	0.25	1.61	1.23	5.43
0.5	20	1296.63	0.25	1.11	1.23	1.23
0.5	20	1296.63	0.25	0.98	1.23	6.63
0.5	40	1296.63	0.25	1	0.93	0.49
0.5	40	1296.63	0.25	0.96	0.93	0.10
0.5	40	1296.63	0.25	0.83	0.93	1.44
1	20	377.96	0.33	7.13	7.00	0.04
1	20	377.96	0.33	6.5	7.00	0.58
0.5	20	377.96	0.33	3.5	3.38	0.11
0.5	20	377.96	0.33	3.15	3.38	0.54
				Averaged Error		**1.54**

APPENDIX G
TESTING RESULTS ON EXTRA TREE REGRESSOR WITH 4 FEATURES

Table G.1 Testing results based on the ET model with 4 features (best model).

Pressure (Pa)	Speed ($mm.s^{-1}$)	G_0^*	n	S exp	S testing	Err. (%)
0.5	10	737.91	0.34	3.61	2.90	3.92
0.75	10	737.91	0.34	4.14	4.18	0.01
1	10	737.91	0.34	5.28	5.35	0.02
1	25	737.91	0.34	3.3	3.25	0.02
1	40	737.91	0.34	2.56	2.63	0.06
1.5	10	737.91	0.34	7.46	7.24	0.09
1.5	25	737.91	0.34	4.69	4.22	1.00
1.5	40	737.91	0.34	3.57	3.19	1.16
0.5	10	737.91	0.34	3.22	3.09	0.16
0.5	25	737.91	0.34	2.25	1.72	5.55
0.5	40	737.91	0.34	1.83	1.42	5.02
0.75	10	737.91	0.34	4.57	3.96	1.75
0.75	25	737.91	0.34	2.84	3.07	0.66
1	10	737.91	0.34	6.06	4.96	3.32
1	25	737.91	0.34	3.6	3.10	1.93
1	40	737.91	0.34	2.91	2.45	2.50
1.5	10	737.91	0.34	7.67	7.13	0.50
1.5	25	737.91	0.34	4.52	4.31	0.23
1.5	40	737.91	0.34	3.43	3.26	0.26
0.5	10	737.91	0.34	2.57	3.42	10.81
0.5	25	737.91	0.34	1.72	2.25	9.49
0.5	40	737.91	0.34	1.42	1.83	8.34
0.75	10	737.91	0.34	3.79	4.36	2.22
1	10	737.91	0.34	4.63	5.67	5.05
1	25	737.91	0.34	2.9	3.45	3.60
1	40	737.91	0.34	2.34	2.74	2.85
1.5	10	737.91	0.34	6.8	7.57	1.27
1.5	25	737.91	0.34	3.92	4.61	3.05
1.5	40	737.91	0.34	2.94	3.50	3.63
0.5	10	130.76	0.51	4.76	5.12	0.57
0.5	25	130.76	0.51	2.66	2.80	0.28

0.5	40	130.76	0.51	2.22	2.25	0.01
0.75	10	130.76	0.51	6.05	6.57	0.74
1	10	130.76	0.51	8.48	8.46	0.00
1	25	130.76	0.51	5.43	4.53	2.75
1	40	130.76	0.51	4.24	3.81	1.03
1.5	10	130.76	0.51	12.99	11.47	1.38
1.5	25	130.76	0.51	7.6	6.65	1.55
1.5	40	130.76	0.51	5.98	5.12	2.09
0.5	10	130.76	0.51	5.37	4.82	1.07
0.5	25	130.76	0.51	2.83	2.72	0.17
0.5	40	130.76	0.51	2.25	2.23	0.01
0.75	10	130.76	0.51	6.65	6.27	0.33
0.75	25	130.76	0.51	4	4.04	0.01
1	10	130.76	0.51	8.54	8.42	0.02
1	25	130.76	0.51	5.01	4.74	0.29
1	40	130.76	0.51	3.92	3.97	0.02
1.5	10	130.76	0.51	11.39	12.27	0.59
1.5	25	130.76	0.51	6.76	7.08	0.22
1.5	40	130.76	0.51	5.19	5.51	0.38
0.5	10	130.76	0.51	4.87	5.07	0.16
0.5	25	130.76	0.51	2.77	2.75	0.01
0.5	40	130.76	0.51	2.24	2.24	0.00
0.75	10	130.76	0.51	6.49	6.35	0.05
1	10	130.76	0.51	8.37	8.51	0.03
1	25	130.76	0.51	4.05	5.22	8.35
1	40	130.76	0.51	3.7	4.08	1.05
1.5	10	130.76	0.51	11.54	12.19	0.32
1.5	25	130.76	0.51	6.55	7.18	0.93
1.5	40	130.76	0.51	5.04	5.59	1.17
0.5	10	23.89	0.72	10.73	8.58	4.03
0.75	10	23.89	0.72	14.91	12.30	3.06
1	10	23.89	0.72	21.6	15.97	6.79
0.5	10	23.89	0.72	8.48	9.70	2.07
0.5	25	23.89	0.72	5	6.48	8.82
0.75	10	23.89	0.72	11.54	13.99	4.49
0.75	25	23.89	0.72	6.64	10.31	30.54
1	10	23.89	0.72	15.87	18.84	3.49
1	25	23.89	0.72	9.08	10.85	3.79
0.5	10	23.89	0.72	8.67	9.61	1.16
0.75	10	23.89	0.72	13.06	13.23	0.02
1	10	23.89	0.72	16.07	18.74	2.75

0.5	10	4.83	0.88	20.5	26.09	7.42
0.5	10	4.83	0.88	28.33	22.17	4.73
0.5	25	4.83	0.88	15.54	22.27	18.77
0.75	25	4.83	0.88	20.84	20.83	0.00
1	25	4.83	0.88	27.29	20.84	5.59
0.5	10	4.83	0.88	23.84	24.42	0.06
0.5	10	0.86	0.97	52.08	69.09	10.66
0.5	10	0.86	0.97	68.56	60.85	1.27
0.5	10	0.86	0.97	69.61	60.32	1.78
0.5	10	377.96	0.33	6.26	5.85	0.43
1	10	377.96	0.33	10.59	11.47	0.70
1	20	377.96	0.33	7.72	6.82	1.37
1	40	377.96	0.33	5.2	4.77	0.67
1	10	377.96	0.33	14.78	10.95	6.72
1	10	377.96	0.33	14.34	11.01	5.41
0.5	10	377.96	0.33	6.22	5.87	0.32
1	10	377.96	0.33	9.81	11.57	3.22
1	20	377.96	0.33	7.13	6.96	0.06
1	40	377.96	0.33	4.9	4.93	0.00
1	10	377.96	0.33	11.06	11.42	0.10
1	10	377.96	0.33	10.34	11.51	1.27
0.5	10	377.96	0.33	5.48	6.24	1.92
1	10	377.96	0.33	9.21	11.65	7.00
1	20	377.96	0.33	6.5	7.12	0.91
1	40	377.96	0.33	4.65	5.05	0.74
1	10	377.96	0.33	11.32	11.38	0.00
1	10	377.96	0.33	10.93	11.43	0.21
0.5	20	377.96	0.33	3.61	3.32	0.62
0.5	20	377.96	0.33	3.5	3.35	0.18
0.5	20	377.96	0.33	3.15	3.44	0.85
0.5	40	377.96	0.33	2.89	2.54	1.47
0.5	40	377.96	0.33	2.73	2.62	0.16
0.5	40	377.96	0.33	2.35	2.81	3.83
0.5	10	1296.63	0.25	2.56	1.88	7.06
1	10	1296.63	0.25	3.85	3.52	0.74
1	20	1296.63	0.25	3.59	2.08	17.69
1	40	1296.63	0.25	2.81	1.73	14.77
1	10	1296.63	0.25	5.11	3.36	11.71
1	10	1296.63	0.25	4.32	3.46	3.96
0.5	10	1296.63	0.25	2.01	2.16	0.52
1	10	1296.63	0.25	3.13	3.61	2.34

1	20	1296.63	0.25	2.24	2.76	5.29
1	40	1296.63	0.25	1.95	2.16	1.16
1	10	1296.63	0.25	3.79	3.53	0.48
1	10	1296.63	0.25	3.55	3.56	0.00
0.5	10	1296.63	0.25	1.75	2.29	9.35
1	10	1296.63	0.25	2.42	3.70	27.87
1	20	1296.63	0.25	1.92	2.92	26.86
1	40	1296.63	0.25	1.51	2.38	33.20
1	10	1296.63	0.25	2.87	3.64	7.22
1	10	1296.63	0.25	2.96	3.63	5.12
0.5	20	1296.63	0.25	1.61	1.05	12.32
0.5	20	1296.63	0.25	1.11	1.30	2.78
0.5	20	1296.63	0.25	0.98	1.36	15.04
0.5	40	1296.63	0.25	1	0.90	1.10
0.5	40	1296.63	0.25	0.96	0.92	0.22
0.5	40	1296.63	0.25	0.83	0.98	3.27
1	20	377.96	0.33	7.13	6.96	0.06
1	20	377.96	0.33	6.5	7.12	0.91
0.5	20	377.96	0.33	3.5	3.35	0.18
0.5	20	377.96	0.33	3.15	3.44	0.85
				Averaged Error		**3.58**

APPENDIX H
CUBE PRINTING G-CODE

```
;LAYER_COUNT:25
;LAYER:0
M107
;MESH:cube.stl
G0 F1200 X127 Y127 Z0.8
;TYPE:WALL-OUTER
G1 F1200 X108 Y127 E7.89928
G1 X108 Y108 E15.79856
G1 X127 Y108 E23.69785
G1 X127 Y126.936 E31.57052
G0 F1620 X127 Y127
G0 F1200 X125.411 Y126.559
;TYPE:FILL
G1 F1200 X126.559 Y125.411 E161.28522
G0 F1200 X126 Y125.411
G0 X126 Y123.996
G0 X126.559 Y123.996
G1 F1200 X123.996 Y126.559 E162.49078
G0 F1200 X123.996 Y126
G0 X122.582 Y126
G0 X122.582 Y126.559
G1 F1200 X126.559 Y122.582 E164.36144
G0 F1200 X126 Y122.582
G0 X126 Y121.168
G0 X126.559 Y121.168
G1 F1200 X121.168 Y126.559 E166.8972
G0 F1200 X121.168 Y126
G0 X119.754 Y126
G0 X119.754 Y126.559
G1 F1200 X126.559 Y119.754 E170.09806
G0 F1200 X126 Y119.754
G0 X126 Y118.339
G0 X126.559 Y118.339
G1 F1200 X118.339 Y126.559 E173.9645
```

G0 F1200 X118.339 Y126
G0 X116.925 Y126
G0 X116.925 Y126.559
G1 F1200 X126.559 Y116.925 E178.49604
G0 F1200 X126 Y116.925
G0 X126 Y115.511
G0 X126.559 Y115.511
G1 F1200 X115.511 Y126.559 E183.69268
G0 F1200 X115.511 Y126
G0 X114.097 Y126
G0 X114.097 Y126.559
G1 F1200 X126.559 Y114.097 E189.55442
G0 F1200 X126 Y114.097
G0 X126 Y112.683
G0 X126.559 Y112.683
G1 F1200 X112.683 Y126.559 E196.08126
G0 F1200 X112.683 Y126
G0 X111.268 Y126
G0 X111.268 Y126.559
G1 F1200 X126.559 Y111.268 E203.27368
G0 F1200 X126 Y111.268
G0 X126 Y109.854
G0 X126.559 Y109.854
G1 F1200 X109.854 Y126.559 E211.1312
G0 F1200 X109.854 Y126
G0 X108.97 Y126.03
G0 X108.44 Y126.559
G1 F1200 X126.559 Y108.44 E219.65382
G0 F1200 X126.03 Y108.97
G0 X125.145 Y109
G0 X125.145 Y108.439
G1 F1200 X108.44 Y125.145 E227.51158
G0 F1200 X109 Y125.145
G0 X109 Y123.73
G0 X108.44 Y123.73
G1 F1200 X123.731 Y108.439 E234.704
G0 F1200 X123.731 Y109
G0 X122.317 Y109

G0 X122.317 Y108.439
G1 F1200 X108.44 Y122.316 E241.23131
G0 F1200 X109 Y122.316
G0 X109 Y120.902
G0 X108.44 Y120.902
G1 F1200 X120.903 Y108.439 E247.09353
G0 F1200 X120.903 Y109
G0 X119.489 Y109
G0 X119.489 Y108.439
G1 F1200 X108.44 Y119.488 E252.29064
G0 F1200 X109 Y119.488
G0 X109 Y118.074
G0 X108.44 Y118.074
G1 F1200 X118.074 Y108.439 E256.82241
G0 F1200 X118.074 Y109
G0 X116.66 Y109
G0 X116.66 Y108.439
G1 F1200 X108.44 Y116.659 E260.68885
G0 F1200 X109 Y116.659
G0 X109 Y115.245
G0 X108.44 Y115.245
G1 F1200 X115.246 Y108.439 E263.89018
G0 F1200 X115.246 Y109
G0 X113.832 Y109
G0 X113.832 Y108.439
G1 F1200 X108.44 Y113.831 E266.42641
G0 F1200 X109 Y113.831
G0 X109 Y112.417
G0 X108.44 Y112.417
G1 F1200 X112.417 Y108.439 E268.2973
G0 F1200 X112.417 Y109
G0 X111.003 Y109
G0 X111.003 Y108.439
G1 F1200 X108.44 Y111.003 E269.5031
G0 F1200 X109 Y111.003
G0 X109 Y109.588
G0 X108.44 Y109.588
G1 F1200 X109.589 Y108.439 E270.04355

```
G0 F1200 X109.9 Y109.9
G0 Y235
G4 S50
;MESH:NONMESH
G0 F300 X109.9 Y109.9 Z1.6
G0 F1200 X108 Y108
;TIME_ELAPSED:42.477282
;LAYER:1
M106 S85
;TYPE:WALL-OUTER
;MESH:cube.stl
G1 X108 Y127 E185.1729
G1 X127 Y127 E193.07218
G1 X127 Y108 E200.94485
G1 X108 Y108 E207.94485
G0 F1200 X108.44 Y110
;TYPE:FILL
G1 F1200 X126.56 Y110 E238.02873
G0 F1200 X126.56 Y112.5
G1 F1200 X108.44 Y112.5 E248.61196
G0 F1200 X108.44 Y115
G1 F1200 X126.56 Y115 E229.19518
G0 F1200 X126.56 Y117.5
G1 F1200 X108.44 Y117.5 E219.7784
G0 F1200 X108.44 Y120
G1 F1200 X126.56 Y120 E210.36163
G0 F1200 X126.56 Y122.5
G1 F1200 X108.44 Y122.5 E210.36163
G0 F1200 X108.44 Y125
G1 F1200 X126.56 Y125 E210.36163
;MESH:NONMESH
G0 F300 X127 Y127 Z2.4
G0 F1200 X127 Y127
;TIME_ELAPSED:53.290829
;LAYER:2
M106 S85
;TYPE:WALL-OUTER
;MESH:cube.stl
```

```
G1 F1200 X108 Y127 E255.92801
G1 X108 Y108 E263.8273
G1 X127 Y108 E271.72658
G1 X127 Y127 E279.59925
G0 F1200 X125 Y126.56
;TYPE:FILL
G1 F1200 X125 Y108.44 E289.01603
G0 F1200 X122.5 Y108.44
G1 F1200 X122.5 Y126.56 E298.4328
G0 F1200 X120 Y126.56
G1 F1200 X120 Y108.44 E307.84958
G0 F1200 X117.5 Y108.44
G1 F1200 X117.5 Y126.56 E317.26635
G0 F1200 X115 Y126.56
G1 F1200 X115 Y108.44 E326.68313
G0 F1200 X112.5 Y108.44
G1 F1200 X112.5 Y126.44 E326.68313
G0 F1200 X110 Y126.56
G1 F1200 X110 Y108.44 E326.68313
;MESH:NONMESH
G0 F300 X108 Y108 Z3.2
G0 F1200 X108 Y108
;TIME_ELAPSED:63.828068
;LAYER:3
M106 S85
;TYPE:WALL-OUTER
;MESH:cube.stl
G1 X108 Y127 E185.1729
G1 X127 Y127 E193.07218
G1 X127 Y108 E200.94485
G1 X108 Y108 E200.94485
G0 F1200 X108.44 Y110
;TYPE:FILL
G1 F1200 X126.56 Y110 E238.02873
G0 F1200 X126.56 Y112.5
G1 F1200 X108.44 Y112.5 E248.61196
G0 F1200 X108.44 Y115
G1 F1200 X126.56 Y115 E229.19518
```

```
G0 F1200 X126.56 Y117.5
G1 F1200 X108.44 Y117.5 E219.7784
G0 F1200 X108.44 Y120
G1 F1200 X126.56 Y120 E210.36163
G0 F1200 X126.56 Y122.5
G1 F1200 X108.44 Y122.5 E210.36163
G0 F1200 X108.44 Y125
G1 F1200 X126.56 Y125 E210.36163
;MESH:NONMESH
G0 F300 X127 Y127 Z4
G0 F1200 X127 Y127
;TIME_ELAPSED:74.369365
;LAYER:4
M106 S85
;TYPE:WALL-OUTER
;MESH:cube.stl
G1 F1200 X108 Y127 E255.92801
G1 X108 Y108 E263.8273
G1 X127 Y108 E271.72658
G1 X127 Y126.936 E279.59925
G0 F1620 X127 Y127
G0 F1200 X125 Y126.56
;TYPE:FILL
G1 F1200 X125 Y108.44 E289.01603
G0 F1200 X122.5 Y108.44
G1 F1200 X122.5 Y126.56 E298.4328
G0 F1200 X120 Y126.56
G1 F1200 X120 Y108.44 E307.84958
G0 F1200 X117.5 Y108.44
G1 F1200 X117.5 Y126.56 E317.26635
G0 F1200 X115 Y126.56
G1 F1200 X115 Y108.44 E326.68313
G0 F1200 X112.5 Y108.44
G1 F1200 X112.5 Y126.44 E326.68313
G0 F1200 X110 Y126.56
G1 F1200 X110 Y108.44 E326.68313
G0 Y235
G4 S50
```

[…]

The code is then repeated similarly for each odd and even layer with a Z increment of 0.8 mm per layer. The print pause is added every five layers (1, 5, 10, 15, 20, 25). The last layer printed follows the pattern of layer 0 with the correct value.

APPENDIX I

RASPBERRY PI 5 - CAMERA CONTROL CODE

```
# Starting
print("Starting Experiment")

# Define folder to save the experiments
base_dir = "folder/saving"
os.makedirs(base_dir, exist_ok=True)

# Prompt for ink concentration
ink_concentration = input("Ink concentration: ")

# Create folder based on ink concentration within the base directory
experiment_dir = os.path.join(base_dir, ink_concentration)
os.makedirs(experiment_dir, exist_ok=True)

# Camera Setup
sidecamera = Picamera2(0)
topcamera = Picamera2(1)

# Camera Configuration
camera_resolution = (4096, 2160)
topcamera.configure(topcamera.create_preview_configuration(main={"size":
camera_resolution}))
sidecamera.configure(sidecamera.create_preview_configuration(main={"size":
camera_resolution}))

# Start Previews and Cameras
topcamera.start_preview(Preview.QTGL, x=10, y=20, width=800, height=600)
topcamera.start()
topcamera.set_controls({"AfMode": controls.AfModeEnum.Continuous})  # Enable
autofocus
sidecamera.start_preview(Preview.QTGL, x=810, y=20, width=800, height=600)
sidecamera.start()
sidecamera.set_controls({"AfMode": controls.AfModeEnum.Continuous})

try:
    while True:
        num_layers = input("Number of layers: ")

        # Trigger Autofocus on both cameras
        topcamera.set_controls({"AfMode": controls.AfModeEnum.Continuous})
        sidecamera.set_controls({"AfMode": controls.AfModeEnum.Continuous})

        print("Autofocusing...")
```

```
        # Delay for 5 seconds while autofocus completes
        sleep(10)  # 5-second delay for autofocus to settle

        # Capture images and save
        top_image_path = os.path.join(experiment_dir, f"{num_layers}_layers_top.jpg")
        side_image_path = os.path.join(experiment_dir,
f"{num_layers}_layers_side.jpg")
        topcamera.capture_file(top_image_path)
        sidecamera.capture_file(side_image_path)

        print(f"Original image saved for {num_layers} layers in {experiment_dir}")

        # Prompt to continue or stop
        continue_experiment = input("Continue? (y/n): ")
        if continue_experiment.lower() == 'n':
            break
except Exception as e:
    print(f"An error occurred: {e}")
finally:
    # Clean up resources
    topcamera.stop_preview()
    sidecamera.stop_preview()
    topcamera.close()
    sidecamera.close()
```

APPENDIX J

HARMONICS HEAT MAPS

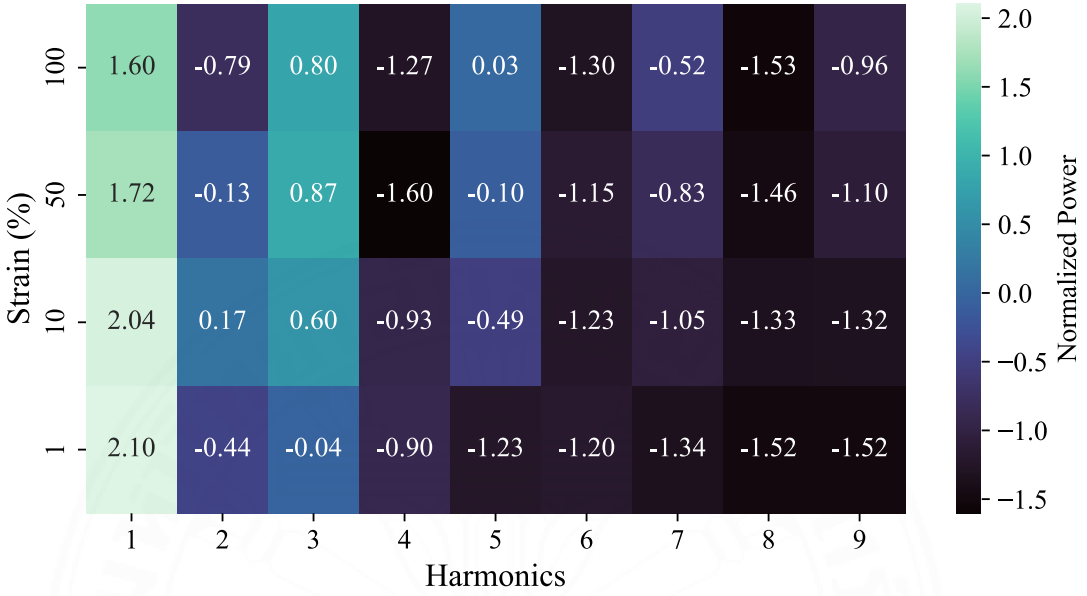

Figure J.1 Harmonics heat map analysis for MB15PT2 at 1 rad.s^{-1}.

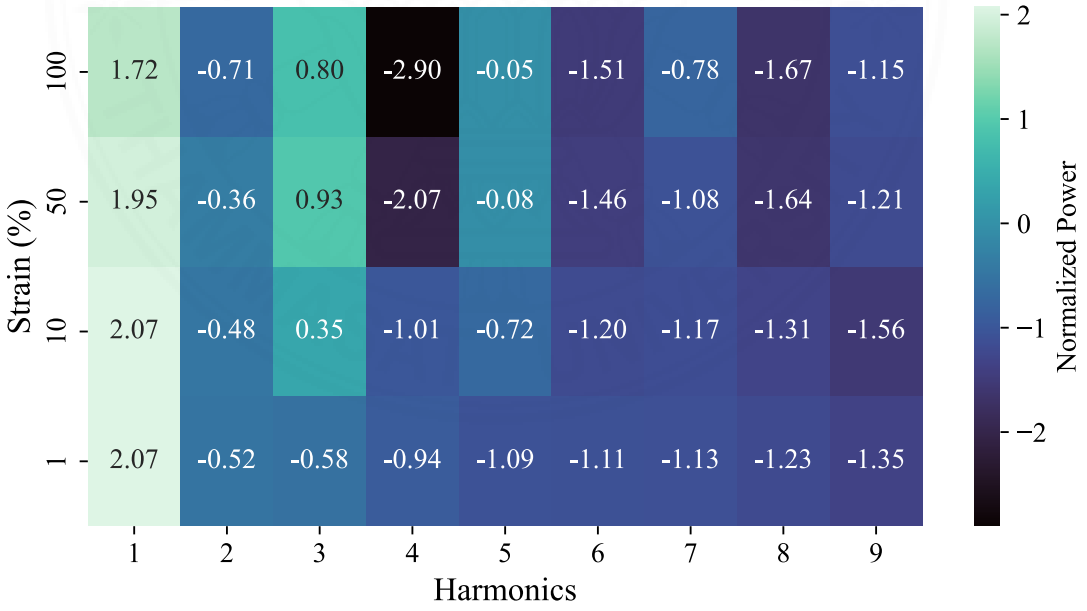

Figure J.2 Harmonics heat map analysis for MB15PT4 at 1 rad.s^{-1}.

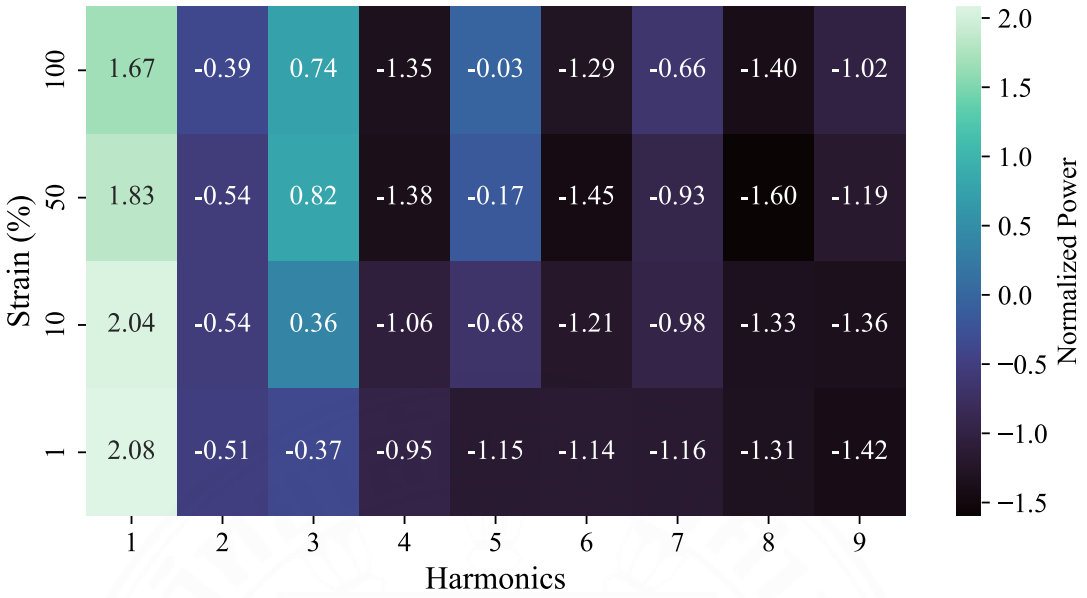

Figure J.3 Harmonics heat map analysis for MB17.5PT2 at 1 rad.s^{-1}.

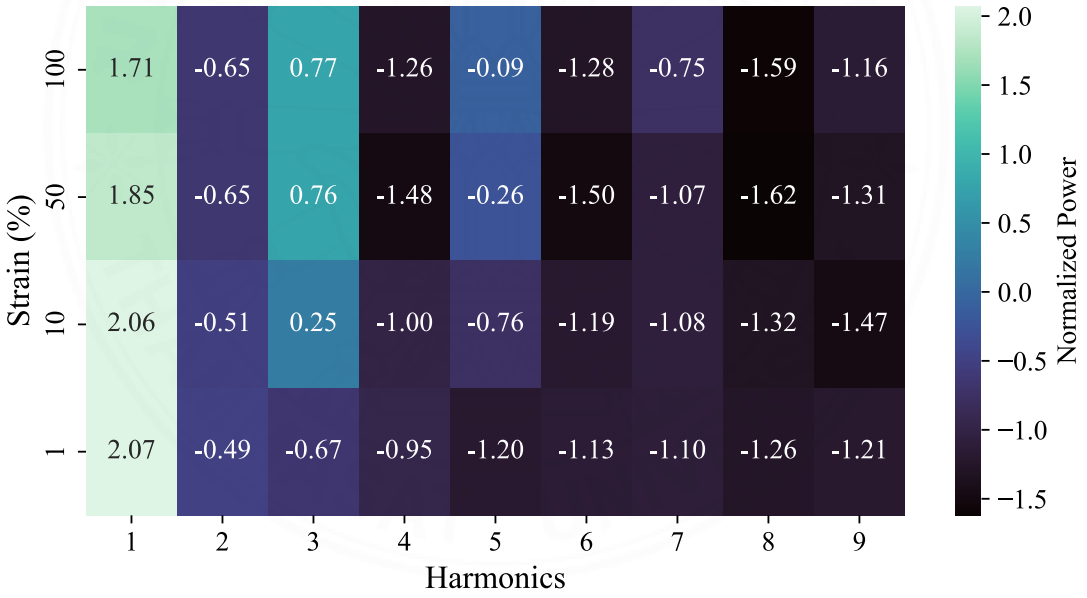

Figure J.4 Harmonics heat map analysis for MB17.5PT4 at 1 rad.s^{-1}.

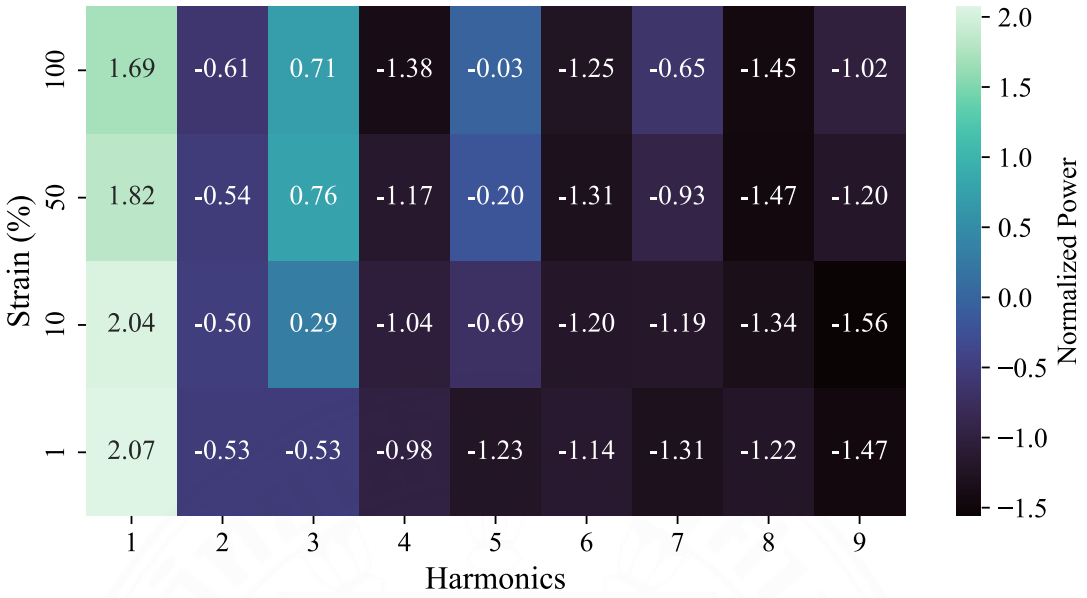

Figure J.5 Harmonics heat map analysis for MB20PT2 at 1 rad.s^{-1}.

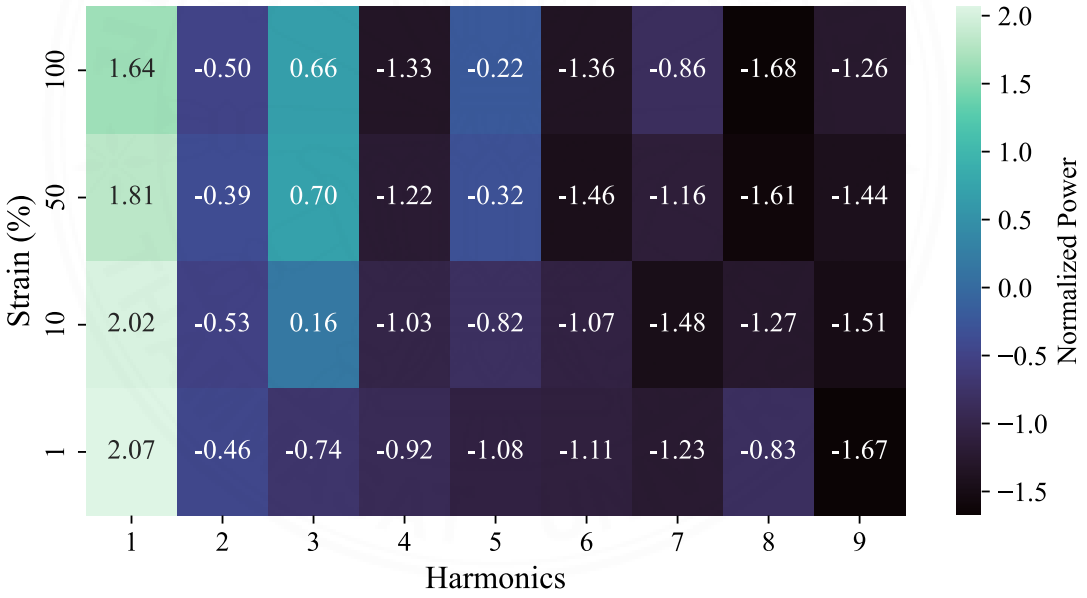

Figure J.6 Harmonics heat map analysis for MB20PT4 at 1 rad.s^{-1}.

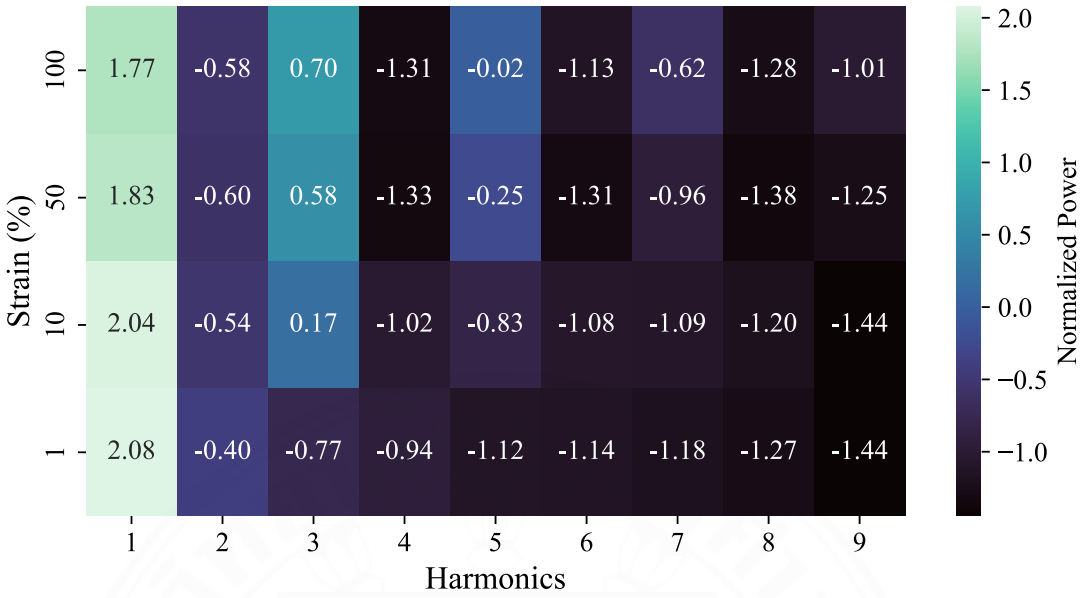

Figure J.7 Harmonics heat map analysis for MB22.5PT2 at 1 rad.s^{-1}.

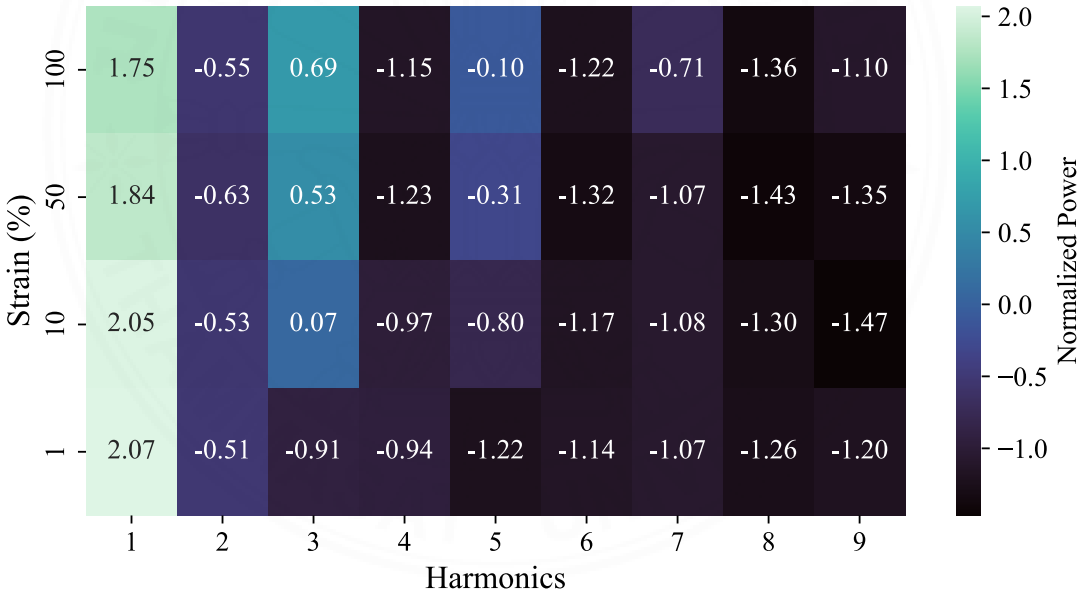

Figure J.8 Harmonics heat map analysis for MB22.5PT4 at 1 rad.s^{-1}.

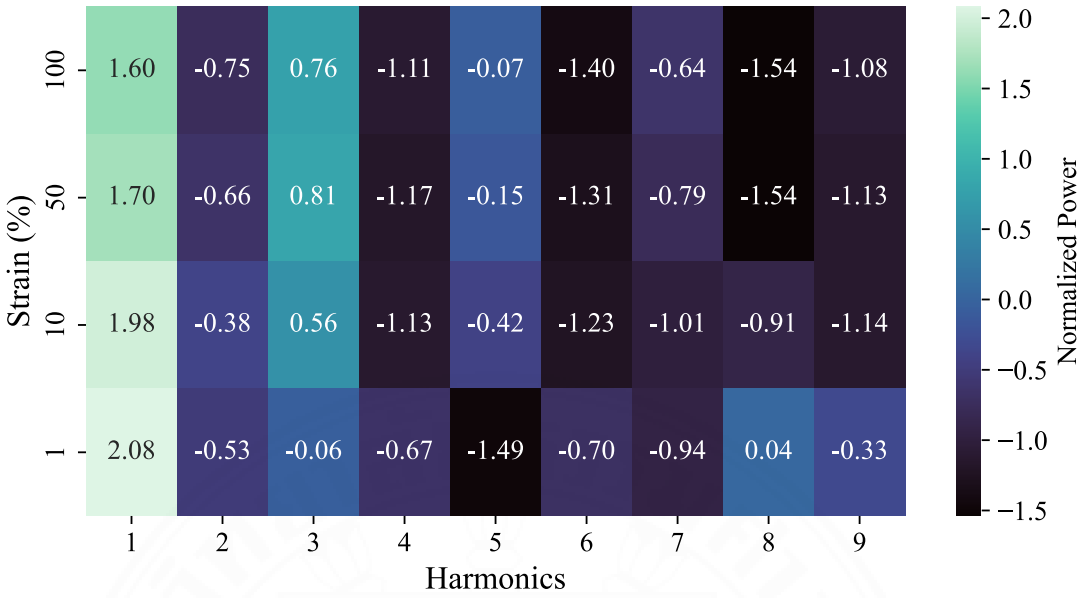

Figure J.9 Harmonics heat map analysis for MB15PT2 at 10 rad.s^{-1}.

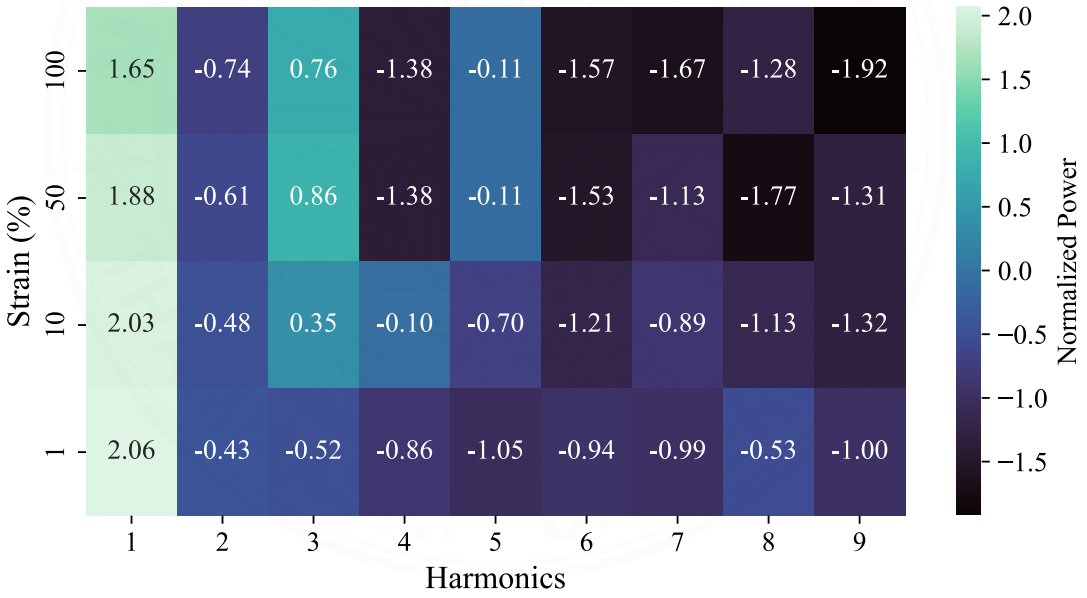

Figure J.10 Harmonics heat map analysis for MB15PT4 at 10 rad.s^{-1}.

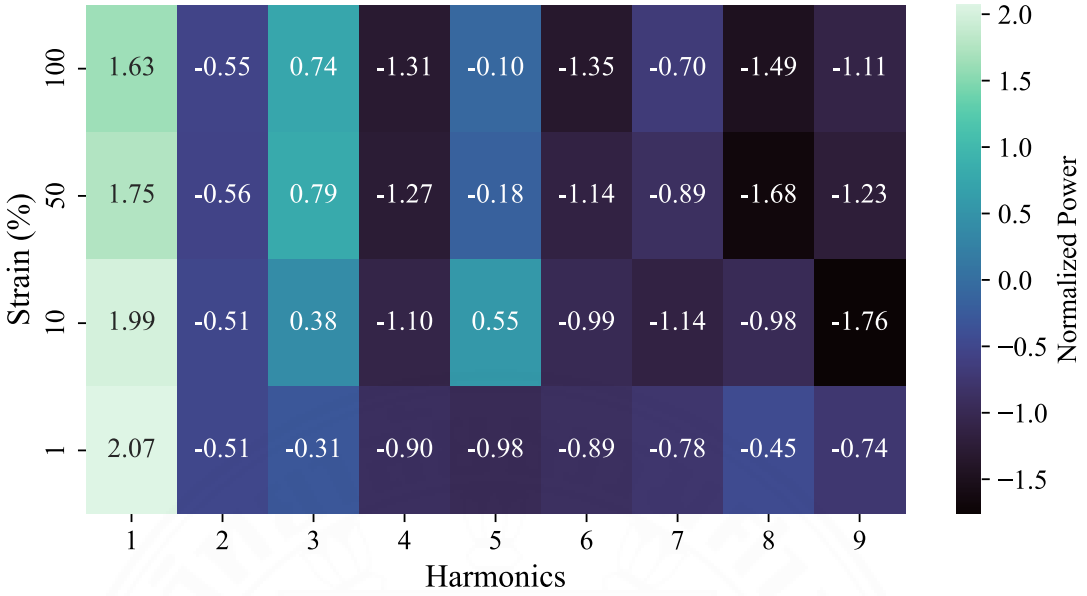

Figure J.11 Harmonics heat map analysis for MB17.5PT2 at 10 rad.s^{-1}.

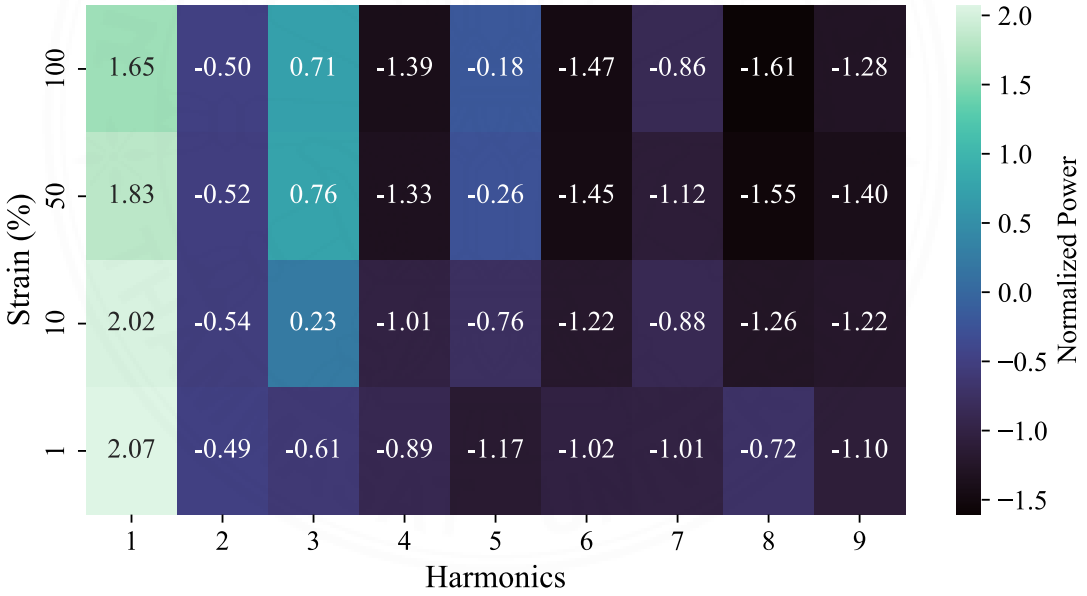

Figure J.12 Harmonics heat map analysis for MB17.5PT at 10 rad.s^{-1}.

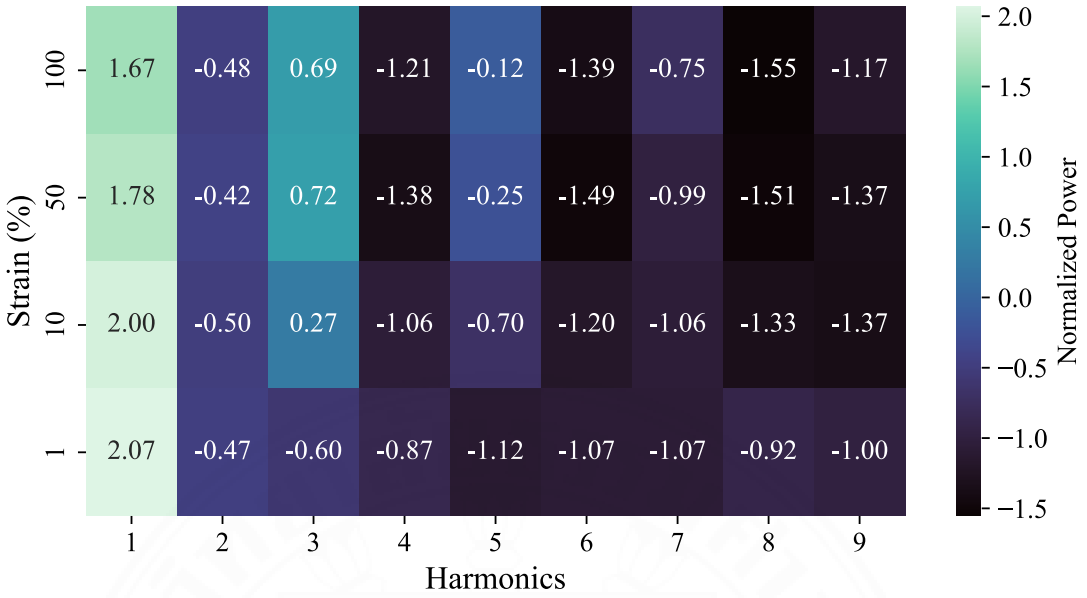

Figure J.13 Harmonics heat map analysis for MB20PT2 at 10 rad.s^{-1}.

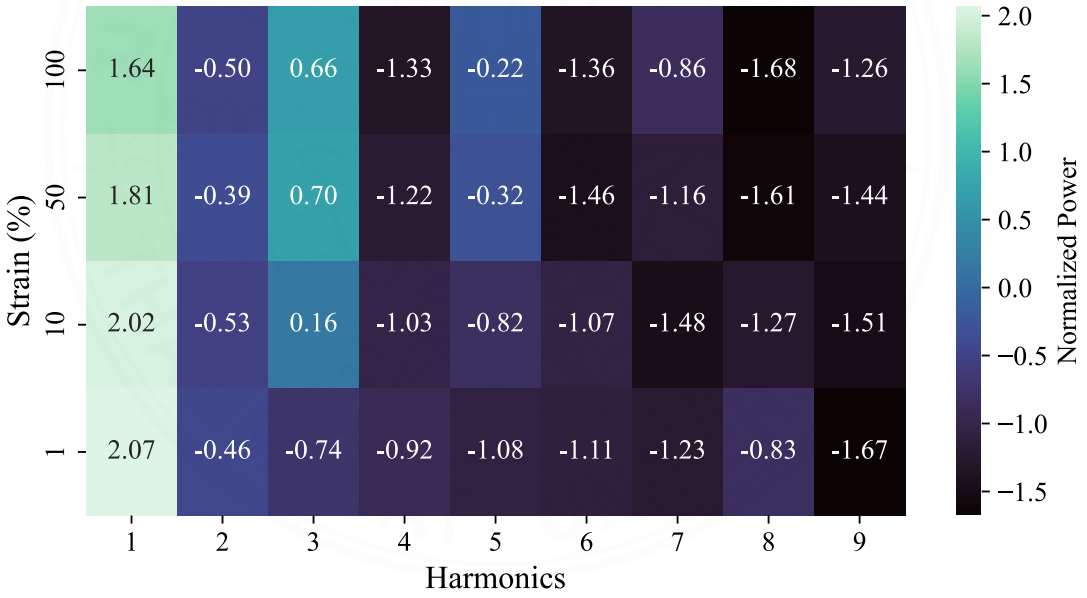

Figure J.14 Harmonics heat map analysis for MB20PT4 at 10 rad.s^{-1}.

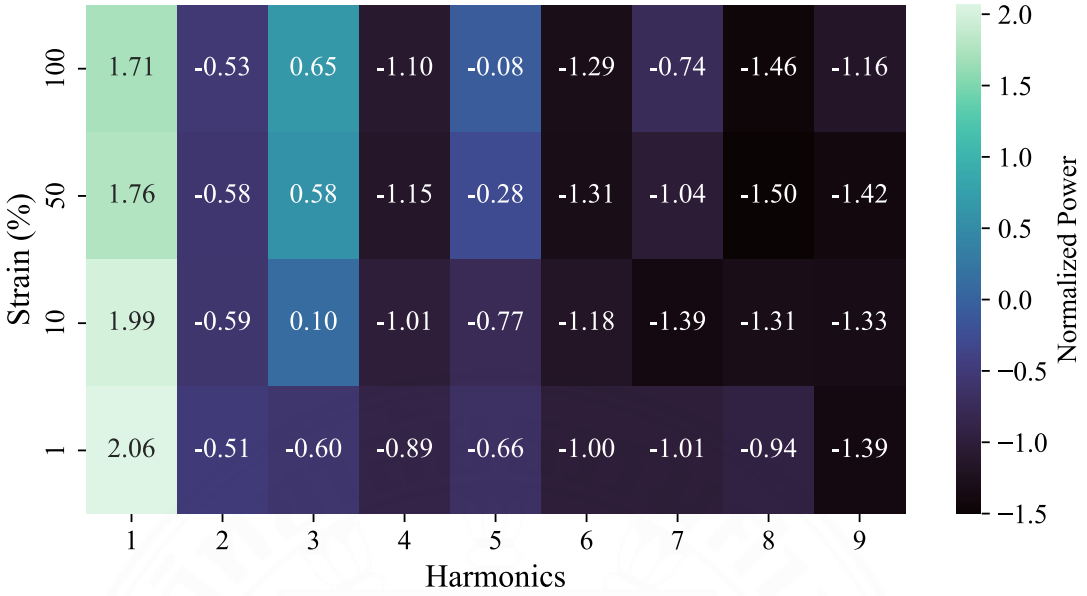

Figure J.15 Harmonics heat map analysis for MB22.5PT2 at 10 rad.s^{-1}.

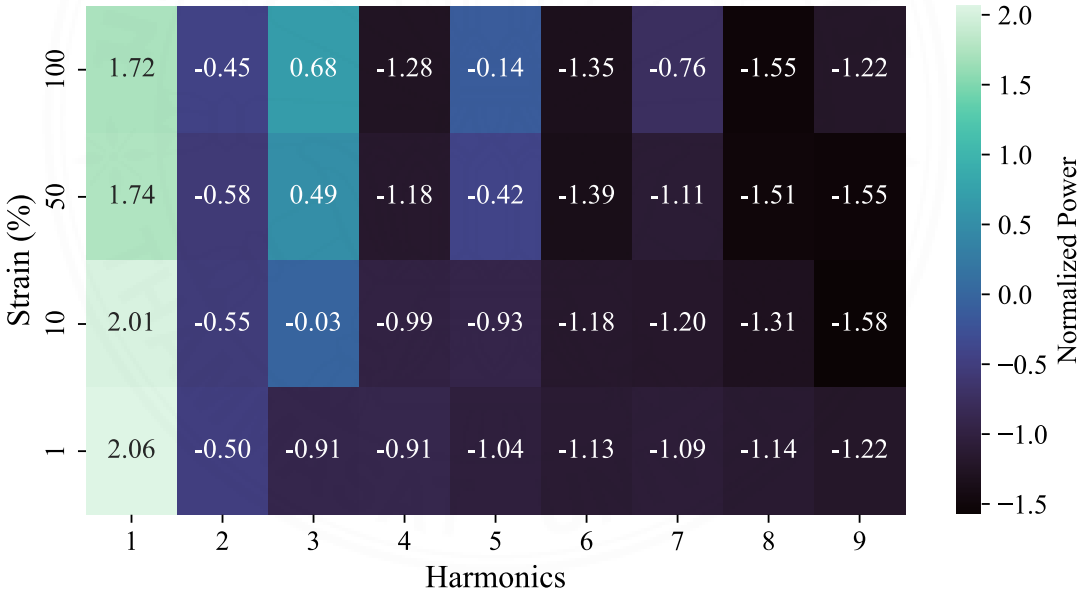

Figure J.16 Harmonics heat map analysis for MB22.5PT4 at 10 rad.s^{-1}.

APPENDIX K
VISCOUS PIPKIN DIAGRAM

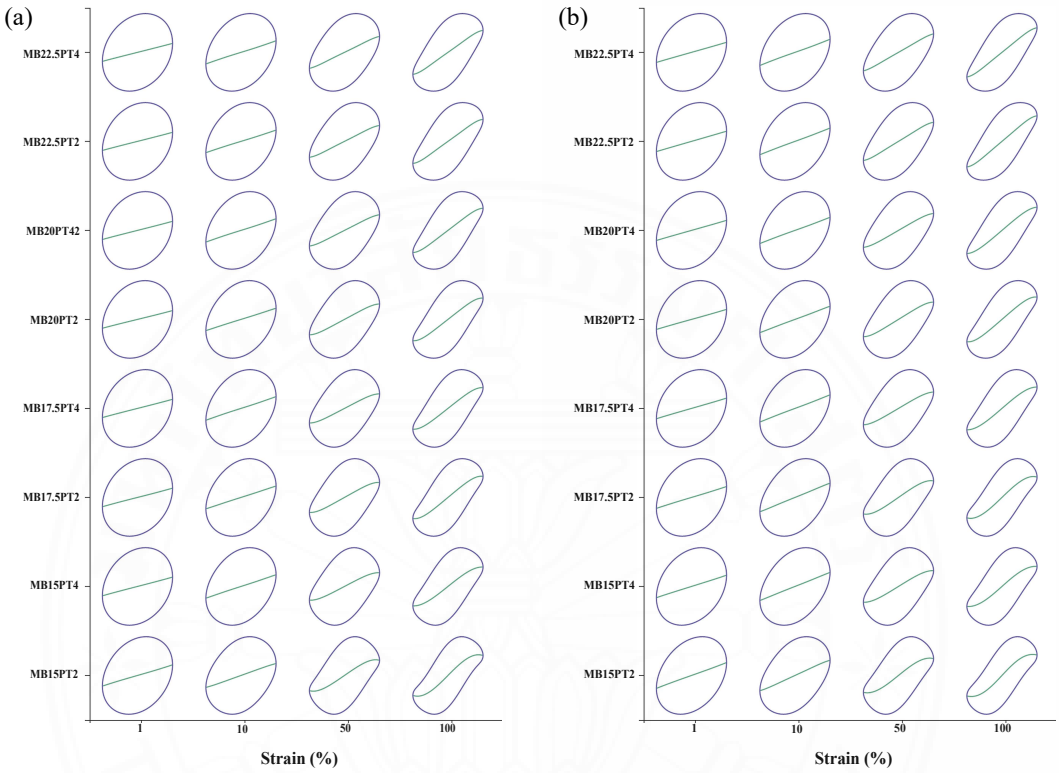

Figure K.1 Viscous Pipkin diagram at (a) 1 rad.s^{-1}. (b) 10 rad.s^{-1}.

APPENDIX L
ELASTIC PIPKIN DIAGRAM ACROSS SAMPLE

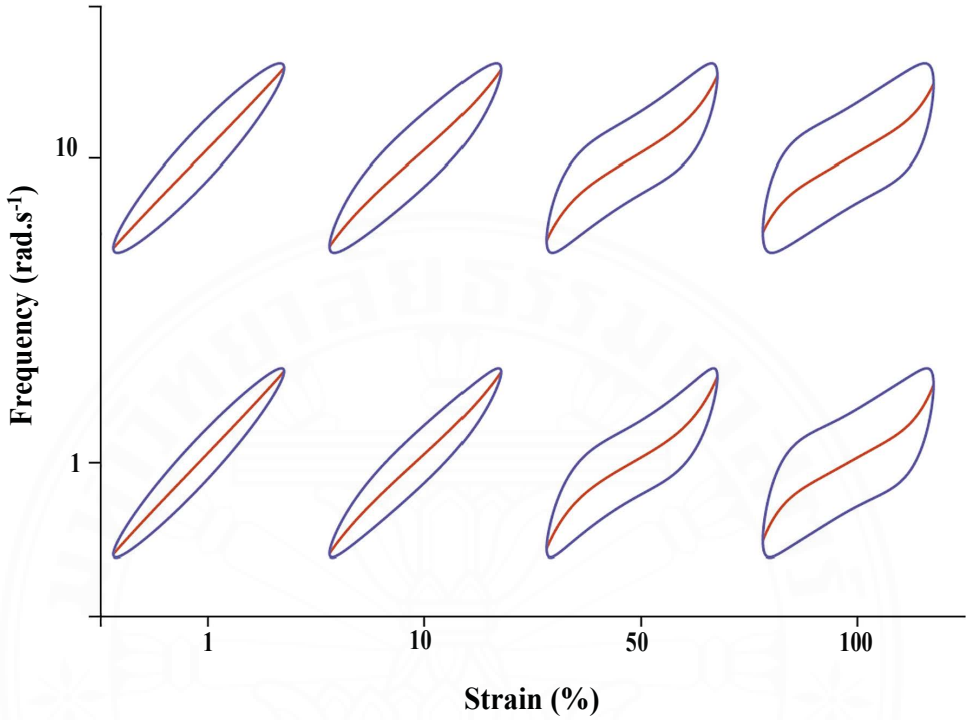

Figure L.1 MB15PT2 Elastic Pipkin diagram at varied frequencies.

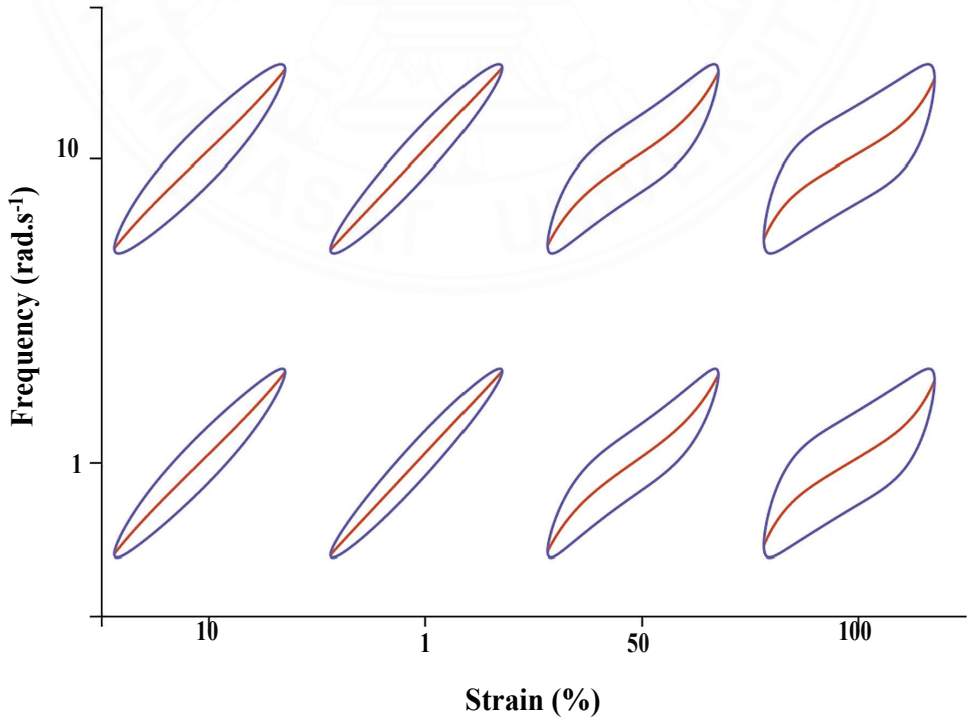

Figure L.2 MB15PT4 Elastic Pipkin diagram at varied frequencies.

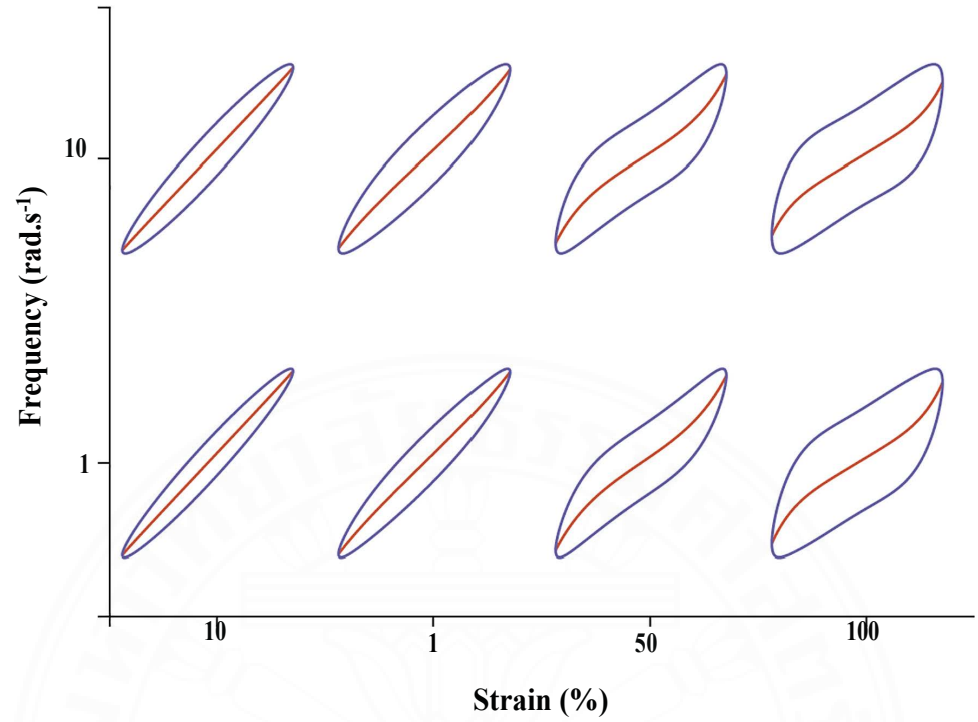

Figure L.3 MB17.5PT2 Elastic Pipkin diagram at varied frequencies.

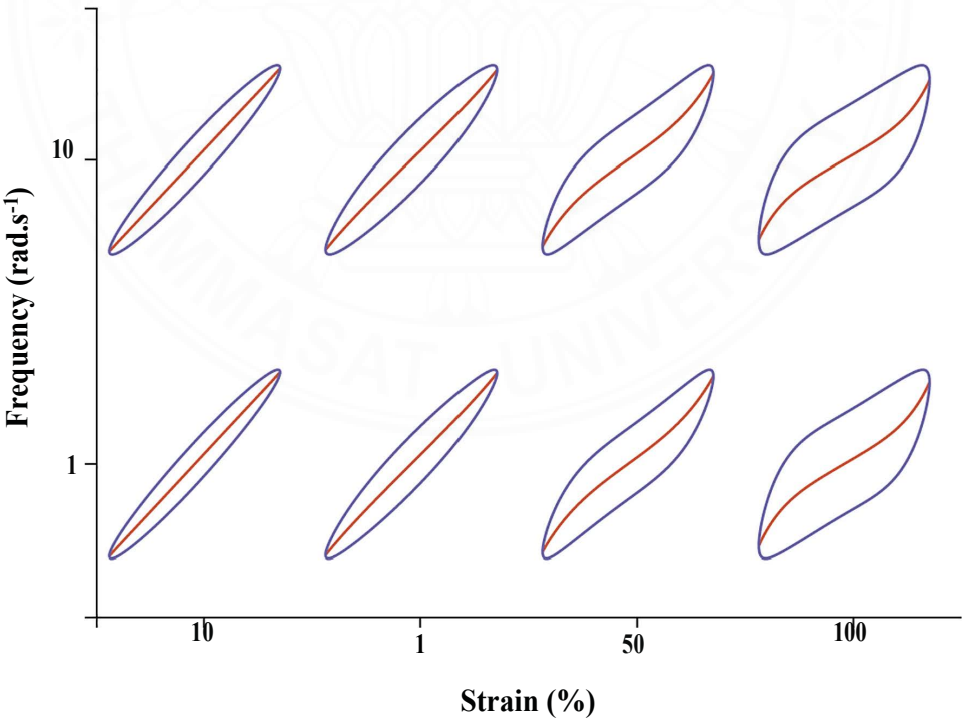

Figure L.4 MB17.5PT4 Elastic Pipkin diagram at varied frequencies.

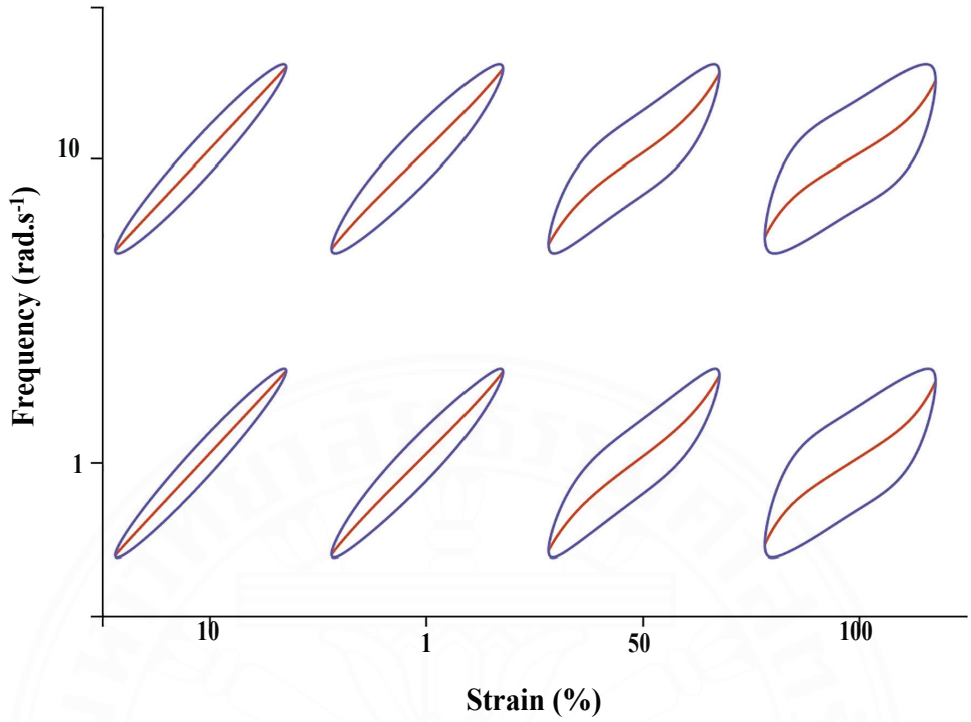

Figure L.5 MB20PT2 Elastic Pipkin diagram at varied frequencies.

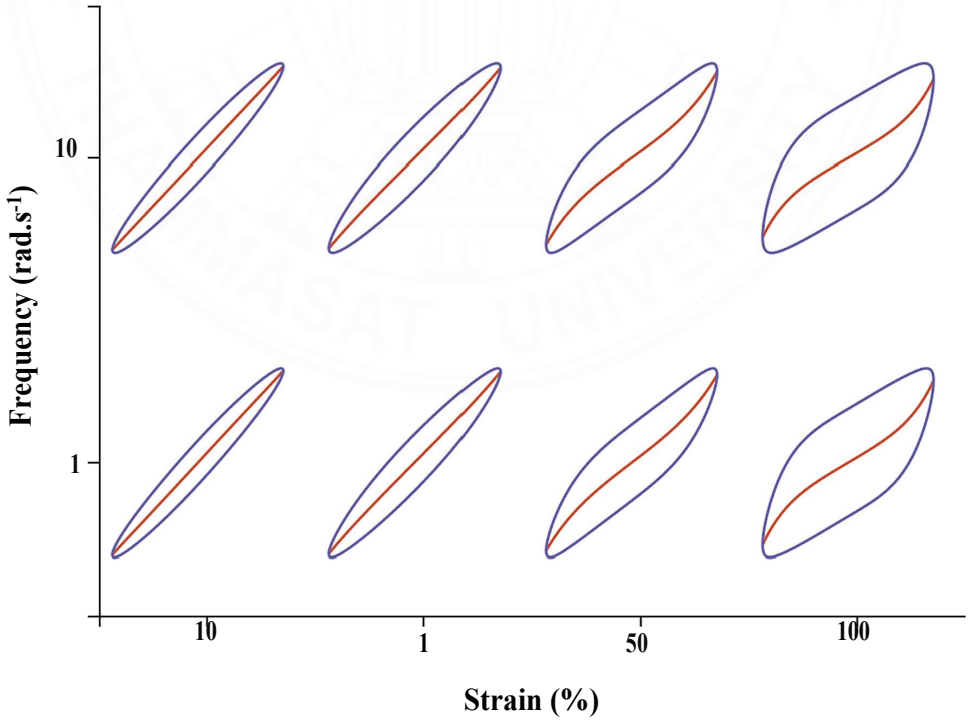

Figure L.6 MB20PT4 Elastic Pipkin diagram at varied frequencies.

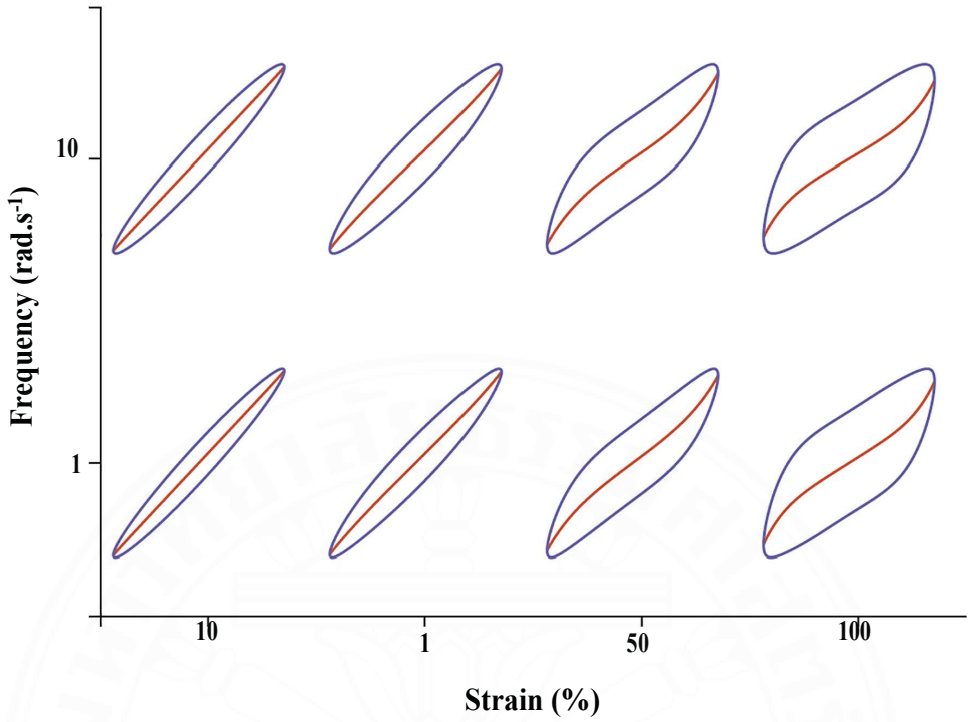

Figure L.7 MB22.5PT2 Elastic Pipkin diagram at varied frequencies.

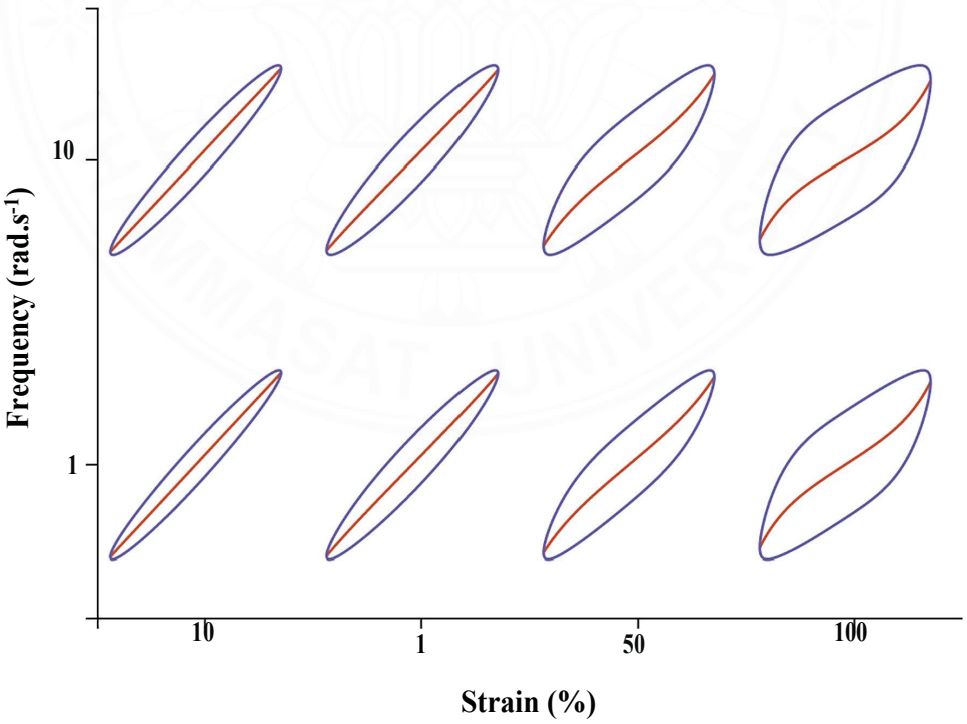

Figure L.8 MB22.5PT4 Elastic Pipkin diagram at varied frequencies.

APPENDIX M
VISCOUS PIPKIN DIAGRAM ACROSS SAMPLE

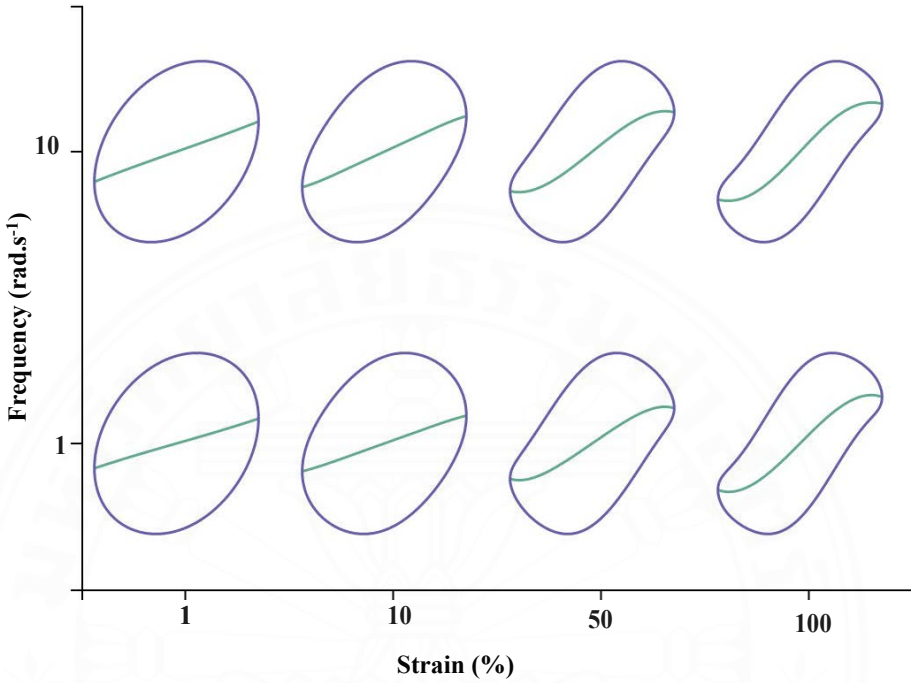

Figure M.1 MB15PT2 Viscous Pipkin diagram at varied frequencies.

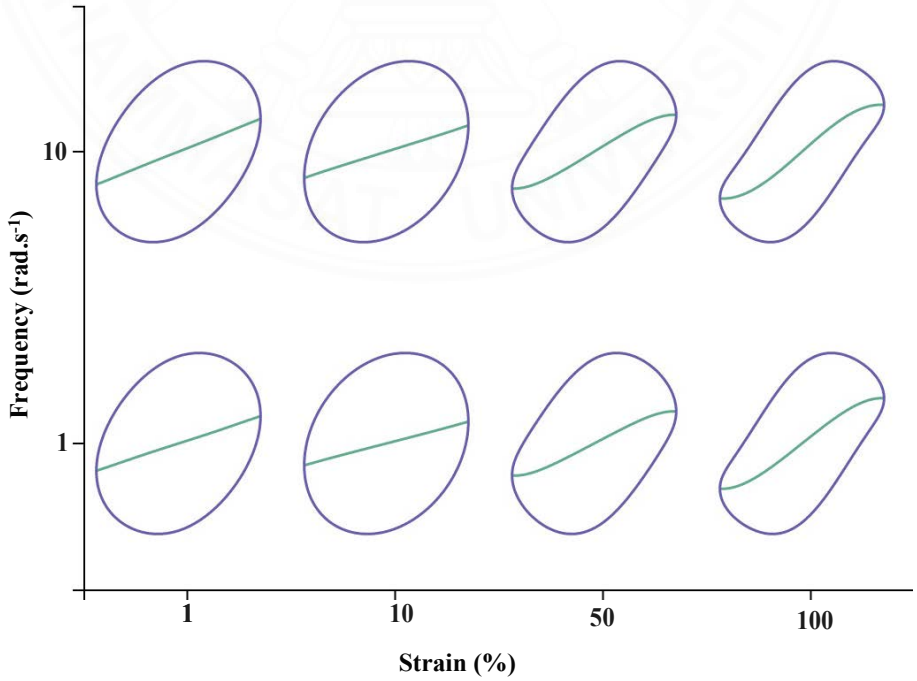

Figure M.2 MB15PT4 Viscous Pipkin diagram at varied frequencies.

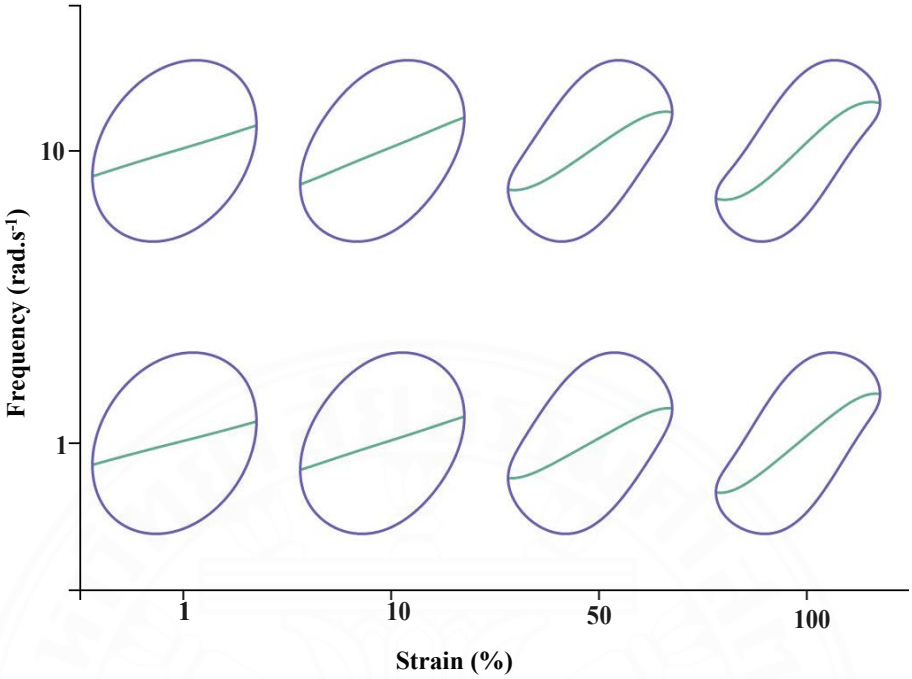

Figure M.3 MB17.5PT2 Viscous Pipkin diagram at varied frequencies.

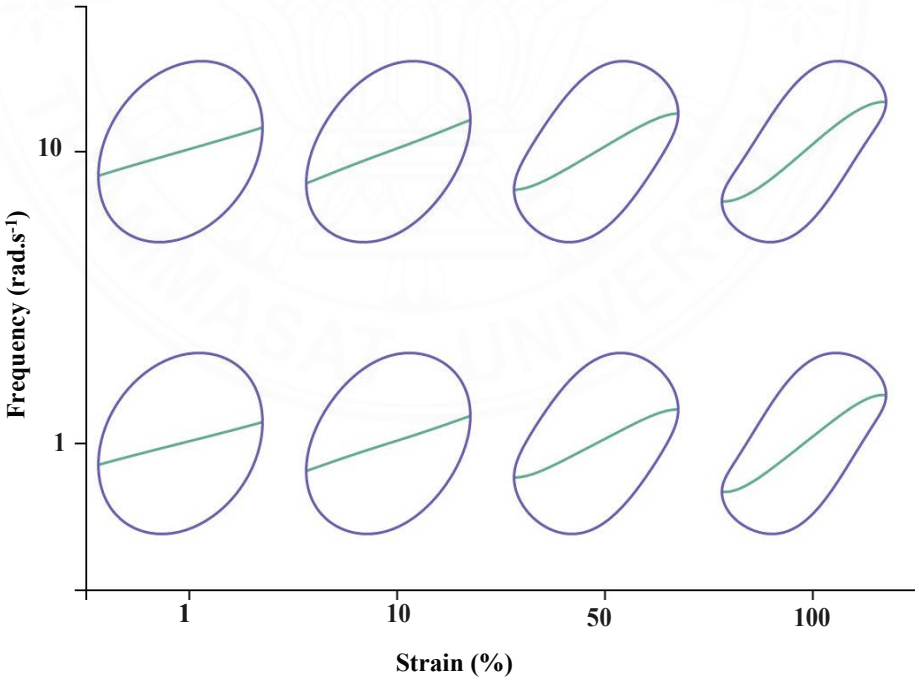

Figure M.4 MB17.5PT4 Viscous Pipkin diagram at varied frequencies.

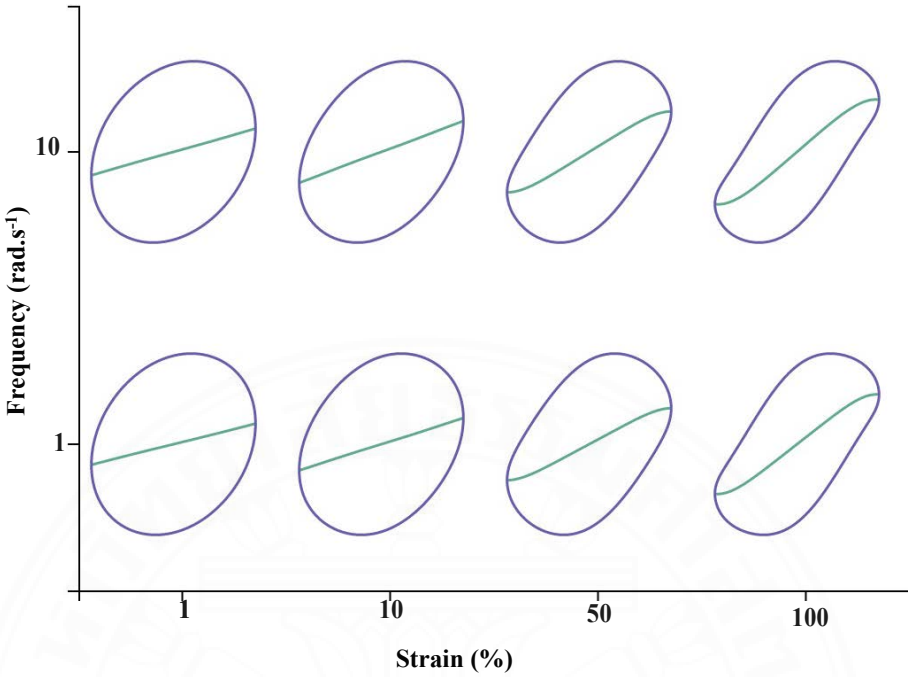

Figure M.5 MB20PT2 Viscous Pipkin diagram at varied frequencies.

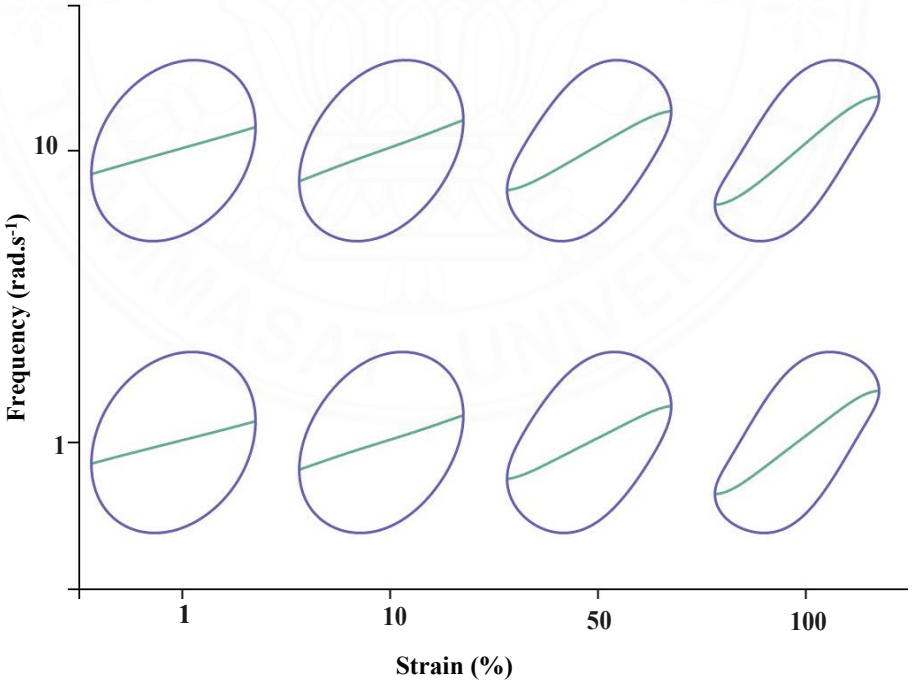

Figure M.6 MB20PT4 Viscous Pipkin diagram at varied frequencies.

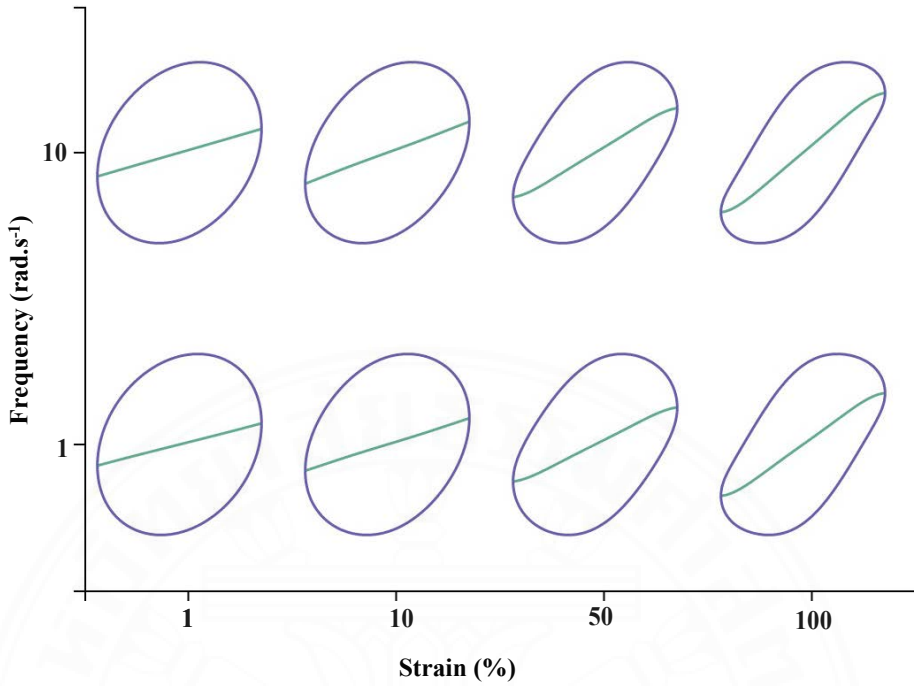

Figure M.7 MB22.5PT2 Viscous Pipkin diagram at varied frequencies.

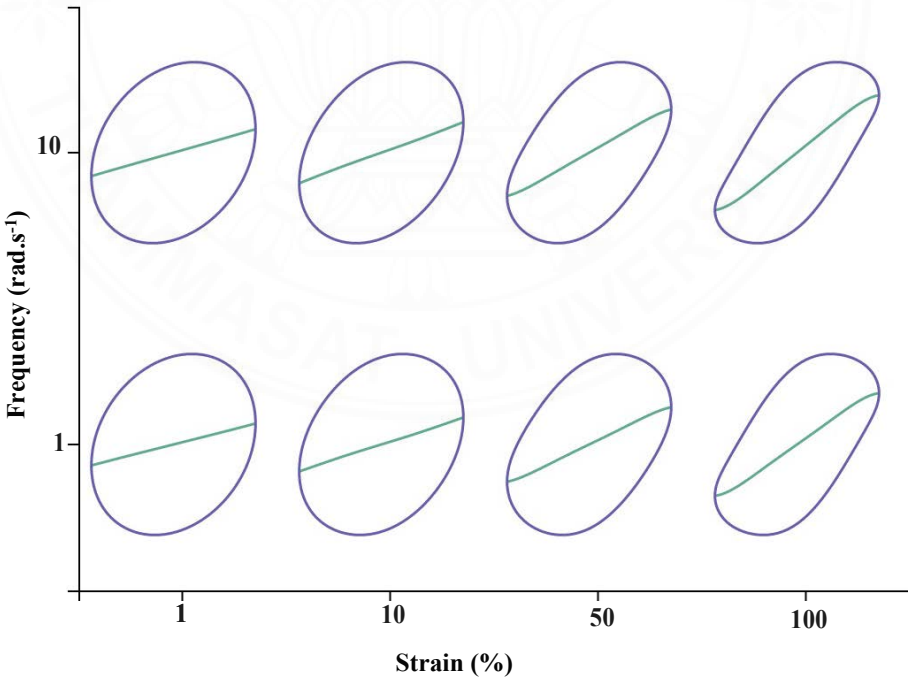

Figure M.8 MB22.5PT4 Viscous Pipkin diagram at varied frequencies.

BIOGRAPHY

Name	Théo Claude Roland Outrequin
Education	2017: Bachelor of Science, National Graduate School of Chemistry and Chemical Engineering of Lille, France 2020: Master of Science (Formulation Chemistry, Chemistry and Chemical Engineering) National Graduate School of Chemistry and Chemical Engineering of Lille, France

Publications

Outrequin, T.C.R., Gamonpilas, C., Deepaisarn, S., Sreearunothai, P. & Siriwatwechakul, W. (2024). Machine Learning assisted evaluation of the filament spreading during extrusion-based 3D food printing: Impact of the rheological and printing parameters. *Journal of Food Engineering, 381,* 112166.

Outrequin, T.C.R., Gamonpilas, C., Siriwatwechakul, W. & Sreearunothai, P. (2023). 3D food printing of biopolymers: effect of the rheological properties and printing parameters on the spreading of pectin inks. Proceedings of the *13th International Polymer Conference of Thailand* (pp. 78-84).

Outrequin, T.C.R., Gamonpilas, C., Siriwatwechakul, W. & Sreearunothai, P. (2023). Extrusion- based 3D printing of food biopolymers: A highlight on the important rheological parameters to reach printability. *Journal of Food Engineering, 342,* 111371.

Buathongjan, C., Israkarn, K., Sangwan, W., Outrequin, T., Gamonpilas, C. & Methacanon, P. (2020). Studies on chemical composition, rheological and antioxidant properties of pectin isolated from Riang (Parkia timoriana (DC.)

Merr.) pod. *International Journal of Biological Macromolecules, 164,* 4575-4582.

Oney, C. L., Outrequin, T., Hubert, C., Yan, X., Arafa, M., Gathercole, N. & Bowen, C. R. (2019). A Novel Arch-Shaped Hybrid Composite Triboelectric Generator Using Carbon Fiber Reinforced Polymers. *Energy Technology, 7*(6), 1801005.